Naresh Kumar Thakur
Sanjeev Rajput

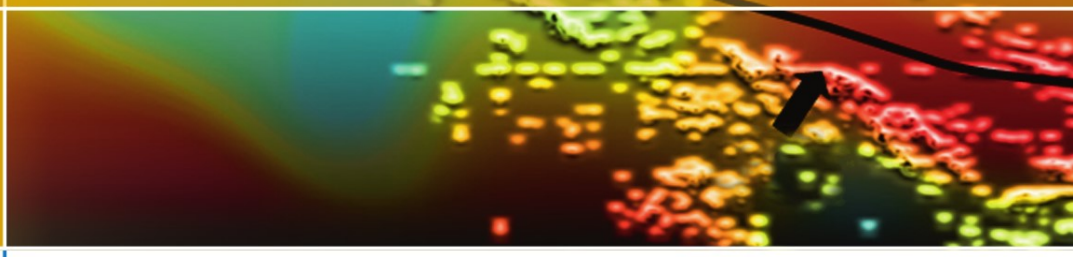

Exploration of Gas Hydrates

Naresh Kumar Thakur • Sanjeev Rajput

Exploration of Gas Hydrates

Geophysical Techniques

Springer

Dr. Naresh Kumar Thakur
National Geophysical Research
Institute (CSIR)
Uppal Road
Hyderabad, Andhra Pradesh
India, 500007
nkthakur46@gmail.com

Dr. Sanjeev Rajput
CSIRO Petroleum Resources
ARRC
26 Dick Perry Ave, Kensington,
Perth, Western Australia, 6151
Australia
Sanjeev.Rajput@csiro.au

ISBN 978-3-642-14233-8 e-ISBN 978-3-642-14234-5
DOI 10.1007/978-3-642-14234-5
Springer Heidelberg Dordrecht London New York

Library of Congress Control Number: 2010937767

Cover design: deblik, Berlin

Printed on acid-free paper

Springer is part of Springer Science+Business Media (www.springer.com)

Preface

"*Exploration of Gas Hydrates: Geophysical Techniques*" adds an important dimension to the story of Natural Gas Hydrates from an energy perspective. Natural Gas Hydrates present an enormous opportunity and also a series of challenges if they are to be exploited on a large scale to bring vast quantities of a relatively clean fuel to market. Among these challenges, characterization and especially quantification of the methane hydrate resource present on our continental margins is of primary concern at this point in time. Geophysics is the best tool we have to meet this challenge.

Seismic reflection methods have been used for several decades as the primary means to detect of gas hydrates in continental margins. However, while the detection of gas hydrates in marine sediments is relatively straightforward from analysis of the anomalous amplitude and phase of reflectors, the accurate determination of gas hydrate quantities in subsurface space is an altogether more difficult task. As a pre-requisite, seismic acquisition parameters must be specified that adequately illuminate and sample the subsurface in a highly repeatable way, and with sufficient spatial resolution and dynamic range for the task. This requires "industry standard" seismic acquisition equipment and protocols rather than the more common standards used for academic research. Even then, quantification of gas hydrate and free gas volumes is only possible by taking a highly systematic approach to seismic data processing and analysis that incorporates forward modelling, inversion and calibration steps. The data analysis must be conducted within the proper geological context, which informs realistic and sufficiently flexible rock physics models of the sediment-fluid-hydrate-gas system.

While seismic methods remain at the cornerstone of geophysical assessment of hydrate resources, the increasing role and value of marine controlled source electromagnetic methods is also well demonstrated. Resistivity responses to hydrate and gas volumes are generally more linear than the seismic responses, and taken together, electromagnetics plus seismics provide an excellent framework for reducing uncertainties in rock property assignments and therefore volumetric calculations of hydrates and gas in place. Downhole logging, direct sampling and

geochemical analysis then provide the final ground-truth needed to validate and calibrate the rock physics models used in the three-dimensional Earth volume.

This book outlines such an approach to quantitative geophysical data analysis, with special reference to India's National Gas Hydrates research programme. While making excellent use of the experience of this concerted effort in marine geophysical, geological investigations on the continental margins of the Indian Subcontinent, the authors have also drawn upon type examples from many other localities worldwide where hydrates have been studied in detail. This compilation of real data examples, with good quality figures and explanations is an especially valuable resource for scientists interested in natural gas hydrate occurrences and their geophysical expression.

Doctors Thakur and Rajput have put in one place an up-to-date review of geophysical methods applied to methane hydrate resource evaluation, and provided the big picture context to reinforce the relevance of this topic to a wider audience.

Perth, WA, Australia Ben Clennell
26 August, 2010

Contents

Chapter 1
Introduction

Abstract Energy is the integral part for the sustenance of human beings. The resources that are being used for generation of energy have to be efficient in terms of economics and emitting least pollutants. Energy derived from fossil fuels resources (fossil fuel energy) is primarily utilized for generation of electricity, industrial production and other day-to-day necessities of the life. Petroleum i.e. oil, natural gas (primarily methane) and coal are the main constituents of the fossil fuel. Energy derived from geothermal resources contributes to about 0.3% with electricity generating capacity of global energy consumption. Primary geothermal provinces are located in tectonic regions are confined to rims of the Pacific Ocean; the region characterized by most active earthquakes and volcanoes and is popularly called the Ring of Fire. Another important energy resource that is extensively promoted is the use of nuclear energy. The energy produced by the fission process is about millions of times the energy produced by the combustion of an atom of carbon from coal. Different forms of energy associated with natural resources such as sun (solar energy) and oceans are quite extensive and inexhaustible and considered as renewable form of energy. The kinetic energy associated with wind, tides, oceanic waves can be utilized to generate electricity. The potential and kinetic energy associated with hydrothermal means and being utilized for generation of electricity works out to be most cost effective and least pollutant. This chapter provides an overview of different forms of energy and their impact on human life.

1.1 Introduction

Ever since time immemorial energy has become the integral part for the survival human beings. The mankind has been constantly putting endeavors to optimize and utilize natural resources as source of energy to meet the growing need of the energy and welfare of society. The availability of different forms resources in a region governs their utilization as energy. Efforts have to be made to harness resources to

N.K. Thakur and S. Rajput, *Exploration of Gas Hydrates*,
DOI 10.1007/978-3-642-14234-5_1,

create energy which is preserved different materials and in different state. Most of the extracted energy is consumed for the generation of electricity, industrial production and mode of transportation. Total worldwide energy consumption was 500 exajoules ($= 5 \times 10^{20}$ J) with 80–90% derived from the combustion of fossil fuels. The ever increasing demand for energy has necessitated looking for efficient and cost effective form of energy and its prolonged availability. The efficiency in normal sense is described as the best possible way a resource is to be utilized to get the maximum output. The performance based efficiency and cost effectiveness of the energy is estimated in terms of amount of energy consumed like for generating a kWh electricity and emission of pollutant and its contribution to greenhouse effect. Percentage wise efficiency for the generation of electricity indicates substantial variation in working efficiency for different form of energy (Corradini 2005, Fig. 1.1). Electricity generated by hydro power plant provides most efficient and moderate cost effective means for production of electricity. The other parameter that defines the efficiency is governed by the quantum of different greenhouse gases emitted in the atmosphere by the combustion/utilization of particular form of energy. Emission of CO_2 in the atmosphere for different energy resource for generating kWh is given in Fig. 1.2 (Corradini 2005). In terms of emission of CO_2 to the atmosphere, combustion of biomass and coal contribute maximum green house effect and to the global warming. Hydropower plants hardly produce any emission of gases and thereby least possibility of its contribution to green house effect.

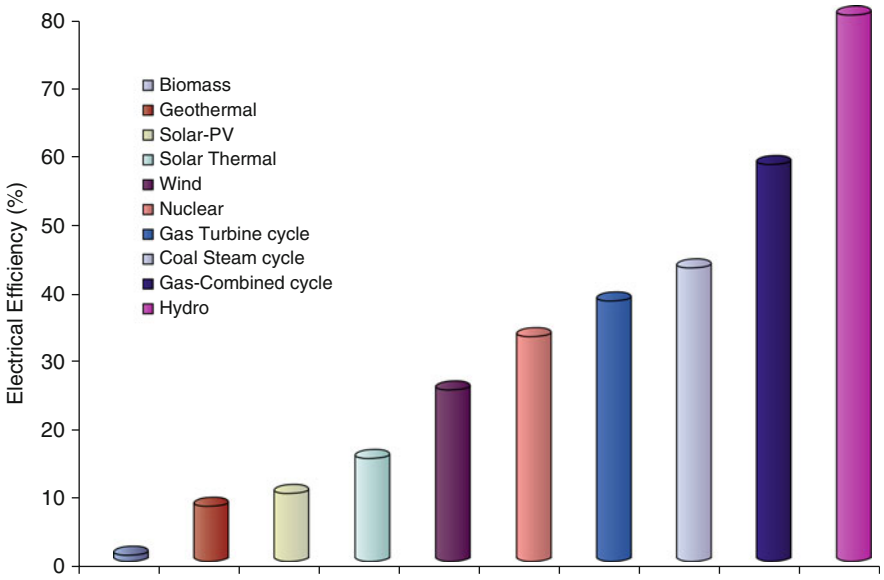

Fig. 1.1 Percentage efficiency of different energy resources for the generation of electricity (modified from Corradini 2005) Nuclear Power: Secure Energy for the 21st Century
Source: http://www.docstoc.com/docs/14677528/NUCLEAR-POWER

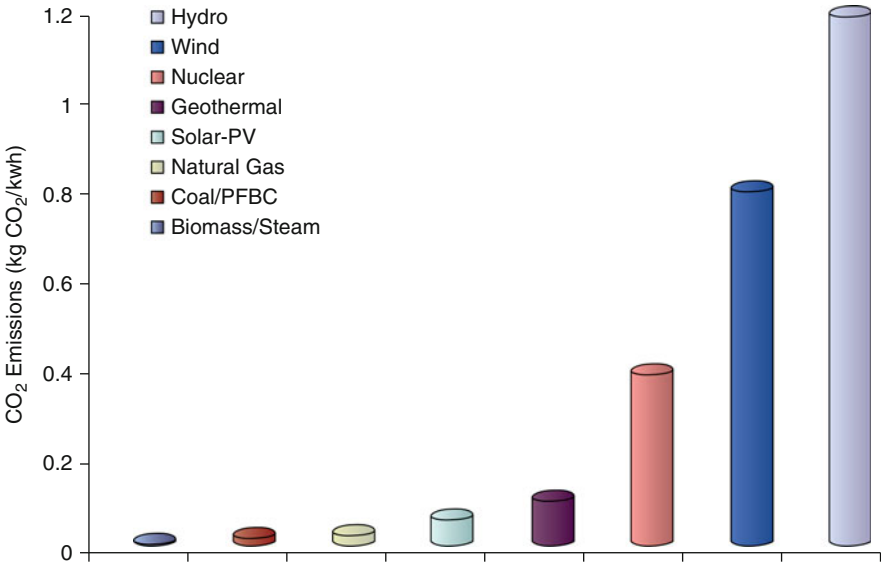

Fig. 1.2 CO2 emission in the atmosphere by utilizing different energy resources. (Modified from Corradini 2005) Nuclear Power: Secure Energy for the twenty-first Century
Source: http://www.docstoc.com/docs/14677528/NUCLEAR-POWER

However, the aspect of consumption differs for developed and underdeveloped countries. Energy consumption is high in most developed countries. On the other hand, the developing countries need to consume more energy to ensure economic growth. According to estimates, energy consumption in developing countries is only one-tenth of that in the developed countries. It is estimated that 80% population in developing countries consume only about 40% of the global energy resources whereas developed countries use higher percentage energy resources of the world.. Even pattern of resource consumption differs from developed to developing countries. The developed countries utilize more oil, natural gas and nuclear power, in contrast coal and hydro power are the main forms of energy being utilized by less developed nations. Figure 1.3 gives global pattern consumption of different forms of natural resources being utilized as means of energy. Fossil fuels mainly, oil, natural gas and coal contribute to about 90% of global consumption as means of energy.

The primary forms of energy that are being presently consumed have limited reserves. The estimated resource potential of these reserves is upgraded on regular basis. The reserve of energy implies that a designated energy resource, which can be extracted by the present day technology. Most of the energy reserves that are being extensively consumed today are not renewable. These reserves came in to existence due to the geological processes over long period of time and cannot be replenished easily. Other energies such as wind, solar, water and geothermal

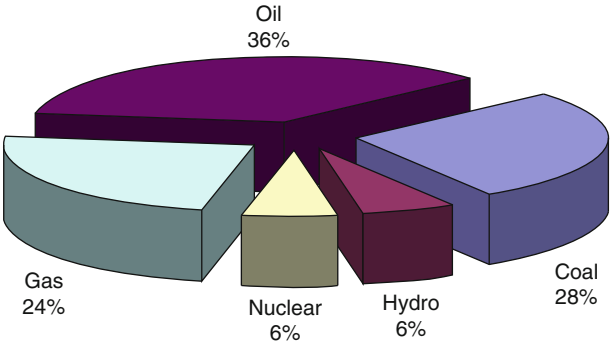

Fig. 1.3 World energy consumption 2006
Source: data from EIA and BP

energies may be considered perpetual and in this sense renewable, which means that these energies are inexhaustible.

1.2 Oil and Natural Gas

Oil and gas along with coal form the main constituents of the fossil fuels. Oil and natural gas are the most extensively used energy resource. Oil and gas and coal are the end product of degradation and decomposition of organic matter. The decomposition of organic matter in nature is a slow biological and chemical process. The organic matter derived mainly from the plants and animal remains decomposes either in aerobic (presence of oxygen) or anaerobic (without oxygen) conditions. Aerobic decomposition mainly takes place on land, where sufficient oxygen is present to make most of organism survive to act as decomposers. The carbon present in the organic matter serves as energy for organism in the process of decomposition. The presence of large amount of organic matter in the form of felled trees and animal remains provides avenues for the decomposer to survive and produce humus under aerobic conditions. On land the swamps and basins provide proper conditions for decomposition. Anaerobic conditions favor organic matter to decompose in the absence of oxygen. Such conditions prevail in bottom of swamps and shallow marine environment. In marine environment the organic matter constitutes dead remains of organisms living in the water column, such as microscopic planktons, which settle down at the sea floor. During the decomposition process the organic matter breaks down to smaller molecular composition mainly comprising elements of carbon and hydrogen due to chemical reaction. Fossil fuels have complex molecular composition. During the burial the organic matter in the sediments undergoes three different stages viz., Diagenesis, catagenesis and metamorphism. Diagenesis relates to the biological and chemical changes that organic-rich sediments under go before they are subjected to higher temperature pressure effects

(<50°C). During the diagenesis stage biological and chemical actions dominates either by oxidation or by attack by microbes thereby converting simpler molecules in to more complex molecular order. Diagenesis stage lot of biogenic gas is also produced, which cannot be preserved and is not a potential economic prospect. At Catagenesis occurs in the temperature range of 50–150°C, is most important aspect of oil and gas formation. Temperature plays important part in producing lighter hydrocarbons from higher molecular kerogens, a waxy material (polymer like structure) by breaking the carbon–carbon bounding through the process known as thermo-catalytic cracking (Robb 2005). This process predominant up to around 120°C. In the regime of metamorphism the temperature (thermal cracking) effects dominate. With increase in depth of burial and increase in temperature with depth further breaking of molecular bonds producing appreciable quantity of gas mainly methane (Fig. 1.4).

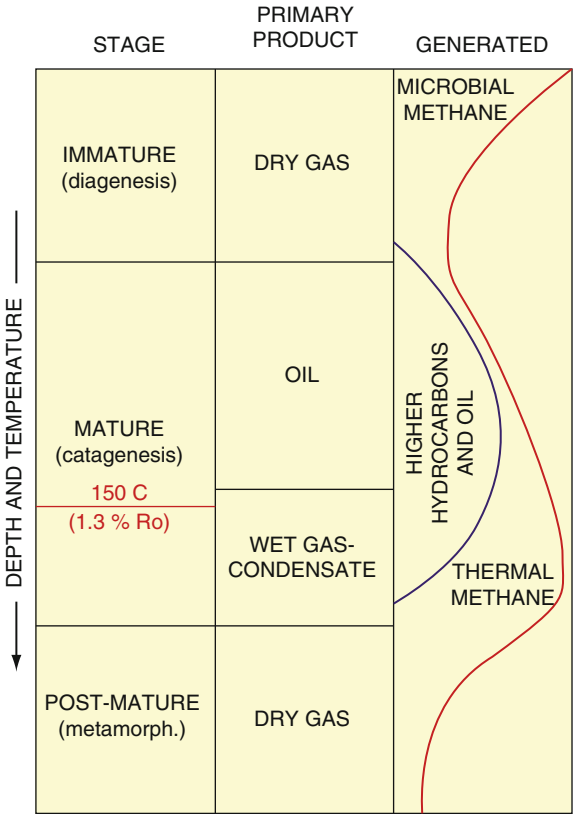

Fig. 1.4 Biogenic and thermogenic gas generation under the subsurface earth. 'Timothy S. Collet': gas hydrates-the world's largest energy resource 'But should I care' (Adapted from oral presentation of AAPG Annual Convention at San Antonio, Texas, April 20–23, 2008)

The reaction that governs the conversion of kerogen to lighter hydrocarbons is time, temperature and pressure dependent. The pressure term being insignificant, the conversion to hydrocarbon liquids or gases depends on the temperature and time. Time and temperature are inversely proportional for the formation of hydrocarbons. Historical data for the formation of oil has shown that oil cannot be produced in young oceanic basins with low geothermal gradients, on the contrary oil can not be found in old basins with high geothermal gradients. In both the aspect a proper temperature –time window is required for the maturation of organic contents for the formation of oil/gas.

Conversion to fuels even requires proper geological conditions of host rock with moderate rate of sedimentation. Oil and gas are formed where suitable biological (total organic content) and physical condition of the source rock. Oil and gas migrate from the source rocks in which they were generated to reservoir rocks that have pore spaces or fractures sufficient to store the petroleum hydrocarbons. The best reservoir rocks are those that have high permeability, which measures the degree and nature of connectivity between pore spaces. If a rock has enough porosity and permeability so that oil or gas can flow through it, then the rock is a potential productive reservoir. The amount of pore spaces depends on factors like the grain size and compaction of sediments. If even porosity is not that high, like in the case of sandstones and conglomerates, the pores have to be large enough and if are interconnected i.e., permeable, then the rock is a potential petroleum reservoir. With sandstones, a porosity of 18% or more is usually needed for an economic oil reservoir. Gas flows easier than oil, so as little as 12% porosity may be enough for a gas reservoir. The presence of fissures/fractures in the host provide improvement in the retentively in the accumulation of oil and gas. Fractured/fissured rocks with porosity of around 9% may work out to be productive reservoirs. Because of fracturing, limestone and dolomite reservoirs can have much lower porosities than sandstone reservoirs, yet be capable of producing greater amounts of oil. However, in nature some pore spaces are occupied by saline (formation) water making effective porosity lower, providing lesser provision for oil and gas accumulation. The percentage occupancy of water and oil and gas in the pores of the host rock determines the economic viability of reservoir. A general rule of thumb is that 40% or more of the pore fluids must be hydrocarbons in order for the reservoir to be economic enough to produce. Formations that transmit fluids readily, such as sandstones, are described as permeable and tend to have many large, well-connected pores. Rocks like shale have high porosity but least permeability. Formations, such as shale and siltstones, tend to be finer grained or of a mixed grain size, with lesser interconnected pores and curtail free flow of oil and gas.

Oil and gas continue to migrate until they come into contact with low-permeability rocks such as shale that prevent the further flow of oil and gas. Such impervious rocks trap/seal the oil and gas in to reservoir and there by restricting its further flow. These rocks work like cap or seal for that they are called cap rocks. Apart from change in physical characteristics, the mode of contact of reservoir with adjacent impervious rock also plays important part in defining geometry of the reservoir. Two types of distinct traps have been most commonly found in nature in confining the reservoir.

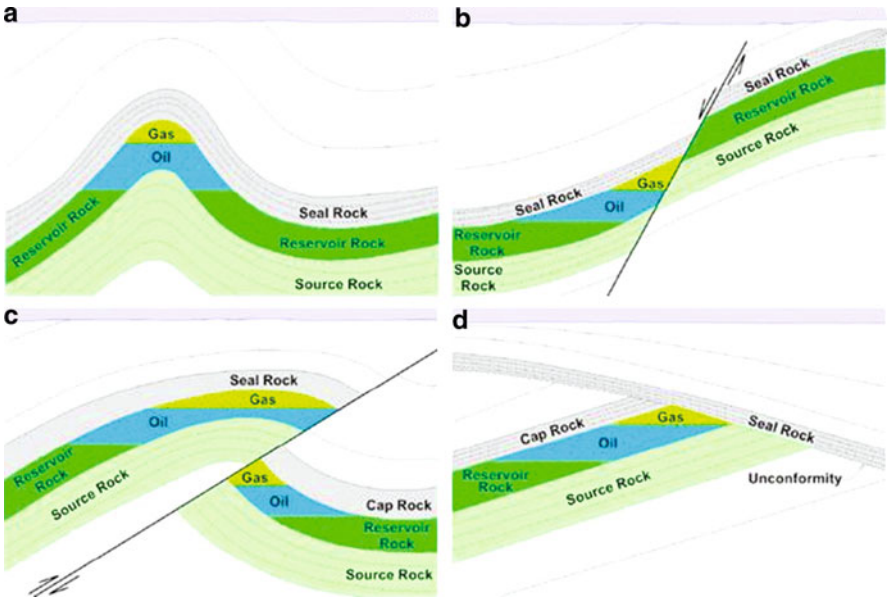

Fig. 1.5 Schematics of some common types of hydrocarbon traps recognized in the producing oil and gas fields around the world. (**a**) Represents anticline trap; (**b**) represents normal fault; (**c**) represent thrust fault and; (**d**) represents stratigraphic trap

They are stratigraphic and structural traps. Structural traps are created when rocks that have been deformed by folding (Fig 1.5a) or faulting (Fig 1.5b and c) prevent the migration of petroleum. Stratigraphic traps occur where the physical characteristics and layering of rock units trap permeable reservoir rocks in between less permeable rocks (Fig 1.5d). The host rock of the reservoir has to be more porous to retain the oil and gas and cap rock with less permeable to mitigate the migration of hydrocarbon fluids from the reservoir.

Oil and gas along with coal form the main constituents of the fossil fuels. Oil and natural gas are the most extensively used energy resources and the affluence of the country primarily determined by their consumption. Only part of the oil present in the reservoir (oil in place) can be put to production. The amount of oil that can be produced (reserve) is appreciably lower than oil in place. Due to complexities associated with reservoir, available technology and economic considerations the recovery factor i.e. the ratio of producible oil to that of oil in place varies from as low as 10 to 80%. Recent studies suggest that the earth crust may hypothetically hold 6,000 Billion Barrels of oil as its reserves, which also include 3,000 Billion Barrel un-recovered oil resource. The estimates of gas reserves are well constrained, the world gas resource are estimated to be of the order of 10,000 Trillion Cubic Feet (TCF) out of which only 6,186 (TCF) are the proven reserves. Oil and gas reserves are mainly confined to couple of countries. The Gulf countries hold the maximum oil and gas resources of the world, making these countries to constrain the rate of production and thereby control the prices of petroleum products. USA followed

by west European countries account for largest oil and gas consumers of the world. The excessive usage of oil and gas by the developed countries has led to maximum CO_2 emission, the main contributor to the green house effect and thereby affecting the climate changes. The Kyoto protocol aims at providing guidelines to restrict the emission of hazardous gases in the atmosphere and make the earth more sustainable to human race.

1.3 Coal Energy

Coal is most abundant and most primitive source of energy. Although coal deposits exist in nearly every region of the world, significant coal resources occur only in Europe, Asia, Australia, and North America. Commercial coal deposits primarily occur in sedimentary rock basins typically sandwiched as layers called beds or seams between layers of sandstone and shale. The genesis of the coal evolved during the Carboniferous era, when most of the plant and animal life perished and got deposited in the swamps and shallow marine environment. Figure 1.6 shows the global plate reconstruction during the carboniferous era. The light blue colored region gives the shallow seas where most of the present coal deposits of the world are found (from http://en.wikipedia.org/wiki/Blakey – http://jan.ucc.nau.edu/~rcb7/). Depending on the volatile content, in terms of water concentration and carbon content and depth of burial coal has been classified in to different categories like Lignite, Bituminous and Anthracite. Anthracite has the highest percentage of carbon content. Most of the coal is used for generation of electricity through the hydrothermal plants. The abundant nature and cheaper utilization cost of coal energy makes it very attractive form of the energy for generation of electricity in most parts of the

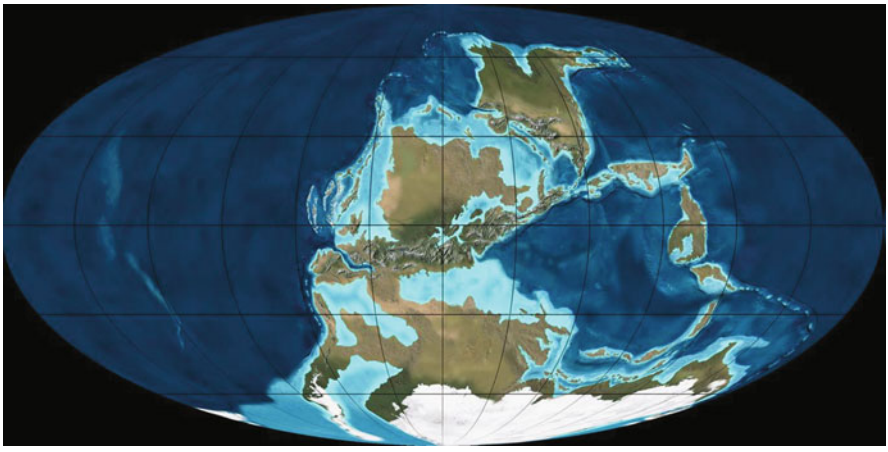

Fig. 1.6 Occurrence of global coal deposits.
Source: http://jan.ucc.nau.edu/~rcb7/mollglobe.html author Dr. Ron Blakey - http://jan.ucc.nau.edu/~rcb7

world. The quantum of coal reserves is well established. According to International Energy Agency (2009) proven coal reserves of the world are about 909 Billion tonnes. Russia, China, USA, India, Australia and Indonesia have the maximum, having about 80% of world coal reserves. The present growth rate of 5% per annum the proven coal reserves may last for about couple of decades. Coal consumption ranks third in the list of energy consumption and rate of consumption has out grown to that of oil and natural gas. The presence of large quantity of coal reserves, the utility of coal energy is extensively being sought in the developing countries for the generation and electricity and industrial production. About 40% of the world electricity generation comes through the utility of coal energy resource. China is most prominent consumer of coal followed by USA and India. In recent times China is extensively using the coal resources and USA utilizes coal energy for the generation of about 40% electricity of the country's requirement.

Coal is burnt in the furnace attached to boiler for heating the water and its conversion to steam. The steam is utilized for running the turbines for generation of electricity. Improvement in the boiler design has increased the coal energy efficiency of the order of 35%. Sensing the bleak future of oil, most of the oil importing countries are seeking to utilize coal reserves for extracting the constituents present in the coal and thereby improve the efficiency of the coal energy. After biomass, utility of coal energy is major contributor for the emission of CO_2 to the atmosphere. To improve up on the efficiency as well as reduce the emission of hazardous gases, modification in the power plants is underway in most of the industrial countries. The utility of coal energy in contrast to other fuels can be enhanced by liquefaction, combined cycle plants, and integrated combined gasification cycles. To mitigate the CO_2, carbon capture and storage is being attempted in many countries. The subsurface locations for preserving the captured CO_2 have been initiated by many countries. Laboratory experiments suggest that preserved CO_2 can utilized for enhancing oil and gas recovery. To increase the efficiency as well as for the reduction of emission of different gases and contamination of soil and other pollutants released from utility of coal, different alternatives have been proposed.

1.3.1 Coal Gasification

Coal gasification is the process of producing coal gas. Gasification procedure breaks down the chemical constituents of coal. In coal the carbon to hydrogen atomic ratio is of the order of 12:1, whereas for natural gas this is of order of 1:4. In the process of gasification, steamed coal is oxidized by mixing oxygen under suitable temperature and pressure conditions. The process is repeated for increasing the heating value of coal. Under these conditions carbon molecules in the coal break apart resulting in chain chemical reaction to produce mixed gas (coal gas) having combination of hydrogen and carbon monoxide:

$$(\text{Coal}) + O_2 + H_2O \rightarrow H_2 + CO$$

This processed coal is treated with nickel to produce gas. The coal gas is a synthetic gas. The presence of sulfur and carbon dioxide has to be reduced before the coal gas is fed for its liquefaction. The liberated synthetic gas can be converted to different type of hydrocarbons by the Fischer-Tropsch process under suitable temperature–pressure conditions and can be transported like the gasoline. The reaction can be altered to liberate hydrogen, which can be utilized for different purposes. The non-economical coal seams can be subjected to produce the coal gas.

1.3.2 Coal Liquefaction

Coal liquefaction process is more efficient than coal gasification. Coal liquefaction is the process of converting the coal in to synthetic oil, which may compensate the shortfall in the supply of oil and natural gas. Countries like China and Japan have taken up major projects for producing clean hydrocarbon fluids from the coal. Coal liquefaction relies on the process of compensating for deficient hydrogen in coal to convert it to one of the hydrocarbon fluids. These can be attained by one of the processes, directly treating coal with catalyst under high temperature and by adding hydrogen, by liquefying coal gas by Fisher-Tropsch process or by removal of part of carbon content by pyrolysis (Larry Thomas 2002). The liquefaction technique depends on the ratio of H/C content in the coal and which depends on the quality of coal. Depending on the hydrogen concentration in the coal productivity of fluids can be assessed. To overcome the hydrogen deficiency the coal is treated with a hydrogen donor in presence of catalyst to make the process workable under moderately higher temperatures (450–700°C). This process may yield coal tar with lighter hydrocarbons. The coal tar may again be proceed to produce hydrocarbon fluids (Speight 2008). In the Fisher-Tropsch process the synthetic fuel containing hydrogen, carbon monoxide and methane produced in the gasifier is utilized for producing hydrocarbons. Hydrogen and carbon monoxide is passed through circulating water in the container having iron and cobalt as catalyst. Depending on the degree of contact of catalyst with coal either with iron or cobalt may lead to the production of gasoline and diesel respectively. The process of liquefaction of coal may also be attained without catalyst under high temperatures (pyrolysis). Pulverized coal is treated in very high temperatures in vacuum to liberate gas and tarry substance present in the coal. The liberated gas/tarry fluids are hydrogenated to produce hydrocarbons. Commercial liquefaction of coal, using expensive hydrogen, still not fully put in to practice due to higher cost of productivity of hydrocarbons from the coal.

1.3.3 Coal Bed Methane

Since the late twentieth century coal bed methane (CBM, natural gas) has received increased emphasis as a potential energy resource. The decomposed organic matter

when subjected to higher temperature, pressure conditions bring out physical and chemical changes and which in turn leads to the coalification. In the process of coalification, gases like methane, carbon dioxide, and nitrogen are produced. In the lower temperature regime (<50°C), the biological processes dominate producing biogenic methane. In the higher temperature regime (>50°C) methane is generated by the catagenesis of the constituents of decomposed organic matter (Larry Thomas 2002). Coal beds contain a mixture of gases in which methane makes up 80–99%, with minor amounts of carbon dioxide; nitrogen, hydrogen sulfide, and sulfur dioxide make up the other components of coal bed gas. CBM naturally exists as gas absorbed in coal deposits. CBM is likely to provide significant contribution to energy requirement to coal rich countries. The world reserve estimate of CBM varies from 164.2 to 685.7 Tm^3. CIS countries hold about 90% of the estimated CBM reserves. The production of methane from CBM will make countries like China and India self-sufficient and thereby avoiding importing natural gas from other countries. Drilling technology is commonly used to produce methane from virgin coalfield. However, out poring of water as by product and its surface discharge may cause problems to agricultural lands. With development of new techniques injection of nitrogen and CO_2 in the coal seams are being sought to enhance the recovery rate of methane. The estimate of the CBM is not quite accurate and owing to its likely higher cost of production, CBM may not work out as replaceable energy resource in near future.

The primary forms of energy that are being presently consumed have limited reserves. The estimated resource potential of these reserves is upgraded on regular basis. These resources are not renewable, as these reserves came in to existence due to the geological processes over long period of time and cannot be replenished easily. Other energies such as wind, solar, water and geothermal energies are renewable, which means that these energies are inexhaustible.

1.4 Geothermal Energy

Geothermal energy has its genesis in deeper part of the earth, where the radioactive elements in the minerals decay to produce heat and which in turn diffuse to subsurface layers through conduction. Resource estimate indicate that present rate of production of the geothermal energy may last for couple of thousand years making it sustainable and even to the extent of being categorized as renewable form of energy. Geothermal energy contributes to about 0.3%; with electricity generating capacity of 8,000 MW to the global energy basket, United States being the most productive country for this form of energy. Primary geothermal provinces are located in tectonically active regions, mostly on the peripheries of the continental plate boundaries. The outstanding province is confined to rims of the Pacific Ocean; the region characterized by most active earthquakes and volcanoes and is popularly called the Ring of Fire (Fig. 1.7).

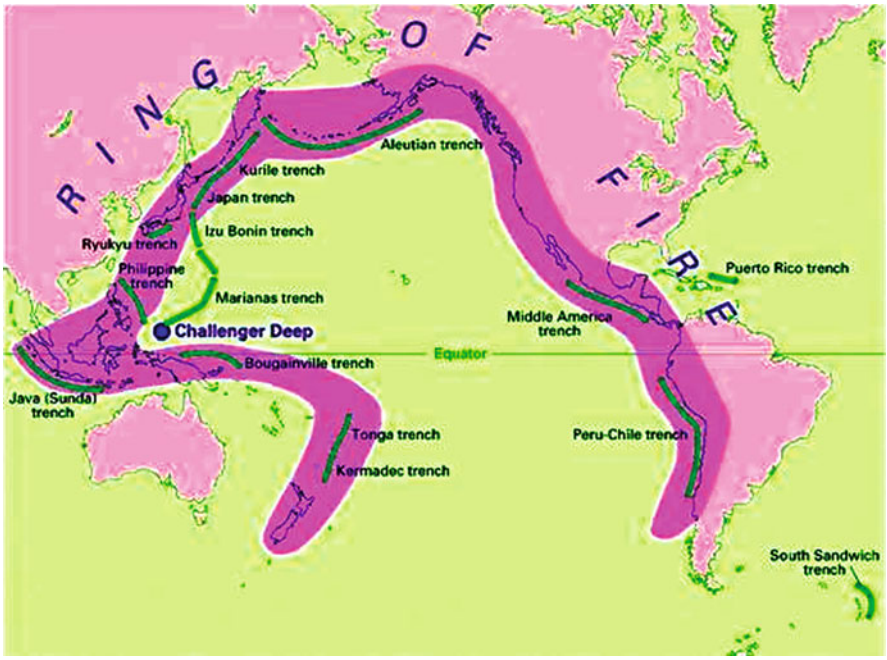

Fig. 1.7 The map of Pacific region over which major earthquakes and volcanism occurs. *Source:* Modified from Data source: http://www.evl.uic.edu/pape/data/WDB

When the magma chamber lie at shallower depths, the water content in the rocks heated up and under favorable conditions of faulting and fracturing, fluids are brought to the surfaces in the form of hot springs and geysers. When this rising hot water and steam is trapped in impermeable rocks in subsurface earth, it is called a *geothermal reservoir*. The utility of geothermal energy for space heating and hot springs as medical aid have been reported from historic times. Geothermal energy is directly used for space heating and pools.

Based on the heat generating capacity, geothermal energy is being primarily used for generating electricity. Deeper geothermal reservoirs may hold dry steam ($>235°C$) or flash steam (hot water $>182°C$) or moderately lower temperature fluids ($<182°C$) (Shibaki and Beck 2003). These forms of resources having been utilized for generating electricity. The dry heat drawn from the reservoir is fed to turbines to rotate turbine blades in presence of magnet to generate electricity on the basic principle such as of dynamo. The flow of steam can be kept constant through regulators. Flash steam is produced, when hot water from the deeper reservoirs is pumped to surface, part of water gets vaporized due to the pressure difference at the deeper part and surface. The steam and water is separated in the steam/water separators. The steam is utilized for running the generator and the excess of hot water, not converted in steam is injected back in to reservoir. Moderately hot water from the geothermal reservoir is fed to one of chamber to heat exchangers, in the

other chamber which is in contact with first one is filled with organic fluids with low boiling point such as iso-butane and iso-pentane. The vaporized organic fluid in the heat exchanger is fed to turbines for generating electricity. In areas where sufficient surface water is available; water is pumped in the geothermal reservoir and the converted output steam and hot water are utilized for the production of electricity from the processes as has been done at Nesjavellir Power Plant in Iceland (Fig. 1.8). The excess water is let out at surface.

Apart from heat generated in deep interior the near surface earth maintains a constantly moderate hot temperature of the order of 10–16°C. This source of heat is being utilized to keep the home warmer in colder regions by using heat pump. The process can be reversed to cool the interior of the houses during the summers. Hot water near the earth's surface can be piped directly into buildings and industries for heat. A district heating system provides heat for 95% of the buildings in Reykjavik, Iceland. Examples of other direct uses include: growing crops, and drying lumber.

Geothermal plants can run about 90% of the time and comparatively has better capacity factor when compared to other forms of energy. Apart from the higher investment cost, the operational and maintenance cost of geothermal plants work out to be of the same order to that of power generated from the conventional fuels with lesser pollutants. Utilization of geothermal energy has some disadvantages in terms drilling and emanating gases brought to the surface during its exploitation. The exploitation of geothermal energy requires drilling through high temperature regimes, when compared to normal drilling for hydrocarbons and corrosive elements in the fluids in the geothermal fields makes the drilling problematic and expensive. The variations in drilling depths depends on the potential of geothermal

Fig. 1.8 Nesjavellir Power Plant is the largest geothermal of the world, situated in the southern part of Iceland;
Source: http://commons.wikimedia.org/wiki/Main_Page

reservoirs. In the moderate geothermal systems, the drilling depth may be of the order of couple of hundred meters and for deeper resources drilling depth may touch up to 3,000 meters. The cost estimate of drilling varies from $1–4 million depending on type geothermal system (Shibaki and Beck 2003; Gupta and Sukanta 2006).

Apart from the high cost of drilling the geothermal fluids are primarily contaminated by H_2S and CO_2. They may hold other gases and minor elements, boron, arsenic and mercury, which may cause health hazards. Moderate geothermal regimes do not contribute much to the global warming as CO_2 release to atmosphere is appreciably low when compared to deeper geothermal regimes. However, the release of CO_2 is comparatively lower than the conventional hydrocarbons. The stagnation in the production and increasing costs of conventional form of fuel resources necessitate looking for alternative forms of energy. With abundant resource estimate of geothermal energy and its lower operation cost make this form of energy more attractive for its exploration and exploitation specifically for the countries where the conventional fuel resources are meager and possibility of having suitable locale of geothermal reserves.

1.5 Nuclear Energy

Nuclear energy is the energy that is trapped inside each atom. Nuclear energy primarily is derived from the disintegration of heavier unstable isotopes (atoms) or fusion of two lighter elements. Nuclear energy is obtained by fission of uranium (Fig. 1.9), plutonium or thorium or the fusion of hydrogen into helium. Fusion of

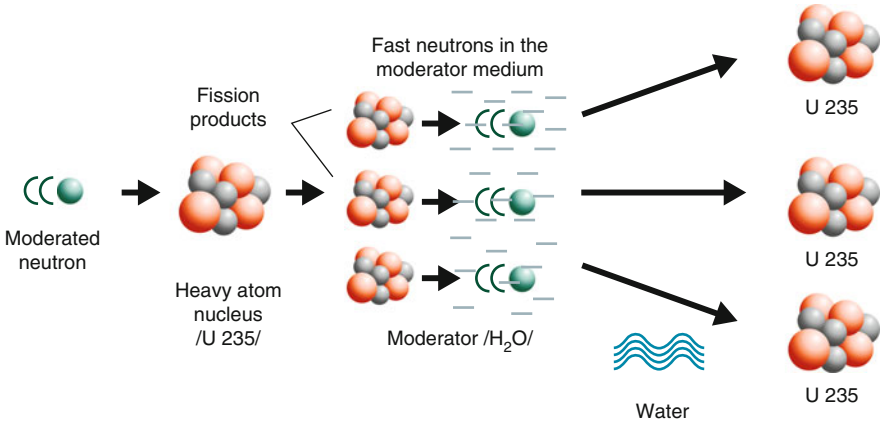

Fig. 1.9 The fission of Uranium 235 into smaller fragments producing more protons. (Adapted from http://www.kznpp.org)

two elements requires very high temperature and in this regard it is being examined on experimental basis. Fission of heavy elements is an exothermic reaction which can release large amounts of energy both in electromagnetic radiation as well as kinetic energy. Energy produced from the nuclear process does not emit any CO_2 in the atmosphere for that it is environment friendly. The energy produced by the fission process is about millions of times the energy produced by the combustion of an atom of carbon from coal. Presently all most all the nuclear energy is produced from uranium. During the process of disintegration the isotopes loose the mass. The mass gets converted in to energy according to Einstein's equation $E = mc^2$, where is E is the energy, m the mass and c is the velocity of light. The instability in an isotope results from imbalance of number of protons and neutrons in the nucleus. Because of the instability in the nucleus, it is always disintegrating and emitting neutrons. Further if these neutrons hit or absorbed by the nucleus of other atom, the nucleus may split in to two fragments and release of two or more neutrons and give off more energy due to loss of mass of atom.

In normal conditions the energy released due to the disintegration of uranium atom is significantly low. The capturing of neutrons by the uranium-235 is rather easy and to fission it for release of the energy. In a chain reaction, particles released by the splitting of the atom strike other uranium atoms and split them. The particles released by this further split other atoms in a chain process. The chain reaction gives off heat energy (Fig. 1.9). This heat energy is used to boil heavy water in the core of the reactor. So, instead of burning a fuel, nuclear power plants use the energy released by the chain reaction to change the energy of atoms into heat energy. The heavy water from around the nuclear core is sent to another section of the power plant. Here it heats another set of pipes filled with water to make steam. The steam in this second set of pipes rotates a turbine to generate electricity, so that it does not occur too fast. These are called moderators.

In uranium ore, generally two types uranium isotopes; uranium-238 and uranium-235 are present. Uranium-238 is abundant, constituting to about 99% of the ore and uranium-235 concentration is always significantly low (<1%). Before feeding the uranium to nuclear reactor, the uranium-235 is enriched to about 4% and this is used as the fuel to start fission process. Under normal conditions the nuclei of unstable isotopes are continuously disintegrating. The neutrons from the nucleus are always being released and travel in all directions with very high speeds. Their kinetic energy can be utilized for any meaningful purpose or else neutrons generally escape the bounding medium.

There are more than 400 nuclear power plants providing about 7% of the world's primary energy and about 25% of the electric power in industrialized nations. Cost wise the energy produced by nuclear plants is comparable to that of coal and oil and gas. In fact, for a country with abundant coal reserves, production of energy from coal works out less expensive when compared to other resources. However, lesser emission of CO_2 by nuclear plants may encourage countries to opt for utility of nuclear energy in future.

1.6 Nuclear Fusion

Another form of nuclear energy comes from the fusion of two nuclei. Fusion joins together two small nuclei to form a heavier nucleus and in the process release large amounts of energy (Fig. 1.10). The principle behind fusion is that in fusing two small nuclei like deuterium (^{2}H, or one neutron and one proton), a great deal of energy is released. Deuterium (^{2}H) and tritium (^{3}H) are both isotopes of hydrogen which are obtainable in normal water. Fusion of ^{2}H and ^{3}H would result creating ^{4}He and freezing of neutron and release of 17.59 MeV energy.

$$2\mathrm{H} + 3\mathrm{H} \rightarrow 4\mathrm{He} + \mathrm{n}$$

In the simple fusion process two protons of lighter elements are brought together overcoming the repulsion of electric charges by nuclear forces resulting in high energy release by transfer mass to energy in agreement of Einstein's energy equation. Such processes in sun provide its immense heat and light. The induced nuclear fusion reaction requires a dense concentration of low isotope fusion elements and very larger temperature source. It has been estimated that, nuclear fusion of only 1 g of deuterium will release energy equivalent to energy obtained by the burning of hundreds of gallons of gasoline.

The induced nuclear reaction can be obtained in cold and hot fusion conditions. In the cold fusion process the ions can be accelerated to high kinetic energy to initiate the nuclear process. The hot fusion is most prevalent in the stars, where four protons are fused to produce an alpha particle, with release of two positrons and neutrinos and large amount energy. The energy released in the form of heat can be utilized in running the steam turbines for the generation of electricity. The expected energy generation from the nuclear fusion almost matches with energy that is likely to be economically compatible to that energy generated from the nuclear fission

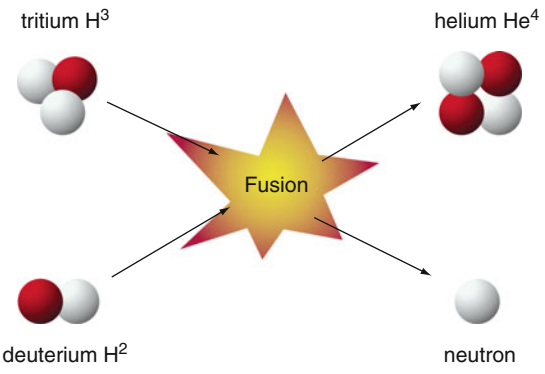

Fig. 1.10 The fusion of two nuclei. Two small nuclei, i.e., Tritium (^{3}H) and Deuterium (^{2}H) combined (fusion) together to produce Helium (^{4}He), and freezing of Neutron and release of 17.59 MeV energy

process. However, the generation of energy from the fusion reaction is still in the experimental stage. In near future it is expected that nuclear fusion processes may be utilized by defense organizations for developing the nuclear weapons.

1.7 Renewable Energy

Natural resources which are everlasting may be harnessed to create energy. Renewable energy sources are even larger than the traditional fossil fuels and in theory can easily supply the world's energy needs. Most of renewable energy resources are controlled by the sun. The sun's radiation directly heat up the earth's atmosphere creating dynamics of wind pattern, ocean currents, providing the life cycle to the plants through photosynthesis. All these phenomena are time and space depending over micro to macro wavelengths. If the small fraction content of these resources is exploited, it may cover the entire spectrum of energy requirement for the survival of human beings.

1.7.1 Hydropower

Water has been the perennial source for agricultural and other applications for the sustenance of human beings. The advantages of using water for a power source are that the resource is free, and it can be stored effectively and put to use quickly. It is the most widely used form of renewable energy. Hydroelectric power is considered as the largest of the renewable energy resource. Moreover there is one sense in which part of the hydro resource is 'reusable', in that it is quite common for a series of power plants on the same watercourse to 're-use' the same flow of water, thus effectively increasing the utilization of its technical potential. Water for hydropower may be stored in a reservoir or above a dam forming a lake. Rivers and streams are re-directed through hydro generators to produce energy. Generation of energy from flowing water comes from the flow of stream and falling of water from height. In the case of flowing water (river, stream) kinetic energy of the water is converted in to mechanical energy to run the turbine and eventually through generators it is converted to electrical energy. The height from which water falls i.e. the potential energy is converted to electrical energy. The stream flow i.e. the amount water runs through the system and drop (or head), which is the vertical distance the water will fall through the water turbine. The head and the flow are two variables that essentially determine the potential efficiency of a site for a hydropower system. The greater the head, the higher the velocity of the water falling will be, and hence the greater the pressure with which it hits. The quantum of moving water on a site is also directly related to the amount of power generated. The quantum of power generated at the dam can be estimated as (http://new.wvic.com)

Power = (height of the dam) × (river flow) × (efficiency) /11.8

Height from which waterfalls, the height of the dam in feet. River flow is the quantity of water flowing in cubic feet per second. A factor of 11.8 is being used for conversion of units feet and seconds into kilowatts.

Hydro power produces a continuous supply of electrical energy in comparison to other renewable technologies. The efficiency of hydropower unit depends on how best the kinetic and potential energy of water is converted to electrical energy by turbines and generators. Most of the hydropower units run with an efficiency of 60–90%. The hydroelectric complex project produces no direct waste. The water flowing out of hydroelectric plant after generating electricity can subsequently be utilized downstream at micro-hydro power stations and for agricultural purposes. Small-scale hydropower systems are quite efficient when used to supply local needs. They require appreciably small amount of flowing water with not high head to generate electricity for local needs. Many such micro scale hydroelectric units can be operated on the downstream of bigger power projects. The micro-hydroelectric units can be linked to grid for the supply of power to distant places. The flow of water can also be utilized for generating mechanical energy, which in turn helps in agricultural applications.

Renewable energy accounted for one-fifth of total power generation, of which hydropower holds the major share, at 87%. Hydro power contributes to electricity generation in 160 countries. Five countries (Brazil, Canada, China, Russia and the USA) account for more than half of global hydropower production. Worldwide, hydroelectricity supplied, an estimated 816 GW in 2005. This was approximately 20% of the world's electricity generated. Hoover Dam is an example of a large-scale hydroelectric plant still in use in the United States today (Fig. 1.11). The United States and Canada have the greatest number of hydroelectric plants.

Fig. 1.11 Hoover dam built over river Colorado, one of the outstanding examples for the generation of hydro-electric energy. Aerial view of Hoover Dam on the Colorado River—the colossal project built during the Great Depression 30 miles from Las Vegas on the Nevada, Arizona border http://www.inetours.com/Las_Vegas/Photos/Hoover-Dam-above.html

There are some concerns over the utility of hydroelectric power. The generation of electricity in hydropower unit primarily depends on the inflow of water to the dam site from the rivers and most of the water in the rivers is sustained through rains, which are seasonal dependent. So the hydropower effectively works when it rains. Further, rivers bring in lot of debris, which are collected in the reservoir, leading to silting in the reservoir thereby reduction in the dam height, which affects the efficiency of the hydropower production. Heavier imputes from river leads to inundation of adjoining regions near the dam site, creating environmental problems like erosion. The improper upkeep of dam may also lead weed growth, disease spread by small organisms that live in stagnant water. Induced seismicity owing to dam height and excess presence of water in dam has given rise to earthquakes in countries like India and Turkey.

1.7.2 Solar Energy

The earth receives about 123 pettawats (PW) at its upper atmosphere but only half of it reaches the earth's surface and interacts with atmosphere and biosphere (Fig. 1.12). The total solar energy absorbed by Earth's atmosphere, oceans and land masses is approximately 3,850,000 exajoules (EJ) per year. The interaction of incoming radiation from the sun with different elements of earth such as the atmosphere and oceans gives rise to different dynamic phenomena, which may be utilized as natural resources for creating energy. By utilizing only small part of incoming energy from sun the present energy requirement can easily be fulfilled.

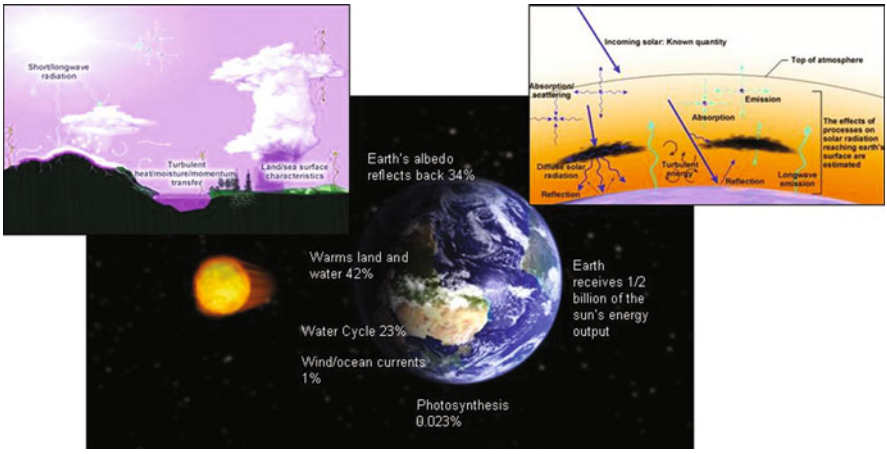

Fig. 1.12 The interaction of incoming radiations from the Sun with Atmosphere and Biosphere of the Earth, resulting different physical processes and thereby generation of energy. (Modified from www.meted.ucar.edu)

The incoming radiations from the sun can be directly utilized for heating the houses or generating electricity from them. In the passive mode the incoming radiations from sun may directly be utilized in heating room or water. The house has to have proper orientation to cover in such a way to have maximum sunlight during the entire day. The house has to be designed to have maximum absorption of incoming sun's energy and minimum radiation. As the sun shines only during the day time, the absorbed energy has to be stored for its utility during night hours. With proper design of distribution system the heat can be regulated to different rooms from the place where heat energy is stored. The water heated through passive mechanism in turn can be utilized to heat anti-freezing liquid and pumped to a heat exchanger to heat water for use inside a building. Many innovative passive solar heating systems have been designed to optimize the efficiency of the passive solar home.

Solar energy can also be used to generate electricity directly. They are considered as active solar systems or photovoltaic systems. Photovoltaic (PV) cells are semiconductor devices, usually made of silicon, which contain no liquids, corrosive chemicals or moving parts. Photovoltaic is the direct conversion of light into electricity at the atomic level. Some materials (semi-conductor, silicon) exhibit a property known as the photoelectric effect that causes them to absorb photons of light and release electrons. Photovoltaic systems use solar cells to directly produce electricity from solar radiation. For solar cells, a thin semiconductor wafer is specially treated to form an electric field, positive on one side and negative on the other. When light energy strikes on one front side of solar cell (a flake of semi conductor material) electrons are knocked loose from the atoms in the semiconductor material. This results in charge separation across the two faces of the conductor. Electrical conductors are attached to the positive and negative sides, forming an electrical circuit, the electrons can be captured in the form of an electric current – that is, electricity. PV cells are bundled together in modules or panels to produce higher voltages and increased power. They produce electricity as long as light shines on them, they require little maintenance, do not pollute and they operate silently, making photovoltaic energy the cleanest and safest method of power generation.

Electricity generated during the day time have to stored to be utilized during the night. Batteries are required to store energy during the hours of need. Special type batteries –deep-cycle batteries (lead-acid and nickel cadmium) are being used as storage batteries. These batteries provide continuous power for longer period of time without much discharge. Unfortunately, batteries add a lot of cost and maintenance to the PV system. One way around the problem is to connect your house to the government or corporation utility grid and utilize the power whenever required. Globally, solar generation is the fastest growing source of energy, seeing an annual average growth of 35% over the past few years. Developing countries in the low latitude region, where sun shines during most of the year, are the major growing investors in solar energy. Advances in technology and on economics scale, along with demand for solutions to global warming, have led photovoltaic cells to become the most likely candidate to replace fossil fuels and other energy resources.

1.7.3 Bio-Energy

Bio-energy mainly produced from use of vegetable (organic) matter. Biomass, the remains of animals and plants and waste from paper and pulp making industry as well as day-to-day organic wastages from houses can be utilized as bio fuels for the generation of energy (Fig. 1.13). The heat generated from combustion of these fuels can be utilized for the production of electricity and household purposes. Wood energy is derived both from direct use of harvested wood as a fuel and from wood waste. The energy produced when wood is burned is originally stored in the bonds of the glucose formed during photosynthesis in the leaves of the tree. The largest source of energy from wood is pulping liquor, a waste product from processes of the pulp, paper and paperboard industry. Waste organic materials such as plants, food scraps, and paper products, can be recycled using biological composting and digestion processes to decompose the organic matter. The resulting organic material is then recycled for agricultural or landscaping purposes. In recent times bio-ethanol is being produced from starch and sugar content in wide variety of crops. Bio-ethanol can easily be produced from crops like sugar cane, potato and corns. Ethanol is presently used in gasohol (10% ethanol, 90% gasoline), making it cleaner burning fuel, which emits an average of 20% less carbon monoxide than unblended gasoline. Bio-ethanol is being increasingly added to gasoline to reduce the fuel costs and is being considered as alternative to gasoline. Brazil and USA combinely produce 89% world's ethanol production. Many other countries are increasing efforts for large scale production of biofuels. The other significant biofuel is biodiesel, which is currently derived from vegetable oils, animal fats and grease by etherification. The resulting product is blended with conventional diesel oil, in proportions ranging from 5 to 20%.

Fig. 1.13 The Garbage dump, containing organic matter, which eventually decomposes to produce methane by bacterial (methanogenes) activity. (Courtesy of MARIO LAPORTA/AFP/Getty Image)

The sewage and organic matter in the garbage decomposes and under anaerobic conditions in presence of microorganism (methanogens) produces methane. Landfill garbage is relatively slow process for the generations of fuels from the garbage. Installing plants near the garbage sites is accelerating the process of decomposition. Swine farmers collect the manure and add methane-producing bacteria called methanogens in a controlled environment. The methane is collected and burned to produce electricity for the hog confinement buildings. Plastics from biomass, like some recently developed to dissolve in seawater, are made the same way as petroleum-based plastics. These plastics are actually cheaper to manufacture and meet or exceed most performance standards, but they lack the same water resistance or longevity as conventional plastics.

The estimated worldwide generation of electricity from biomass amounted to about 183 TWh in 2005, of which nearly three-quarters was produced from solid biomass, 14% from bio and 12% from municipal solid waste. Burning of wood and charcoal in underdeveloped countries still is the main source of energy for cooking and day to day energy requirements. This contributes significantly to the release of hazardous gases to the atmosphere. Attempts to generate substantial quantum of energy from the garbage (Fig. 1.9) and other resources is in the process of development. Energy generated mainly from biofuels may provide some hope in working out as alternative source to fossil fuels in near future.

1.7.4 Wind Energy

The incoming radiations from sun strike the earth surface differentially depending on location of a place on the earth, leading differential heating and thereby driving to global atmospheric convection confined in between earth's surface to the stratosphere. This convection pattern results in blowing of wind and again the speed of the wind depends on the location of place on earth. Very high wind speeds are found at high altitudes where continuous wind speeds of over 160 km/h (99 mph) occur. Sailors through ancient times have been utilizing the wind energy to sail for long distances across the globe. In recent times the kinetic energy contained in the wind is being utilized to generate electricity. Kinetic energy (wind speed) of the wind is made to rotate large blades of wind mill (Fig. 1.14) arranged in suitable pattern. The rotating blades connected through shaft to turn the turbines and this in turn results in generation of electricity through the use of generator.

Wind turbine is a non-polluting means of generating electricity. Because of pattern of distribution of wind speed, the wind mills have to be installed at higher altitudes or large open places on earth's surface. Such regions can be located near the seashore or on the hillocks. The strength of wind varies from day to day, season to season as well as over long period of time. A statistical data for region under study has to be ascertained before installation of wind mill for generation of electricity.

Different locations will have different wind speed distributions. The Wiebull model (Weibull 1951), closely mirrors the actual distribution of hourly wind speeds

Fig. 1.14 An artist image of the wind mill used for the generation of wind energy

at many locations. Maximum power through a wind mill is generated when wind speed is quite high and this happens in bursts. So the power generated by the wind plant is never constant. The ratio of actual productivity in a year to this theoretical maximum is called the capacity factor. The capacity factor of modern wind mills ranges from 20 to 40%. The capacity factor of wind mill directly related to its wind speed not on the consumption of fuel resources as it happens in the other energy producing devices.

Owing to inconsistent power generation by the wind plants, the electric energy produced by the wind mill either consumed locally, where other means of power are not available or the generated power is fed to grid system, or stored in batteries from where the power can be drawn whenever required. For generating consistent electricity during the periods of lower as well during the wind bursts, advancement in existing technologies are being proposed (Hau and von Renouard 2006; Ahilan et al. 2009). Other aspects relate to the use of stronger inter-regional transmission lines to link widely distributed wind farms. Interconnecting ten or more wind farms can allow an average of 33% of the total energy produced to be used as reliable (Archer and Jacobson 2007).

In early 2008, global installed wind capacity passed the 100 Gigawatt (GW) thresholds from only about 74 GW in 2006. Developing countries like India and China have extensive plans to increase the wind power growth. Wind energy project costs have declined and wind turbine technical availability is now consistently above 97%. Wind energy project plant capacity factors have also improved from 15% to over 30% today, for sites with a good wind regime. With this growth rate continuing, one expects 160 GW to be installed worldwide by the year 2010. Most of wind mills are presently installed on the land, however, consistent higher wind speeds almost twice that of land, may provide avenues for installing wind mills in the shallow offshore regions in future.

1.7.5 Tidal Energy

Due to the gravitational forces and the positions of sun –moon with respect to the earth, the level of ocean water on the rotating earth's surface under goes changes creating tides. Due to nearness of moon to the earth the tides produced by moon have higher magnitude when compared that of the sun. The magnitude of the tide at a location is also due the effects of earth's rotation and local shape of the sea floor and coastline. Tides can be found with varying degrees of strength on any coastline, and sometimes even at sea. The magnitude of tide in the open ocean is significantly smaller and increases dramatically when it reaches the continental shelves attaining heights of the order of 16–17 m on the coastlines. This brings in huge influx of water mass (Gorlov 2001). A flood tide is one that is coming in or rising and an ebb tide is one that is going out. The kinetic energy and potential energy contained in the tides can be utilized for creating electricity i.e. tidal energy. As it utilizes the gravitational forces of moon and sun acting on the ocean water of the rotating earth, the energy generated from tidal phenomena is everlasting or renewable energy source.

Tide mills have been in existence for more than 900 years. These work rather like a hydro-electric scheme, except that in the case of hydroelectric plant the dam is much bigger. Generating electricity from tides works on three elements namely, construction of dam across the flow to create a basin across it and the dam (Fig 1.15) providing the head to run the turbines as it is done in the hydroelectric power

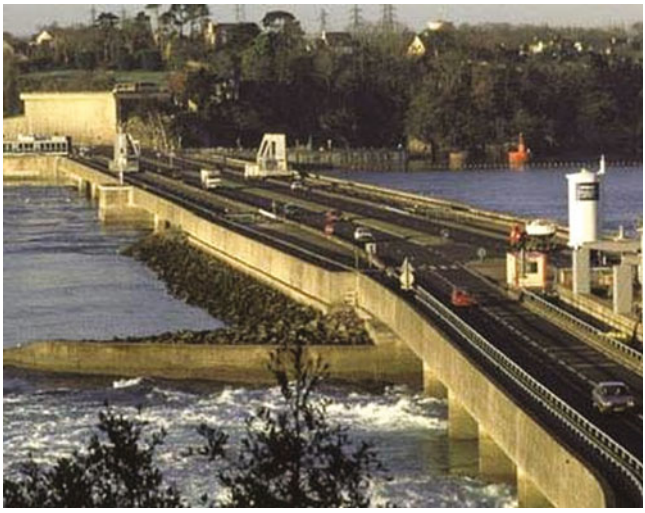

Fig. 1.15 Aerial view of the La Rance Tidal Power Plant. Only operating tidal power plant built on the mouth of river La France estuary. At the La Rance tidal power station the river is blocked by a wall as long as seven football pitches and as high as three double-decker buses. La Rance Tidal Power Station today (Image courtesy of Science Museum (www.sciencemuseum.org.uk) Photograph by Michel Coupard/Stillpictures)

generation. During the flood tide time water flows through sluice gates into the basin, the head of water column to turn blades of turbine. When the tides go back out, the water flows back into the sea through a water wheel making again the turbines blades to rotate. Electricity is generated by connecting the turbines to generators. The difference between the locally operated tide mill and power plant is the dimensions of units and the amount of energy generated.

Another method of utilizing tidal energy is to build a barrage or barrier with gates of some kind at the opening of a bay or a river system to create an estuary or a big basin. The gates create differences in the water levels between the estuary and the ocean, therefore enabling the generation of electricity. For example, when the tide falls, the receding water retreats back to the ocean by passing through a turbine located in the barrage generating electricity. Electricity can also be generated when the open gate lets water flow into the estuary during peak periods of high tide. This is commonly called the barrage technique.

In recent times a new technology, tidal stream generators draw energy from currents in much the same way as wind turbines. The higher density of water, 800 times the density of air, means that a single generator can provide significant power at low tidal flow velocities. In the regions where the high velocity water flow is concentrated, an array of turbines can be installed to generate electricity. Generating power through this technique has merits as it does not destroy the ecological balance as well the out flowing water can further be utilized down stream.

The most important advantage of tidal energy is its economical benefits, as tidal energy does not require any fuel. Tides rise and fall every day in a very consistent pattern. The economic life of a tidal plant is very high. A plant is expected to be in production for 75–100 years, in comparison with the 35 years of a conventional fossil fuel plant. Besides the economical factors, tidal energy is clean and renewable, unlike fossil fuels. Tidal energy offers a lot of potential to be a substitute for hydrocarbon and fossil fuels. A very important feature of tidal energy is that it is non-polluting. A tidal barrage can prevent approximately one million tons of CO_2 per TWH generated. A barrage can also safeguard coastlines from storms. Approximately 3,000 GW of energy are available from the tides worldwide. However, considering the limitations only about 2% (= 60 GW) can potentially be exploited for electricity generation. A major drawback of tidal power stations is that they can only generate when the tide is flowing in or out – in other words, only for 10 h each day. However, tides are totally predictable, so one can plan to have other power stations generating at those times when the tidal station is out of action.

1.7.6 Wave Energy

The blowing of wind on the ocean surface produces ocean waves. In general the winds over the ocean have higher speeds as well as systematic pattern to generate consistent waves. There is tremendous energy in the ocean waves. Wave power

devices extract energy directly from the surface motion of ocean waves or from pressure fluctuations below the surface. The potential as well as the kinetic energy associated with waves is utilized primarily to generate electricity, and water desalination. Many technologies have been proposed to harness energy from the ocean waves. These technologies have been designed to withstand the physical conditions and utilize the wave characteristics of waves at near shore, offshore and far offshore. The technique involved different orientation aspects for optimally generating electricity from the waves.

Different types of mechanism are utilized for generating electricity from the ocean waves. The terminator devices are oriented perpendicular to the wave motion. They are being put in operation in the near offshore and offshore regions. Water from the incoming wave is pushed to in to a large chamber from below. The water in the chamber oscillates in phase with wave action pushing the trapped air in the chamber up and down. The up and down movement of the wave is used to power a piston that moves up and down inside a cylinder. That piston can also turn a generator.

In the case of point absorber the up and down motion of the wave is utilized to generate EMF induced in the coil due to the movement of fixed magnet fixed in the chamber. The magnet through shaft is connected to sea floor. The EMF generated in the coil is connected to cable for the flow of electricity (Fig. 1.16).

Attenuators are long multi-segment floating structures oriented parallel to the direction of the waves. The differing heights of waves along the length of the device

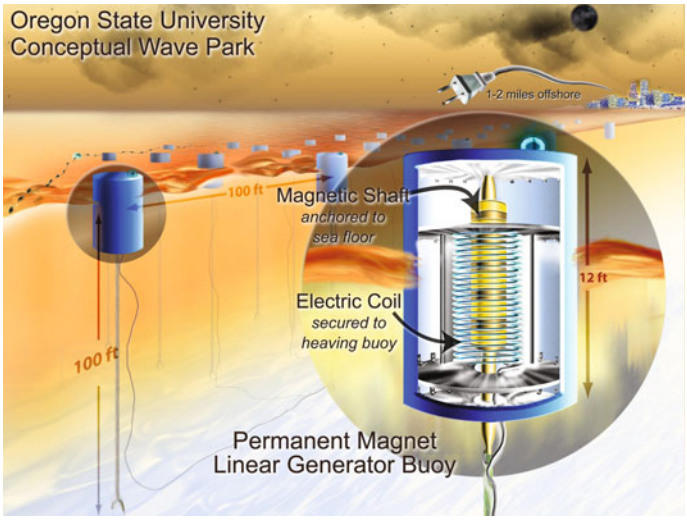

Fig. 1.16 A point absorber is a floating structure with components that move relative to each other due to wave action (e.g., a floating buoy inside a fixed cylinder).
Source: http://significantdistraction.wordpress.com/2007/06/18/locals-only-jurisdiction-over-the-waves

causes flexing where the segments connect, and this flexing is connected to hydraulic pumps or other converters. The wave motion can also be utilized to generate electricity similarly to that as is done in tidal action. The oceanic wave feeds the water to a reservoir, which stands high above the surrounding region. Water from the reservoir is allowed to fall on other side of reservoir, making the turbines to spin, which are placed on the lower side. The reservoir simulates dam conditions to generate electricity due the head of water column. Deep water wave power resources are truly enormous, between 1–10 TW, but it is not practical to capture all of this. Favorable locations of wave energy include the western coast of Europe, the northern coast of the UK and the Pacific coastlines of North and South America, Southern Africa, Australia and New Zealand. The present technological advancement may encourage for utilization of wave phenomena to generate electricity and the wave energy may contribute significantly in near future.

References

Ahilan T, Mohammed K.P., Arumugham S. (2009) A critical review of global wind power generation, American Journal of Applied Sciences 6(2):204–213.

Archer C.L., and Jacobson M.Z. (2007) Supplying baseload power and reducing transmissions requirements by interconnecting wind farms, Journal of Applied Meteorology and Climatology 46:1701–1717.

Corradini M. (2005) Nuclear Power: Secure Energy for the 21st Century. http://www.docstoc.com/docs/14677528/NUCLEAR-POWER. Accessed Dec, 2009.

Gorlov M. (2001) Tidal Energy, in Encyclopedia of Science and Technology, pp. 2955–2960.

Gupta H.K., and Sukanta R. (2006). Geothermal Energy: An Alternative Resource for the 21st Century, Elsevier Science, St. Louis, MO, ISBN 044452875X.

Hau E. and von Renouard H. (2006) Wind Turbines Fundamentals, Technologies, Application, Economics, Springer, Berlin Heidelberg, pp 21.

International Energy Agency (2009) Statistics Publication, Coal Information, ISBN 978-92-64-06105-7 (CD-ROM: 978-92-64-06107-1).

Robb L.J. (2005) Introduction to ore forming processes, Willey-Blackwell, USA, ISBN 978-0-632-06378-9.

Shibaki M., Beck E. (2003) Geothermal energy for electric power, A Ripp issue brief, Renewable energy policy project, Washington DC, 2003.

Speight J.G. (2008) Synthetic fuels handbook, properties, processes and performance, McGraw-Hill Professional, New York, ISBN-10:007149023X.

Thomas L (2002) Coal Geology, John Wiley & Sons, New York, pp 392, ISBN: 978-0-471-48531-5.

Weibull W. (1951) A statistical distribution function of wide applicability, Journal of Applied Mechanics 18(3):293–297.

Chapter 2
World's Oil and Natural Gas Scenario

Abstract Recent studies suggest that the earth's crust may hypothetically hold 6,000 Billion Barrels of oil as its reserves, which also include 3,000 Billion Barrel un-recovered oil resource. However, owing to the complexities in geology associated with the reservoirs one can only indirectly get some inference about the quantum of reserves based on some probabilistic distribution. With 95% probability the world may touch ultimate recovery of 2,248 Billion Barrels. Owing to the non-encouraging scenario of oil production and likely higher cost of oil in future, may lead to search for alternative replacement to oil. The world gas reserves are estimated to the order of 10,000 Trillion Cubic Feet (TCF) out of which only 6,186 TCF are the proven reserves. The projected world natural gas consumption may reach to 158 TCF by 2030. This chapter provides an overview of present oil production, its consumption and future prospects.

2.1 Introduction

Oil, natural gas and coal form the main constituent of fossil fuel energy. These energy resources were formed millions of years ago as the consequence of decomposition of organic remains trapped in the sediments and subjected to high temperature and pressure conditions in the subsurface of the earth. Such temperature–pressure regimes prevail in the shallower part of the crust. The presence of high order of total organic content in the sediments under this regime over long periods of time would provide most likely sites for the formation of oil and gas. Large extent of the world (expect some deeper part of the oceans) has been explored to assess the oil resources and the most favorable geological structures have already been mapped where oil and gas are likely to be found. However, it has been noticed that the potential oil resources are unevenly distributed over the globe (Fig. 2.1). Most of the favorable locations of oil deposits are confined to former Soviet Union, Middle East and North Africa and Asia Pacific and some other regions of the world.

N.K. Thakur and S. Rajput, *Exploration of Gas Hydrates*,
DOI 10.1007/978-3-642-14234-5_2,

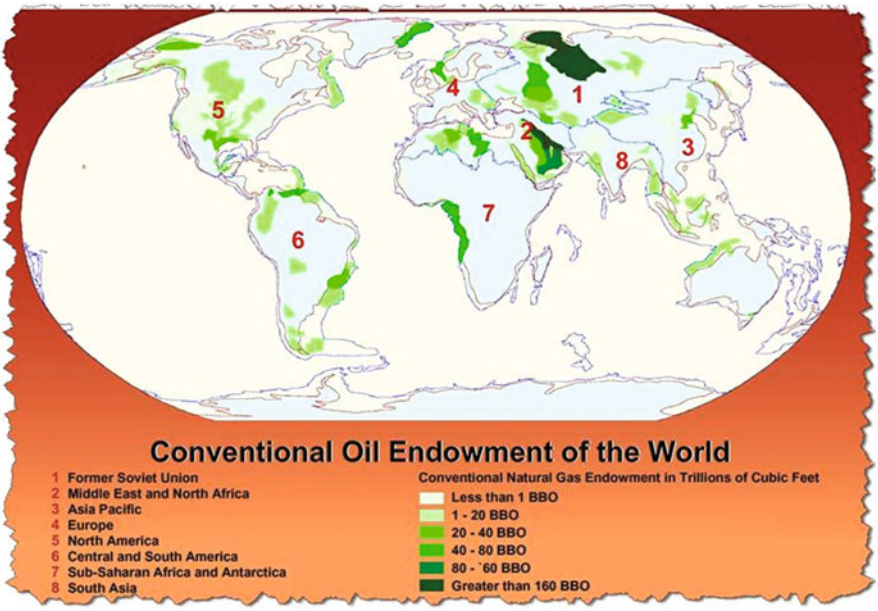

Fig. 2.1 Oil endowment (cumulative production plus remaining reserves and undiscovered resources) for provinces assessed. *Darker green* indicates more resources. The USGS world oil and gas assessment- Thomas S. Ahlbrandt, United States Geological Survey, Denver, CO, US Geological Survey Fact Sheet 062-03 (supersedes FS-070-00)

Hypothetically, estimated in place crude oil of the world are of the order of 6,000 billon barrel (B, barrel ~ 159 l) which includes the recoverable and non-recoverable oil in the reservoirs. From this about 3,000 BB could be technically recovered and produced. The quantum of recoverable oil is estimated based on the present geological information and technological development. The estimate of recoverable oil in region has three contributing components i.e. the cumulative production to given date, proven reserves and un-recovered resources (yet-to find) (Fig. 2.2, adopted from Wood et al. 2004). Based on the degree of uncertainty the oil reserves can be classified as proven and unproven. The proven reserves are "the estimated quantities of oil which geological and engineering data demonstrate with reasonable certainty to be recoverable in future years from known reservoirs under current economic and operating conditions" (Lyons and Plisga 2005). The proven reserves are the estimates of oil resources, which are based on geological information and could be produced by the present day technology certainty (probability). In practice a probability of 90% is used to ascertain the quantum of proven reserves in a region (Gregory and Rogner 2004). Unproved reserves can be classified into possible reserves and probable reserves, based on the low order probabilistic distribution. Possible reserves are estimated with 50% probability and with assigned probability of 10% the quantum of probable reserve are estimated. In general, most early estimates of the reserves of an oil field are conservative and tend to grow with

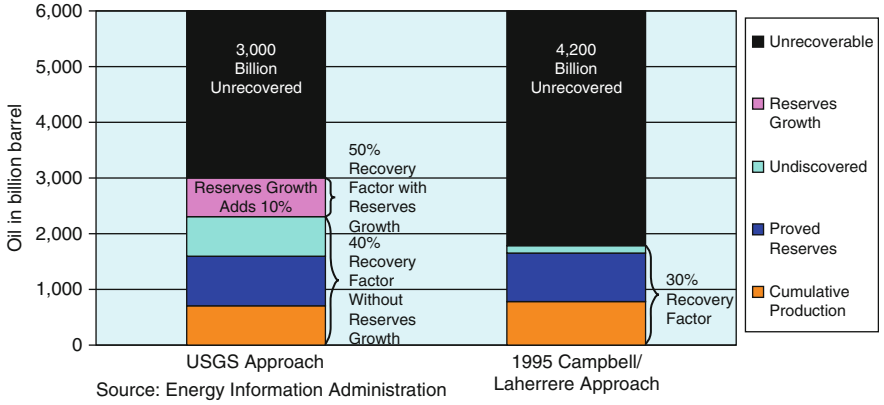

Fig. 2.2 Different interpretations of a hypothetical 6,000 Billion barrel World Original Oil-in-Place resource base
Source: http://www.eia.doe.gov/pub/oil_gas/petroleum/feature_articles/2004/worldoilsupply/oilsupply04.html

time. This phenomenon is called reserves growth. Governments can also withhold details of oil reserves for economic and national security reasons, are considered as strategic reserves. EIA estimates approximately 4.1 billion barrels of oil are held in strategic reserves. These reserves are generally not counted when computing a nation's oil reserves.

Based on the technological aspect, the configuration of the geological structure and economical consideration, only a part of the oil can be produced from the oil in place. The ratio of the producible oil to oil in place is termed as the recovery factor. The recovery factor varies from 10 to 60 and even as high as 80. The recovery factor can be enhanced depending on the characteristics of the reservoir, technological development and on the investment. The producible oil also incorporates small quantum of undiscovered (yet-to-find) oil. The non-producible/unrecoverable oil pertains to the oil that cannot be recovered by present technology and economic consideration. These estimates may change as knowledge for the formation of oil grows, technology advancement and change in the economics scenario. The model estimate of USGS has a component of reserve growth, suggesting improving the recovery factor may enhance estimates of reserve. Primarily about 10–15% oil can be recovered by upward flow towards the surface of oil by its buoyancy. The recovery factory can be enhanced by means of injecting fluids and thereby increasing the pressure in the reservoir (secondary), and in the tertiary process by thermally heating oil by injecting steam and thereby reducing its viscosity. Chemical agents like surfactants can also be used to reduce the surface tension in the oil and allow the oil to flow easily to the surface. Other means is pumping gases like carbon dioxide in to the reservoir, which may either reduce the pressure or get mixed up with the oil and thereby reducing its viscosity and permits easy out ward flow to the surface. Such attempts may enhance the recovery factor to as high as 60%. With the

introduction of 3-D seismic survey, demarcating the physical limits (geometry) of oil reservoir has become more reliable and the scope of drilling dry wells has substantially reduced. The time lapse 4-D seismic surveys not only provide locating oil reservoir more precisely but also helps in real time estimates of oil reserve quantum by the identification of oil-water contact. Advancement in drilling technology also helped prevention of blow outs. Logging while drilling (LWD) providing real time in situ measurement and thereby ascertaining the health of reservoir. Introduction of horizontal and target oriented drilling has resulted in improving the recovery enhancement. These advancements in technologies have enhanced recovery factor from 10 to 60% to as high 80% depending on the characteristics of the reservoir, technological development and the investment.

Figure 2.3 shows the pattern of oil reserves estimates based on the different confidence level (probability). The distribution suggest that with least confidence level, reserve estimate is significantly high, whereas with 95% confidence level the reserve quantum is appreciable low. With these probabilities the global reserve is estimated to be about 2,500 BB with 95% probability and 3,900 with 5% (possible reserves) probability respectively. Under the prevailing technological conditions a figure 2,500 BB reserve looks to be quite optimistic. However, experiences have shown that the estimate of oil made in the past is rather low. Improvement in the understanding the characteristics of reservoirs are leading to increase in the recovery of oil and thus growth in reserve estimates.

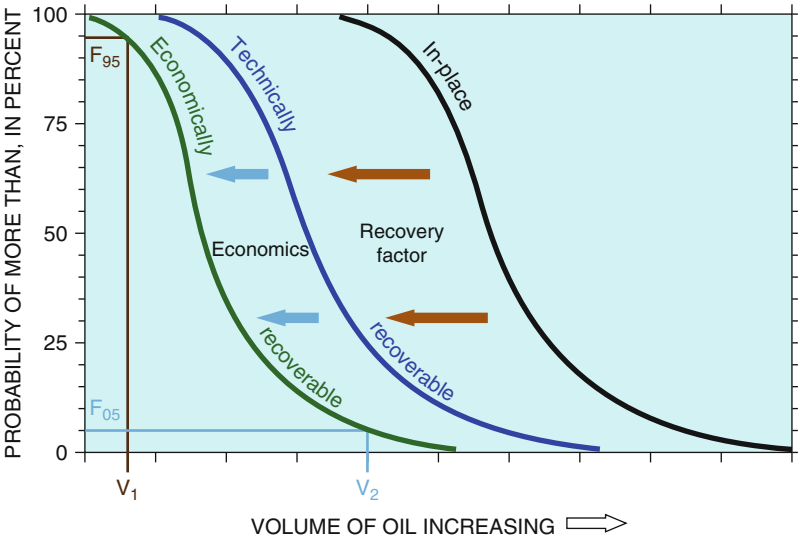

Fig. 2.3 Schematic graph illustrating petroleum volumes and probabilities. *Curves* represent categories of oil in assessment. There is a 95% chance (i.e., probability, F95) of at least volume V1 of economically recoverable oil, and there is a 5% chance (F05) of at least volume V2 of economically recoverable oil

Source: pubs.usgs.gov/fs/fs-0028-01/fs-0028-01.html

The present oil reserve estimates only take in to consideration the cumulative figure of oil already produced and likely to be produced with present day technology and which is economically viable. In this regard it is considered as the conventional form of energy.

The OPEC members hold around 75% of world crude oil reserves. The countries with the largest oil reserves are, in order, Saudi Arabia, Iran, Iraq, Kuwait, United Arab Emirates (UAE), Venezuela, Russia, Libya, Kazakhstan and Nigeria (Fig. 2.4).

2.2 Oil Scenarios

The amount of oil in place is estimated by different methods. They are categorized in three categories, viz. volumetric, material in balance and production performance. Volumetric method provides the estimate of oil in the reservoir depending on the size, the physical properties of the host rock and the liquid content. The product of the size of the reservoir and the recovery factor determines the oil in reserve. The material in balance method relies on the quantum of petroleum already extracted and the prevailing physical conditions, such as pressure, temperature and pressure history to determine the quantum of reserve the reservoir holds. The production performance methods depend on the history of production of the reservoir. As the

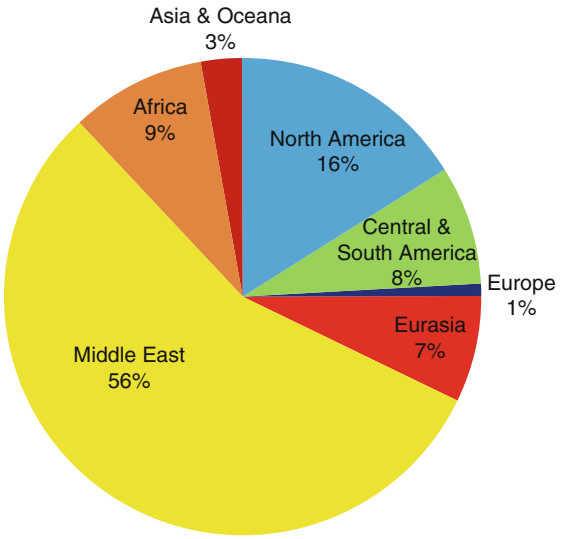

Fig. 2.4 World oil reserves by region
Source: www.absoluteastronomy.com/topics/Oil_reserves

production continues the rate of production will tend to decline. Based on the statistical analysis the pattern of decline in the production can be ascertained and strategies for production from the reservoir in future can be worked out.

The present oil reserve estimates have remained mainly unaltered. There have been no giant oil field discoveries after late 1960s. This is due to the fact that major oil fields tend to get explored easily. The estimated recoverable oil remained almost constant from around 1960s. This ultimately recoverable reserve of oil also incorporates the quantity of yet to find oil for estimating the total reserves, which can be put to production with some percentage of recovery factors. It is assumed that possibly around 2,000 BB can be recovered from existing oil in place. A periodical analysis based on the assumed ultimate recoverable oil 2,000 BB, suggests that the contributory elements to ultimate recoverable have been modified/re-categorized, the total quantum remaining unchanged since 1950 (Bentley 2002). The analysis indicated (Fig. 2.5) that as cumulative production has grown, the proved reserves have increased from 540 BB in 1970 to 1,050 BB in 1998. The quantum of yet-to-find resources have substantially contributed to the improvement in the proved reserves. This may suggest that estimates of proved reserves have been under quoted or due to part of probable and possible reserves estimates have been put in the proved reserve category with technological developments and thereby improving the recovery factor. The re-categorization leads to improvement in the estimates of proved reserves and with reserve/production ratio of 1998, the world's oil production can sustain in future for two to three decades.

However, for most of countries around the world have shown decline in the production of conventional oil. Figure 2.6 gives the yearly production of oil from the major oil producing countries of the world. The quantum of oil which is likely to be produced including a appreciable quantum from deep water reservoirs, Polar Regions as well as liquids converted from natural gas reserves does not provide encouraging scenario for oil production in future. In US oil production has substantially come down from couple of decades. The Middle East, most prolific contribution to oil production also seems to be approaching peak production.

Figure 2.7 shows world wide consumption of oil (dark colours represents more consumption based on the reserve estimates during late nineties of the order 1,750 BB (www.globalresourcesplus.com/Petroleum_by_ country.html). Most of oil producing countries except perhaps Middle East and Russia has already consumed more than half of their estimated oil reserves. In recent time it is being debated how long the conventional oil reserves are going to last. It is argued that global conventional supply is at political and physical risk (Bentley 2002). It is estimated that maximum oil reserves are still preserved in the Middle East. Under any political strain the Middle East may curtail its oil production and it would be quite difficult for other oil producing countries to substitute the shortfall resulting in higher cost and leading to turmoil in the international market. As most of the oil producing countries in the world have already crossed the peak limit of the oil production, the burden on Middle East countries will be immense to increase the production leading to the decline in their oil reserves (Bentley, 2002).

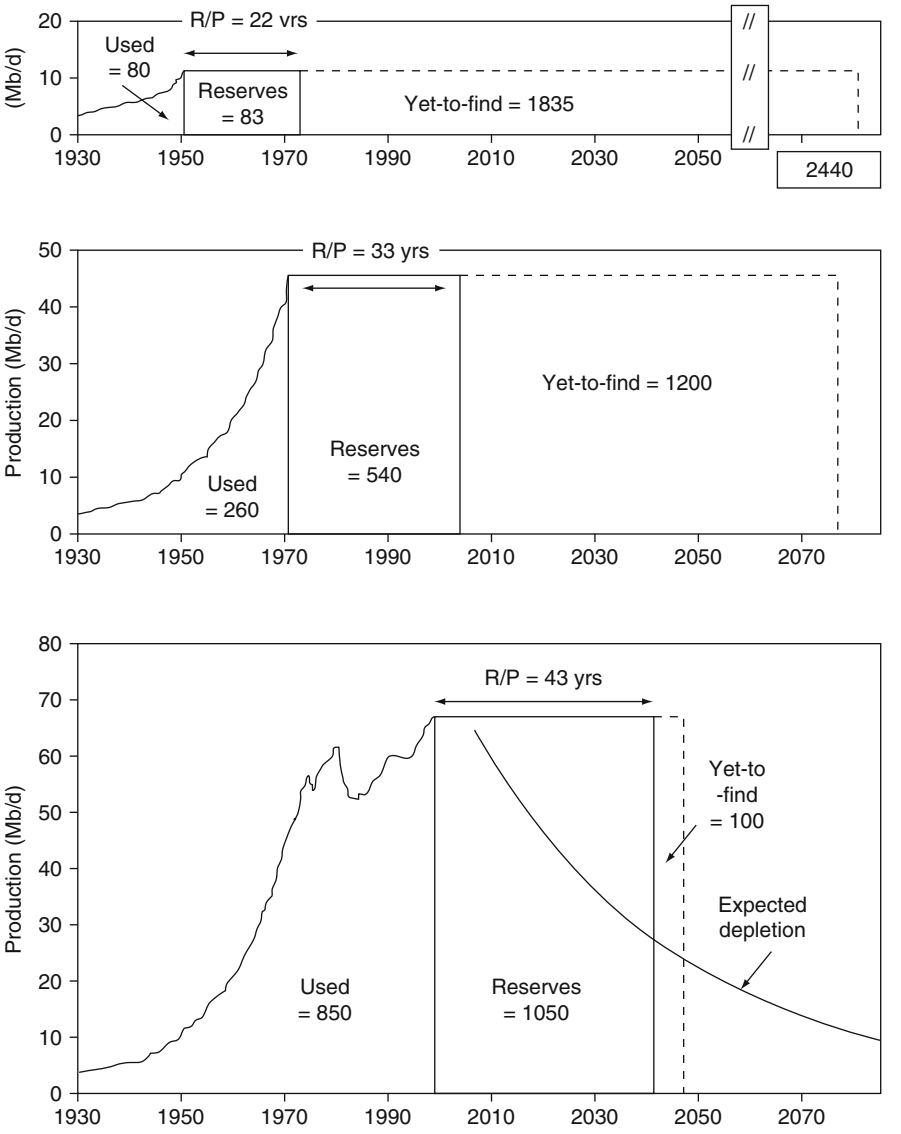

Fig. 2.5 A history of world oil: production, reserves, and yet-to-find in 1950, 1970 and 1998. *Notes*: excludes NGLs. Data in billion barrels (Gb). Assumes a conventional ultimate of 2,000 Gb, and calculates: Yet-to-find ¼ Ultimate Cumulative production Reserves: Reserves here are public domain proved reserves. (This makes the end-'98 yet-to-find somewhat misleading. The industry end-'98 figure for (proved+probable) reserves, excluding NGLs, is around 850 Gb, giving a yet-to-find, based on a 2,000 Gb ultimate, of about 300 Gb). Depletion curve: Exponential decline once 1,000 Gb has been produced
Sources: Reserves data from BP Statistical Reviews, and as supplied by EDA Ltd. Production data pre-1965 from Campbell. NGL's estimated

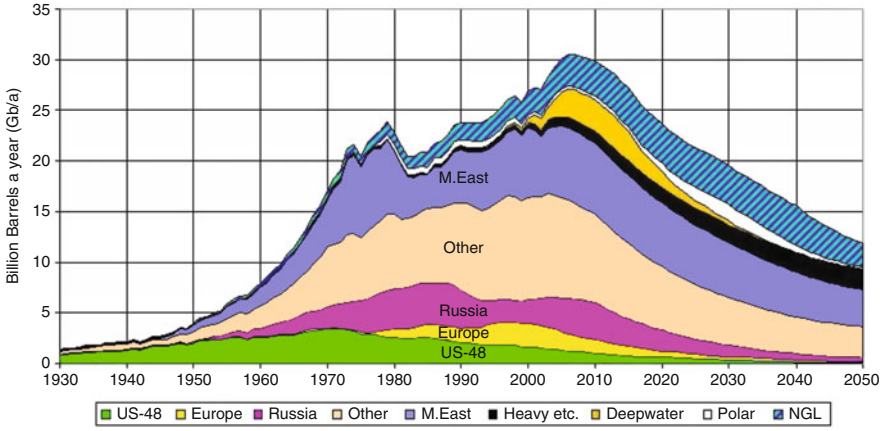

Fig. 2.6 Yearly production of oil from major oil producing countries of the world. The peak is the top of the curve, the halfway point in the consumption of the world's oil and gas resources
Source: visions2200.com/EnvironmentEnergyFossil.html

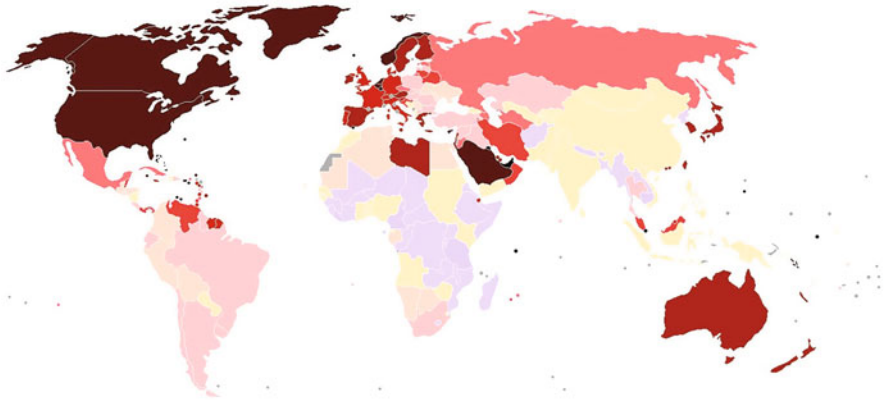

Fig. 2.7 Worldwide consumption of oil (per capita) *darker colours* represents more consumption
Source: globalresourcesplus.com/Petroleum_by_country.html)

The consumer demand for crude oil has been increasing with annual rate in excess of 2%. This demand is even higher in the advanced Asian countries like China, India and South Korea owing to increase in transportation, using cars and trucks powered by internal combustion engines. Extensive analysis of demand-supply by petroconsultants, geologists has predicted that the oil production will peak with in a span of 20 years in the near future. Based on the King Hubbert (1973) and Gillette (1974) approach, USGS analyzed long term world supply data and predicted the nature of oil production scenario in the future. Figure 2.8 shows the pattern of annual demand production growth of 2% for different resource levels and with decline for reserve/production (R/P) ratio of 10. It is estimated that with 95%

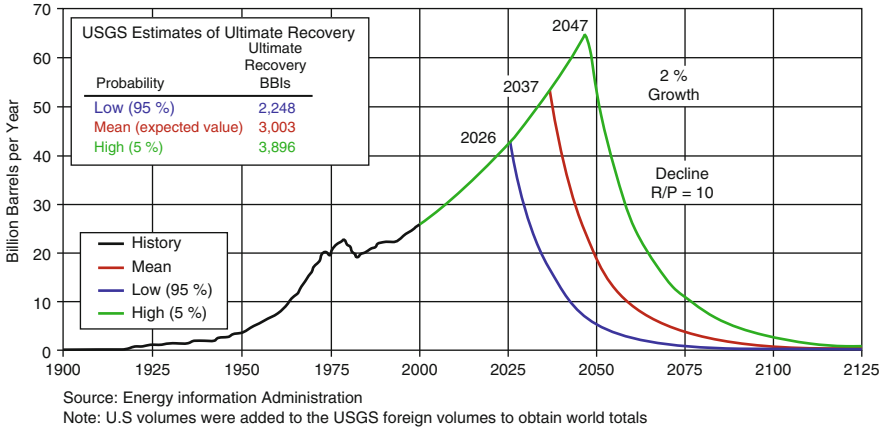

Fig. 2.8 The pattern of annual demand production growth of 2% for different resource levels and with decline for reserve/production ratio (R/P) of 10 (Adopted from Wood et al. 2004)

probability the oil reserve is estimated to be of order of 2,248 GB and with demand growth rate of 2% the oil production will peak around 2026 touching a figure of around 42 BB per year, which eventually will decline sharply with assumed R/P ratio. The oil production will peak to about 52 BB in 2037 with estimated mean value of oil reserves. With lowest probability of 5% of oil reserve estimate the peak production will touch value of around 65 GB per year during 2047. Even with least probability of 5% the world oil reserve touch a figure of 3,898 BB and eventually decline very fast leading to severe energy crisis all over the globe.

2.3 Natural Gas

The present trend in oil consumption and its not encouraging prospects make natural gas a viable replacement for oil in near future. The decomposition of organic matter in oxygen- poor (anaerobic) conditions and aided by bacterial activity leads to the formation of natural gas. The presence of high content of organic matter in most of the young sediment basins may favor the generation of methane gas in such locales. The gas when formed diffuses in surrounding regions unless it is trapped by suitable geological structures. Commercial amounts of gas also can accumulate as a gas cap above an oil pool or, if reservoir pressure is sufficiently high, dissolved gas in the oil is derived from both land plants and marine organic matter. The gas found in nature is formed due to physical, chemical, biological and geological conditions prevailing in different at levels in the earth's crust. Most of the methane gas is of biogenetic nature and formed at shallow levels of the crust, where biological and chemical processes dominate and is confined to swamps, lake beds and shallow marine environment. In the deeper parts of the earth

the physical parameters of temperature and pressure dominate the formation of thermogenic gas (see details – Chap. 1). Natural gas primarily comprises methane and ethane. Other gases like propane and butane may also be present in the natural gas and such mixture without presence of any liquid component is considered as dry natural gas. The inclusion of higher isotope elements such as pentane containing liquids at standard pressure and temperatures may be considered as natural gas liquids. Natural gas reserve may also contain non-hydrocarbon elements such as carbon dioxide, water vapor, hydrogen sulfide and such mixed gas is considered as wet natural gas. The wet gases are processed to remove the contaminants before the gases are used for normal purposes.

Gas is found abundant in nature; with its higher recovery rate, higher fuel efficiency and low order pollutant may work out to be a good future energy prospect. Natural gas remains the main energy resources for many industrial plants and the generation of electricity. Worldwide natural gas is third most prominent energy resource amounting to 23% of global energy consumption. It is expected that in future, industry will consume 40% of total gas production. In absence of good transport system for transporting the gas to industrial plants most of the gas associated with oil reservoirs is burnt at the wellhead. Owing to its low calorie content it has lesser priority than oil for its use as the energy source. In order of priority Russia, Iran, Qatar, Saudi Arabia and UAE have the highest gas reserves of the world. Russia is also highest gas producer of the world. Global gas reserves are abundant, but unevenly distributed (Fig. 2.9).

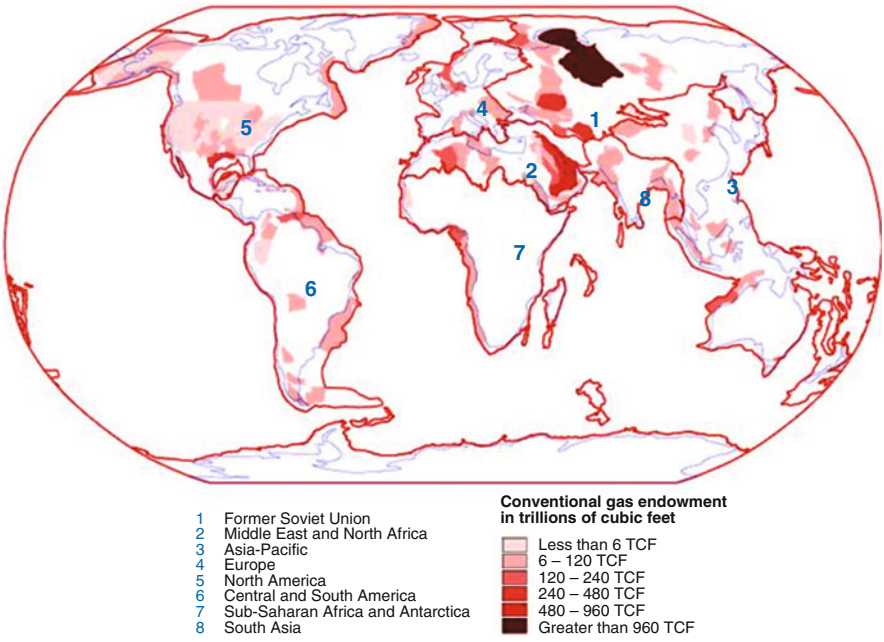

Fig. 2.9 Global gas reserves. (Adopted from Ahlbrandt (2002))

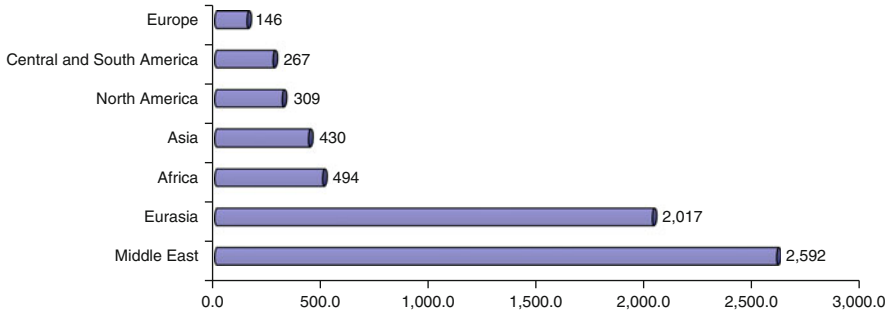

Fig. 2.10 World Natural Gas Reserves by Geographic Region as of Jan 1, 2009
Source: Worldwide look at reserves and production, "Oil and Gas Journal. 106(48), (Dec 22, 2008) pp 22–23

The projected estimated reserves of the world are of the order of 10,000 trillion cubic feet (TCF), out of which around 6,254 TCF are the proven reserves. Middle East and Eurasia hold almost three-quarter of world's natural gas (Fig. 2.10), Russia, Iran and Qatar alone contributing 57% of this. It has been suggested that the quantum of gas reserves have not substantially improved over last couple of years. However, Iran and USA in recent times have added significantly to their reserves, followed by small incremental rise in the reserves in Indonesia, Kuwait, Venezuela and Libya (EIA 2009). Most of the reserves growth in USA during the last couple years has come from shale resources, outside USA there were not much serious attempts to exploit natural gas from the shale resources.

2.3.1 Natural Gas Scenario

The global market for gas is much smaller than for oil because gas transport is costly and difficult. Only about 16% of global gas production is internationally traded, with less than 4% of the trade accounted for by liquefied natural gas (LNG). However, in spite of the high cost of gas transportation and the remote location of potential future supply regions, increasing international trade in natural gas is expected. A significant portion of gas production by major gas producing countries is meant for export in the form of LNG. Middle East and Africa are likely to be main contributors for the supply of LNG in the coming future. These two countries are likely to have tremendous growth (~21 TCF) in the production of natural gas and especially in terms of LNG and may cover a bigger portion for the demand of gas from other countries (EIA 2008, 2009). Recent discovery in China and India may help these countries to reduce their import from other countries. The industrialized countries are the major gas importers, but the major gas supplies are located in the Former Soviet Union and the Middle East. Thus, similar to world

oil, the expanded use of natural gas by Europe and Japan will become increasingly dependent on the world's politically unstable regions. Canada provides most of the natural gas imports to the United States.

The Organization of Economic Co-operation and Development (OECD) comprising mainly of developed countries (USA, Canada, Japan, South Korea and others) and Non-OECD (Russia, China, India and others) consumed around 104 TCF during the year 2006. The yearly world demand for natural gas is 104 TCF and likely to rise to 153 TCF in 2030. In the year 2006 the OECD countries consumed 52 TCF and non-OEBD countries utilized 53 TCF. The consumption of natural gas by non-OEBD countries is likely to surpass to that of OEBD countries, with 2.2 average annual growth almost twice that of 0.9% growth of OEBD countries (Fig. 2.11). In the year 2006 OEBD produced 38% of total natural gas production and consumed about 50% of the total gas production making them to depend heavily on imports from other countries. The projected production and consumption of natural gas by OEBD countries is likely to fall during the year 2030 and their dependence on import of gas may likely to fall as projected during 2030. Russia is largest consumer natural gas in the list of non-OEDB countries and by 2030 the gas consumption is likely to surpass that of oil and coal consumption. The non-OEBD presently consumes about 9% of world gas production and which is likely to increase to 31% in the year 2030. Developing countries China and India are likely to heavily increase their consumption to match with the expected industrial growth. Presently China and India utilize very small percentage of gas towards their energy consumption and which is likely to show an increase of 5% in their consumption. In order to meet the growing demand of natural gas in the future a substantial increase in the production of gas is required. The non-OEBD countries are likely to contribute significantly to world's natural gas production. In the non-OEBD countries the

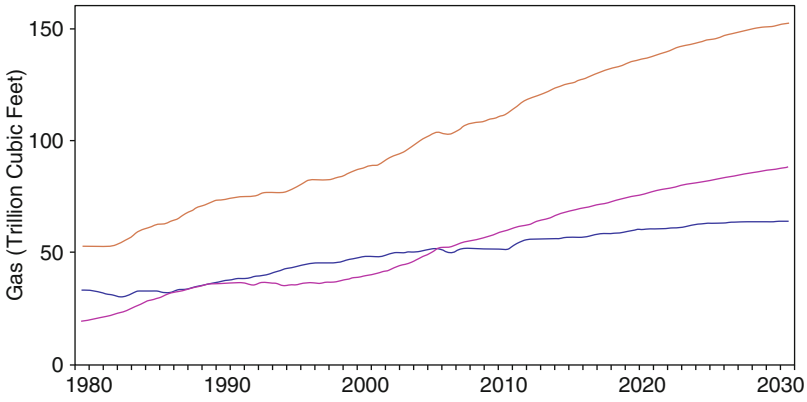

Fig. 2.11 World Natural Gas Consumption 1980–2030
Source: Energy Information Administration (EIA), International Energy Annual 2006 (June-Dec 2008). Brown line represents the total world consumption pattern, Blue line is for OEBD countries and Red line for Non- OEBD countries consumption
Source: http://www.eia.doe.gov.iea. Projections EIA, World Energy Projections Plus (2009)

production is likely grow by 2.1% per year. On the contrast the OEBD countries will show smaller growth rate of 0.9% and may likely to add about 7 TCF to increase in global demand of 48 TCF during the period of 2026–2030. India and China is likely to double their production by 2030. However, the rate of consumption is also, increasingly sharply in the developing countries like China and India.

The study suggests that the Non-OCED countries will start consuming more gas in future. Like in the oil scenario most of the proven world gas reserves have already been consumed. With higher rate of recovery the peak production for many countries has already surpassed.

2.4 Unconventional Oil

The conventional form of oil contributes only a small percentage of the existing oil basket under the subsurface earth. The existence of other types of large petroleum deposits over vast areal extent have been identified. These oil reserves have slightly different physical characteristics and cannot be recovered from normal conventional techniques. The unconventional resources require greater than industry-standard levels of technology or investment to harvest and are termed as unconventional oils. The total amount of unconventional oil resources in the world considerably exceeds the amount of conventional oil reserves (Fig. 2.12). It is estimated that earth may hold about 45,000 BB of unconventional oil and about 1,000 BB can be recovered and put to production. This substantial fossil fuel energy resource may supplement and overcome the depleting conventional fossil fuels in the near future.

Unconventional fossil fuels have been put in four distinct groups, based on their higher density, viscosity and ratio of hydrogen and carbon in the oil. These oil types do not flow easily due to their high viscosities. They can be categorized in heavy and extra-heavy, bitumen and shale oil, depending on their specific gravity or American Petroleum Institute (API) gravity values. API values define the density of petroleum liquids compared to water. Petroleum liquids having lesser than 10

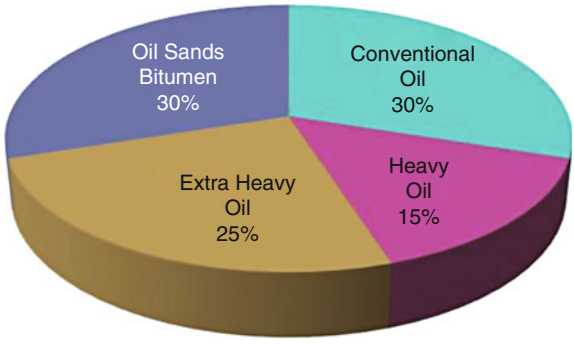

Fig. 2.12 World proven oil reserves
Source www.landartgenerator.org/.../date/2009/09

API value sinks in water and greater than 10 are lighter when compared to water. Most of the unconventional oils have lower API when compared to conventional oil. Oils are considered to be heavy, extra heavy or bitumen, when their API values range from 25 to 7 covers mobile and less mobile (bitumen) oils. The shale oil constitutes mainly of bitumen and primarily considered as source rock (Total 2006).

Most of unconventional oil deposits are confined to shallow portion of the crust and have been identified in many parts of the world. These deposits are considered as degraded products of conventional oil. It is being hypothesized that conventional oil field formed at deeper level migrated to shallower levels. In the shallower levels most of the lighter carbons were consumed due to biodegradable action by the bacteria, exposure to water and air, leaving the hydrocarbon containing carbon, asphaltenes and resins in the oil. They are contaminated by heavy metals, sulfur and nitrogen. These deposits are found mainly in unconsolidated permeable sands.

Oil sands, also known as tar sands, or extra heavy oil, are a type of bitumen deposit. The sands are naturally occurring mixtures of sand or clay, water and an extremely dense and viscous form of petroleum called bitumen. Depending on the viscosity of the heavy oils different types of methods are proposed for production. Heavier oils with comparable lower viscosity can be produced by injecting hydrogen (hydro-cracking) or depleting carbon content (cracking) of the heavier oils. The viscosity of the heavy oils decreases appreciably with increase in temperature. Steam is injected in the reservoir for the production of oil. Because of very high viscosity of the bitumen containing oil, normal treatment processes cannot be applied

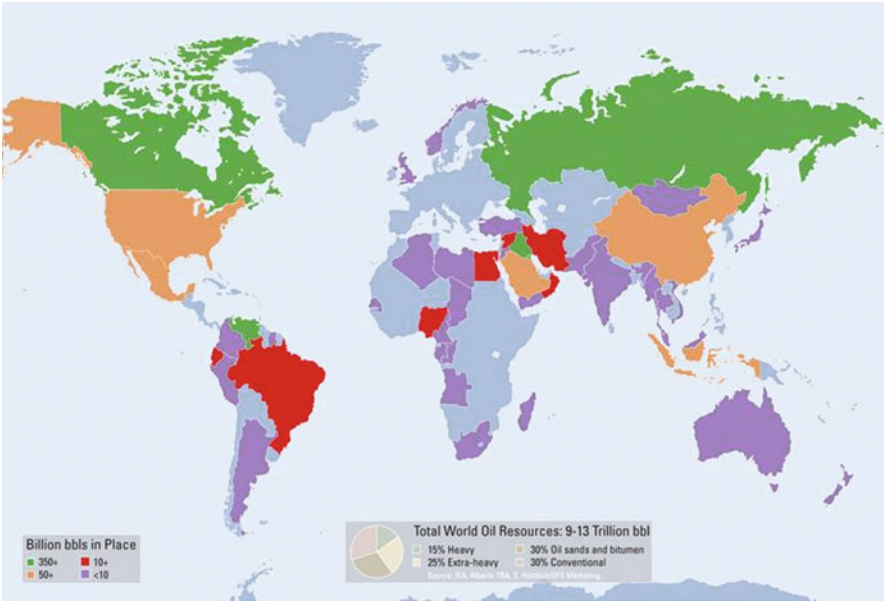

Fig. 2.13 Worldwide heavy oil reserves by country
Source: Schlumberger open database; http://www.slb.com/services/industry_challenges/heavy_oil.aspx

for production of oil. The deposits present at shallow levels of the earth are mined along with host rock and treated in plants for recovery of oil. The heavy, extra heavy and bitumen oil deposits are found in large amounts in many countries throughout the world (Fig. 2.13, adopted from http://www.slb.com), but are found in extremely large quantities in Athabasca Oil Sands in Alberta, Canada and the Orinoco extra heavy oil deposit in Venezuela. These two countries produce around two-third heavy and extra heavy oil of the world. IEA estimates that earth may hold about six trillion barrels of heavy oil and from which about two trillion barrels is recoverable.

2.4.1 Shale Oil

Historically shale oil has been referred by many different names, such as cannel coal, boghead coal, alum shale, stellarite, albertite and kukersite. Some of these names are still used for certain type of oil shales. Shale oil is primarily a fine grained sedimentary rock containing lots of organic material (kerogen). The chemical decomposition of kerogen begins at temperature 480–520°C. Appreciable quantity of oil can be extracted from these sediments. The extraction process requires mining of the rock and subjecting it to heat treatment (retorting) or from the chemical process of pyrolysis. Shale oil is likely to be present in many parts of world; the highest concentration is being in the USA. The estimated quantum of shale oil of the world is around 2.8–3.3 trillion barrels and small percentage of that can be recovered.

2.5 Unconventional Gas

Natural gas in most of the countries is being produced from conventional reservoirs. Except USA, most of the countries have not put serious efforts to look for the vast extent of gas trapped in complex geological environment. One way of defining unconventional gas is as 'natural gas that cannot be produced at economic flow rates nor in economic volumes of natural gas unless the well is stimulated by a large hydraulic fracture treatment, a horizontal wellbore, or by using multilateral wellbores or some other technique to expose more of the reservoir to the wellbore' (Perry et al. 2007). Unconventional gas resources are likely to be present in tight gas sand, coal seams (coal bed methane) and in shale gas. Growing concerns about the green house effects and depleting oil scenario have necessitated USA to increase the gas production by proper understanding of the geological regimes and applying new techniques for the extraction of natural gas from unconventional resources. This has led to boosting of gas production in USA by the order of 30%. It is estimated that a total 32,000 TCF of natural gas to be present in coal bed methane, shale gas and tight gas sands (Rogner 1997; Kawata and Fujita 2001). During the last decade development of tight gas reservoirs have occurred in Canada, Australia, Mexico, Venezuela, Argentina, Indonesia, China, Russia, Egypt, and Saudi Arabia. Most of the recent

discoveries of giant gas field in United States are located in unconventional gas resources. Unconventional gas deposits are confined to low permeable reservoirs and mainly contain dry gas and are categorized based on their flow rates.

Unconventional gas also been associated with coal bed formation (coal bed methane) and is emerging as good resource potential for natural gas in near future (Detailed in Chap. 1). Other prominent gas resources which have been extensively reported in recent times are the presence of methane gas in form of gas hydrates.

2.5.1 Tight Sands

Tight sands are characterized by their low permeability because of compaction, the nature of the fine sediments, or pore space infilling. The tight sand reservoirs are mainly associated with compact rock types such as sandstones and limestones. It is assumed that tight sands occur in vast quantities world over but their quantum is not well defined. It is estimated that gas from tight sands contributes to about 30% of total domestic supply in the United States. The flow rates of tight sands are uneconomical and it takes special technologies to produce this unconventional resource. A great deal more effort has to be put into extracting gas from a tight formation. Several techniques exist that allow natural gas to be extracted, including fracturing and acidizing.

2.5.2 Shale Gas

Shale formations act both as source and reservoir for natural gas. The gas in shale is stored in pore spaces, in the fractures and absorbed gas. The presence of gas in different settings makes extraction of gas from the shale difficult. Abundant occurrences of shale gas have been reported from USA, Canada and Asia Pacific (Perry et al. 2007). It is expected world over about 16,000 TCF of natural gas may exist in the from shale formations. Hydraulic fracturing, horizontal and directional drilling techniques are being used to extract gas from the shale gas reservoirs.

2.5.3 Geopressured Zones

Geopressured reservoirs or aquifers occur in most parts of the world in the deeper parts of the earth. These zones/reservoirs are located in a higher pressure regime under the earth's surface. These deep reservoirs/zones hold methane dissolved in hot (150–200°C) brine solutions. The natural gas present in the aquifer is under very high pressure hence the term 'geopressure'. The reservoirs are formed when the water and methane gas present in the clay is squeezed out and percolates down in

the more porous sand and silt deposits due to the rapid compaction overlying clay beds. Subsequent sedimentations increase pressure conditions in the aquifer. The geopressurized reservoir zones are located at great depths, usually 3,000–6,000 m below the surface of the earth. The dissolved methane content is generally of the order of 30–80 cubic feet in one barrel of brine solution. The dissolved gas content in the geopressurized reservoir is appreciably low in comparison to normal liquid hydrocarbons under pressure. However, the occurrences of these zones over large —— extent make these deposits as possible future resource potential. The higher fluid pressure gradient in the reservoir may lead to easier recovery of gases when the reservoir is tapped.

The geopressurized zones provide three types of energy resources. They form unconventional gas reserves; the high pressurized fluids impart mechanical energy and the hot brine may provide geothermal energy. However, geopressurized zones are estimated to hold largest unconventional gas reserves of the world. Most of the geopressurized natural gas in the U.S. is located off Louisiana and Texas Gulf Coast region. In these regions most of the productive strata is confined to sand beds, which are interbedded with shale. The amount of natural gas in these geopressurized zones is uncertain. However, experts estimate that anywhere from 5,000 to 49,000 TCF of natural gas may exist in these areas. Given the current technically recoverable resources are around 1,100 TCF, geopressurized zones offer an incredible opportunity for increasing the nation's natural gas supply.

Emergence of new technology and proper understanding of mode of formation of unconventional oil/gas resources in recent times has provided some hope that these resources may compliment the conventional oil/gas reserves and thereby reduce the energy resource crunch in future. However, such efforts require large financial resources and unconventional oil/gas production economical viable for its production and utility. Even with probable abundant accumulations of unconventional form fossil fuel energy special types of processes, present economic conditions and political considerations may forbid extensive attempts to extract and utilize unconventional energy resources. The easier processes of recovery of conventional form fossil fuel energy and its economic still hold advantageous this over unconventional oil and gas resources. In this context unconventional form of oil and gas may not significantly add to present oil and gas reserve scenario. The present recession in the global market may make unconventional oil economical not viable source of energy in the near future.

2.6 Hydrogen

Hydrogen is being considered as viable source of energy carrier in the future. It can be used in any application in which fossil fuels are being used today. Hydrogen works as an energy carrier, and like electricity must be produced from other resources. Because hydrogen doesn't exist on Earth as a gas, it must be separated from other elements. It can be produced from water by using a variety of energy

sources, such as solar, nuclear and as the by-product of chemical reaction and it can be converted into useful energy form efficiently and without detrimental environmental effects. The only by-product is water or water vapor. The utility of solar energy for separating hydrogen molecules from water may provide hydrogen as renewable source of energy carrier.

Most commonly used methods for producing hydrogen are the steam reforming and electrolysis. Steam reforming method is less expensive is commonly used for producing hydrogen from methane gas. About 90% of hydrogen produced in United States comes from steam forming method. The steam forming method emits high quantity of green house gases, which may lead to global warming. The electrolysis process is used to separate hydrogen atoms from water molecules. It is very expensive process and utilized only on smaller scale and as emergency standby.

It is suggested that usage hydrogen as energy may substantially reduce the greenhouse effect and thereby controlling global warming. Hydrogen can be used as a fuel in furnaces, internal combustion engines, turbines and jet engines, even more efficiently than fossil fuels, i.e., coal, petroleum and natural gas. Hydrogen can also be converted directly to electricity by the fuel cells, with a variety of applications in transportation and stationary power generation. It has been successfully demonstrated that light vehicles as well as buses as mode transportation can be run utilizing hydrogen energy. The National Aeronautics and Space Administration (NASA) is the primary user of hydrogen as an energy fuel; it has used hydrogen for years in the space program. Liquid hydrogen fuel lifts NASA's space shuttles into orbit. Hydrogen batteries, fuel cells, power the shuttle's electrical systems. The only by-product is pure water, which the crew uses as drinking water. Unfortunately the production of hydrogen from the renewable energy resources is extremely high and production of hydrogen from fossil fuels may lead to green house effects. The utility of hydrogen as energy resource needs large quantum of hydrogen and its conversion to energy requires planning and cost effective and its efficient transition to energy is quite complex processes. Such efforts require large capital and human endeavors for making this form of energy as alternative source of energy fruitful.

References

Ahlbrand T. (2002) Future Petroleum Energy Resources of the World, International Geology Review, 44(12), 1092–1104.

Bentley R.W. (2002) Global Oil & Gas Depletion: An Overview, Energy Policy 30, 189–205.

EIA (2008) Annual Energy Outlook 2009 Early releases overview. Online http://www.eia.doe.gov. Accessed between June 2009 to April 2010.

EIA (2009) Annual Energy Outlook 2010 Early releases overview. Online http://www.eia.doe.gov Accessed between June 2009 to April 2010.

Gillette R. (1974) Oil and Gas Resources: Did USGS Gush Too High? Science 185, 27–130.

Gregory K. and Rogner H.H. (2004) Energy Resources and Conversion Technologies for the 21st Century, Mitigation and Adaptation Strategies for Global Change, 3(2–4), 171–230, December, 1998, DOI 10.1023/A:1009674820623.

Kawata, Y. and Fujita K. (2001) Some predictions of possible unconventional hydrocarbons availability until 2100, Presented at SPG Asia Pacific Oil and Gas Conference, Jakarta, Indonesia.

King H.M. (1973) Survey of World Energy Resources, Canadian Mining and Metallurgical Bulletin 66, 37–53.

Lyons W.C. and Plisga G.J. (2005) Standard Handbook of Petroleum and Natural Gas Engineering (2nd Edition). Elsevier Publication. Online version available at: http://knovel.com/web/portal/browse/display?_EXT_KNOVEL_DISPLAY_bookid=1233&VerticalID=0

Perry K., Lee J., and Holditch S.A. (2007) Unconventional gas reservoirs-Tight sands, Coal seams and shales, Working document of NPC global oil and gas study, pp 54.

Rogner H. (1997) An Assessment of World Hydrocarbon Resources, Annual Review of Energy and the Environment 22, 217–262, doi:10.1146/annurev.energy.22.1.217, online: Downloaded from http://www.arjournals.annualreviews.org.

Total (2006) Extra-Heavy Oil and Bitumen Reserves for the Future, The Know-How Series, pp. 28.

Wood J.H., Long G., and Morehouse D. (2004) World conventional oil supply expected to peak in 21st century, Offshore, 63, 90 (online version available at http://www.eia.doe.gov/pub/oil_gas/petroleum/feature_articles/2004/worldoilsupply/oilsupply04.html).

Chapter 3
Gas Hydrates

Abstract The present non-encouraging oil and gas scenario in terms of their depletion and variability of day-to-day cost of production necessitates for looking for alternative means of resource. Natural gas hydrate in terms of their existence over vast areas with abundant presence of methane has provided more impetus towards its exploration and technological development for its utilization as energy resource in future more so for energy starved countries like India and Japan. Methane hydrate is a clathrate composed of water and natural gas, mainly methane, which forms under conditions of low temperature, high pressure, and proper methane concentration. In the scientific jargon the term natural gas hydrates, indicating that methane gas occupies most of the cavities in the hydrates, which burns more efficiently with lesser emission compared to conventional fossil fuels. The methane content in gas hydrate per unit volume far exceeds the natural gas and slightly less than the LNG. The maximum amount of methane that can be trapped depends on the geometry, free space available in the lattice of the water molecule. A fully saturated unit m^3 gas hydrate sample at standard pressure and temperature (STP) is likely to hold 164-m^3 methane gas. The estimated carbon content in gas hydrates is likely to be double to that of entire carbon content of the fossil fuel resources. The estimated quantum of gas hydrates exceeding 1,000 Gt with high probability and in the range of 1,000–10,000 Gt, equivalent to ~2,000–20,000 trillion cubic meters with medium probability. The chapter provides details about the basic definition of gas hydrates, crystal structure, mode of formation, occurrence in nature in the subsurface earth, geophysical, geological and geochemical means for identification and drawing inferences about the presence of gas hydrate in the subsurface earth and estimates of their total quantum as energy resource.

3.1 Introduction

The non-encouraging future prospects of oil and gas in terms of higher cost, political, physical risks and high effective production costs of unconventional petroleum envisages to look for utility of other energy resource alternatives. Absence

N.K. Thakur and S. Rajput, *Exploration of Gas Hydrates*,
DOI 10.1007/978-3-642-14234-5_3,

of state of art technologies and lower quantum of energy generation from renewable resources makes them unviable alternative to present energy scenario. The uneconomic production of hydrogen fuels makes use of hydrogen as energy carrier a remote possibility in near future. Methane hydrates are expected to become an important source of energy in bridging carbon-intensive fossil fuel energies. With least emission methane stands out as clean energy among all hydrocarbons being utilized today. The relevance of gas hydrates as viable alternative to declining/stagnant fossil fuel energy resources provide more impetus towards its exploration and technological development for its exploitation more so in energy starved countries like Japan and India. In recent times gas hydrates with immense resource gas potential is being considered as viable alternative to overcome the present energy crisis.

In the scientific jargon they are termed as natural gas hydrates, indicating that methane gas occupies most of the cavities in the hydrates. The nomenclature is in accordance to the petroleum industry, where methane is formed under subsurface earth by natural process (Hunt 1996). The methane gas contained in the gas hydrates burns more efficiently with lesser emission of hazardous gases when compared to convention petroleum and coal. On the utility front methane gas is fast replacing as feedstock in power plants as well as running cars and other conveyance modes (Sloan, 2003). Gas hydrates are stable in the shallow regions of earth where pressure–temperature regimes are favorable for their formation. Gas hydrates cement the sediment grains, thereby increasing the rigidity and shearing strength of the medium. The occurrence of gas hydrates in the shallow subsurface earth makes them vulnerable to physical and chemical changes taking place on the surface of earth. The changes in the environmental conditions may lead to destabilize hydrates resulting release in large quantity of gases in the atmosphere. The instability may also lead to bulk changes in the properties of the sediments causing slope failures. In this aspect in the recent times keen interest has arisen to investigate gas hydrate as (a) energy resource (b) factor in global climatic change and (c) submarine geohazard (Sloan 2003).

3.2 What Are Gas Hydrates?

Ice-like crystalline materials have structured water molecular framework linked together to create cages, in which guest gas molecules can be trapped. They are considered as one of classes of clathrates (clathratus- cages/gratings, Brown 1962). Clathrates are inclusion chemical compounds in which a molecule of chemical component gets trapped in the cavities of the host molecule (Webster 1994). In terms of inorganic chemistry a ‘hydrate’ is stoichiometric compound, where water is one of the integral parts of a crystal structure and guest molecule may be of any other chemical compound. At the standard atmospheric pressure freezing point (0°C) of water, the molecules of water are arranged in an ordered (hydrogen bonding) manner and occupy more spaces creating hexagonal structure. At higher pressures, during cooling the water molecules get solidified with complex structures at

temperature above the freezing point. These complex structures unlike ice are inherently unstable, have network of small and large cavities developed in the crystal lattice. The presence of certain other compounds causes the crystalline structure to stabilize. Water molecules are host and molecules of other compounds are the guest molecules.

The guest molecules are considered as hydrate formers. Guest molecules in the hydrate fill the cavities without chemical bonding the crystal structure. The structure is held together not by the electrostatic hydrogen bonding but other weak forces termed as Van der Waals forces and the guest molecules are free to rotate in the cages (Carroll 2003). When the guest molecules occupy sufficient numbers of cavities the crystal structure becomes stable. The size and the geometry of the cages (voids) and availability of gases determine the formation of hydrates. Hydrates are formed under suitable high pressure and sub-zero temperature regime, when sufficient low molecular gases (formers) and enough quantity of water is present. Lower molecular gases, such as hydrogen and helium, lower than the size of small cavities (3.8 Å), and higher molecular gases, like pentane, hexane and paraffin hydrocarbons higher than the sizes of large cavities (>9 Å) forbids the formation of hydrates in the natural conditions. However, in recent times attempts have been made to synthesyze hydrates with low molecular gases in the laboratories. Most low molecular weight hydrocarbon and non hydrocarbon gases such as O_2, H_2, N_2, CO_2, CH_4, H_2S, Ar, Kr, as well as some higher hydrocarbons and freons are trapped in the cavities and form hydrates at suitable temperatures and pressures. Without the support of the trapped molecules, the lattice structure of hydrate clathrates would collapse into conventional ice crystal structure or liquid water. When the cavities are fully occupied by guest molecules of single chemical component then the composition can be expressed in terms of definite formula. However, in nature, depending up on the physical conditions (pressure, temperature) and availability of suitable gases, only parts of the voids are filled with guest molecules (degree of saturation).

The maximum amount of gas molecules that can be trapped depends on the geometry i.e. the free space available in the lattice of water of molecules and pressure and temperature. The hydrate sample can hold more gases under low temperatures and/or higher pressures. Based on the degree of saturation the water molecules can hold 70–160 volumes of gases. The terminology of clathrate hydrate or gas clathrate generally refers crystalline structures such as that of ice, whereas gas hydrate is commonly referred by geoscientist to crystalline structure where low molecular hydrocarbon gases such as methane (CH_4), ethane (C_2H_6), propane (C_3H_8) and pentane (C_5H_{12}) are trapped in the water molecules (Hardage and Roberts 2006). Gas hydrates of low order molecular hydrocarbons (<9 Å) such as methane, ethane and others are formed under low temperatures (<300 K) and moderate pressures (>0.6 MPa, Sloan 2003). In the case of gas hydrates, in general most of the cavities are filled and are occupied methane gas molecules; some of the cavities are filled with ethane and other gases. As not all the cavities are filled with methane gas, gas hydrates are considered as non-stoichiometric compound, which means chemical compound cannot be expressed with simple formula.

3.3 Crystal Structure

Higher pressure and sub-zero temperatures alter the arrangement of water molecules and thereby leading to 3-D geometry and interconnection of water molecules gives rise to crystalline structure having cavities inter-bedded in them. Each unit structure with geometry creates small and large cages in which the gas molecules are accommodated (Fig. 3.1). Three primary types of hydrate structures are known to exist commonly in nature, termed simply, structure I and structure II and rarely H structure. These structures represent different arrangements of water molecules resulting in slightly different shapes, sizes, and assortments of cavities. Formation of a typical structure depends on various aspects of the available guest gas. The pentagonal twelve-faced dodecahedron, (5^{12} structure) building block is common to all three-types of hydrate structures.

Structure I hydrates (Figs. 3.2 and 3.3a) are formed when the guest molecule having diameter ranging between 4 and 6 Å. A unit cell (the smallest repeatable element) of a structure I hydrate consists of 46 water molecules surrounding two small cavities (5^{12}) and six medium-sized cavities created by cubic tetrakaidecahedron ($5^{12}6^2$), a 14 faced polyhedron with 12 pentagonal and two hexagonal faces (Fig. 3.2). Methane, ethane, carbon dioxide and hydrogen sulfide are common hydrate formers of structure I. CH_4, CO_2 and H_2S can occupy small and large cages, whereas ethane because of higher molecular size can only occupy the large cages. All the small molecular gases with molecular sizes in the range of 3.73–4.33 Å can fill the small and medium size cavities in the hydrate structure I. When the cages of unit structure I is fully occupied by methane then on average the gas hydrate composition will have one mol of methane for every 5.75 mol of water.

The unit cell of structure II hydrates (Fig. 3.3b) consists of 136 water molecules creating 16 small cavities by 12 pentagonal (5^{12}) and eight large cavities created by cubic hexakaidecahedron-16 sided polyhedron with 12 pentagonal and four hexagonal faces ($5^{12}6^4$). Lower molecular gases like propane, isobutane and other with cavity radii 3.93 Å for smaller cavities and 4.73 for large cavity size can be accommodated in hydrate structure II. When the cages of unit structure II is fully occupied by methane then on average the gas hydrate composition will have one mol of methane for every 5.67 mol of water. Both structures I and II, hydrates can be stabilized by filling at least 70% of the cavities by a single guest gas, are therefore known as *simple hydrates*.

Structure H hydrates is not common in nature. The crystalline geometry of structure H hydrates is more complex (Fig. 3.3c) when compared to hydrate structure I and II. Structure H (Fig. 3.3c) hydrate have some cages larger tan structure II hydrates. Structure H hydrates is formed by the combination of three types of hexagonal crystalline structures (Ripmeester et al 1987; Sloan 1998). A dodecahedron (5^{12}), an irregular dodecahedron with three square faces, six pentagonal faces and three hexagonal faces ($4^3 5^6 6^3$), an irregular icosahedron, a 20 sided polyhedron with 12 pentagonal faces and eight hexagonal faces ($5^{12}6^8$) (Carroll

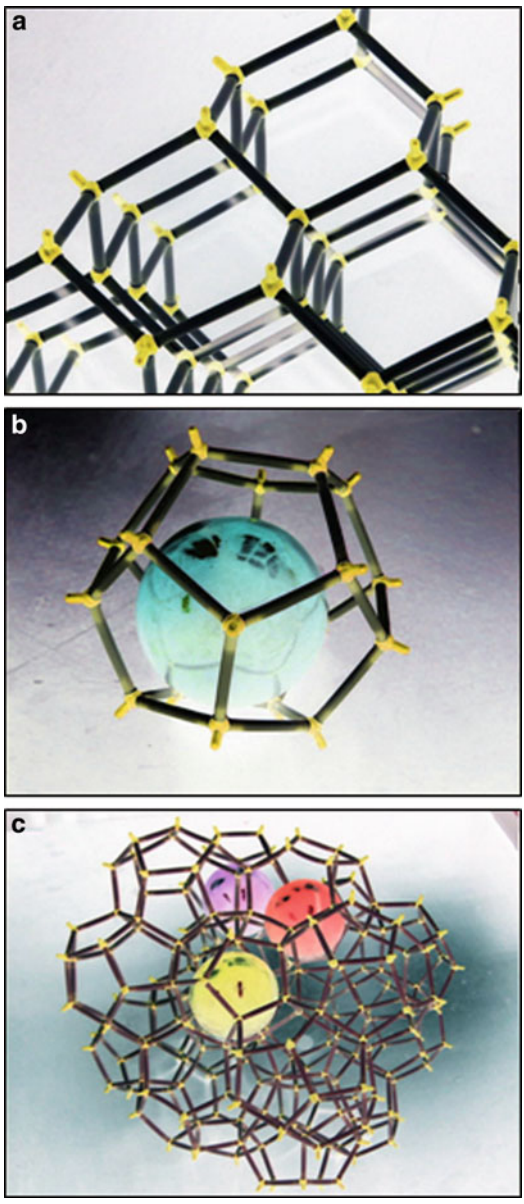

Fig. 3.1 Crystalline structure of ice (**a**). Crystal structure of gas hydrates for small and large cavities (**b**, **c**). The ice structure is made up of hexagonal rings of water molecules forming an honeycomb structure with hexagonal symmetry, where as the gas hydrate structure is formed by pentagonal rings of water netted together to form polyhedra

2003; Sloan 2003). A unit structure creates three small, two medium and one relatively large cavity and consists of 34 water molecules. The smaller guest molecule such as methane occupies the small and medium cavities and the large cavities can hold butane, neohexane, cycloheptane and other high order molecules.

According to present knowledge the most of regions over continents and margins indicated worldwide occurrence of methane hydrates, suggesting crystalline

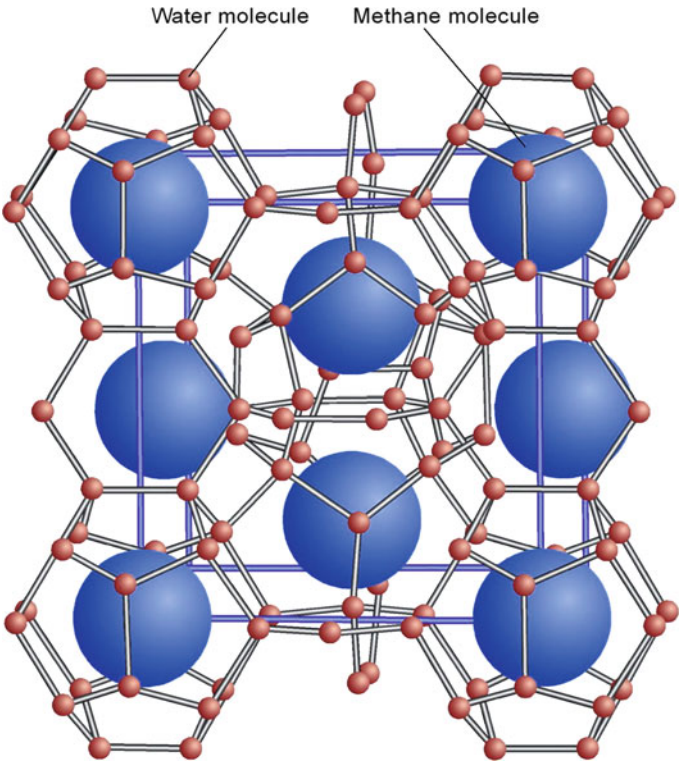

Fig. 3.2 Structure I hydrates is made up of pentagonal rings of water molecules netted together to form polyhedra, 12-sided and larger 14-sided cages called (*pentagon*) dodecahedra and tetrakaidecahedra. One unit-volume of Structure I hydrate showing eight cavities (small (2) and large (6)) where guest molecules are trapped. (Adapted from a drawing by Bjorn Kvamme, University of Bergen, Norway (Ref: Hardage and Roberts 2006)

structure I controls formation of hydrates in these regions. Methane saturation is as high as 99% has been reported from many drilled sites (Kvenvolden 1995). Hydrates with mixed composition of methane and higher molecular gases like ethane and propane were identified in Gulf of Mexico (Brooks et al. 1984) and in Caspian Sea (Ginsburg et al. 1992). The hexagonal crystal structure of H hydrates for the first time have been identified in the Bush Hill of Gulf of Mexico (Sassen and Macdonald 1994), Cascadian margin (Hailong et al. 2007).

3.4 Where Gas Hydrates Are Found?

The gas hydrates are shallow reservoirs less than about 1,500 m depth below the surface of earth. The formation and occurrence of gas hydrates in specific sites is controlled by numerous factors. In most parts of the world the thermo-baric

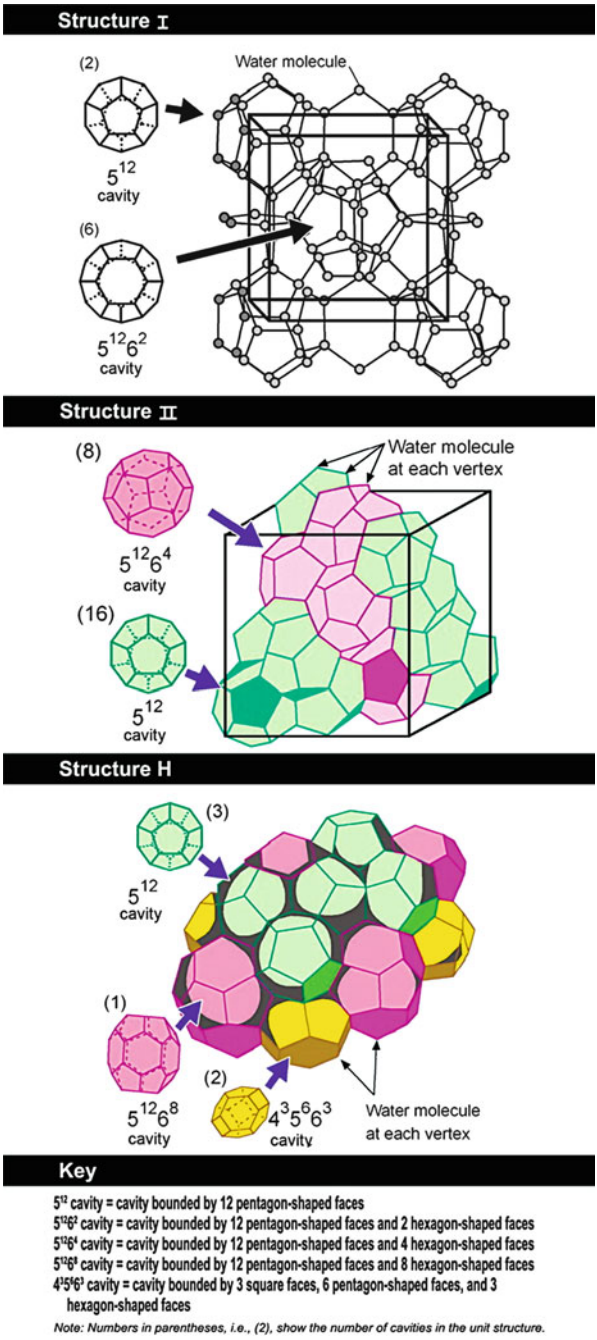

Fig. 3.3 Clathrate structures of gas hydrate. Structure I (*top*): Bodycentered cubic structure of 512 cavities linked at their vertices. This unit volume has eight cavities (eight possible gas molecules)

(temperatures–pressure) conditions for the stability of gas hydrates are met in the permafrost and continental margins. Favorable stability conditions are not the only requirement, gas composition, ionic strength of the water and availability of excessive of gas (methane), are the prime controlling factors for the formation gas hydrates in a region (Kvenvolden 1993). Presence of gases such as ethane, propane and others gases along with methane alter the position and thickness of hydrate stability zone. Gas hydrates occur in less than 10% of the total oceanic area, as they are restricted to slopes and rises of outer continental margins where water depth exceeds more than 300 m (Shipley et al. 1979). Kvenvolden (1995) contented that gas hydrates may not occur in most of the oceanic regions but may be confined to slopes and rises on the outer continental margins.

Sub-aquatic gas hydrates are found in the polar continental shelf sediments associated in permafrost regions at depths of about 150 m. Ginsburg et al. (1992) proposed that sub-aerial exposure of gases and gas saturated waters to lower temperatures resulted in the sub-aquatic gas hydrates on the polar shelves. It is suggested that gas hydrate formation in most of the region is due to the filtration of methane rich fluids into/through gas hydrate stability zone (pressure–temperature regime). Over the passive margins gas hydrates are formed in the stability zone by biogenic gas generated during the sedimentation (Trofimuk et al. 1979). Continuous sedimentation, burial and compaction result in release of methane from hydrates. Subsequent upward movement of methane in to the stability zone leads to formation of hydrates with higher saturation (Claypool and Kaplan 1974). Free-gas below the gas hydrate may also occur in such processes. The formation of gas hydrate in the Blake Ridge in Atlantic is outstanding example of such process. Over the active margins the methane gas could be either locally generated biogenic gases or thermogenic gases from deeper sources. These gases migrate upwards through the channels in to the stability zone to form gas hydrates near to the seafloor or may even seep though seafloor resulting in formation of different geological structure such as pockmarks and others. Most of the locales of gas hydrate formation on the convergent margins are mainly governed by this process, such as in case of Gulf of Mexico (Brooks et al. 1984) and Caspian Sea (Ginsburg et al. 1992). The third process, which is likely to help the formation of gas hydrate, is related to rapid

Fig. 3.3 (continued) and 46 water molecules. The host molecule is smaller than propane. Structure II (*center*): Diamond lattice within a cubic framework with 512 cavities linked at their faces. This unit volume has 24 cavities (24 possible gas molecules) and 136 water molecules. The host molecule is larger than ethane but smaller than pentane. Structure H (*bottom*): Hexagonal structure with layers of 512 cavities connecting layers of 51268 and 435663 cavities. This unit volume has six cavities (six possible gas molecules) and 34 water molecules. The host molecule is a wide range of sizes. The cavity *diagrams* are views looking down on a cavity with solid lines showing face edges on the top half of the cavity and *dotted lines* showing face edges on the bottom half. These hydrate diagrams depict unit volumes, the smallest repeating structural elements of hydrate growth. The cluster of cavities in the structure II diagram shows only 12 of the 24 cavities needed for a structure II unit volume. The cluster in the structure H diagram is larger than a six-cavity structure H unit volume. The distributions of the colored cavities are suggestive, not precise (after Sloan 1998) (Ref: Hardage and Roberts 2006)

movement of sediments containing gases along the steep slopes in to zone of hydrate stability. Such process may occur in active margins like Middle American Trench offshore Guatemala (Kvenvolden and MacDonald 1985).

The solubility of methane is appreciably low of the order of 0.045 volumes per unit volume of water. In absence of gas hydrates the solubility increases with decrease in temperature and increase in pressure as per Henry's law (Osegovic et al. 2006). The presence of hydrates facilitates further hydrate formation and hence the equilibrium concentration of gas in water decreases in water and the solubility in water increases with temperature (Duan and Mao 2006). In this regard the quantum of methane has to vary much more than the solubility of methane in the water to sustain the formation of gas hydrates. In many parts of the world the methane is generated locally by the conversion of organic content in the sediments in the shallower levels (biogenic) or due to migration of methane rich fluids from deeper sources in the earth. Predominantly biogenic methane is the main constituent of hydrates in most of cases. Regions of faster hemipelagic deposition with rapid burial are favorable for production of abundant methane by bacteria within sediments (Claypool and Kaplan 1974). The continuance of sediment deposition makes the hydrate layer thicker. The subsidence of this layer below the stability zone makes the hydrate unstable, releasing methane as free gas. This free gas migrates back in to hydrate stability zone. This cyclic procedure leads to higher concentration of hydrates in stability zone. However, methane from deeper sources (thermogenic) has been found to occur in hydrates in regions like Gulf of Mexico and Cascadian basin. The occurrence of gas hydrates has been identified in many parts of the world where the suitable conditions for the formation of gas hydrates are met.

The chemistry of gas hydrate was discovered in the laboratory in early nineteenth century when Sir Humphrey Davy found that ice-like crystal was formed when aqueous solution was cooled (Sloan 1990). The laboratory studies of Sir Humphrey Davy were mainly confined to chlorine hydrates. Hydrates became nuisance in 1930s and 1940s when they were found in the gas pipelines obstructing the flow of gas. The clogging of gas pipelines in the permafrost regions by ice like material has led to the idea that methane hydrates could be stable under the subsurface earth (Katz et al. 1959). However, the interest in gas hydrates has increased steadily in 1960s, when gas hydrate deposits were first discovered in the Soviet Union (Vasil'ev et al. 1970). Russian scientists were first to postulate that favorable pressure and temperature conditions prevailed in most of the permafrost and oceanic regions for the formation of gas hydrate (Makogon et al. 1973; Trofimuk et al. 1977). The well logs obtained during the drilling in the Arctic region for the first time established the presence of gas hydrates in the permafrost region. The Messoyakha field in Siberia was developed and methane gas was recovered by injecting methanol (Makogon 1978). Since then worldwide gas hydrates occurrences have been identified either by inferences drawn indirectly by geophysical/geochemical methods or by direct sampling under Deep Sea Drilling Program (DSDP) and Ocean Drilling Program (ODP). Most of the countries formed national programs for the investigations and exploitation of gas hydrate as

energy resources. The studies also included the impact on climate and geological hazard by the dissociation of gas hydrates and escape of methane and other gases in the atmosphere.

Gas hydrates samples have been recovered from permafrost regions in the Messoyakha gas field in the western Siberia (Makogon 1981) Prudhoe Bay oil field of Alaska (Collet 1993) and Mallik field in the Mackenzie delta in Canada (Dallimore et al. 1999). The presence of the anomalous reflector, BSR, on the Blake Ridge in the Atlantic Ocean was quite intriguing and attempts were made to understand the nature of this characteristic reflector (Marl et al. 1970; Stoll et al. 1971). BSR is considered to coincide with base of gas hydrate stability predicted from the pressure and temperature conditions at the seafloor (Shipley et al. 1979). Since then presence of gas hydrates in most of the oceanic region was inferred from identification of BSR on the seismic reflection data. The occurrences of BSR have been reported from many regions of the world. Most extensively studied area utilizing seismic and other methods are Blake Ridge (Coren et al. 2001), Gulf of Mexico (Bouma et al. 1999), Cascadian Basin (Yuan and Hyndman 1994) and Nankai Trough (Ashi et al. 2002).

Drilling at Blake Ridge (Paull et al. 1996) at Cascadian margin (Tre´hu et al. 2004), Nankia Trough on the Japan's margin (Henriet and Mienert 1998) and recently over the margin of India under NHGP program (Collet et al. 2008) has established the presence of gas hydrates in these regions. The recovery of gas hydrate samples under DSDP leg 76 lends credence to the BSR's relevance as the identifier of presence of gas hydrates (Kvenvolden and Barnard 1983). Worldwide, over 70 locations (Fig. 3.4, Council of Canadian Academies Energy From Gas Hydrates 2008) have been identified both by indirect inferences and by direct sampling. Most (~60 location) of the hydrate bearing locations fall in the oceanic regions. Identification of BSR in the seismic records has been the main criteria for

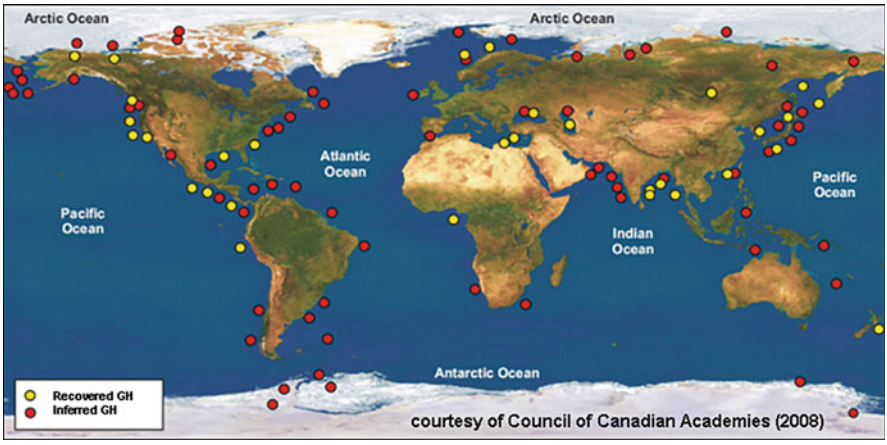

Fig. 3.4 Distribution of known methane hydrate accumulations (courtesy of Council of Canadian Academies Energy From Gas Hydrates (2008), based on data from Kvenvolden and Rogers (2005)

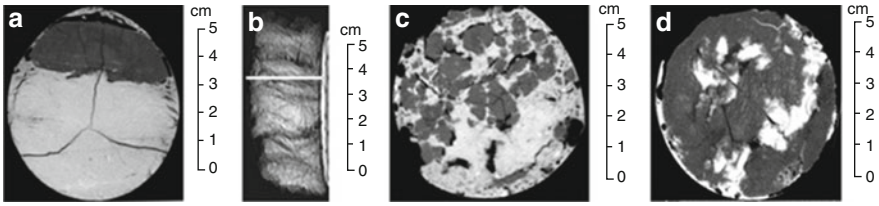

Fig. 3.5 The mode of occurrence of gas hydrate deposits having different shapes and sizes, like veins and layers of comparable size, (**a**, **b**), spherical to oblate features, sometimes with edges are considered as nodules (**c**); and massive hydrate (**d**), which on a larger scale most probably looks like a lens, were obtained during the drilling over the Blake Ridge (Site 570: Shipboard Scientific Party Site 570 Leg 84 1985)

inferring the presence of gas hydrate in the oceanic regions. In about 23 sites gas hydrate sample have been recovered by drilling or by gravity coring.

Gas hydrates in the subsurface earth may exist as individual grains or particles dissimilated through the sediments but also may cement the sediment grains as nodules and laminate, layers of different shapes and size with dimension of the order of few centimeters and less (Collett 2003). 2-D samples such as laminae or layers were associated with fine-grained sediments. 3-D samples such as granules and nodules also occurred in fine-grained sediments and mixed grains sizes also. Hydrates cementing was more prevalent with coarse-grained samples. In many cases the difference between such defined shapes is based only on the orientation of the hydrate within the sedimentary bedding. Primarily gas hydrates occupy the pore spaces in the sediments and cement the sediments. They are also found to form in secondary voids in fractures and joints. Hydrates during growth create their own space by disturbing the sediment matrix (Suess et al. 1979). The mode of occurrence of gas hydrate deposits having different shapes and sizes, like veins and layers of comparable size, (Fig. 3.5a, b), spherical to oblate features, sometimes with edges are considered as nodules (Fig. 3.5c); and massive hydrate (Fig. 3.5d), which on a larger scale most probably looks like a lens, were obtained during the drilling over the Blake Ridge (Site 570: Shipboard Scientific Party 1985).

3.5 Gas Hydrates Indicators

3.5.1 Geophysical Signatures

The inference about the presence of gas hydrate in a region is primarily arrived on the geophysical/geological and geochemical signature observed in different data sets. The presence of gas hydrate deposits is inferred primarily on the basis of their acoustic expression. The indirect evidence for the presence of gas hydrates on the

continental margins was inferred by the identification of anomalous reflector in the seismic data. Crystalline ice has a velocity of the order of 3.6 km s^{-1}. Hydrates have acoustic velocity of the order of 3.3 km s^{-1}, slightly lower than ice. Sediments saturated with saline have acoustic velocities in the range of 2.0–2.5 km s^{-1}. Hydrates either occupy the pores and/or cement the sediment grains thereby enhance acoustic velocity of the medium. The hydrated layer is if underlain by brine/free-gas saturated layer, creates impedance contrast across this interface. As hydrates are formed under some thermo-baric conditions, this interface (reflector) is not a specific geological boundary. This reflector had special characteristics in contrast to the normal bedding planes of the sediments and owing to its parallelism to the sea floor was termed as bottom simulating reflector (BSR). BSR has tendency to cut across the bedding plane and owing to its occurrence at the base of gas hydrate stability zone (Shipley et al. 1979) is easily recognizable on the seismic reflection stack sections. The inference about the presence of gas hydrates in the marine environment mainly comes from the identification of BSR in the seismic reflection data. The identification of BSRs on most of the continental margins has led occurrence of gas hydrates over Blake Ridge in North Atlantic Ocean (Tucholke et al. 1977), Gulf of Mexico (Brooks et al. 1986) and many more parts of the world. A classic example of BSR occurrence over Green Canyon, offshore USA is presented in Fig. 3.6. In event of absence of BSR geological/geo-chemical proxies can be utilized to assess the presence of gas hydrate-free gas in a region.

Gas Hydrates have also been recovered from the regions where BSR was not observed in the seismic data (Westbrook et al. 1994; Wood and Ruppel 2000 and Ashi et al. 2002). On the contrary gas hydrates have not been recovered from the

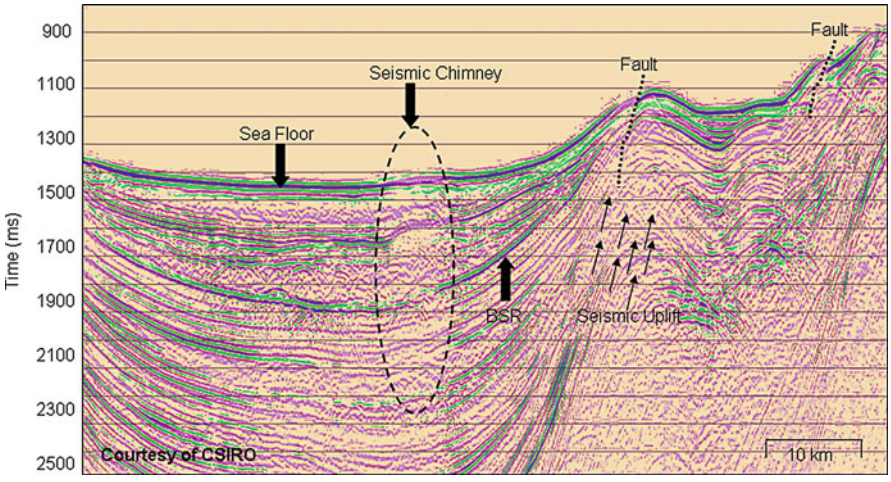

Fig. 3.6 Multi-channel seismic stack section of Green Canyon, Offshore USA The BSR at a depth from 1,300 to 1,900 ms below the sea floor has all the characteristics can easily be identified on the seismic section. The presence of gas hydrate in this region can be inferred from BSR and Gas escape feature (seismic chimneys) (courtesy of CSIRO)

regions where BSRs were identified (CSIRO, Sydney Basin Technical Report 2009). Geological, geochemical and microbiological studies become relevant for the understanding the occurrences and genetic processes of gas hydrate formation.

3.5.2 Geological Proxies

Geological, tectonic and climate changes, like sea-level fluctuations alter the stability conditions of sub-surface gas hydrates leading to the dissociation of gas hydrates and release of methane. The escaping gases through the conduits manifest the seismic and other geophysical records. Geological–geophysical studies carried out in many parts of the oceans revealed widespread fluid/gas escape features in the seismic data. On the records these fluid/gas escape features are expressed, such as pockmarks venting, mud volcanoes, clay diapirs and other geophysical features such as VAMPS. Large-scale fluid migration towards sea floor and their escape from the sea floor alter the sediment properties and produce the clear signature of venting and distinctly can be observed in high-resolution seismic data. Most of the fluids venting features are associated with mud volcanoes and clay diapirs. These features are generally observed tectonically active convergent margins (Soloviev and Mazurenko 2003). The eruption of mud volcanism by alteration of stability of gas hydrates conditions; results in abundance mud and rock fragments bringing in morphological characteristics and these signatures are distinct seismic records (Baraza and Ercilla 1996; Aloisi et al. 2000). The V-shaped depressions observed in the seismic records (Fig. 3.7) were considered to be originated from expulsion of gas from over-pressured shallow gas pocket, gas hydrate and hydrocarbon bearing sediments on the continental margin and slopes (Hovland and Judd 1988).

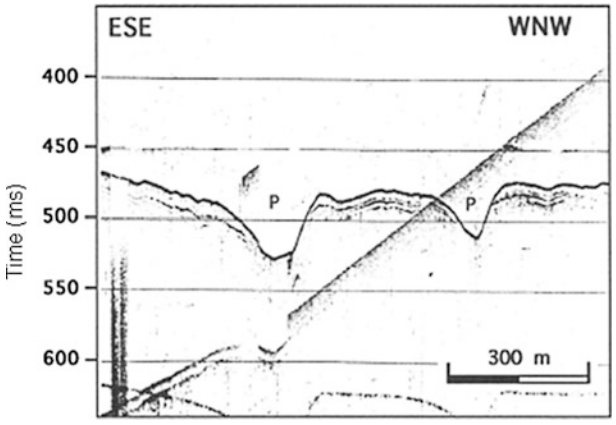

Fig. 3.7 Geological proxies like pockmarks and V type features indicating the gas escape features in the Gulf of Cadiz –SW Spain (Adopted from Baraza and Ercilla 1996)

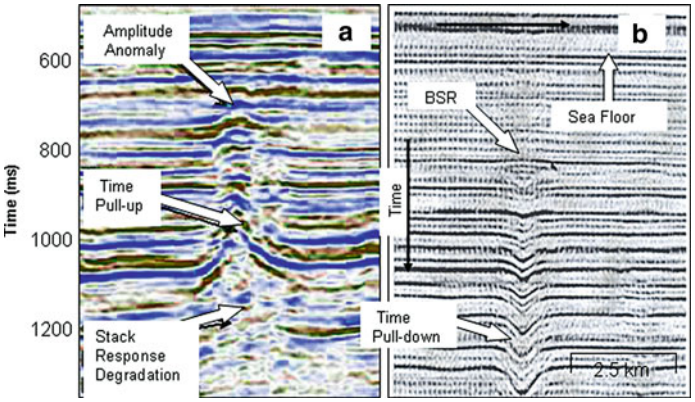

Fig. 3.8 Velocity amplitude pull-downs (VAMPS) and time pull-up exhibiting the pseudo-structural pattern developed due to large impedance contrast generated by hydrate and free-gas. (**a**) Velocity time pull-up example adopted from www.explorationist.com/APPEA_Seismic.htm (**b**) The pull downs are clearly below the identified BSR, indicating the presence of free-gas below the hydrate layer (Adopted from Scholl and Cooper 1978)

Velocity amplitude pull-downs (VAMPS, Scholl and Cooper 1978) are pseudo-structure observed in the multi-channel seismic data. The high impedance contrast between hydrated and free gas layers creates pseudo up-warp like features in hydrate layer and buckling like features in the free gas zone. Such pseudo structures have extensively observed in the Barents Sea region (Fig. 3.8, modified from Scholl and Cooper 1978)

3.5.3 Geochemical Evidences

During gas hydrate formation process dissolved ions such as Na^+ and Cl^- are excluded from the hydrate structure and only water molecules crystallize in to cubic lattice structure (Hesse and Harrison 1981). Surrounding pore waters initially become more saline during the process of hydrate formation. Over geologic time, advective and diffusive processes remove the excess salt and the background pore water chemistry is re-established. The presence of gas hydrate in situ has often been inferred by freshening of pore water chlorinity/salinity relative to a defined baseline (Kastner et al. 1995). In case of rapid and relatively recent gas hydrate formation, this process is incomplete and high-pore water chlorinity/salinity brines are observed. The average chlorinity in the seawater is of the order of 19.8%. By virtue of tendency of gas hydrates to form in pure water, the salinity content in the gas hydrate is significantly low, in the range 3.5–0.5%. During hydrate crystallization the exclusion of salinity (chlorine) and intake of $\delta^{18}O$ is due to the solid–fluid isotope fractionation that causes preferential uptake of the heavy isotope $\delta^{18}O$ in the solid phase and depletion in the fluid (Hesse 2003). This phenomenon is outcome of

the entire history sediment burial, compaction, advective and diffusion processes. During the dissociation of hydrates the release of pure water in the host sediments reduces the chlorinity. During the dissociation of hydrates release of heavy isotope water and its mixing up with lower order isotopic water component results in enrichment of $\delta^{18}O$ in the host sediment's pore waters. The $\delta^{18}O$ values increase with increasing depth and appreciable higher values recorded in the hydrate bearing sediments. The observed combined anomalies of chlorinity and $\delta^{18}O$ in the pore water chemistry of the host sediments provides a reliable measure for identification of gas hydrates. These coupled geochemical pore water anomalies for the first time were observed in the Mid-American Trench Slope of Guatemala during DSDP expedition in the year 1979 (Hesse and Harrison 1981) and on Blake Ridge (Hesse et al. 2000). Lower values of chlorine concentration in the hydrate stability zone may suggest the occurrence of hydrates even when the prominent geophysical signature (BSR) is found missing (Holbrook et al. 1996)

3.5.4 In-Situ Measurements

Remote sensing geophysical methods are extensively used for the exploration of gas hydrates. Spatial resolution of these methods ranges from couple of meters to tens of meters. Physical measurement made in the bore wells after and during the drilling lay constraints on the data acquired through remote sensing and make the remotely sensed data more meaningful and realistic. These measurement ground truths the remote sensing data. The scale ratio from log to seismic survey generally is of the order of 10^6–10^7. Measurements made in the drilled wells are most commonly used to ground truth remotely sensed data for exploration, production and ascertaining the health of the hydrocarbon reservoir. Equipments are lowered in the drilled well and measurements made down hole (logging) are analyzed and interpreted to arrive at characteristics well dimensions, lithological and geological information. Based on the procedure of logging measurement, they have been categorized as wireline logging, logging while drilling (LWD) and measurement while drilling (MWD). In the process of Wireline logging, instruments are deployed down hole immediately after drilling. Measurements made are communicated to surface site through communication cable. In wireline logging measurements are made from the deepest part upwards towards the seafloor. During wireline logging the data is recorded at fixed depth intervals. Wireline logging measurements are sometimes unsuccessful due to caving in of the borehole in the unstable portion. Owing to this, subsequently new techniques have been developed and put in operations. In these techniques (LWD and MWD) data is recorded while drilling. These techniques can be utilized for taking measurements even during horizontal drilling. LWD tools measure in-situ formation properties with instruments that are located in the drill collars immediately above the drill bit. The difference between LWD and MWD tools is that LWD data are recorded into down hole computer memory and retrieved when the tools reach the surface, whereas MWD data are transmitted

through the drilling fluid within the drill pipe by means of a modulated pressure wave, or "mud pulsing," and monitored in real time. MWD tools can be utilized to send both MWD and LWD measurements to the surface in real time. LWD tools record data versus time. In all these techniques electrical (resistivity), nuclear (neutron scattering) and acoustic and density measurements have been made.

The most important parameter for the characterizing the hydrates and free-gas underlying the hydrates is through the determination of acoustic velocity of the medium. Cementation of sediment grains by hydrates results in appreciable increase in the compressibility and rigidity of the host sediment and thereby increases in acoustic (P and S) velocities (Guerin et al. 1999). The presence of free gas in the sediments reduces the P wave velocity. Shear wave velocity is not much affected by the presence of free-gas but shows increase in velocity with presence of hydrates in sediments. Determination of P and S wave velocities by vertical seismic prospecting (VSP) and well logs provide information about poison's ratio and estimating the saturation of hydrates and free-gas in the sediments. The measured P and S sonic velocity in site 997, using ODP Leg 164 over the Blake Ridge in the Atlantic Ocean has indicated appreciable increase in P wave velocity and comparatively higher S velocity. P wave velocities have sown a drastic reduction over the underlying free-gas layer. However, S wave velocity has not shown any observable change over the free-gas layer (Fig. 3.9 adopted from Rajput 2009).

Resistivity measurements provide the electric images of the borehole well wall. The presence of hydrate (icy form) increases the electric resistivity of medium. Presence of hydrate increase the resistivity of the sediment by about 50 times compared to sediment saturated with pure water and much more compared to pore saturated with saline water. Measurements of resistivity logs are obtained by

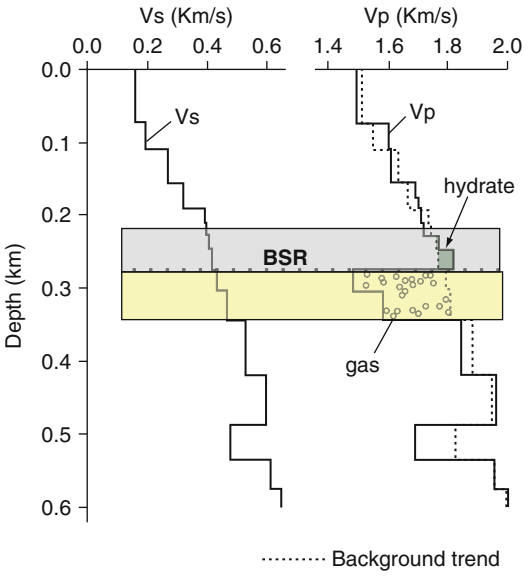

Fig. 3.9 Compressional and shear velocity over hydrate ridge offshore USA (Adopted from Rajput 2009). The P wave velocity shows appreciable increase over the hydrate layer and substantial reduction in values associated with free gas. The data indicates that shear velocity is not affected by the presence of free gas below the hydrated layer

deploying dipole array with high frequency alternating magnetic fields as the source. These fields generate induced secondary currents in the formation and the magnitude of the induced currents depend on the conductivity of the medium. The secondary fields are recorded by the coils and provide and estimate of resistivity (inverse of conductivity) following Ohm's law. The high frequency content source signal provides vertical resolution of couple of meters (Hyndman et al. 1999). The down hole resistivity data from site 880/890 during ODP Leg 146 operation on the Cascadian basin exhibits pronounced values compared to reference resistivity without hydrates. Estimation of hydrate concentration obtained by resistivity through Archie's law indicates 30% pore saturation (Fig. 3.10; adopted from http://gsc.nrcan.gc.ca/gashydrates/ncascadia/index_e.php). The value of saturation is slightly higher than what is obtained by modeling the seismic velocity data.

Estimation of in-situ porosity is yet another important factor for the formation of gas hydrates. The pattern of connectivity of pores (permeability) primarily governs the migration of fluids. The estimation of porosity and permeability of the sediments permits differentiation of lithological units and thereby help in modeling for ascertaining the quantum of hydrate pore saturation. Neutron porosity obtained by

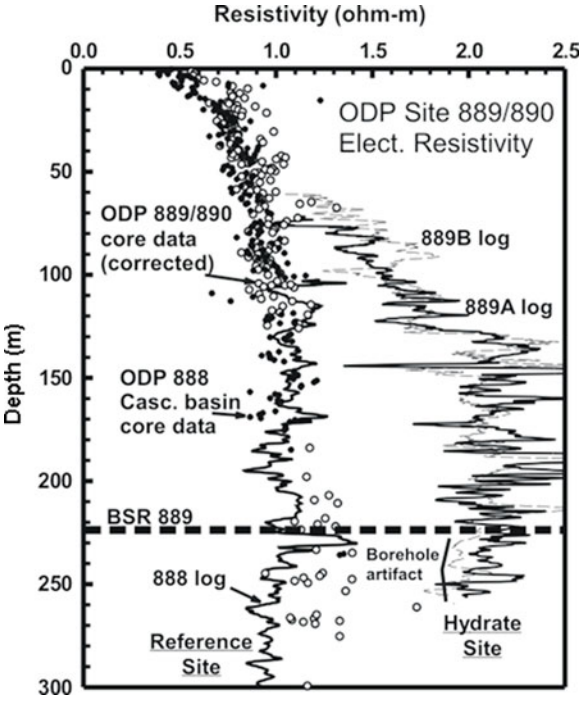

Fig. 3.10 Resistivity has been determined from downhole log measurement and resistivity and porosity measured in the core samples off Vancouver islands. The resistivity values almost show the twice over the hydrate layer when compared to regions with hydrates (Adopted from http://gsc.nrcan.gc.ca/gashydrates/ncascadia/index_e.php)

neutron scattering along with density logs provides a reasonably accurate estimation of porosity (Schlumberger 1989). An estimate of porosities also can be obtained from resistivity log data by modeling through Archie's Law. LWD surveys were successfully conducted during seven previous ODP legs since almost two decades. Some notable legs are: Leg 156 (Shipley et al. 1995), Leg 170 (O'Brien et al. 2001), Leg 196 (Mikada et al. 2002) and more recently NGHP1 project in India (Collet et al. 2008).

3.6 Possible Resource Estimates

Ever since the first identification of occurrence of gas hydrate in Western Siberia in the permafrost region in early 1970s and likelihood of its occurrence in tropical oceanic conditions, has prompted most of the coastal countries to explore for this form of energy. Till this day about 70 sites have been identified all around the world (Fig. 3.5), where gas hydrates are likely to occur and this number may likely to go up. Most of the identified locales are confined to oceanic regions and in some of these regions the presence of gas hydrates has been confirmed from drilling. The methane content in gas hydrate per unit volume far exceeds the natural gas and slightly less than the LNG. The maximum amount of methane that can be trapped depends on the geometry, free space available in the lattice of the water molecule. A fully saturated unit m^3 gas hydrate sample at standard pressure and temperature (STP) is likely to hold 164-m^3 methane gas (Kvenvolden 1993). However, in nature only at the maximum 60–70% of the cages are filled with methane in a hydrate structure.

The estimates of gas hydrate as resource potential have been quite speculative and uncertain ever since first attempts were made to quantify them since 1970s (Kvenvolden 1999). Parameters like thickness of hydrated layer, porosities, saturation in sediment pores, areal extent, volume, hydrate and gas yield parameters were considered for estimating the global gas content in hydrates (Collett 2003; Milkov 2004). The estimates have been getting modified in view of new information about their formation processes, development of new techniques, high resolution data acquisition and ground truth by well log data acquisition/interpretation and obtaining hydrate samples under suitable conditions. The global estimates of methane gas in hydrate shows large variations. During seventies and eighties the gas content, mainly methane gas was estimated to be of the order of 10^{17}–10^{18} m^3 which in eighties and nineties reduced to the order of 10^{16} m^3, which eventually come down to 10^{14}–10^{15} m^3 during the present times (Fig. 3.11, Adopted from Milkov 2004).

Trofimuk et al. (1979) considered that about 90% oceanic regions are likely to hold gas hydrates and his resource estimate included shelf, slope and abyssal planes in the oceanic areas to arrive at estimate of 1.135×10^{18} of methane gas in the submarine gas hydrates. The Potential Gas Committee (1981) report indicated that during eighties the permafrost/oceanic regions the estimates hydrate ranged from as

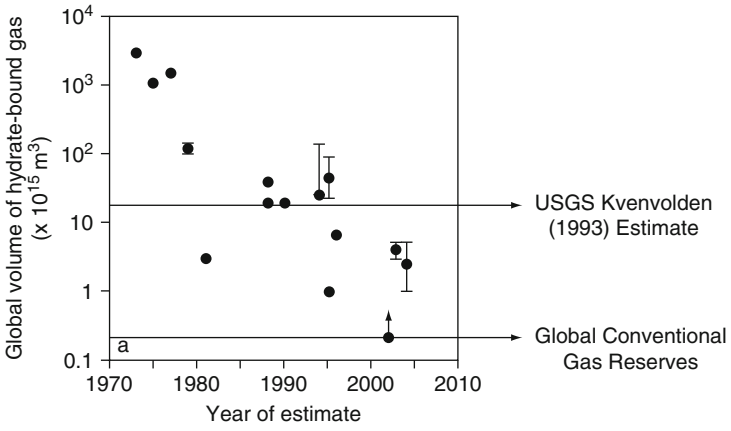

Fig. 3.11 Global gas hydrate estimate since 1970. With improvement all methodologies and with the establishment form in situ measurements in some regions the global estimates have become more realistic and authentic. The figure shows the quantifiable decline global estimates over the last three decades (Adopted from Milkov 2004)

low as 1.4×10^{13} / 3.1×10^{15} (Meyer 1981) to as high as 3.4×10^{16} / 7.6×10^{18} (Dobrynin et al. 1981).

With more precise figures emerging during mid 1980s and early 1990s the assessment of quantum of gas in gas hydrates reduced by order of magnitude than what was proposed earlier. The estimated values of 2×10^{16} m^3 (Kvenvolden 1988) and 4×10^{16} m^3 (Kvenvolden and Claypool 1988) is in agreement with estimates of quantum of methane gas in hydrates of the order of 2.1×10^{16} m^3 (MacDonald 1990). Kvenvolden (1998) considered this as consensus value for estimates of global methane content in hydrate. The well logs as well the pressurized sample collected during the DSDP and ODP drilling programs have provided constraints on various parameters for estimating the volume of gas hydrates and hydrate-bound gas in the hydrates. With these constraints the recent results indicate that most of the earlier studies had over estimated the gas hydrates reserves. It appears that global volume of gas hydrate bearing sediments may be in the range $(1–5) \times 10^{15}$ m^3 of methane, which may be 4–20 times less than what is estimated earlier (Milkov 2004). The global estimates of methane gas contained in gas hydrates have substantially reduced from 1970s to present and reduction significantly differs by an order 2–4 of magnitude (Milkov 2004). The estimated quantum of gas hydrates exceeding 1,000 Gt (high probability) and in the range of 1,000–10,000 Gt, equivalent to ~2,000–20,000 trillion cubic meters (medium probability) was arrived at recently held workshop (Bohannon 2008).

However, most of the studies did not incorporate free-gas beneath the hydrated layer for estimating the global resources. The difference of estimates of methane in gas hydrate (Dillon and Paull 1983; Dickens et al. 1997) was attributed to the vast quantity of free-gas directly underlying hydrate layer in the Blake Ridge.

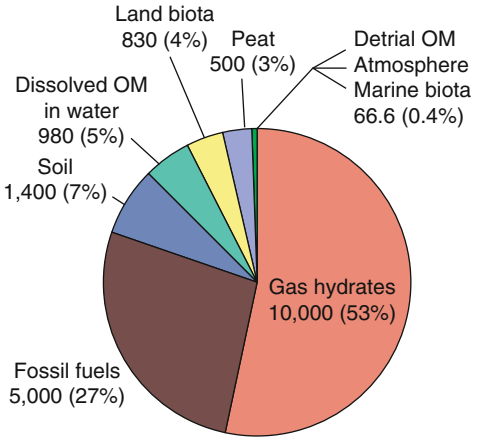

Fig. 3.12 Distribution of organic carbon in the earth. With present estimates gas hydrate hold almost twice energy resources when compared to all the other carbon resources put together (Kvenvolden 1988)

Gas hydrate investigation in different parts of the world is still continuing and the exact quantum will only be ascertained with the completion of major projects undertaken by different countries. However, based on the present estimates, even a small recoverable fraction of the from the gas hydrates might still be sufficient to enter a 'methane age' (Nakicenovic 2002). As little as one thousandth part of the global methane hydrates inventory would suffice to cover current annual global energy needs. Even with reduced estimate the quantum of methane present in the hydrate is two-order magnitude larger (Fig. 3.12) than the estimated total recoverable conventional methane resources, estimated to about 250 TCF (Master et al. 1991).

The laboratory-made hydrates (from methane-rich systems) may differ slightly in composition from in situ hydrates, which can form in methane-lean systems. This methane hydrates composition difference, although small (4%), when multiplied by the entire hydrate reserve is sufficient to supply the USA for 600 years at the current energy usage (Sloan 2003).

References

Aloisi G, Pierre C, Rouchy J et al (2000) Methane-related authigenic carbonates on eastern Mediterranean Sea mud volcanoes and their possible relation to gas hydrate destabilization. Earth and Planetary Science Letters 184:321–338.

Ashi J, Tokuyama H, Taira A (2002) Distribution of methane hydrates BSRs and implications for the prism growth in the Nankai Trough. Marine Geology 187:77–191.

Baraza J, Ercilla G (1996) Gas-charged sediments and large pockmark-like features on the Gulf of Cadiz (SW Atlantic). Marine and Petroleum Geology 13:253–261.

Bohannon J, (2008) Energy: weighing the climate risks of an untapped fossil fuel. Science 319:1753.

Bouma AH, Roberts HH, Coleman JM (1999) Acoustic and geological characteristics of near surface sediments, upper continental slope of northern Gulf of Mexico. Geo-Marine Letters 10:200–208.

Brooks JM, Kennicutt MC III, Fay RR et al (1984) Thermogenic gas hydrates in Gulf of Mexico. Science 225:409–411.

Brooks JM, Cox BH, Bryant WR et al (1986) Association of gas hydrate and oil seepage in the Gulf of Mexico. Organic Chemistry 10:221–234.

Carroll JJ (2003) Natural Gas Hydrates, a Guide to Engineers. Gulf Professional Publishing, Amsterdam, The Netherlands.

Claypool GE, Kaplan IR (1974) Methane in marine sediments. In: Kaplan IR (ed) Gas in Marine Sediments. Plenum Press, New York, London.

Collet TS (1993) Natural gas hydrates of the Prudhoe Bay and Kuparuk river area north slope Alaska. AAPG Bulletin 77:793–812.

Collet TS, Riedel M, Cochran J et al (2008) NGHP expedition 01 2006 Initial Reports. Directorate General of Hydrocarbons and Ministry of Petroleum and Natural Gas, India.

Collett TS (2003) Natural gas hydrate as a potential energy resource. In: Max MD (ed) Natural Gas Hydrate in Oceanic and Permafrost Environment. Kluwer Academic, London.

Coren F, Volpi V, Tenivella U (2001) Gas hydrate physical properties imaging by multi-attribute analysis-Blake Ridge BSR case history. Marine Geology 178:197–210.

Council of Canadian Academies Energy From Gas Hydrates (2008) Assessing the opportunities and challenges for Canada,180 Elgin Street, Ottawa, ON Canada K2P 2K3.

CSIRO confidential Sydney Basin Technical Report 09-023, 2009, Advent Energy Seabed Studies.

Dallimore SR, Uchida T, Collet TS (1999) Scientific results form JAPEX/JNOC/GSC Mallik 2L-38 gas hydrate research well Mackenzie Delta Northwest Territories Canada. Geological Survey of Canada Bulletin 544:1–10.

Dickens GR, Castillo MM, Walker JCG (1997) A blast of in the latest Paleocene: simulating first-order effects of massive dissociation of oceanic methane hydrate. Geology 25:259–262.

Dillon WP and Paull CK (1983) Marine hydrate II geophysical evidences. In:Cox JS (ed) Natural Gas Hydrate: Properties, Occurrence and Recovery. Butterworth Publishing, London.

Dobrynin VM, Korotaiev Yu P and Plyuschev DV (1981) Gas hydrate-A possible energy resource. In: Meyer RF, Oslon JC (eds) Long-Term Energy Resources. Pitman Publishing, Boston.

Duan ZH, Mao SD (2006) A thermodynamic model for calculating the methane solubility, density and phase composition of methane-bearing aqueous fluids from 257 to 523 K and from 1to 2000 bar. Geochemi Cosmochim Acta 70:3369–3378.

Ginsburg GD, Guseynov RA, Dadashev AA et al (1992) Gas hydrates of the southern Caspian International. Geology Review 42:765–782.

Guerin G, Goldberg D, Meltser A (1999) Characterization of in situ elastic properties of gas-hydrate bearing sediments on the Blake Ridge. Journal of Geophysical Research 104:17781–17795.

Hailong L, Seo Y, Lee J et al (2007) Complex gas hydrate from the Cascadian margin. Nature 445:303–306.

Hardage BA, Roberts HH (2006) Gas hydrate in the Gulf of Mexico: What and where is the seismic target. Leading Edge 25:566–571.

Henriet JP, Mienert J (1998) Gas hydrates: the Gent debates outlook on research horizons and strategies. In: Henriet JP, Mienert J (eds) Gas Hydrate: Relevance to World Margin Stability and Climate Change. Geological Society of London Special Publication, London.

Hesse RD (2003) Pore water anomalies of submarine gas-hydrate zones as tool to assess hydrate abundance and distribution in the subsurface: What have we learned in the past decade? Earth Science Reviews 61:149–79.

Hesse R, Harrison WE (1981) Gas hydrates (clathrates) causing pore-water freshening and oxygen-isotope fractionation in deep-water sedimentary sections of terrigenous continental margins. Earth and Planetary Science Letters 55:453–461.

Hesse RD, Frape SK, Egeberg PK et al (2000) Stable isotope studies (CL, O, and H) of interstitial waters from Site 997, Blake Ridge gas hydrate field, West Atlantic. In: Paull CK, Matsumoto R, Wallace PJ, Dillon WP (eds) Gas Hydrate Sampling on the Blake Ridge and Carolina Rise Proc Ocean Drilling Program Scientific Results, 164.

Holbrook WS, Hoskin H, Wood WT et al (1996) Methane hydrate and free gas on the Blake Ridge from vertical seismic profiling. Science 273:1840–1843.

Hovland M, Judd AG (1988) Sea Bed Pock-Marks and Seepages, Impact on geology. Graham and Trotman Ltd, London.

Hunt JM (1996) Petroleum Geochemistry and Geology, 2nd edn. WH Freeman, San Francisco, CA.

Hyndman RD, Yuan T, Moran K (1999) The concentration of deep sea gas hydrates from downhole electrical resistivity logs and laboratory data. Earth and Planetary Science Letters 172:167–177.

Kastner M, Kvenvolden KA, Whiticar MJ et al (1995) Relation between pore fluid chemistry and gas hydrate associated with bottom-simulating reflector at Cascadia margin sites 889 and 892. Proceedings of the Ocean Drilling Program, Scientific Results 146:175–187.

Katz D, Cornell D, Kobayashi R et al (1959) Handbook of Natural gas Engineering. MacGraw-Hill, New York.

Kvenvolden KA (1988) Methane hydrate – a major reservoir of carbon in the shallow geosphere? Chemical Geology 71:41–51.

Kvenvolden KA (1993) Gas hydrate as potential energy resource – a review of their methane content. In: Howell DG (ed) The Future of Energy Gases: US Geological Professional Paper, 1570.

Kvenvolden KA (1995) A review of geochemistry of methane in natural gas hydrates. Organic Geochemistry 23:997–1008.

Kvenvolden KA (1998) A primer on the geological occurrence of gas hydrates. In: Henriet JP, Mienert J (eds) Relevance to World Margin Stability and Climate Change, Geological Society of London Special Publication, London, 137.

Kvenvolden KA (1999) Potential effects of gas hydrate on human welfare. proceedings of the National Academy of Sciences (USA) 96:3420–3426.

Kvenvolden KA, Barnard LA (1983) Hydrates of natural gas in continental margins. In: Watkins JS, Drake CL (eds) Studies in Continental Margin Geology: AAPG Memoir 34:631–640.

Kvenvolden KA, Claypool GE (1988) Gas hydrate in oceanic sediments: US Geological Survey Open File Report 88:216.

Kvenvolden KA, MacDonald TJ (1985) Gas hydrates of the Middle American Trench, Deep Sea Drilling Project Leg 84. In: von-Huene R, Aubouin J et al (eds) Initial Reports of the Deep Sea Drilling Project, 84 US Government Printing Office, Washington, DC.

Kvenvolden KA, Rogers BW (2005) Gaia's breath-global methane exhalations. Marine and Petroleum Geology 22:579–590.

MacDonald GJ (1990) The future of methane as an energy resource. Annual Review of Energy 15: 53–83.

Makogon YF (1978) Hydrates of natural gas. (Translated from Russian by Ciesleswicz), Geoexplorer Associates Inc., Denver.

Makogon YF (1981) Hydrates of Natural Gas. Pennwell Publishing Company, Tulsa, OK.

Makogon YF, Trofimuk AA, Tsarev VP et al (1973) Possible origin of natural gas hydrates at floors of seas and oceans. Doklady Akademi Nauk SSSR, Sibirskoe otdeleniye Geologiya I Geofizika,4, 3–6, International Geology Review 16:553–556.

Marl RG, Bryan GM, Ewing JL (1970) Structure of Blake Bahamas outer ridge. Journal Geophysical Research 75:4539–4555.

Master CD, Root DH, Attanasi ED (1991) Resources constraints in petroleum production potential. Science 253:146–152.

Meyer RF (1981) Speculations on oil and gas resources in small fields and unconventional deposits. In: Meyer RF, Oslon JC (eds) Long-term Energy Resources, Pitman Publishing, Boston.

Mikada H, Becker K, Moore JC et al (2002) Proc ODP Initial Reports, 196 Ocean Drilling Program, Texas A&M University, College Station TX 77845-9547.
Milkov AV (2004) Global estimates of hydrate-bound gas in the marine sediments: how much is really out there? Earth Science Reviews 66:183–197.
Nakicenovic N (2002) Methane as energy source for the 21st century. International Journal Global Energy Issues 18:6–22.
O'Brien PE, Cooper AK, Richter C et al (2001) Proc. ODP Initial Reports, 188 Ocean Drilling Program, Texas A & M University, College Station TX 77845-9547.
Osegovic JP, Tatro SR, Homan SA (2006) Physical chemical characteristics of natural gas hydrates. In: Max MD, Johnson AH, Dillon WP (eds) Economic Geology of Natural Hydrates, Springer, Germany.
Paull CK, Matsumoto R, Wallace P et al (1996) Proceedings of Ocean Drilling Program Initial Report 164. College Station, TX.
Potential Gas Committee (1981) Potential Supply of Natural Gas in the United States. Potential Gas Agency, Colorado School of Mines, Golden, CO.
Rajput S (2009) Analysis of Ocean Bottom Seismometer data for gas hydrate studies and subsurface models. Ph.D Dissertation, Kurukshetra University Kurukshetra.
Ripmeester JA, Tse JS, Ratcliffe CI et al (1987) A new clathrate hydrate structure. Nature 325:135–136.
Sassen R, MacDonald IR (1994) Evidence of Structure H hydrates, Gulf of Mexico slope. Organic Geochemistry 22:1029–1032.
Schlumberger (1989) Log Interpretation Principles/Applications. Schlumberger, Houston.
Scholl DW, Cooper AK (1978) VAMPs possible hydrocarbon bearing structures in the Bearing Sea Basin. AAPG Bulletin 62:2481–2488.
Shipboard Scientific Party Site 570 (Leg 84) (1985) In: Huene R et al (eds) Proceedings Deep Sea Drilling Project, Initial Reports Washington DCUS Government Printing Office, USA.
Shipley TH, Houston MH, Buffler RT et al (1979) Seismic reflection evidence for widespread occurrence of possible gas-hydrate horizon on continental slopes and rises. AAPG Bulletin 63:2204–2213.
Shipley TH, Ogawa Y, Blum P et al (eds) (1995) Proc. ODP, Init. Repts., 156: College Station, TX, doi:10.2973/odp.proc.ir.156.1995.
Sloan ED (1990) Clathrate Hydrates of Natural Gases. Marcel Dekker, New York.
Sloan ED (1998) Clathrate Hydrates of Natural Gases. 2nd edn. Marcel Dekker, New York.
Sloan ED (2003) Review article fundamental principles and applications of natural gas hydrates. Nature 426:353–363.
Soloviev VA, Mazurenko LL (2003) Seafloor venting and gas hydrate accumulation. In: Max MD (ed) Natural Gas Hydrate in Oceanic and Permafrost Environment, Kluwer Academic Publishers, London.
Stoll RD, Ewing JI, Bryan GM (1971) Anomalous wave velocities in sediments containing gas hydrates. Journal of Geophysical Research 84:15101–15116.
Suess E, Bohrmann G, Lausch E (1979) Flammable ice. Scientific American 281:76–83.
Tre´hu AM et al (2004) Three-dimensional distribution of gas hydrate beneath southern Hydrate Ridge: Constraints from ODP Leg 204. Earth and Planetary Science Letters 222:845–862.
Trofimuk AA, Cherskii NV, Tsaryov VP (1977) The role of continental glaciations and hydrate formation on petroleum occurrence. In: Meyer RF (ed) The Future Supply of Nature-Made Petroleum and Gas, Pergamon Press, New York.
Trofimuk AA, Cherskii NV, Tsaryov VP (1979) The gas-hydrate sources of hydrocarbons. Priroda 1:18–27.
Tucholke BE, Bryan GM, Ewing JI (1977) Gas-hydrate horizon detected in seismic-profiler data from western North Atlantic. AAPG Bulletin 61:698–707.
Vasil'ev VG, Makogon YF, Trebin FA et al (1970) The property of natural gases to occur in the earth crust in solid state and to form gas hydrate deposits. Otkrytiya v SSSR 198:15–17.
Webster M (1994) Webster Dictionary. Houghton Miffin Co, Boston.

Westbrook GK, Carson B, Musgrave RJ et al (1994) Proceedings Ocean Drilling Program Interim Reports 146/1 College Station, TX.

Wood WT, Ruppel C (2000) Seismic and thermal investigation of the Blake Ridge gas hydrate area: a synthesis. In: Paull CK, Matusumoto R, Wallace PJ, Dillon WP (eds) Proceedings of the Ocean Drilling Program, Scientific Results.

Yuan T, Spence GD, Hyndman RD (1994) Seismic velocities and inferred porosities in the accretionary wedge sediments at the Cascadia margin. Journal Geophysical Research 99:4413–4427.

Chapter 4
Stability Conditions

Abstract Natural gas hydrates are confined to shallow parts of the geosphere. Hydrates crystallize under moderate pressures and low temperatures, when molecules of methane and other low order hydrocarbon gases occupy the voids in water molecules. Specific Pressure–Temperature (P–T) regime governs the stability of gas hydrates. In most parts of the world the necessary P–T conditions are met, but gas hydrates are likely to form only on the present continental margins and their relict in the permafrost regions, where high inputs of organic carbon and focusing of methane bearing fluids, supply methane required for the formation of gas hydrates. Methane the prime constituent gas of gas hydrates is formed in the earth by different biological, chemical and physical processes. Biogenic methane is generated in sediments by the decomposition of the organic matter due to chemical reactions When the rate of sedimentation is slow (<1 cm/kyr) and total organic carbon (TOC) in the sediments is low (TOC $<1\%$), with higher concentration of oxygen, anaerobic bacteria uses up all the organic matter in the sediments. But when sedimentation rate is high and with high TOC the anaerobic bacteria produces methane few cm below the sea floor. The present chapter in brief describes the factor controlling the stability of gas hydrates and consequent climatic impact and geological hazard that follow the release of gas hydrate during their dissociation.

4.1 Introduction

Gas hydrates crystallize under moderate pressures and low temperatures, when the lattice structure of water molecules hold molecules of methane and other hydrocarbon gases such as ethane to pentane. Sufficient concentration of gas, far exceeding the solubility of gas in water and ionic strength of water is important for formation of gas hydrates (Kvenvolden 1993a, b). Specific Pressure–Temperature (P–T) regime governs the stability of gas hydrates. In most parts of the world the necessary P–T conditions are met, but gas hydrates are likely to form only on the

N.K. Thakur and S. Rajput, *Exploration of Gas Hydrates*,
DOI 10.1007/978-3-642-14234-5_4,

continental margins, where high inputs of organic carbon and focusing of methane bearing fluids, supply methane required for the formation of gas hydrates (Davie et al. 2004). Methane gas in the shallower regions of the earth gets trapped in the voids (cages) present in the crystal lattice of water molecules under moderate pressure and lower temperature. Such conditions are prevalent in the permafrost regions where the lower temperature on the surface and lithostatic (pressure created due the sediments) provide proper conditions for the formation of gas hydrates in the subsurface earth. In the tropical regions temperature at the sea bottom at depths tens of meters reduces appreciably from the observed temperatures at the sea surface. The thickness of water column provides necessary pressures for the formation of gas hydrates in the subsurface earth. In both the environments enough availability of methane far exceeding the solubility of methane in water is prerequisite for formation of gas hydrates.

4.2 Availability of Methane

Methane the prime constituent of gas hydrates is formed in the earth by different physical, chemical and biological processes. Biogenic methane is generated in sediments by the decomposition of the organic matter due to biological processes (methanogens) and chemical reactions. When the rate of sedimentation is slow (<1 cm/kyr) and total organic carbon (TOC) in the sediments is low (TOC <1 %), with higher concentration of oxygen, anaerobic bacteria uses up all the organic matter in the sediments. But when sedimentation rate is high and with high TOC the anaerobic bacteria produces methane few cm below the sea floor. Microbial methane formation in the oceans sediments is usually accompanied by sulfur reduction and the release of hydrogen sulfide. These take place inside the upper part of sediments from the seafloor surface to tens and even hundreds of meters deep. In deeper parts of earth, temperature forms an important part in producing methane by catagenesis, where temperature and pressure play important part in breaking the higher order hydrocarbons to lighter hydrocarbons. In the deeper sediments methane is formed by temperature dependent reactions.

Methane can form in the shallower parts of the oceans not only due to microbial and biochemical decomposition of the organic substance in bottom sediments, but it can also migrate due to seepage of natural gases from shallow oil- and gas-bearing structures. In many parts of the world the methane is generated locally by the conversion of organic content in the sediments in the shallower levels (biogenic) or due to migration methane rich fluids (thermogenic) from deeper sources in the earth. Predominantly biogenic methane is the main constituent of hydrates in most of cases. However, methane from deeper sources has also been found to occur in hydrates in regions like Gulf of Mexico and Cascadian basin. Regions of faster hemipelagic deposition with rapid burial are favorable for production of abundant methane by bacteria within sediments (Claypool and Kaplan 1974). The amount of total organic content (TOC) in the host sediments is thought to be insufficient for

the formation of gas hydrates from in situ biogenic methane production (Hyndman and Davis 1992; Davie and Buffett 2003). The continuity of sediment deposition makes the hydrate layer thicker and its subsidence below the stability zone makes the hydrate unstable, releasing methane as free gas. This free gas migrate backs in to hydrate stability zone. This cyclic procedure leads to higher concentration of methane and formation of hydrates in the stability zone (Paull et al. 1994). Over the passive continental margins, where sedimentation provides high inputs of organic matter methane production in such regions takes place in the hydrate stability zone itself (Claypool and Kaplan 1974; Paull et al. 1994). Over the convergent plate boundaries, i.e. methane produced remotely is focused in the region of accretion through fluid flow (Hyndman and Davis 1992; Ginsburg and Soloviev 1997). The occurrence of gas hydrates has been identified in many parts of the world where the suitable conditions for the formation of gas hydrates are met. Most of the gas hydrates in the oceanic regions has major contribution from biogenic methane. Microbial methane is likely to migrate only a short distance to form gas hydrates occurring at or near surface whereas thermogenic methane in Gulf of Mexico might have to travel long distances to reach in to the hydrate stability zone (Kvenvolden 2003).

4.3 Pressure–Temperature Conditions

Gas hydrates are stable in the subsurface earth under in situ favorable pressure temperature conditions. In practice the thickness of the stability zone is defined with its upper limit as that of seafloor and the region encompassing at the intersection of geothermal gradient curve and that of methane hydrate stability in equilibrium with pure or sea water as the lower limit (Kvenvolden 1988; Ginsburg and Soloviev 1997). The other parameters that control the stability of gas hydrate are the sea bottom temperature, gas composition, salinity of water and local geology. In fact it is difficult to accurately estimate the thickness of gas hydrate stability zone as these parameters shows variations in situ and can not be precisely predicted (Ginsburg and Soloviev 1997). Reliable in situ information of the all the parameters is necessary for accurately determining the stability of gas hydrates and the characteristics of gas hydrates reservoir. Proper assessment of these parameters also determines the magnitude of the pressure reduction and/or temperature increase required to force gas hydrate crystal to dissociate into its constituent liquid water and free gas phase (Wright and Dallimore 2004). Errors associated with estimating any of these parameters propagate as errors in determining the thickness of stability zone and thereby on estimates of global quantum of gas hydrate reserves. Theoretical depths to the base of a gas hydrate layer in ocean bottom can be estimated by assuming:

- Constant hydrostatic pressure gradient
- Typical hydrothermal gradient

- Variable geothermal gradient
- Methane hydrate with connate water
- Methane mixed with other gases

4.3.1 Hydrostatic Pressure

The atmospheric pressure is at its maximum at sea level where it is almost one atmospheric (~101.325 kPa). The weight of water in the sea also creates pressure, and because water is so heavy, the pressure changes rapidly by about one atmosphere for every 10 m of depth. So the pressure at 100 m below the sea is ~1,013.25 kPa (1.013 MPa). At around 1,000 m water depth pressure exerted by the seawater column exceeds the pressure required for gas hydrate to stabilize. In subsurface earth the water content in the pores also adds to hydrostatic pressures. Gas hydrate stability in the subsurface earth is not always expressed in the units of pressures but in the units of depth. Considering the hydrostatic relationship, the pressure below seafloor is estimated from the depth and is expressed as:

$$\mathrm{P(depth)} = \mathrm{Depth(m)} * \mathrm{density} * \mathrm{acceleration\ of\ gravity}$$

Where, depth (m) corresponds to depth of seafloor + depth below the seafloor and density is the density of seawater (10.35 kg/m^3) and acceleration of gravity is taken as 9.8 m/s^2.

As the gravity varies with latitude, the estimation of pressure in terms of depths should incorporate latitude dependence. Apart from this the density of water varies with depth. So the estimation of pressure in the units of depth becomes site specific (Peltzer and Brewer 2003).

4.3.2 Hydrothermal Gradients

The surface temperatures of the oceans range from 30°C in tropical to about freezing point for seawater in Polar Regions. Warm waters in Open Ocean are restricted to a shallow, near-surface band (mixed layer) 100–200 m thick due to the surface currents. The mixed layer has hardly any change in the temperature from the sea surface to lower end of the layer. Irrespective of pattern of warm shallow surface layers, temperature decreases rapidly in the thermocline layer between 200 m and 1,000 m and may attain temperature of about 5°C at lower part of the thermocline. The thermocline reaches its maximum depth at mid-latitudes and is shallowest at the equator and at its northern and southern limits. The absence of thermocline has been observed in some polar regions. The temperature gradient in this region is maximum and the gradient ranges from 0.2 to 0.5 per 100 m. In the deeper part of the sea temperatures steadily fall with increasing depth and the temperature may attain about 4°C at the depth of 2,000–3,000 m even beneath

the hottest tropical regions. The temperature gradients in this region are quite low Fig. 4.1. Given the smaller temperature gradients in the sea and error up to 0.5°C in temperature measurement may lead to error of depth estimation of the order of 100 m.

4.3.3 Geothermal Gradients

Temperature is one of important parameter for determining the stability of gas hydrate in the subsurface earth. The temperature at the sea floor becomes the reference point for determining the temperature distribution in the sediments. The temperature in the sediments is expressed as linear function of depth (Davie et al. 2004):

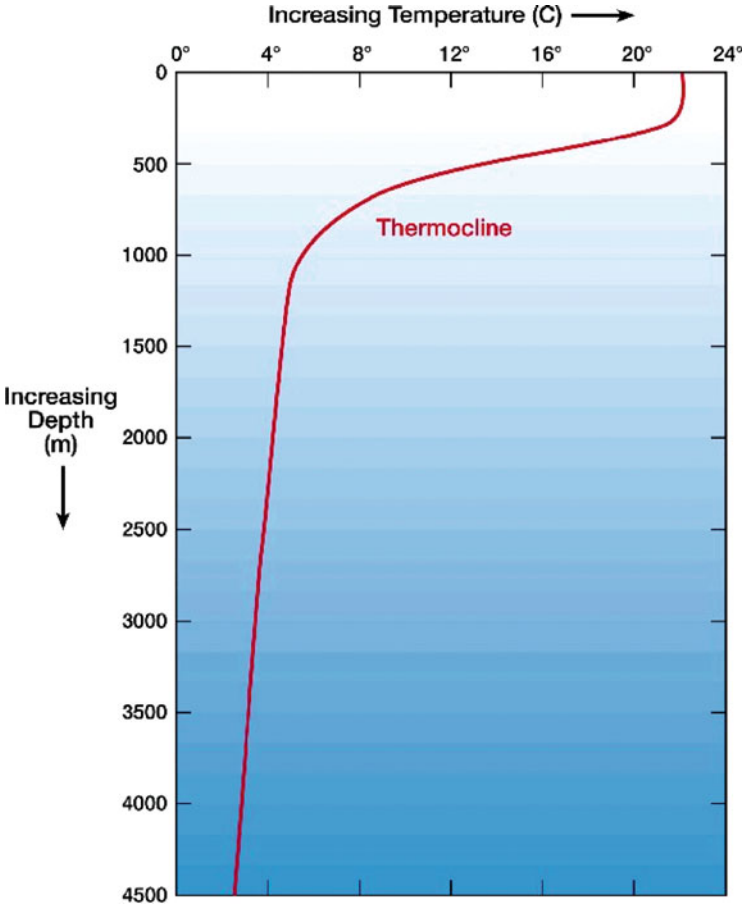

Fig. 4.1 Observed temperature variations in the ocean for the tropical regions. Sharp temperature gradients are confined in the region of thermocline

$$T(z) = T(0) + Gz$$

Where, T(0) is temperature at seafloor and G is geothermal gradient, T(z), temperature at depth z.

As mentioned above the temperature at the seafloor at water depths of 2,000–3,000 m reaches to around 3–4°C, the temperature in sediments increases with increase in depth. The pattern of increase of temperature in the sediments depends on the geothermal gradients. In the near subsurface rock it is strongly dependent on the heat flow by simple relation:

$$Q = K\Delta T/\Delta Z$$

Where, Q is the heat flow, K the thermal conductivity of the rock and $\Delta T/\Delta Z$ is the geothermal gradient.

Geothermal gradient varies considerably with both tectonic setting and the thermal properties of the rock. High gradients (> 5°C/100 m) are observed along the oceanic spreading centers (for example, the Mid-Atlantic Rift) and along island arcs (Aleutian chain). Low gradients (1.2–1.8°C/100 m) are observed in tectonic subduction zones in the Andaman Sea (Max 2003). In the sedimentary basins have average gradients that typically vary from 1.5 to 3.0°C/100 m. The geothermal gradient as well as the thermal conductivity can be determined from the thermal probes in the field. Geothermal gradients have been obtained in many parts of the world either by deployment of thermal probes over the seafloor or in the downhole measurements. The depths of occurrence of BSRs have also been utilized to estimate geothermal gradients and heat flow (Yamano et al. 1982) and obtained geothermal gradients from BSRs in Peru region agrees well field measurements (Kvenvolden and Kastner 1990). Often, one assumes a constant geothermal gradient for a region, and the gas hydrate stability modeling is carried out accordingly. In regions of higher geothermal gradients the gas hydrates are likely to stable in the thinner part and on the other hand gas hydrate could be stable over thicker part of subsurface with lower geothermal gradients. Field evidence indicates that anomalously warm, presumably methane rich fluids can rise as conduits in the gas hydrate areas (Zwart et al. 1996). These fluids ultimately produce clathrates when they attain thermal equilibrium with respect to the regional isotherm that is, they create their own localized, moving phase boundary front until they dissipate their excess heat, if it fails to happen, the gas escapes in to over laying water column.

4.4 Gas Hydrate Stability Zone

The three-phase equilibrium i.e. hydrate-water-free-gas can be determined for given pressure–temperature and gas composition by synthesis of hydrates in the laboratory, empirical methods and by theoretical considerations Fig. 4.2. Methane

hydrate can be stable at 6°C and pressures of the order of 4 MPa, when most of the cages in the lattice of water molecules are filled with methane. The intersection point where hydrate stability phase boundary cuts across decreasing temperature and increasing pressure regime defines the top hydrate stability zone. The base gas hydrate stability zone commonly coincides with the depth of intersection of local geothermal curve with the three phase equilibrium curve for methane hydrate stability for pure or seawater. As the composition of gas as well as the ionic strength is not exactly known, the position of phase boundary is generally evaluated under hydrostatic pressures for methane gas and pure water (Kvenvolden 1998). The seafloor temperatures and the hydrostatic pressure due the sediment thickness of the order of 150 m control the depth of upper boundary of hydrate stability in the Polar Regions. Over the oceanic regions the upper boundary may reach to about 300 m, in the regions where seafloor temperatures attain 0°C and pressure created by water column and sediments. However, as mentioned above, the surface temperature in the tropical countries is of the order of 25°C or so and temperatures at seafloor at the depths of the 300 m are slightly lower. In this regard the upper limit of gas hydrate stability in oceanic sediments occurs at higher depths when compared to the polar region. The thickness of gas hydrate stability zone (GHSZ) depends on the sea floor depth, geothermal gradient and composition of gas. The increase of pressure with depth of water column, the thickness of GHSZ also increases for a constant geothermal gradient, in view of the pressure increase compensating for the increase of temperature with depth below the sea floor.

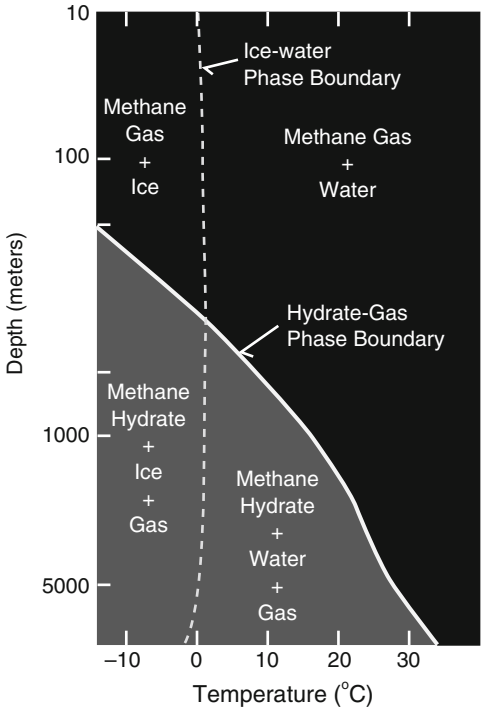

Fig. 4.2 Estimated hydrate stability phase curve obtained considering pure methane composition and pure water system. Only two phases exist across the stability cure. Water content is always present, either in liquid form or as ice at temperature below its freezing point. Free gas and water can exist below the stability zone (Kvenvolden 1998)

Given the average geothermal gradient of 3°C/100 m below the sea floor, it is expected that gas hydrates can be stable in 300 m water depth in high latitude regions. In the region of high geothermal gradients (tectonically active) the thickness of GHSZ may reduce appreciably.

Only two phases are expected to occur in the stability zone and below the stability zone. Methane hydrate with methane gas at temperatures below freezing point (Polar Regions) or methane hydrate with water at temperature above the freezing point (tropical oceanic regions) is likely to be present in the hydrate stability zone. Methane as free-gas can occur below the stability zone and beyond the phase stability curve. With presence of abundant water in the sediments, water may coexist along with other phases as either in liquid form at higher temperatures beyond the stability phase curve or as ice at temperatures below the freezing. Analysis of pore water obtained from the cores in the Mallik 2002 gas Hydrate Production Research Well suggests that gas hydrate may exists at near or near its stability threshold at many locations in the reservoir.

Having a global estimate of pressure–temperature distribution the gas hydrate stability over continental margins as well as in the polar region can be ascertained from different procedure available. Figure 4.3 (modified from Krey et al. 2009) global pattern of upper limit gas hydrate stability determined with assumed hydrostatic pressure and constant geothermal gradient. It can be visualized that most of the Polar Regions and on the continental margins proper stability condition exists, and these regions can hold gas hydrates provided the availability of excess of methane gas far exceeding the solubility of methane in water.

4.4.1 Salinity

The most characteristic feature of seawater is that it is salty. It is a complex solution of many different chemicals; about 35 g of salt in every liter (3.5%) is present in seawater. Almost nine-tenths of this is common salt or sodium chloride. The remainder probably includes all the chemicals that occur naturally on earth. Many of the chemicals in seawater occur in very low concentrations and vary over time and space. But several of the major constituents, including sodium and chlorine, maintain very similar concentrations throughout the seas and have done so over many millions of years. Dissolved salts as electrolytes have inhibition effects on hydrate formation. When salts are added to the liquid phase the equilibrium is shifted, because dissolved ions decrease the chemical potential of water. Decreasing the chemical potential of water would dissolve methane hydrate; if the system were closed then the pressure of CH_4 would be increased until a new equilibrium is reached (Sloan 1998).

Pore water salinity appears to impose limits on the capacity of the sediments to host gas hydrate, with a direct relation apparent between the hydrate saturation levels achieved in sediments of varying salinity, making hydrates to be stable at lower temperatures. Considering 3.35% salinity for the seawater, a reduction of −1.1K has

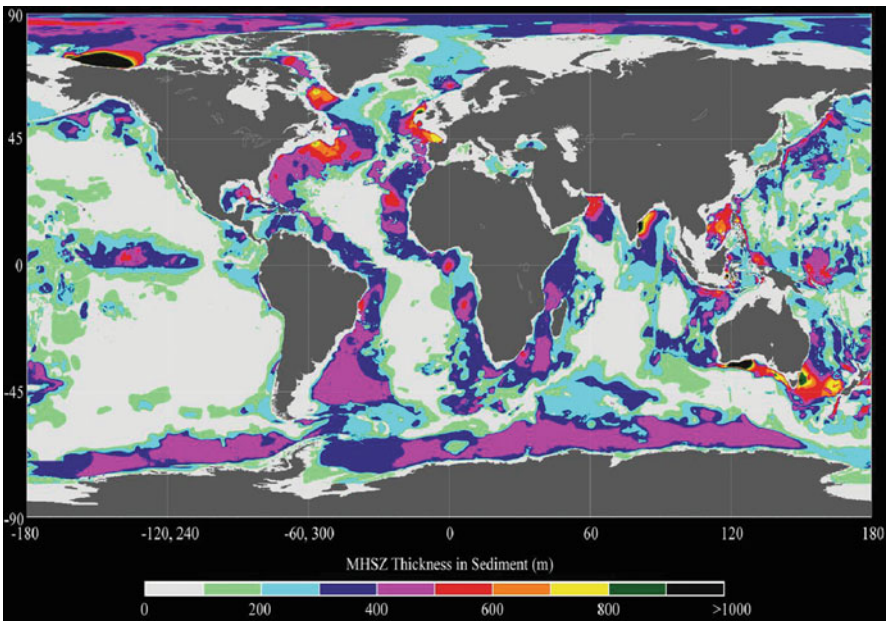

Fig. 4.3 Global hydrate stability zone estimated considering an assumed geothermal gradient for the oceanic regions. The figure shows that in most part of the world favorable pressure temperature conditions exist for the formation of gas hydrates in the oceanic regions (Krey et al. 2009)

been obtained for the dissociation of hydrates in relation to pure methane–pure water system (Fig. 4.4, adopted from Dickens and Quinby-Hunt 1994). On the other hand the content of salinity in pore water lowers methane solubility. The reduction of methane solubility leads to reduction in amount of gas required for hydrate formation. The thermodynamic model calculations suggest that profile of gas solubility permits hydrate to crystallize directly from dissolved gas.

Salinity in the pore water causes two opposite effects, which partially compensate each other. On one hand the salinity of the water decreases the solubility of methane hydrate, but the existence of salts inhibits the formation of hydrate, which increases the dissociation pressure and the concentration of methane in solution. However, the solubility effect overweighs the effect of an increasing dissociation pressure. Therefore, the solubility of gas hydrate decreases with increasing salinity (Zatsepina and Buffet 1997; Tishchenko et al. 2005).

4.4.2 Gas Composition

Hydrate formation is primarily dominated by the high-pressure low temperature regime when appreciable quantity of gas mainly methane is present in the region. Depending on the chemical composition of gases the hydrate stability will vary, and

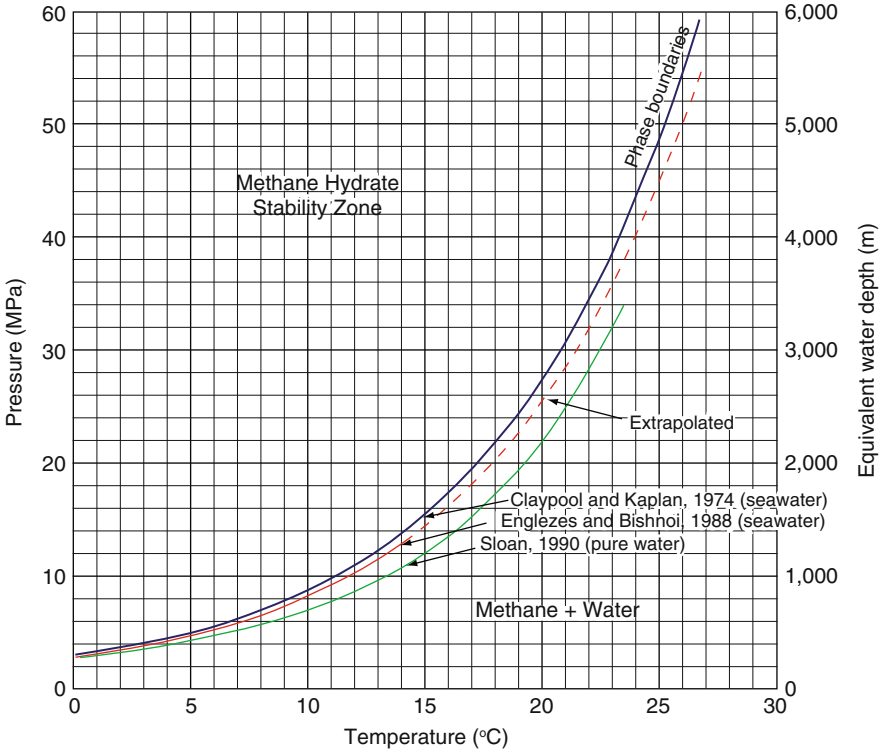

Fig. 4.4 Hydrate stability phase curves (Booth et al. 1998), for estimated for pure water and pure methane (Sloan 1990) and for saline water (3.5%, Claypool and Kaplan 1974) and thermodynamic estimates of stability considering simple salts (Engle and Bishnoy 1988)

also is governed by the geomorphic and geological conditions where gas hydrates are likely to occur. The precise chemical composition of gas hydrates forming gases in shallower and as well as in the deeper parts of the earth is not known exactly. Due to this hydrate stability in the earth is evaluated considering mainly methane gas. Methane hydrates require lower temperatures and higher pressures for their formations. Laboratory experiments have shown that methane hydrates are stable up 30°C at pressures around 86 MPa within limits of normal petroleum operations (Carroll 2003). However, in nature low order and higher order isotopic gases are also trapped in the hydrate structures. Presence of gases other than methane in the hydrate frame significantly alters the stability conditions. Hydrate will be stable at appreciably higher temperatures and lower pressures when hydrogen sulfide (H_2S), carbon dioxide (CO_2), ethane (C_2H_6) and propane (C_3H_8) form part of the hydrate forming gas mixture (Carroll and Mather 1991; Sloan 1998; Kvenvolden 1998). In both the cases the presence of H_2S and CO_2 gases with methane make the hydrate phase equilibrium to be stable at higher temperatures and lower pressures. On the contrary, the presence of nitrogen with methane may make hydrates to form at higher pressures. Figure 4.5 shows several gas hydrate stability

curves (listed by guest molecule). Note that they all have swooping parts, but some have a vertical line as well. The vertical line represents the formation of gas hydrates from liquid water and liquid guest (the curved parts of the phase boundary can be calculated using the program (Sloan and Koh 2008)

Pure methane hydrates will be stable at 6°C and pressures exceeding 4 MPa (400 m seafloor depth). Whereas, hydrates formed by ethane can be stable at very shallow depths within this temperature range. Adding 10% ethane in the gas mixture will result in formation of hydrate at around 0.6 MPa (60 m seafloor depth) approximately about one-sixth reduction in pressure conditions, (Baker 1972). The stability of gas hydrate is sensitive to the composition of gas mixture makes hydrate to occur in shallower depths under warmer natural conditions. On the contrary presence of saline water and nitrogen gas (N_2) makes the hydrates to be stable at lower temperature regimes.

Heterogeneous hydrates have been found in many parts of earth such as Gulf of Mexico, Caspian Sea, and Hydrate Ridge offshore Oregon in U.S. Most of the locales in Gulf of Mexico have shown the presence of heavier hydrocarbon gases. The region in Gulf of Mexico covers Bush Hill, and Green Canyon, Nankai Trough offshore Japan (Taylor 2002). The presence of methane, ethane, propane and ethylene was detected in the core samples collected during the drilling at Site 1247 in the southern summit of Hydrate Ridge. The data collected over the Barkley Canyon west of Vancouver Island has indicated the presence of methane and heavier hydrocarbons suggesting wide range of stability of gas hydrates in this region (Lu et al. 2007). Consideration of salinity as factor for the gas hydrate formation may also marginally alter its stability. Figure 4.6, shows pressure–temperature (*P–T*) curves for a number of sII, sH and sI hydrates (Adopted from Lu et al. 2007). The sII

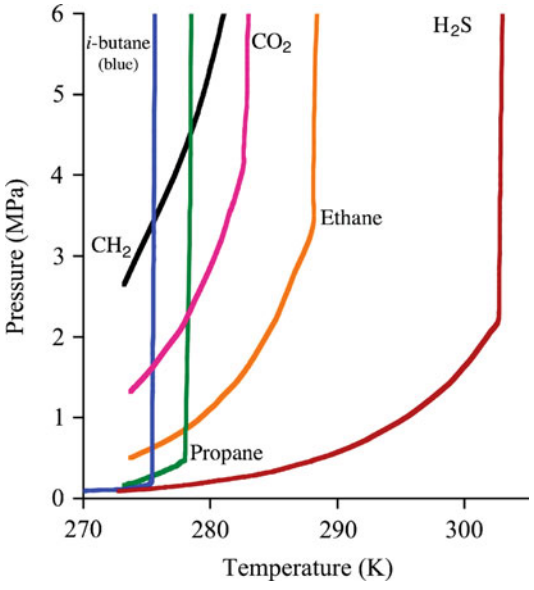

Fig. 4.5 Hydrate phase equilibrium for different hydrocarbon gases. Most the gases require lower pressures and higher temperature to form as hydrates as against the methane. Nitrogen on the other hand requires very higher pressures to stabilize as hydrate
source: knol.google.com/k/gas-hydrates

double hydrates containing methane are the most stable over the temperature range investigated. The plot for the mixed sII-H hydrate falls between those for the sII double hydrates and sH hydrate. This suggests that sH in the mixed sII-H sample decomposes first, following more or less the curve for the pure sH hydrate. After that, the *P–T* curve becomes parallel to the sII hydrate curves. All of the methane-containing double hydrates are considerably more stable than sI methane hydrate. It is clear that the complex hydrate will have a much greater regime of stability in natural environments than sI methane hydrate. From the evidence presented, the complex gas hydrate is composed of sII and a smaller amount of sH hydrate. The two structures appear to be independent but closely associated.

4.4.3 Solubility of Methane

The solubility of methane is appreciably low of the order of 0.045 volumes per unit volume of water. Methane dissolved in water can coexist with free gas at high temperature and with solid hydrates at high pressures and low temperatures. In

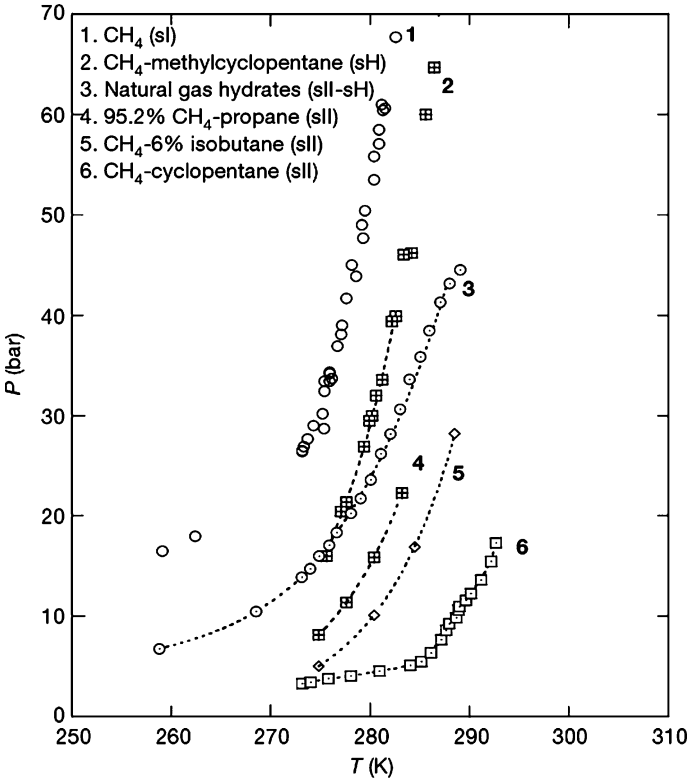

Fig. 4.6 The dissociation conditions for natural gas hydrates from Barkley canyon and reference samples of sI, sII and sH gas hydrates. Adopted from Hailong et al. (2007)

absence of gas hydrates the solubility increases with decrease in temperature and increase in pressure as per Henry's law (Osegovic et al. 2006). The equilibrium of methane solubility is important, because it determines the minimum quantum of methane required for formation of hydrates. The presence of hydrates gas solubility decreases sharply with decrease in temperatures. This decrease is attributable to the hydrate directly forming from aqueous solution, without need for free gas (Zatsepina and Buffet 1997). The presence of hydrate facilitates further hydrate formation and hence the equilibrium concentration of gas in water decreases and gas solubility increases with increase in temperature (Duan and Mao 2006; Davie et al. 2004). In this regard the numerical models for gas hydrate formation show that the shape of methane solubility profile with depth has important hydrate formation and bearing on the vertical distribution of hydrates in the sediments (Davie and Buffet 2001). The peak solubility of methane occurs at the three-phase equilibrium and coincides with base of hydrate stability zone. Within the hydrate stability zone the solubility is insensitive to pressure and is a function of only temperature and it increases with temperatures (Fig. 4.7 adopted from Davie et al. 2004). At temperature above the equilibrium phase curve, methane and water are in stable phases and the solubility is a function of both temperature and pressure. Below the hydrate stability zone, pressure and temperature both increasing with depth and affecting the solubility in different ways. The solubility increases with pressure but decreasing with temperature. Below the hydrate stability zone there are hardly any appreciable changes in solubility due to counter acting effects of pressure and temperature (Zatsepina and Buffet 1997).

Due to prohibitive cost of collection pressure and temperature data in the oceanic regions, different approaches have been followed to determine the equilibrium condition gas hydrate stability for varying pressure and temperature conditions. The experimentally determined dissociation of hydrate for pure and salinities resembling the seawater data has been utilized and interpolated either by linear fitting and second order polynomial to estimate the hydrate phase equilibrium for desired pressure temperature conditions (Dickens and Quinby-Hunt 1994; Sloan 1998). The other method utilizes searching for state for minimizing the Gibbs Free Energy through intensive development of computer routines. Following the approach the CSMHYD (Sloan 1998) program calculates hydrate stability for pure water, seawater as well as for different gas compositions.

4.4.4 Geological Controls

In addition to pressure and geothermal gradient other variables affecting the stability of gas hydrate are hydrothermal gradient sediment thermal conductivity, heat flow, and geological heterogeneity (Macleod 1982). The geological processes can shape a potential gas hydrate reservoir is evident by the explanation given for why gas hydrates occupy position well above their regional phase boundary. The stability of gas hydrates in situ is the controlled by (a) localized pressure and temperature or the pore water chemistry effects rather than as a consequence of regional geothermal and hydrostatic conditions (b) site specific gas enrichment,

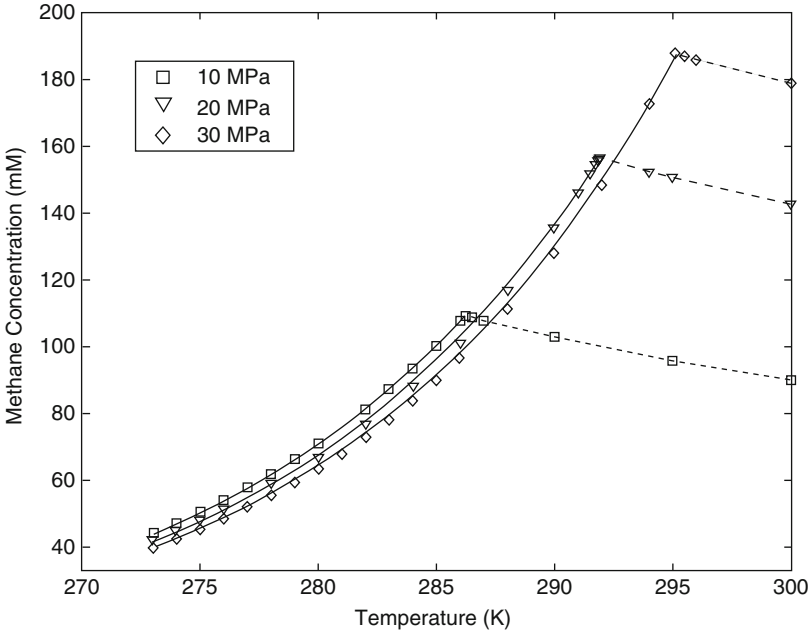

Fig. 4.7 Thermodynamic predictions of methane solubility in pure water as a function of temperature for three values of pressure. The peak in the solubility occurs when the hydrate phase equilibrium curve coincides with the base of the hydrate stability zone (Davie et al. 2004)

either in absolute or relative sense (c) formed at a time when the base of gas hydrate stability zone was shallower, (d) the stability attained elsewhere (relict) and transported to the present location by mass movement processes, it is allochthonous (Booth et al. 1998). The geothermal gradient is also affected by the heterogeneities in the local geological configuration and associated thermal conductivity, as has been observed in the Gulf of Mexico (Ruppel et al. 2005) and in the Barents Sea (Bugge et al. 2002). The proximity specific geological features, such as mud diapirs, shale diapirs and salt domes, shallow basement and the presence of faults causing focused fluid flow (Chand et al. 2008). It has been observed worldwide that shallow salt structures can enhance the temperature of the nearby sediments up to 30°C due to the high conductivity of salt (Thomsen and Lerche 1991). Vertical fluid migration due to the mud diapirism brings in the gases along with heat to shallower level thereby disturbing the local stability conditions (Chow et al. 2000). The thermal conductivity of salt dome is high thereby lowering of geothermal gradients in the dome. This result in compressed isotherms above the salt dome and which may produce thinning of stability zone above the salt dome in comparison to its flanks (Dillon et al. 1980). The thinning hydrate stability zone over the salt dome has been observed in the southeast offshore areas the United States (Dillon and Max 2003). The presence of salt ions in the interstitial fluids acts as inhibitors and thereby resulting in higher temperature and thereby prevents the formation of gas hydrate (Taylor et al. 2000). The thermal conductivity of shale is in general lower.

In case of shale diapirism, the geothermal gradient inside the diapir is high making the isotherm to deepen in the diapir, which results in deepening of gas hydrate stability zone over the diaper (Macleod 1982).

There is a clear association between gas hydrate occurrence and fault zones, as well as other tectonically active related features, as has been observed by Hyndman and Davis (1992), Soloviev and Ginsburg (1994). All but one 15-drill hole is sites in which hydrates are present lie within tectonically active continental margin environments. The Blake Ridge off the southeastern United States is the only site in a passive margin. It is nonetheless characterized by presence of extensive fault zones. If we assume a basic proportionality between porosity and permeability, then the higher the porosity would also suggest a greater capability to transport fluids. Simplistically high porosity and permeability favor the accumulation of clathrates. Because permeability tends to be anisotropic (more permeable normal to the direction of compaction) in the consolidating sediments, more porous beds may also favor clathrate accumulation through pathways that trend towards horizontal.

4.5 Planetary Hydrates

Gas hydrates can be stable under high pressures and low temperature. Initially it was thought that gas hydrate may occur only in the outer regions of Solar systems, where the temperatures are appreciable low and water in the form ice is quite common. The stability conditions of methane hydrates for different planets is presented in Fig. 4.8 (adopted from Osegovic et al. 2005). Titan's surface and atmosphere constitutes gases which may form suitable hydrate formers. The presence of methane (5%), carbon dioxide, nitrogen, ethane and propylene, other gases in smaller percentage and content of water vapor have been identified on the surface of Titan (Niemann et al. 2005). The presence of hydrates have been reported in the Titan's subsurface since eighties (Lunine and Stevenson 1987) and on the surface later on (Fortes and Stofan 2005). It is proposed that compound hydrate is likely a sink for many of the hydrate formers found on the surface of Titan. Moderate formation of hydrates is likely to occur owing to lesser availability of water on Titan (Osegovic and Max 2005). Planet Mars may hold condensate in terms of pure H_2O ice, CO_2 (clathrate), a eutectic mixture of solid CO_2 and either clathrate or H_2O ice and under limited conditions pure solid CO_2 Seasonal frosts are likely to consist of thin layers of water ice and/or clathrate overlain by eutectic assemblage (Longhi 2006).

4.6 Climatic Impact

Drilling and geophysical techniques have established that the earth subsurface clathrates hold a larger quantum of carbon (~11,000 Gt) on the continental shelves and ocean basins. Comparatively smaller quantity carbon (~4,000 Gt) is preserved

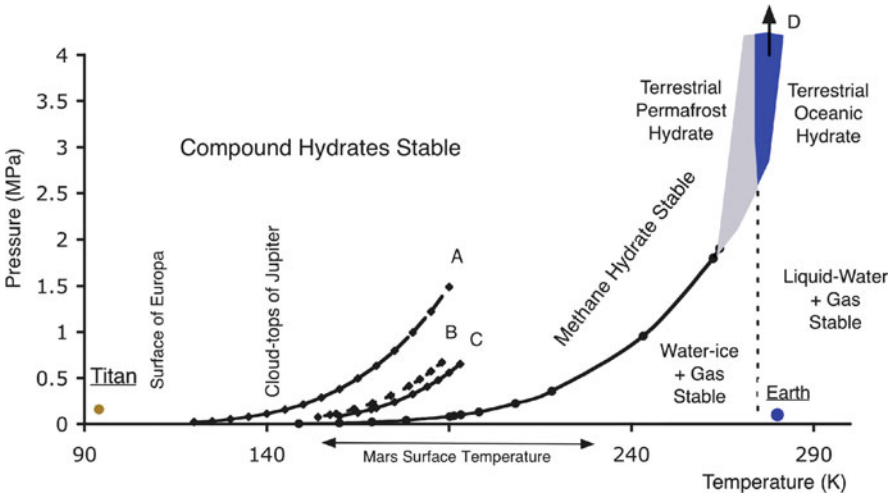

Fig. 4.8 Hydrate stability on different planets. Methane (D) and nitrogen (A) clathrate hydrate pressure–temperature stability fields. Methane hydrate exists above the solid line (Sloan 1998). *Vertical dashed line* is the water–liquid → water–ice phase boundary. *Dashed curved lines* are 6% (B) and 10% (C) methane gas in nitrogen gas. (Adopted from Osegovic and Max 2005)

with the clathrates in the permafrost regions (MacDonald 1990). Gas hydrates in the sediments are in state of metastable equilibrium with the environment. Methane as guest molecule is held captive in structural frame of hydrates and provides stability to hydrates over higher range of temperatures. Pressure–temperature regime makes them stable in shallow subsurface depths of the earth. Changes brought about in temperature and pressure by any mechanism leads to destabilizing or stabilizing of clathrates/hydrates over the time scales of the order of hundreds to thousands of years. The time scales depend on the thermal properties of surface sediments (MacDonald 1990). The amount of methane trapped in the hydrates is almost 3,000 times the quantum of methane in the atmosphere (Kvenvolden 1998). The methane concentration in the atmosphere is increasing at the rate of about 1% every year (Watson et al. 1990). Release of large amount methane from hydrate either as unaltered methane or as oxidized to carbon dioxide could have large impact on the composition of atmospheric gases. Methane being radiatively active it is a green house gas and major contributor to global climatic change (MacDonald 1990). It is suggested that methane released as green house gas from hydrates has 20 times larger effect on the global warming when compared to carbon dioxide integrated over from during last 100 years span (Shine et al. 1990). Shallowness of hydrate stability zone makes it vulnerable to near surface changes.

Any changes brought around in pressure–temperature conditions on the surface/near surface by means of sea level fluctuation during the periods of glaciations, warming of atmosphere due to climatic change and tectonic activities in terms of faulting and earthquakes may lead to perturbing the stability conditions of hydrates.

These phenomena alter temperature and/or pressure regime and thereby altering the stability conditions. Methane releases from hydrates that could be most significant to climate change are more likely to be of chronic nature. During the global warming period, the glaciers and ice caps melt; increase water flow in the oceans, polar shelves and thermal expansion of oceans causes rise in sea levels. The rise in sea levels results in increasing the hydrostatic pressure and stabilizing hydrates in continental margins and in polar continental shelves. On the other hand on the continental regions the hydrostatic pressure is reduced due to melting of ice destabilizing hydrates and release of methane in to the atmosphere (Kvenvolden 1998).

During the global cooling cycles the whole system reverses. Glaciers and ice caps grow resulting in fall sea levels over the continental shelves reducing the hydrostatic pressure over the continental shelves. The reduction of hydrostatic pressure due to the sea level drop of 120 m during the last glacial maximum (~18,000 years ago) might have resulted in shallowing the hydrate stability zone about 20 m with temperature being assumed constant (Dillon and Paull 1983). The reduction of stability zone thickness depends on the rate of sea level fall and thermal properties of near seafloor sediments. To test the hypothesis that free gas zone (FGZ) thickness is mechanically regulated globally, critical FGZ thickness as a function of BSR depth was calculated and compared to nine hydrate provinces, where conjugate normal faults and where the FGZ thickness is well constrained by seismic analysis or drilling (Fig. 4.9, adopted from Matthew et al. 2004)

The reduction in the thickness would destabilize about 200–400 GT of carbon and the time scale of release of carbon from clathrates is around 1,000 years. The fall in sea level also changes the near surface temperature and warms up the oceanic waters. A few degrees of warming in the deep ocean can have a significant impact on the stability of the hydrate, and it is known that the temperature of the deep ocean responds to changes in surface climate, albeit with a lag of centuries to millennia (Schiermeier 2008). Different mechanisms have been proposed to explain the cyclic link between dissociation of gas hydrates (release of methane) and climate change/global warming. Nisbet (1990) suggested that the methane released from the continental gas hydrates has led to rapid rise in the global temperatures and which in turn might almost have stopped glacial activity about 13.5 ka ago. The termination of glacial period makes higher latitude regions to get exposed to higher temperature and results in melting ice sheets/caps and thereby reduction of pressure. The change of thermo-baric conditions leads to destabilization of gas hydrates and release of uncontrolled methane to the atmosphere.

On the other hand Paull et al (1991) postulated that during periods of global cooling; the water inputs over the outer continental margins are curtailed resulting to sea levels to fall. The fall in the sea level reduces the pressure over the margins leading to dissociation of gas hydrates, release of methane to atmosphere resulting in global warming triggering to deglaciation. Both the proposed models suggest the interconnectivity between different regions (high latitude-tropical) of gas hydrate occurrences through atmosphere. Physical changes brought about in one-region leads perturbing the physical conditions in other region via atmospheric connectivity.

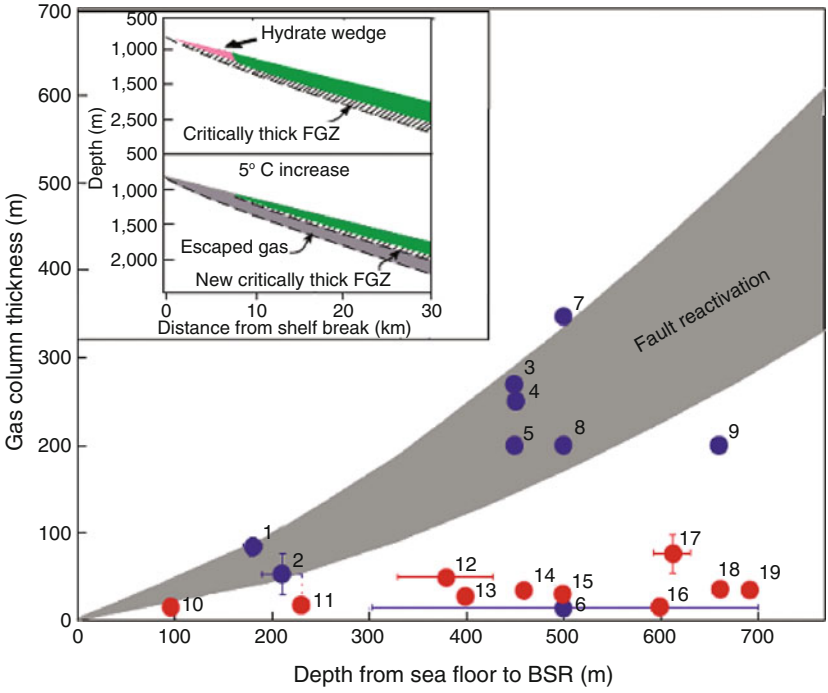

Fig. 4.9 *Blue* symbols (numbered 1–9) show gas column thickness below BSRs at several hydrate provinces in basin settings where 1 is near vertical. *Red* symbols (10–19) show gas column thickness below BSRs at hydrate provinces in compressional settings where 1 is probably near horizontal. Note that gas column thickness generally increases with depth for the *blue* points, but remains nearly constant for the *red* points. The *grey* area indicates the interconnected FGZ thickness required for fault reactivation. The *upper* bound of the *grey* area corresponds to values of $\alpha = 0.77$ (zero hydrate at the BSR) and $\upsilon = 0.45$; the *lower* bound corresponds to low end values of $\alpha = 0.67$ (25% bulk hydrate) and $\upsilon = 0.41$. Point locations: 1, Barents Sea (Andreassen et al. 1990); 2, the Norwegian margin (Mienert et al. 2000); 3, Bering Sea basin (Scholl and Hart 1993); 4, 5, Blake ridge (Holbrook et al. 1996); 6, Beaufort Sea (Andreassen et al. 1995); 7–9, basin in Makran accretionary prism that has experienced rapid sedimentation (Sain et al. 2000; Grevemeyer et al. 2000); 10, offshore Cascadia (Hyndman et al. 2001); 11, offshore Chile (Bangs et al. 1993; Miller 1996), Niger delta (Hovland et al. 1997); 13, 15, offshore Colombia (Minshull et al. 1994); 14, Gulf of Oman anticline (Minshull and White 1989); 16, offshore Peru (Pecher et al. 1996); 17, South Shetland islands (Tinivella et al. 1998); 18, 19, Oman accretionary toe (White 1977, 1979). Top inset, model of the hydrate stability zone and critically thick FGZ below for a bottom-water temperature of 0°C. The BSR is located at the interface between the sediment overburden where hydrate can exist (*green*) and the FGZ (*black* and *white* stripes). The *pink* area marks the hydrate wedge. Bottom inset, new BSR depth and critical FGZ thickness for a 5°C temperature rise at the sea floor. The *grey* area denotes the area over which gas (and dissociated hydrate) must escape. Note the thinner critical FGZ due to bottom-water warming, which results in less sediment overburden above the BSR (Adopted from Matthew et al. 2004)

However, due to the long ventilation times of the deep ocean (~100–1,000 years), where the bulk of methane hydrates resides, and the slow propagation of the temperature signal into the sediment column (~180 m/1,000 years), a new

equilibrium is only reached on a timescale of 1,000–10,000 years. Moreover, the fraction of methane from the bottom of the ocean that reaches the atmosphere is uncertain and dependent on the transport mechanism (e.g. bubbles, dissolved, Lamarque 2008). However, the susceptibility of hydrates dissociation to near surface natural or human induced changes in pressure and temperature might have played an important role in past climates and may also bring about significant global climatic change in future due to activities for extraction of gas hydrates as energy resource. Therefore there is an increasing interest in assessing the potential of methane release in a warmer world and its consequences for future climate change (Brooks et al. 1984; Schiermeier 2008; Westbrook et al. 2009).

4.7 Geological Hazards

Sub-aerial and submarine landslide occurs when the stresses exerted on the sediments exceed the sediment strength. These stresses are either from external sources or changes brought around within the sediment matrix itself. In the marine environment the slope failure may result from over-steepening of slopes, faster sediment deposition, tectonics and by earthquakes. Submarine gas hydrate deposits are found on continental slopes, where average gradients are only a few degrees. Basic fracture mechanics theory suggests that low angle failures cannot result from slow changes of earth's stresses or mechanical properties. Low angle failures, including those found in the geological record, can only result from (1) large transient stresses, such as those associated with earthquakes, (2) sudden changes in material properties, such as might be associated with rapid decomposition of gas hydrate, or (3) sudden changes of pore pressure, which might be due to hydrate decomposition or migration of gas from other sources (Kleinberg 2004).

The internal mechanisms, which weaken the sediments strength, are related to increase porosity, pore pressure and presence of gas bubbles in the pores. The gravity driven mass transport of sediments on the continental slope has quite distinct characteristics, slides occur on large planar surface, no internal deformation and the end member is debris flow (Haq 1998). The presence gas hydrates in sediments alters mechanical properties of the sediments and support as load bearing matrix (Helgerud et al. 1999). The evidences of which can be seen geological, geophysical and geochemical properties of the sediments (Kvenvolden 1998). Gas hydrates occupy pore spaces also cement sediments to increase the shear strength and thus enhancing the slope stability. On one hand, hydrates may strengthen the sediments by cementing grains; on the other hand, if hydrates impede fluid flow due to the reduced permeability, may weaken the underlying sediment by trapping fluids and free gas. During the formation of gas hydrates, the water and the gas content in the sediment pores is converted to solid form and thereby increasing the sediment strength. On the contrary the dissociation gas hydrate will freshen the sediment with water and gases, which may reduce the sediment strength. Laboratory studies have indicated that dissociation of even a small amount of hydrate can

cause significant loss of sediment strength. Hydrate dissociation could be critical in inciting slope failures for low permeability sediments in shallower water depths (Nixon and Grozic 2006). The prevailing thermo-baric conditions in the oceanic regime make the hydrate stability zone to thicken with increase in the level of water column due to the dominance of pressure component. When gas hydrate dissociates due to any aforementioned causes the released methane either partly gets dissolved in the overlying seawater and can also remain in gas phase with the seawater. The dissolution of methane in seawater reduces the density of seawater (Xu and Ruppel 1999), due to mass transfer and is a slow process (Zhang and Xu 2003). The estimated values of methane release due to the dissociation of unit volume gas hydrate in an oceanic regime exhibit a distinct trend (Max and Dillon 1998; Puall et al. 2003). The pore pressures on sediment that are close to up-dip end of the gas hydrate stability zone are significantly higher when compared to deeper parts of the ocean resulting larger quantity methane release near to up-dip side in the shallow regions of the ocean during the process of dissociation of gas hydrates.

During the process of hydrate dissociation, gas hydrates liquefy and sediments unconsolidate. The free-gases trapped beneath the remaining gas hydrates would constitute a weak layer of over pressurized sediments. The combined effect of these processes may lead to slope failure (Bunz et al. 2003). Since almost three decades the link between gas hydrates and slope failure has been examined and debated extensively. Most of the studies have attempted to link between gas hydrate decomposition and slope failures. The inference about the connectivity between the gas hydrate and slope failure is drawn on the basis of identification of slope failure in the vicinity of occurrence of gas hydrate bearing sediments either by means of presence of BSRs or other geophysical, geochemical and geological signatures (Summerhayes et al. 1979; McIver 1981; Nisbet and Piper 1998 and others). The most extensively studied slope scars connected to gas hydrate dissociation are the U.S. Atlantic margin (Booth et al. 1994) and Storegga slide in the Norwegian margin (Brent et al. 2002). Around 200 slump scars have been identified in the Atlantic region and the occurrence of BSRs in vicinity of scars in the shallow regions 500–700 m water depths in up dip side of hydrate stability zone suggest gas hydrate dissociation might have played important role generating these slope failures (Puall et al. 2003). The Storegga composite slump scar runs to about 290 km with run off distance of about 800 km (Fig. 4.10; adopted from Brent et al. 2002). Sea floor collapse within the Storegga Slide and above the dissolved gas hydrate suggests that hydrate reservoir is highly dynamic, and methane released due to landslide may contribute significantly to greenhouse effect (Brent et al. 2002). Large amount of methane is released in the atmosphere due to submarine sediment failures. Link between releases of methane due to dissociation of hydrate, its climatic impact can be ascertained through Clathrate gun hypothesis. More than 70% of slope failures in North Atlantic occurred during two time spans between 15 and 13 ka and between 11 and 8 ka and correlate with rising sea level and peaks in methane record during BØlling-ÅllerØd and Preboreal periods. These data support clathrate gun hypothesis for glacial-interglacial transitions (Maslin et al. 2004)

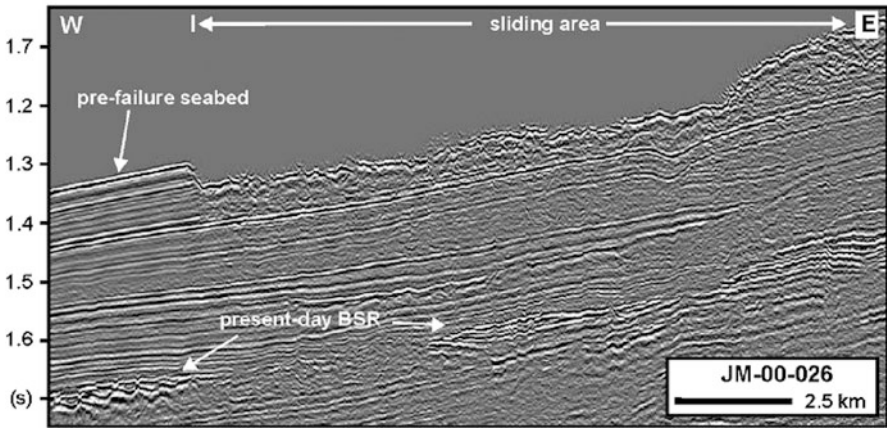

Fig. 4.10 Migrated high-resolution seismic data over Storegga region off Norwegian margin showing the slope failure and present day BSR in the region (Brent et al. 2002)

References

Andreassen, K., Hogstad, K., and Berteussen, K.A., 1990, Gas hydrate in the southern Barents Sea, indicated by a shallow seismic anomaly, First Break, 8, 237–245.

Andreassen, K., Hart, P.E., and Grantz, A., 1995, Seismic studies of a bottom simulating reflection related to gas hydrate beneath the continental margin of the Beaufort Sea, Journal of Geophysical Research, 100, 12659–12673.

Baker, P.E., 1972, Experiments on hydrocarbons gas hydrates in unconsolidated sand, in: Kaplan, I.R., (ed)., Natural gases in marine sediments, Plenum Press, New York, 227–234.

Bangs, N.L.B., Sawyer, D.S., and Golovchenko, X., 1993, Free gas at the base of the gas hydrate zone in the vicinity of the Chile triple junction, Geology, 21, 905–908.

Booth, J., Winters, W., and Dillon, W., 1994, Circumstantial evidence of gas hydrate and slope failure associations on the US Atlantic continental margin, Annals of the New York Academy of Sciences, 75, 487–489.

Booth, J.S., Winter W.J., Dillon, W.P., Clennell, M.B., and Rowe, M.M., 1998, Major occurrences and reservoir concepts of marine clthrate hydrates: Implications of field evidence, in: Henriet, J.P., and Mienert, J., (ed)., Gas hydrate: relevance to world margin stability and climate change, Geological Society Special Publication, London, 137, 113–127.

Brent, C.,Mienert, J., Venneste, M., Bunz, S., and Bryan, P., 2002, Submarine slope-failures offshore Norway triggers rapid gas hydrate decomposition, in: Proceedings the Fourth International Conference on Gas Hydrates, Yokohama, Japan, May 19–23, 71–74.

Brooks, J.M., Kennicutt, M.C., III, Fay, R.R., McDonald, T.J., and Sassen R., 1984, Thermogenic gas hydrates in Gulf of Mexico, Science, 225, 409–411.

Bugge, T., Elvebakk, G., Fanavoll, S., Mangerud, G., Smelror, M., Weiss, H.M., Gjelberg, J., Kristensen, S.E., and Nilsen, K., 2002, Shallow stratigraphic drilling applied in hydrocarbon exploration of the Nordkapp Basin, Barents Sea, Marine and Petroleum Geology, 19, 13–37.

Bunz, S., Mienert, J., and Brent, C., 2003, Geological controls on the Storegga gas-hydrate system of mid-Norwegian continental margin, Earth and Planetary Science Letters, 209, 291–307.

Carroll, J.J., 2003, Natural gas hydrates: A guide to engineers, Gulf Professional Publishing, 565 Amsterdam, The Netherlands, pp 270.

Carroll, J.J., and Mather, A.E., 1991, Phase equilibrium in the system water hydrogen sulphide: Hydrate-forming conditions, Canadian Journal of Chemical Engineering, 69, 1206–1212.

Chand, S. Mienert, J., Andreassen, K., Knies, J., Plassen, L., and Fotland, B., 2008, Gas hydrate stability zone modelling in areas of salt tectonics and pockmarks of the Barents Sea suggests an active hydrocarbon venting system, Marine and Petroleum Geology, 25, 625–636.

Chow, J., Lee, J.S., Sun, R., Liu, C.S., and Lundberg, N., 2000, Characteristics of the bottom simulating reflectors near mud diapers: offshore southwestern Taiwan, Geo-Marine Letters, 20, 3–9.

Claypool, G.E., and Kaplan, I.R., 1974, The origin and distribution of methane in marine sediments, in: Kaplan, I.R., (ed)., Natural gases in marine sediments, Plenum Press, New York, 99–139.

Council of Canadian Academies, 2008, Energy from gas hydrates: Assessing the opportunities and challenges for Canada,180 Elgin Street, Ottawa, ON Canada K2P 2K3.

Davie, M.K., and Buffet, B.A., 2001, A numerical model for the formation of gas hydrates below the seafloor, Journal Geophysical Research, 106, 497–514.

Davie, M.K., and Buffett, B.A., 2003, Sources of methane for marine gas hydrate: inferences from a comparison of observation and numerical models, Earth and Planetary Science Letters, 206, 51–63.

Davie, M.K., Zatsepina, O.Y., and Buffet, B.A., 2004, Methane solubility in marine hydrate environment, Marine Geology, 203, 117–184.

Dickens, G.R., and Quinby-Hunt, M.S., 1994, Methane hydrate stability in seawater, Geophysical Research Letters, 21, 2115–2118.

Dillon, W.P., and Paull, C.K., 1983, Marine gas hydrates-II: Geophysical evidences, in: Cox, J.I. (ed)., Natural gas hydrates: Properties, occurrence and recovery, Butterworth, Boston, 73–90.

Dillon, W.P., and Max, M.D., 2003, Oceanic gas hydrate, in: Max, M.D., (ed)., Natural gas hydrate in oceanic and permafrost environments, Kluwer, London, 61–76.

Dillon, W.P., Grow, J.A., and Paull C.K., 1980, Unconventional gas hydrate seals may trap gas off southeast US, Oil and Gas Journal, 78,124–130.

Duan, Z.H., and Mao, S.D., 2006, A thermodynamic model for calculating methane solubility, density and gas phase composition of methane-bearing aqueous fluids from 273 to 523 K and from 1 to 2000 bar, Geochemica Cosmochemica Acta, 70, 3369–3386.

Engle, P., and Bishnoy, P.R., 1988, Predication of gas hydrate formation conditions in aqueous electrolyte solutions, American Institute of Chemical Engineers Journal, 34, 1718–1721.

Fortes, A.D., and Stofan, E.R., 2005, Clathrate formation in the Near_Surface environment of Titan, Lunar Planet Science Conference, 26, 1123.

Ginsburg, G.D., and Soloviev, V.A., 1997, Methane migration within the submarine gas-hydrate stability zone under deep-water conditions, Marine Geology, 127, 49–57.

Grevemeyer, I., Rosenberger, A., and Villinger, H., 2000, Natural gas hydrates on the continental slope off Pakistan: Constraints from seismic techniques, Geophysical Journal International, 140, 295–310.

Haq, B.U., 1998, Natural gas hydrates: searching for long-term climatic and slope-stability records, in: Henriet, J.P., and Mienert, J., (eds)., Gas hydrates relevance to world margin stability and climate change, 303–318.

Helgerud, M.B., Dvorkin, J., and Nur, A., 1999, Elastic-wave velocity in marine sediments with gas hydrates: Effective medium modeling, Geophysical Research Letters, 26, 2021–2024.

Holbrook, W.S., Hoskins, H., Wood, W.T., Stephen, R.A., and Lizzarralde, D., 1996, Methane gas-hydrate and free gas on the Blake Ridge from vertical seismic profiling, Science, 273, 1840–1843.

Hovland, M., Gallagher, J.W., Clennell, M.B., and Lekvam, K., 1997, Gas hydrate and free gas volumes in marine sediments: Example from the Niger Delta front, Marine and Petroleum Geology, 14, 245–255.

Hyndman, R.D., and Davis, E.E., 1992, A mechanism for the formation of methane hydrate and seafloor bottom simulating reflector by vertical fluid expulsion, Journal of Geophysical Research, 97, 7025–7041.

Hyndman, R.D., Spence, G.D., Chapman, R., Riedel, M., and Edwards, R.N., 2001, Geophysical studies of marine gas hydrates in Northern Cascadia, in: Paul, C.K., and Dillon, W.P., (eds)., Natural gas hydrates: Occurrence, distribution, and detection, American Geophysical Union, Washington DC, 273–295.

Kleinberg, R.L., 2004, Quantitative assessment of submarine slope stability, Abstracts: AAPG Hedberg Research Conference Gas hydrates: Energy resource potential and associated geologic hazards, September 12–16, Vancouver, BC, Canada.

Krey, V., et al., 2009, Gas hydrates: entrance to methane age or climate threat, Environmental Research Letters, 4, 034007 doi:10.1088/1748-9326/4/3/034007.

Kvenvolden, K.A., 1988, Methane hydrates and global climate, Global Biological Cycles, 2, 221–229.

Kvenvolden, K.A., 1993a, Gas hydrates–geological perspective and global change, Review of Geophysics, 31, 173–187.

Kvenvolden, K.A., 1993b, A primer on gas hydrates, in: Howell, D.G., (ed)., The future of energy gases U.S., Geological Survey Professional Paper 150, Washington United States Government Printing Office, 279–291.

Kvenvolden, K.A., 1998, A primer on the geological occurrence of gas hydrates in: Henriet, J.P., and Mienert, J. (eds)., Relevance to world margin stability and climate change, Geological Society Special Publication, London, 137, 9–30.

Kvenvolden, K.A., 2003, Natural gas hydrate: background and history of discovery, in: Max, M. D., (ed)., Natural gas hydrate in oceanic and permafrost environments, Kluwer, London, 9–16.

Kvenvolden, K.A., and Kastner, M., 1990, Gas hydrate in Peruvian outer continental margin, in: Suess, E., and von Huene, R., et al., (eds)., Proceeding of Ocean drilling Program, Scientific Results, College Station, TX, Ocean Drilling Program, 112, 517–526.

Lamarque, J.F., 2008, Estimating the potential for methane clathrate instability in the 1%- CO_2 IPCC AR-4 simulations, Geophysical Research Letters, 35, L19806.

Longhi, J., 2006, Phase equilibrium in the system Co2-H2O: Application to Mars, Journal of Geophysical Reseach, 111, E06011, doi: 10.1029/2005JE002552.

Lu, H., Seo, Y.T., Lee, J.W., et al., 2007, Complex gas hydrates from Cascadian margin, Nature, 445, 303–306.

Lunine, J.I., and Stevenson, D.J., 1987, Clathrate and ammonia hydrates at high pressure: Application to origin of methane on Titan, Icarus, 70, 61–77.

MacDonald, G.J., 1990, The future of methane as an energy resource, Annual Review of Energy, 15, 53–83.

Macleod, M.K., 1982, Gas hydrates in ocean bottom sediments, AAPG Bulletin, 66, 2649–2662.

Maslin, M., Owen, M., Day, S., and Long, D., 2004, Linking continental-slope failures and climate change: Testing the clathrate gun hypothesis, Geology, 32, 53–56.

Matthew, J.H., Saffer, D.M., and Holbrook, W.S., 2004, Critically pressured free-gas reservoirs below gas-hydrate provinces, Nature, 427, 142–144.

Max, M.D., 2003, Gas hydrates potential of the Indian sector of NE Arabian Sea and Northern Indian Ocean, in: Max, M.D., (ed)., Natural gas hydrate in oceanic and permafrost environments, Kluwer, London, 213–224.

Max, M.D., and Dillon, W.P., 1998, Oceanic methane hydrate: Character of the Blake Ridge hydrates stability zone and potential for methane extraction, Journal of Petroleum Geology, 21,343–358.

McIver, R.D., 1981, Role of naturally occurring gas hydrates in sediment transport, AAPG Bulletin, 66, 789–792.

Mienert, J., Andreassen, K., Posewang, J., and Lukas, D., 2000, in: Holder, G.D., and Bishnoi, P.R., (eds)., Gas hydrates: Challenges for the future, New York Academy of Sciences, New York, 200–210.

Miller, A.T., 1996, (ed.), Proc ODP Init. Rep. Leg 164, 179–198.

Minshull, T., and White, R., 1989, Sediment compaction and fluidmigration in the Makran accretionary prism, Journal of Geophysical Research, 94, 7387–7402.

Minshull, T.A., Singh, S.C., and Westbrook, G.K., 1994, Seismic velocity structure at a gas hydrate reflector, offshore western Columbia, from full waveform inversion, Journal of Geophysical Research, 99, 4715–4734.

Niemann, H., et al., 2005, The Cassini_Hygen probe gas chromatograph mass spectrometer (GCMS) experiment first results, LPSC conference, Houston, Texas, Abstract, 14–18.

Nisbet, E.G., 1990, The end of ice age, Canadian Journal of Earth Sciences, 27, 148–157.
Nisbet, E.G., and Piper, D.J.W., 1998, Giant submarine landslides, Nature, 392, 329–330.
Nixon, M.F., and Grozic, L.H., 2006, A simple model for submarine slope stability analysis with gas hydrates, Norwegian Journal of Geology, 86, 309–316.
Osegovic, J.P., and Max, M.D., 2005, Compound clathrate hydrate on Titan's surface, Journal of Geophysical Research, 110, E08004, doi:10.1029/2005JE002435.
Osegovic, J.P., Tatro, S.R., and Holman, S.A., 2006, Physical chemical characteristics of natural gas hydrates, in: Max, M.D., Johnson, A.H., and Dillon, W.P., (eds)., Economic geology of natural gas hydrates, 45–104.
Paull, C.K., Ussler, W., III., and Dillon, W., 1991, Is the extent of glaciation limited by marine gas hydrates?, Geophysical Research Letters, 18, 432–434.
Paull, C.K., Ussler, W., III, and Boroski, W.S., 1994, Sources of biogeneic methane to form gas hydrates, in: Sloan, E.D., Happel, J., and Hnatow, M.A., (eds)., Natural gas hydrates, New York Academy of Sciences, New York, 335–347.
Pecher, I.A., Minshull, T.A., Singh, S.C., and von Huene, R., 1996, Velocity structure of a bottom simulating reflector offshore Peru: Results from full waveform inversion, Earth and Planetary Science Letters, 139, 459–469.
Peltzer, E.T., and Brewer, P.G., 2003, Practical physical chemistry and empirical predictions of methane hydrate stability, in: Max, M.D., (ed)., Natural gas hydrate in oceanic and permafrost environments, Kluwer, London, 17–28.
Puall, C.K., Ussler III, W., and Dillon, W,P., 2003, Potential role of gas hydrate decomposition in generating submarine slope failures, in: Max, M.D., (ed)., Natural gas hydrate in oceanic and permafrost environments, Kluwer, London, 149–156.
Ruppel, C., Dickens, G.R., Castellini, D.G., Gilhooly, W., and Lizarralde, D., 2005, Heat and salt inhibition of gas hydrate formation in the northern Gulf of Mexico, Geophysical Research Letters, 32, L04605.
Sain, K., Minshull, T.A., Singh, S.C., and Hobbs, R.W., 2000, Evidence for a thick free gas layer beneath the bottom simulating reflector in the Makran accretionary prism, Marine Geology, 164, 3–12.
Schiermeier, Q., 2008, Fears surface over methane leaks, Nature, 455, 572–573.
Scholl, D.W., and Hart, P.E., 1993, The future of energy gases. Prof. Pap. US Geol. Surv., 331–351.
Shine, K., Derwent, R., Wubbles, D., and Morcrette, J.J., 1990, Radiative forcing of climate, in: Houghton, J., Jenkins G., Ephraums, J., (eds)., Climate change, the IPCC, scientific assessment, Cambridge University Press, Cambridge, 41–68.
Sloan, E.D., and Koh, C.A., 2008, Clathrate hydrates of the natural gases, 3rd Ed. CRC Press, Boca Raton, FL.
Sloan, E.D., 1990, Clathrate hydrate of natural gases, Marcel Dekker, New York, pp 641.
Sloan, E.D., 1998, Clathrate hydrate of natural gases, Marcel Dekker, New York, pp 705.
Soloviev, V.A., and Ginsburg, G.D., 1994, Formation of submarine gas hydrates. In: Jorgensen, N., (ed)., Gas in marine sediments, Bulletin of the Geological Society of Denmark, Copenhagen, 41, 86–94.
Summerhayes, C.P., Bornhold, B.D., Embley, R.W., 1979, Surficial slides and slumps on the continental slope and rise of South West Africa: A reconnaissance study, Marine Geology, 31, 265–277.
Taylor, C., 2002, Formation studies of methane hydrates with surfactants, 2nd International Workshop on Methane Hydrates, October, Washington, Abstract.
Taylor, M.H., Dillon, W.P., and Pecher, I.A., 2000, Trapping and migration of methane associated with gas hydrate stability zone at Blake Ridge Diapir:New insights from seismic data, Marine Geology, 18, 209–221.
Thomsen, R.O, and Lerche, I., 1991, Salt diapir velocity assessment from temperature and thermal indicator anomalies: Application to Lulu-1, Danish North Sea, Terra Nova, 3, 500–509.
Tinivella, U., Lodolo, E., Camerlenghi, A., and Boehm, G., 1998, Seismic tomography study of a bottom simulating reflector off the South Shetland Islands (Antarctica), in: Henriet, J.P.,

and Mienert, J., (eds)., Gas hydrates: Relevance to world margin stability and climate chance, The Geological Society, London, 141–151.
Tishchenko, P., Hensen, C. Wallmann, K., and Wong, C.H., 2005, Calculation of the stability and solubility of methane hydrate in seawater, Chemical Geology, 219, 37–52.
Watson, R., Rodhe, H., Oeschger, H., and Siegenthaler, U., 1990, Greenhouse gases and aerosols, in: Houghton, J., Jenkins G., and Ephraums, J., (eds)., Climate change, the IPCC, scientific assessment, Cambridge University Press, Cambridge, 1–40.
Westbrook, G.K., et al., 2009, Escape of methane gas from the seabed along the West Spitsbergen continental margin, Geophysical Research Letters, 36, L15608.
White, R.S., 1977, Seismic bright spots in the Gulf of Oman, Earth and Planetary Science Letters, 37, 29–37.
White, R.S., 1979, Gas hydrate layers trapping free gas in the Gulf of Oman, Earth and Planetary Science Letters, 42, 114–120.
Wright, J.F., and Dallimore, S.R., 2004, Pressure-temperature-salinity influence on gas hydrate stability in sediments of the Mallik Gas Hydrate Reservoir, Mackenzie Delta, Canada, AAPG Hedberg Conference 'Gas hydrates resource potential and associated geological hazards', Extended Abstract, September 12–16, Vancouver, BC, Canada.
Xu, W., and Ruppel, C.D., 1999, Predicting the occurrence, distribution and evolution of methane gas hydrate in porous marine sediments, Journal Geophysical Research, 104, 5081–5095.
Yamano, M., Uyeda, S., Aoki, Y., and Shipley, T., 1982, Estimates of heat flow derived fromgas hydrates, Geology, 10, 339–343.
Zatsepina, O.Y., and Buffet, B.A., 1997, Phase equilibrium of gas hydrate: implication for the formation of hydrate in the deep sea floor, Geophysical Research Letters, 24, 1567–1570.
Zhang, Y., and Xu, Z., 2003, Kinetics of convective crystal dissolution and melting, with application to methane hydrate dissolution and dissociation in seawater, Earth and Planetary Science Letters, 213, 133–148.
Zwart, G., Moore, J.C., and Cochrane, G.R., 1996, Variation in temperature gradients indentify active faults in the Oregon accretionary prism, Earth and Planetary Science Letters, 139, 485.

Chapter 5
Geological Indicators

Abstract Marine sediments on the continental slopes require appropriate thickness of sea, methane-generating potential and suitable pressure–temperature regime in order to host gas hydrates. In addition to pressure and geothermal gradient other variables affecting the stability of gas hydrates are the hydrothermal gradient, sediment's thermal conductivity, and heat flow. Other variables such as gas composition, migration pathways for gas and water, seals and reservoir rocks, and pore water salinity are also important for establishing the stability zone for hydrates. Gas hydrate rich provinces can be characterized by different geological indicators like development of hydrate mounds, pockmark depressions, mud volcanism, fault structures and fracture zones. These geological processes can shape a potential gas hydrate reservoir. Field evidence indicates that anomalously warm, presumably methane rich fluids can rise as conduits in the gas hydrate areas. This chapter presents a review and synthesis of the tectono-sedimentary controls on gas hydrate occurrence and aim to establish geological framework for the occurrence of gas hydrates in the continental margins.

5.1 Introduction

Understanding methane hydrate formation is vital for energy potential (Spence et al. 2003), in deep water drilling, in geological mass flow mechanisms, in the global carbon cycle (Kennett 2002; Haq 2003), in separation processes, and in flow assurance of the hydrocarbon transportation systems (Sloan 1998). At low temperature and moderate pressure, they are encountered in Earth in permafrost regions and at moderate temperature and high pressure in submarine sediments. As a result of tectonic deformation, compaction, porosity reduction and dewatering of the sedimentary sequences, gas hydrates reflect the migration of fluids and gas towards seabed (Kvenvolden 1993). Formation of gas hydrates within the stability zone requires that methane, supplied by in situ microbial methanogenesis, migrating fluids, and diffusion from depth. The occurrence of methane hydrate at or near the

N.K. Thakur and S. Rajput, *Exploration of Gas Hydrates*,
DOI 10.1007/978-3-642-14234-5_5,

seafloor indicates active upward advection of methane-rich fluids or methane gas. It has been observed that in advective flow environment, in the absence of source from depth, the rate at which methane is flushed from the gas-hydrate stability zone (GHSZ) exceeds the rate of in situ biogenic production (Xu and Ruppel 1999). Therefore, in order to form hydrate in advective flow systems, additional methane must be supplied by the migrating fluids. To understand the mechanism better, of fluid transport, the characterization of fault and fracture network is very important. These may be influenced by stress state, overpressure and sediment physical properties.

The fine-grained material and the reduction in pore size and water content of formation sediments, could prevent gas hydrate formation. If the gas hydrates do not cement sediment grains enough, their shear resistance may decrease thus affecting the stability of the slope. In this case, the hydrates are more likely to form within the pore spaces as part of the sediments. Over the continental margins the hydrate stability zone becomes shallow gradually, and the limit of stability is often marked by the occurrence of gas venting features such as pockmarks (Buenz et al. 2005). Another important geological feature is "mound", which sometimes may be associated with the occurrence of gas hydrates. In some continental margins the regional distribution of mounds is associated with the occurrence of gas hydrates and submarine landslides suggest a genetic relationship between them (e.g. Talukder et al. 2008). The common geological process is "fluid flow" that delivers and distributes necessary methane to form gas hydrates. High seafloor methane fluxes are associated with the mud volcanoes as well as with the accompanying cold vents and seeps (Charlou et al. 2003; Paull et al, 2000; Schnuele and Wang 1998; Suyehiro 1990). Changes in the GHSZ may alter the slope stability of continental margins (Kvenvolden 1993; Mienert et al. 1998; Paull et al. 1995; Barker 1982; Barker and Austin 1994; Barnes et al., 2009). Because of decreasing permeability of the sediments, gas hydrates could also inhibit the compaction trend in sediments and fluid migration to the surface. Geological and tectonic-sedimentary controls can not be generalized in terms of geological framework for gas hydrate occurrence as they occur worldwide in different geological provinces. This question can be best addressed on regional basis.

5.2 Geological Indicators

Field studies indicate that the geological evidences for gas hydrates are present all over the world on continental margins (Fig. 5.1). On seismic sections the presence of gas hydrate can be identified by the presence of Bottom Simulating Reflectors (BSRs). A classic example of an identified BSR from Hydrate Ridge, offshore USA is illustrated in Fig. 5.2. These reflectors are characterized by large amplitude and reversed polarity compared with the sea-bottom reflection. Most BSR occur due to high acoustic impedance contrast between gas hydrates and associated free gas underneath. They are roughly parallel to the topography of the sea floor and produce a similar reflection with change in polarity. The distribution of the BSR allows to infer the processes that govern the growth and distribution of gas hydrates over

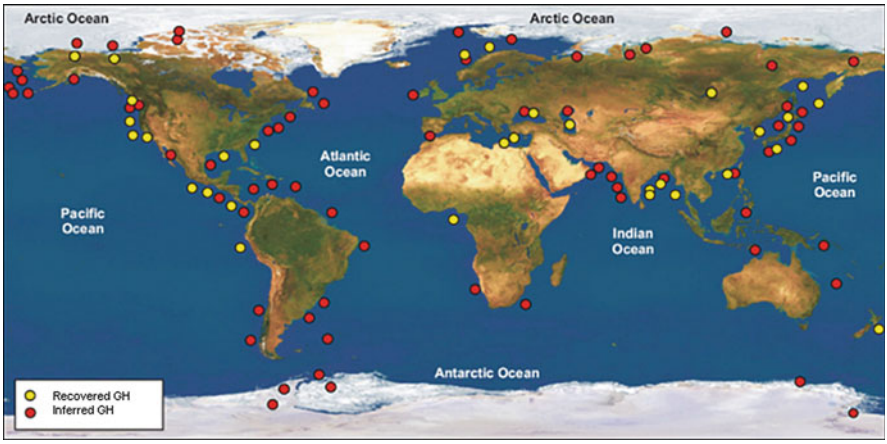

Fig. 5.1 Location of known and inferred gas hydrate occurrences in deep marine and arctic permafrost environments. Courtesy of Council of Canadian Academics
Source: http://www.scienceadvice.ca/uploads/eng/assessments and publications and news releases/hydrates

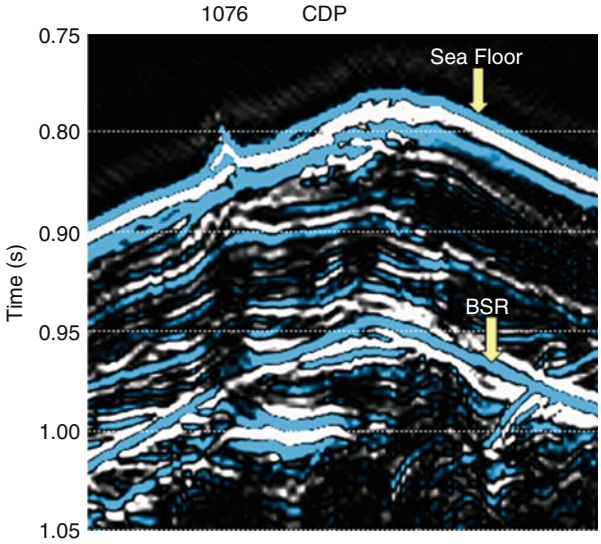

Fig. 5.2 A classic example of identified BSR from Hydrate Ridge Offshore USA. (After Rajput 2009, reproduced with permission)

continental margins. In-order to establish a geological framework for the region where gas hydrates are found; one needs to study the distribution and variability of BSR, sediment deposition and distribution, diapirism, fluid-migration features. There are different geological indicators which help in studying the gas hydrate provinces. These indicators have been found worldwide and explained here under;

5.2.1 Distribution and Variability of BSR

The geologic and geodynamic setting of gas hydrate prone regions exert definite controls on the formation of a BSR and the inferred distribution of gas hydrates. In general, A BSR cut across the stratigraphy of sediments, and its position is relatively sub-parallel to the sea floor. However, the depth between the sea floor and the BSR is irregular. Baba and Yamada (2004) and Lin et al. (2009) describes the BSRs according to their relationship to topography, structural features, and relative position to the geological elements. Based on the (Baba and Yamada 2004; Lin et al. 2009) classification scheme with real and synthetic data examples are discussed here;

5.2.1.1 Ridge-Type BSR

Ridge-type BSRs occur mainly in the upper levels of accretionary wedges at sedimentary plate boundaries, which are formed due to accreted sediments on the over riding plate at a convergent plate boundary. This type of structure is termed as accretionary wedge or accretionary prism. This indicates that the BSR develops within a compressional structure cored by anticlines or thrust faults. Ridge-type BSR can be further categorised into four classes:

Class I: BSRs in Anticlinal Ridge Structures

This type of BSR develops beneath the crest of an active anticlinal ridge. The areal extent of this BSR type is far more widespread than other ridge-type BSRs. The schematic illustration of this BSR is shown in Fig. 5.3a. On a synthetic shot gathers it can be visualized as a reverse polarity event (Fig. 5.3b). A very good example of anticlinal ridge structure BSR (Fig. 5.4) is found in the incipient arc-continent collision zone off southwest Taiwan and studied by Lin et al. 2009.

Class II: BSRs in Buried-Anticline Structures

Buried-anticline types BSRs are found beneath inactive anticlinal structures, which are covered by more or less horizontal strata and show no geomorphic surface expression. Thus, the BSR cuts across the sedimentary strata in both inclined limbs of inactive anticlines because the BSR is sub-parallel to the overlying and flat seabed. The schematic illustration and synthetic seismograms related to the BSR occurred in buried-anticline structures are shown in Fig. 5.5a, b. One field data example for this class from off southwest Taiwan is shown in Fig. 5.6 (Lin et al. 2009).

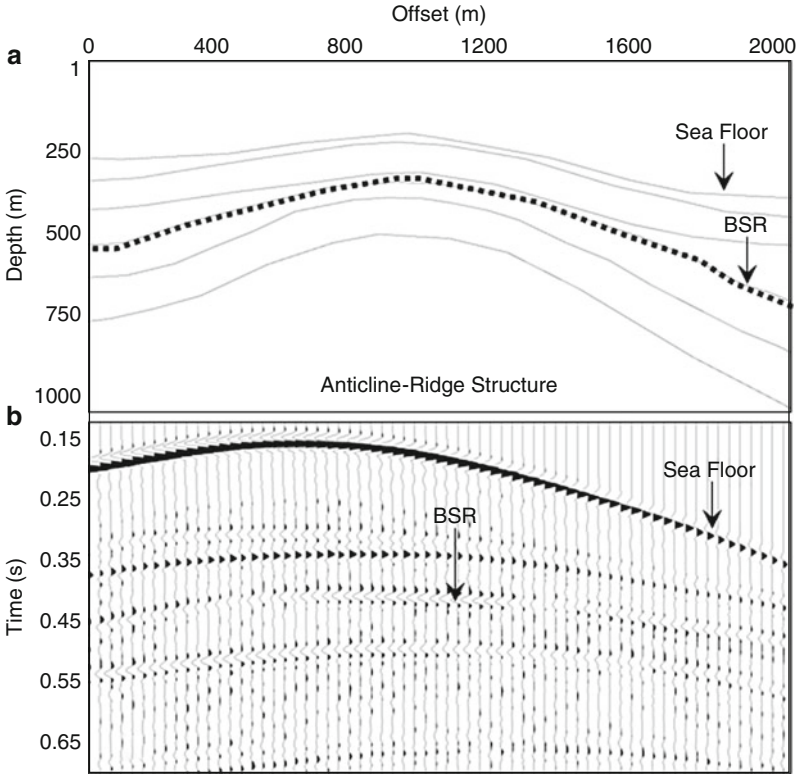

Fig. 5.3 Schematic illustration of Anticline-Ridge structure and corresponding seismic data simulated with finite difference scheme. (**a**); Anticline-Ridge structure BSR denoted by black dotted line. (**b**) BSR corresponding to "Fig. 5.3a" is identified as a reverse polarity event on simulated data

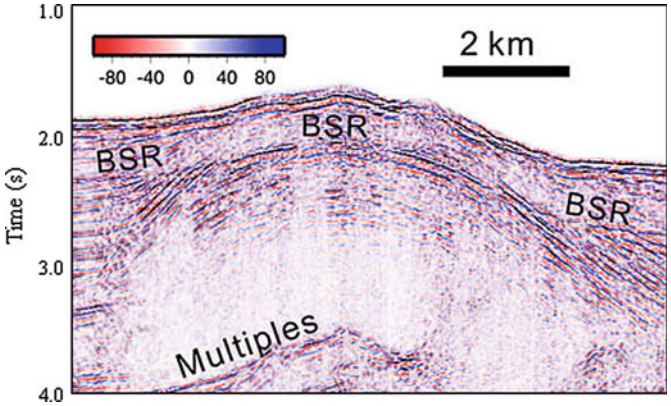

Fig. 5.4 Field data example of Anticline-Ridge structure BSR from incipient arc-continent collision zone off southwest Taiwan. The *red*-to-*blue* scale denotes the seismic amplitude. (After Lin et al. 2009, reprinted with the permission)

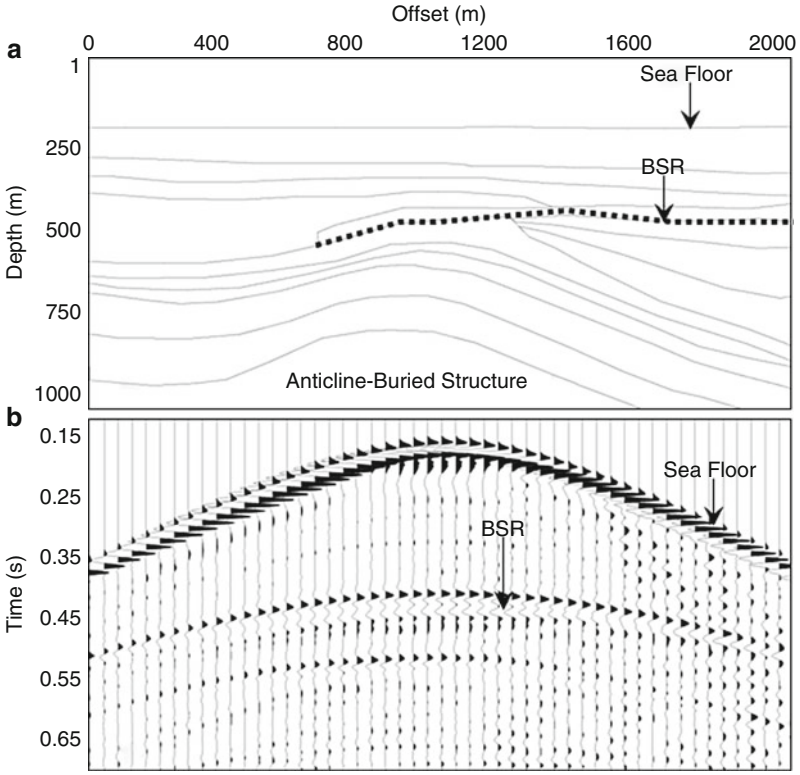

Fig. 5.5 Schematic illustration of Anticline-Buried structure and corresponding seismic data simulated with finite difference scheme. (**a**); Anticline-Buried structure BSR denoted by black dotted line. (**b**) BSR corresponding to "Fig. 5.5a" is identified as a reverse polarity event on simulated data

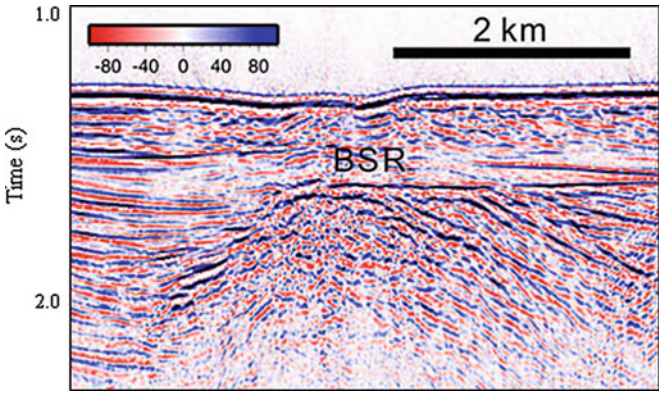

Fig. 5.6 Field data example of Anticline-Buried structure BSR from incipient arc-continent collision zone off southwest Taiwan. The *red*-to-*blue* scale denotes the seismic amplitude. (After Lin et al. 2009, reprinted with the permission)

Class III: BSRs in Thrusted-Ridge Structures

Thrusted-ridge structure BSRs develop in the hanging wall of the thrust fault that forms a bathymetric ridge. The schematic illustration and synthetic shot gather for BSR occurred in thrusted-ridge structure are shown in Fig. 5.7a, b, corresponding field data example off southwest Taiwan is shown in Fig. 5.8 (Lin et al. 2009).

Class IV: BSRs in Thrusted-Footwall Structures

BSRs occurrence in thrusted-footwall structures, in the footwall sediment strata of the thrust fault. The synthetic seismic data example for this class is shown in Fig. 5.9a, b and corresponding field data example from shot gather with off southwest Taiwan is shown in Fig. 5.10 (Lin et al. 2009).

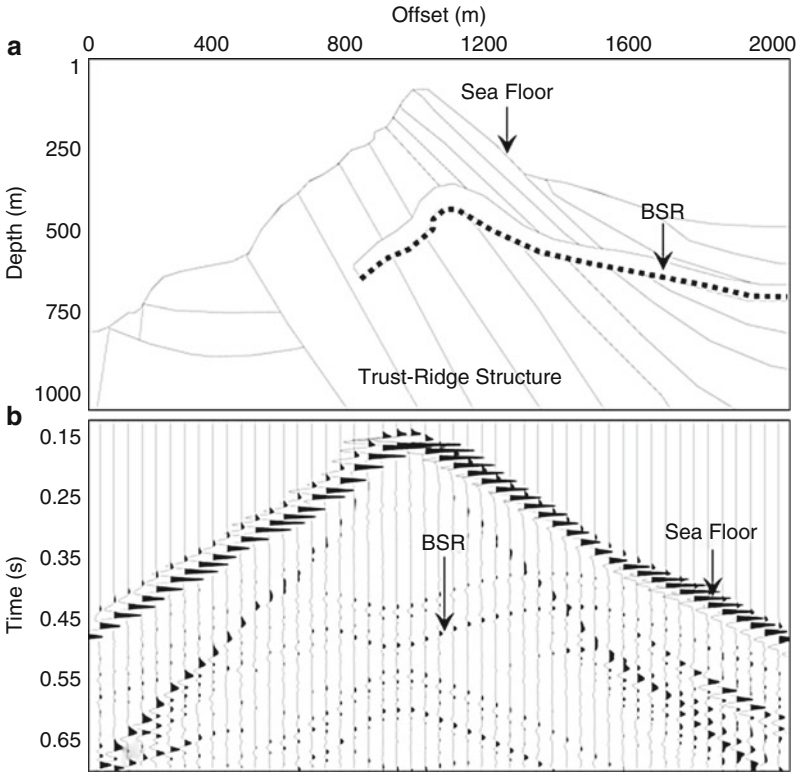

Fig. 5.7 Schematic illustration of Thrusted-Ridge structure and corresponding seismic data simulated with finite difference scheme. (**a**); Thrusted-Ridge structure BSR denoted by black dotted line. (**b**) BSR corresponding to "Fig. 5.7a" is identified as a reverse polarity event on simulated data

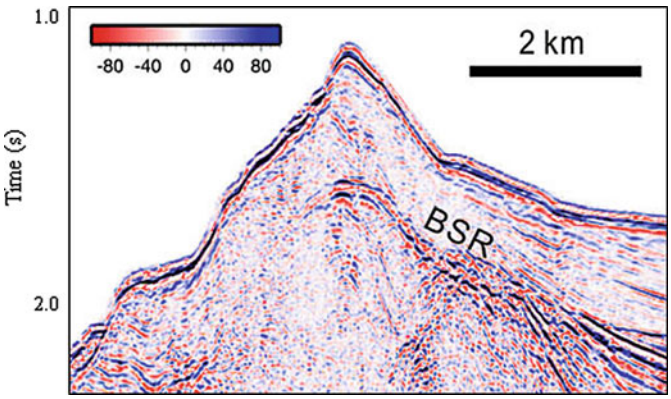

Fig. 5.8 Field data example of Thrusted-Ridge structure BSR from incipient arc-continent collision zone off southwest Taiwan. The *red*-to-*blue* scale denotes the seismic amplitude. (After Lin et al. 2009, reprinted with the permission)

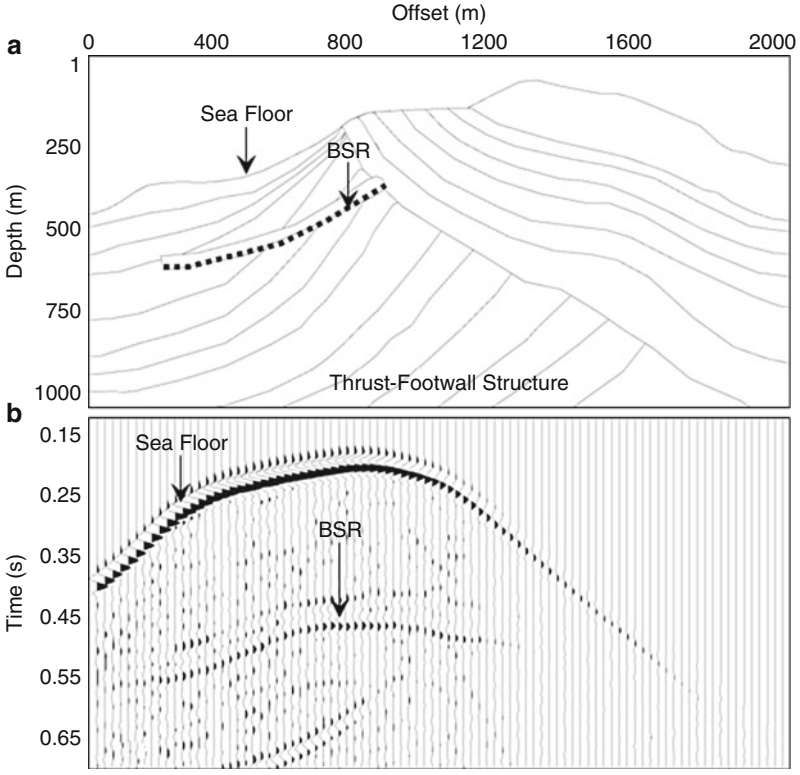

Fig. 5.9 Schematic illustration of Thrust-Footwall structure and corresponding seismic data simulated with finite difference scheme. (**a**) Thrust-Footwall structure BSR denoted by black dotted line. (**b**) BSR corresponding to "Fig. 5.9a" is identified as a reverse polarity event on simulated data

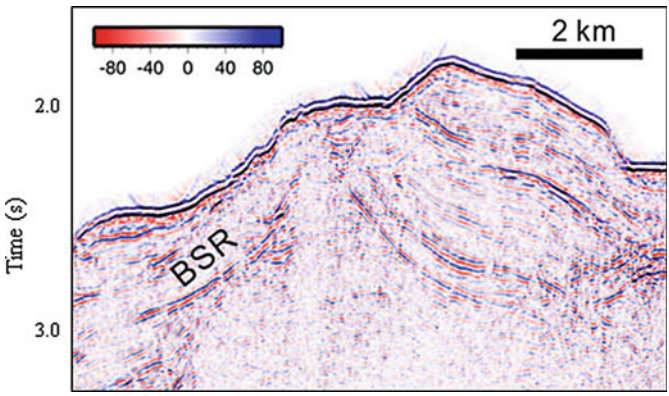

Fig. 5.10 Real data example of Thrust-Footwall structure BSR from incipient arc-continent collision zone off southwest Taiwan. The *red*-to-*blue* scale denotes the seismic amplitude. (After Lin et al. 2009, reprinted with the permission)

5.2.1.2 Basin-Type BSR

This class of BSRs occur along the margins of continental slope basins on the hanging wall of thrusts or in the interior of basins. Therefore the BSRs of this category could also be referred as basin-margin type (Figs. 5.11a, b and 5.12) and intra-basin type (Figs. 5.13a, b and 5.14). The synthetic seismic profile (Fig. 5.11b) and the real data example (Fig. 5.12) show that the dip angle of inclined beds in the margins of slope basins is higher than that in the interior of basins. From these facts, it is evident that the identification of BSR from sedimentary strata in the interior of basin is difficult as the reflections are also parallel to the seafloor. Therefore, the indicators of BSR in this type of conditions are the high amplitude and negative polarity events, which are parallel to the seafloor but crosscut the sedimentary stratal reflections so called intra-basin type BSR (Figs. 5.13 and 5.14) (Lin et al. 2009).

5.2.1.3 Submarine-Canyon Type BSR

BSRs have been recognized in the channel floors beneath submarine-canyons. It can be distinguished in Canyon-Floor and Canyon-margin type of BSR. They appear beneath canyons where the seafloor and underlying stratal reflections are discordant. The synthetic data example of canyon-floor type of BSR is illustrated in Fig. 5.15a, b. Such type of BSRs are difficult to recognize on shot gathers (Fig. 5.15b). There is an "apparent syncline" formed beneath an uplifted and abandoned channel. The apparent syncline is formed because the water velocity of seismic waves in the abandoned channel is lower than the sediment velocity in adjacent channel walls. Lin et al. (2009) has shown a very good real data example (Fig. 5.16). Tucker and Yorston (1973) coined the lateral velocity variation due to

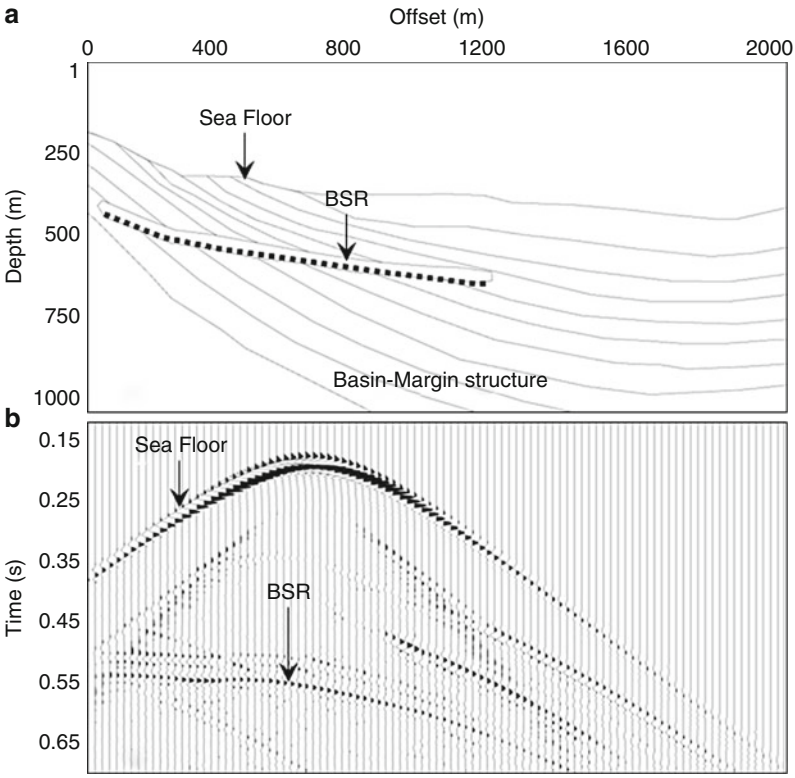

Fig. 5.11 Schematic illustration of Basin-Margin structure and corresponding seismic data simulated with finite difference scheme. (**a**) Basin-Margin structure BSR denoted by black dotted line. (**b**) BSR corresponding to "Fig. 5.11a" is identified as a reverse polarity event on simulated data

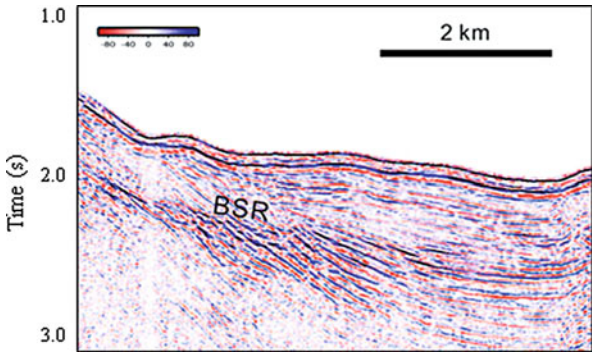

Fig. 5.12 Field data example of Basin-Margin structure BSR from incipient arc-continent collision zone off southwest Taiwan. The *red*-to-*blue* scale denotes the seismic amplitude. (After Lin et al. 2009, reprinted with the permission)

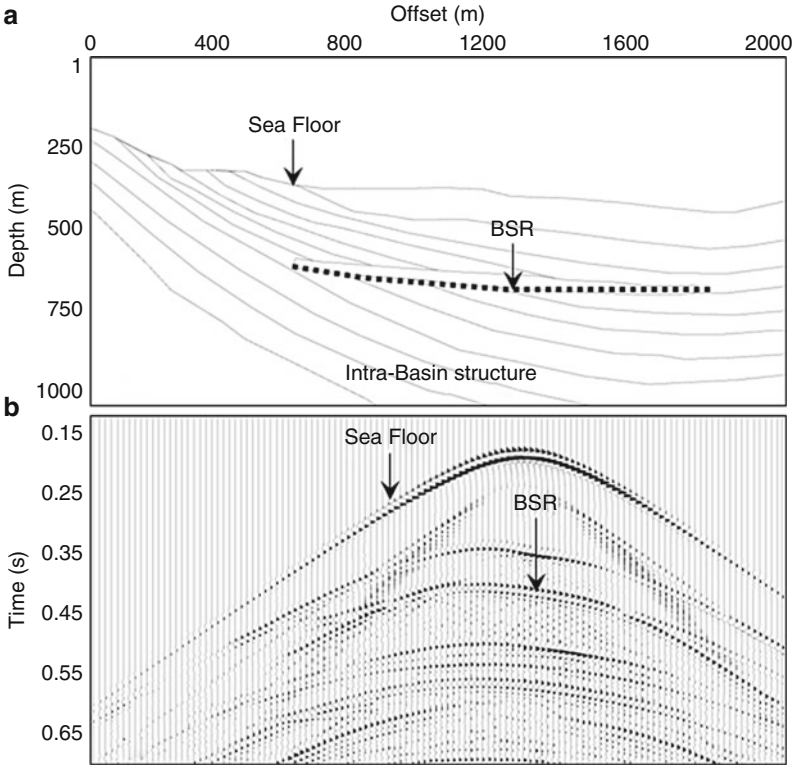

Fig. 5.13 Schematic illustration of Intra-Basin structure and corresponding seismic data simulated with finite difference scheme. (**a**) Intra-Basin structure BSR denoted by black dotted line. (**b**) BSR corresponding to "Fig. 5.13a" is identified as a reverse polarity event on simulated data

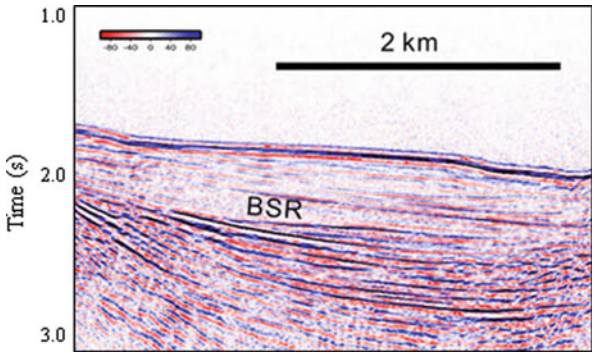

Fig. 5.14 Field data example of Intra-Basin structure BSR from incipient arc-continent collision zone off southwest Taiwan. The *red*-to-*blue* scale denotes the seismic amplitude. (After Lin et al. 2009, reprinted with the permission)

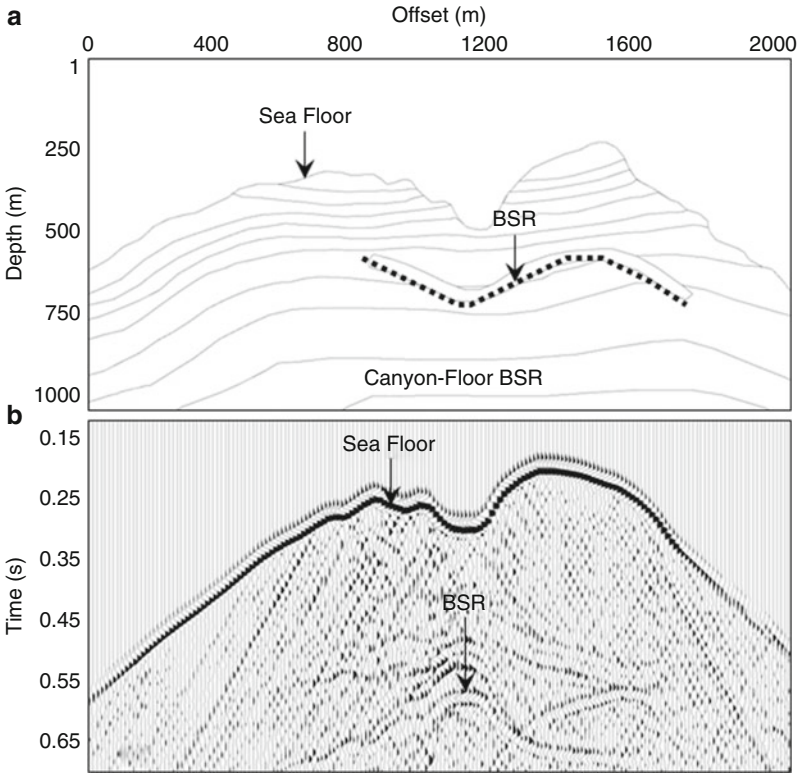

Fig. 5.15 Schematic illustration of Canyon-Floor structure and corresponding seismic data simulated with finite difference scheme. (**a**) Canyon-Floor structure BSR denoted by black dotted line. (**b**) BSR corresponding to "Fig. 5.15a" is identified as a reverse polarity event on simulated data

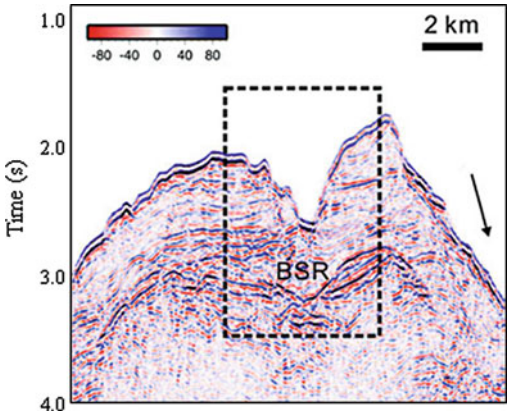

Fig. 5.16 Real data example of Canyon-Floor structure BSR from incipient arc-continent collision zone off southwest Taiwan. The *red*-to-*blue* scale denotes the seismic amplitude. (After Lin et al. 2009, reprinted with the permission)

channelling processes as "velocity anomaly", which often produces "apparent synclines" beneath channels. For this reason, the arrangement of these stratal reflections on the seismic section looks like a syncline; in fact, these strata may be parallel or even in an anticlinal form (Lin et al. 2009). Canyon-margin type of BSR develops on the sedimentary strata which dips away from the canyon axis as can be observed with synthetic data example (Fig. 5.17a, b). Lin et al. (2009) illustrated a good example of this kind of BSR (Fig. 5.18).

5.2.1.4 Continental Slope Type BSR

This BSR type is often located under erosional remnant ridges, but many BSRs are even found beneath erosional gullies. This type of BSR can be characterised into five different types as described by Lin et al. (2009): Slope–ridge type, Slope–trough type, Frontal slope-front-fill type, Erosional-ridge type, and Distal-slope

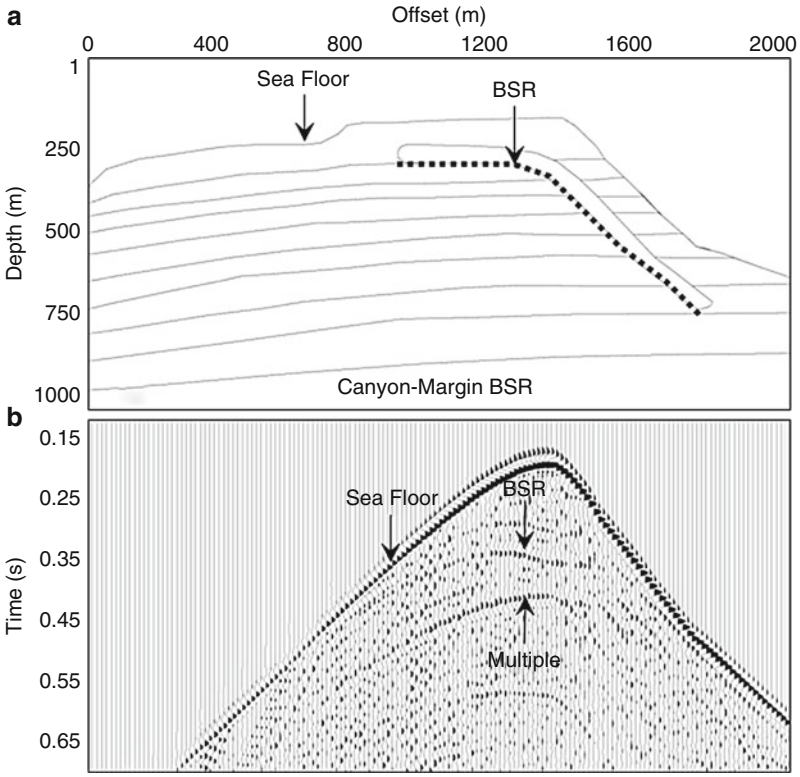

Fig. 5.17 Schematic illustration of Canyon-Margin structure and corresponding seismic data simulated with finite difference scheme. (**a**) Canyon-Margin structure BSR denoted by black dotted line. (**b**) BSR corresponding to "Fig.5.17a' is identified as a reverse polarity event on simulated data

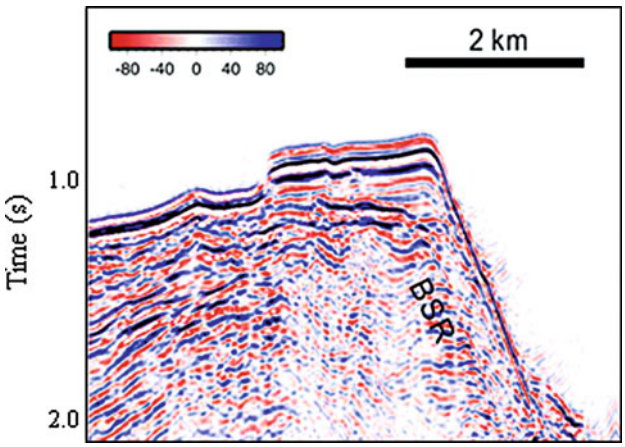

Fig. 5.18 Real data example of Canyon-Margin structure BSR from incipient arc-continent collision zone off southwest Taiwan. The *red*-to-*blue* scale denotes the seismic amplitude. (After Lin et al. 2009, reprinted with the permission)

type. The real and synthetic data examples illustrating these BSRs are shown from Figs. 5.19 to 5.28. In Slope–ridge (Figs. 5.19a, b and 5.20) BSR and Slope–trough (Figs. 5.21a, b and 5.22) type BSR inclined strata is being truncated beneath the slope and is associated with the oceanward-dipping normal faults. Whereas frontal slope-front-fill type BSR is situated between the area of slope front fill and continental slope as shown in Figs. 5.23a, b and 5.24. Erosional-ridge type (Figs. 5.25a, b and 5.26) and Distal-slope type (Figs. 5.27a, b and 5.28) occur mainly beneath remanant erosional ridges at shallower depth and beneath the distal slope respectively.

5.2.2 Sediment Deposition and Distribution

There are four hydrate morphologies disseminated, nodular, vein and massive (Malone 1985). Disseminated hydrate could be found within the pore space of the sediment where as Nodular, vein and massive hydrates are found in the sediments disturbed either by regional tectonic stresses or through the stress resulting from hydrate crystal growth (Long et al. 2009). Cook and Goldberg (2007) found hydrate bearing fractures to be oriented with respect to regional tectonic stresses offshore India. Theoretical work on hydrate formation (Clennell et al. 1999; Henry et al. 1999) explored the influence of capillary pressure and thermodynamics on hydrate growth and provided some physical constraints to hydrate morphology. This work concluded that the hydrate growth in fine-grained muds would be unlikely, and that coarser-grained sediments, exhibiting larger pores, would act as more likely hosts.

Theoretical studies suggested that the hydrate accumulation is controlled by the sediment deposition rate, nature of host sediment as much as by the presence of the

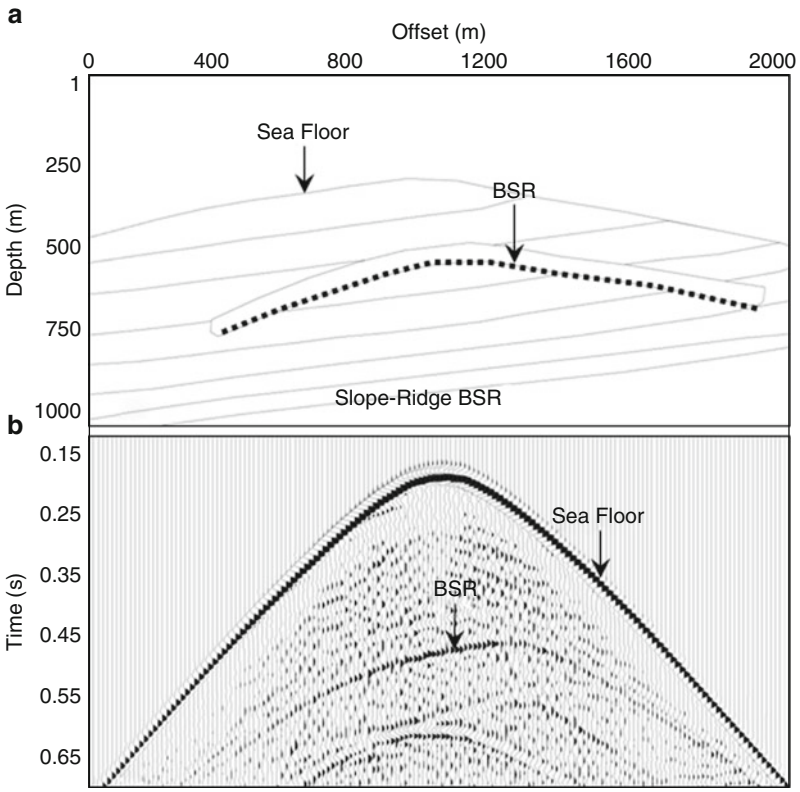

Fig. 5.19 Schematic illustration of Slope–Ridge structure and corresponding seismic data simulated with finite difference scheme. (**a**) Slope–Ridge structure BSR denoted by black dotted line. (**b**) BSR corresponding to "Fig. 5.19a" is identified as a reverse polarity event on simulated data

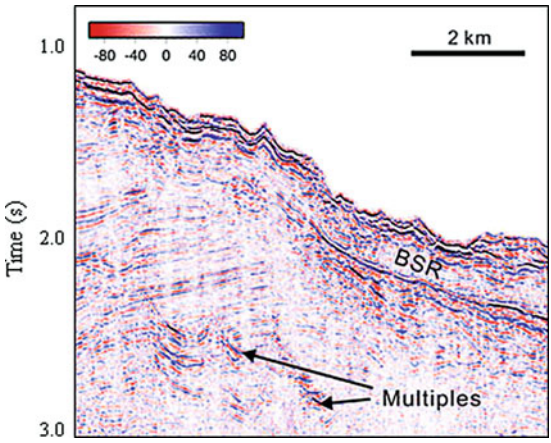

Fig. 5.20 Real data example of Slope–Ridge structure BSR from incipient arc-continent collision zone off southwest Taiwan. The *red*-to-*blue* scale denotes the seismic amplitude. (After Lin et al. 2009, reprinted with the permission)

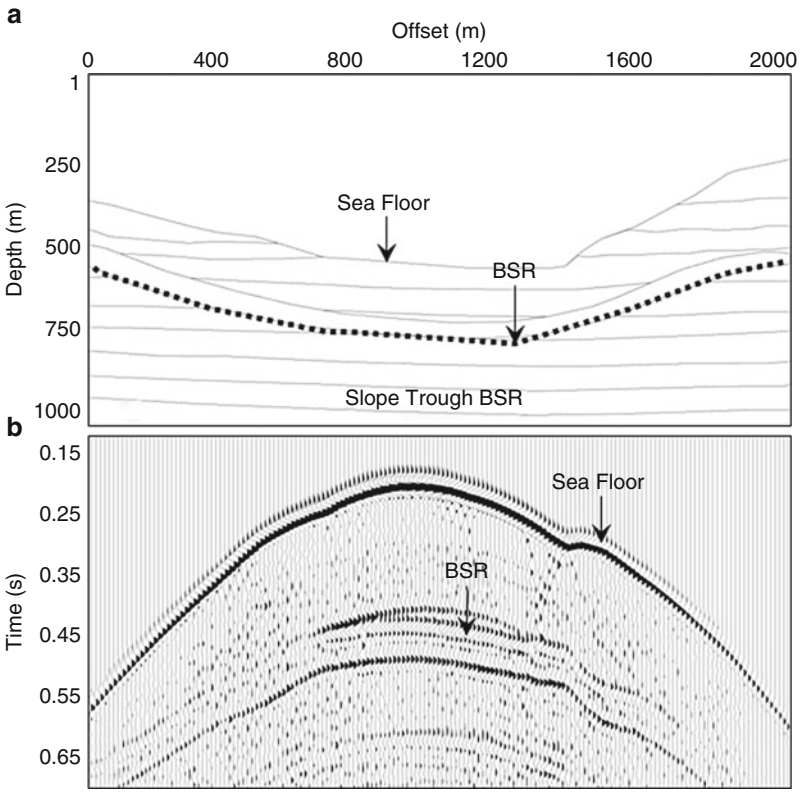

Fig. 5.21 Schematic illustration of Slope–Trough structure and corresponding seismic data simulated with finite difference scheme. (**a**) Slope–Trough structure BSR denoted by black dotted line. (**b**) BSR corresponding to "Fig. 5.21a" is identified as a reverse polarity event on simulated data

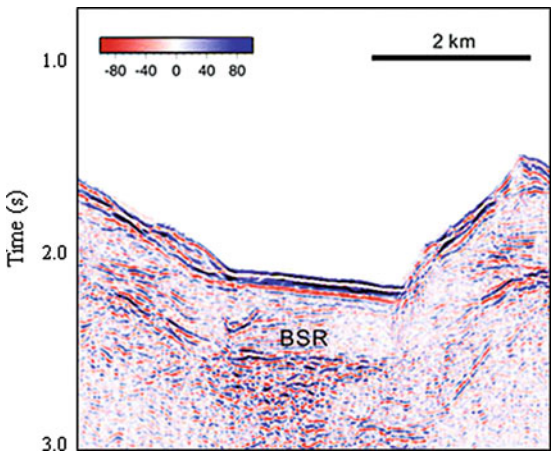

Fig. 5.22 Real data example of Slope–Trough structure BSR from incipient arc-continent collision zone off southwest Taiwan. The *red*-to-*blue* scale denotes the seismic amplitude. (After Lin et al. 2009, reprinted with the permission)

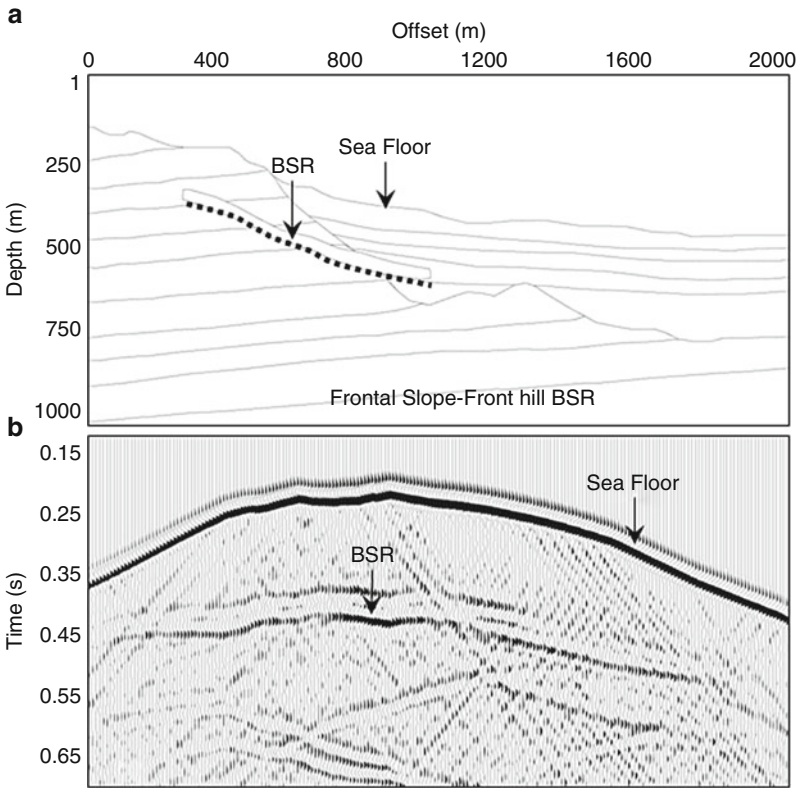

Fig. 5.23 Schematic illustration of Frontal Slope-Front Hill structure and corresponding seismic data simulated with finite difference scheme. (**a**) Frontal Slope-Front Hill structure BSR denoted by black dotted line. (**b**) BSR corresponding to "Fig. 5.23a" is identified as a reverse polarity event on simulated data

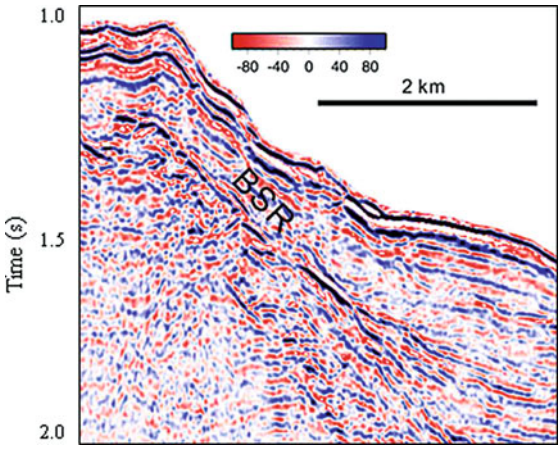

Fig. 5.24 Real data example of Frontal Slope-Front Hill structure BSR from incipient arc-continent collision zone off southwest Taiwan. The *red*-to-*blue* scale denotes the seismic amplitude. (After Lin et al. 2009, reprinted with the permission)

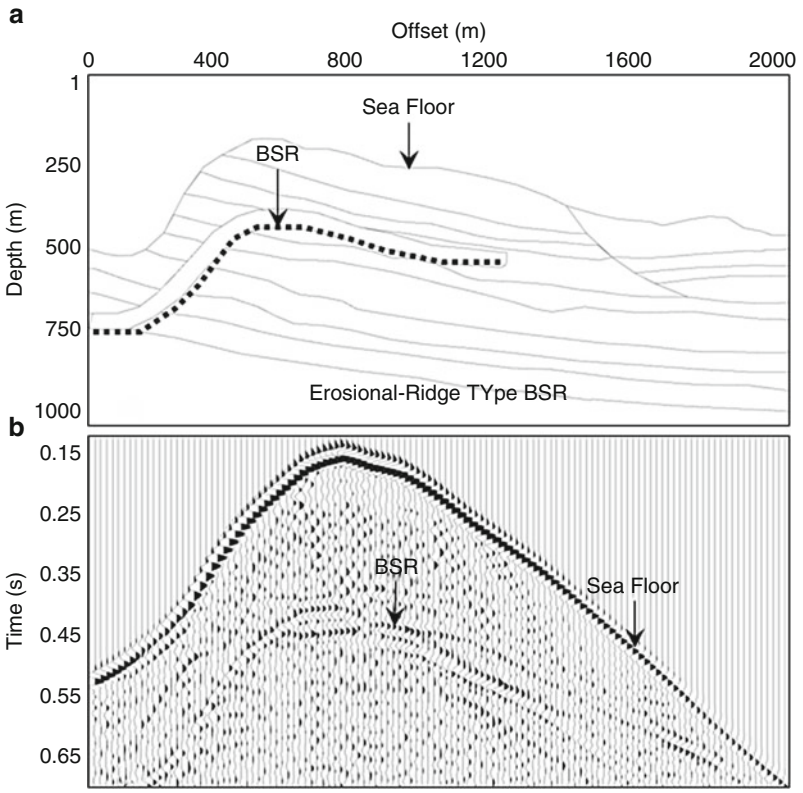

Fig. 5.25 Schematic illustration of Erosional-Ridge structure and corresponding seismic data simulated with finite difference scheme. (**a**) Erosional-Ridge structure BSR denoted by black dotted line. (**b**) BSR corresponding to "Fig. 5.25a" is identified as a reverse polarity event on simulated data

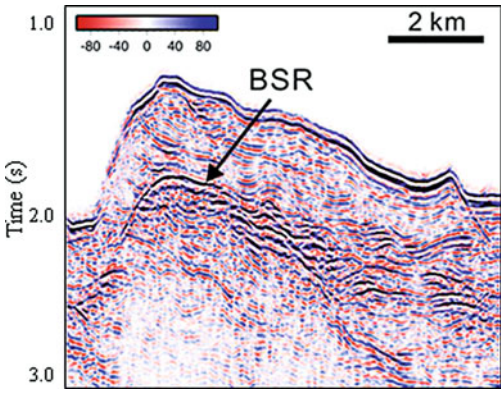

Fig. 5.26 Real data example of Erosional-Ridge structure BSR from incipient arc-continent collision zone off southwest Taiwan. The *red*-to-*blue* scale denotes the seismic amplitude. (After Lin et al. 2009, reprinted with the permission)

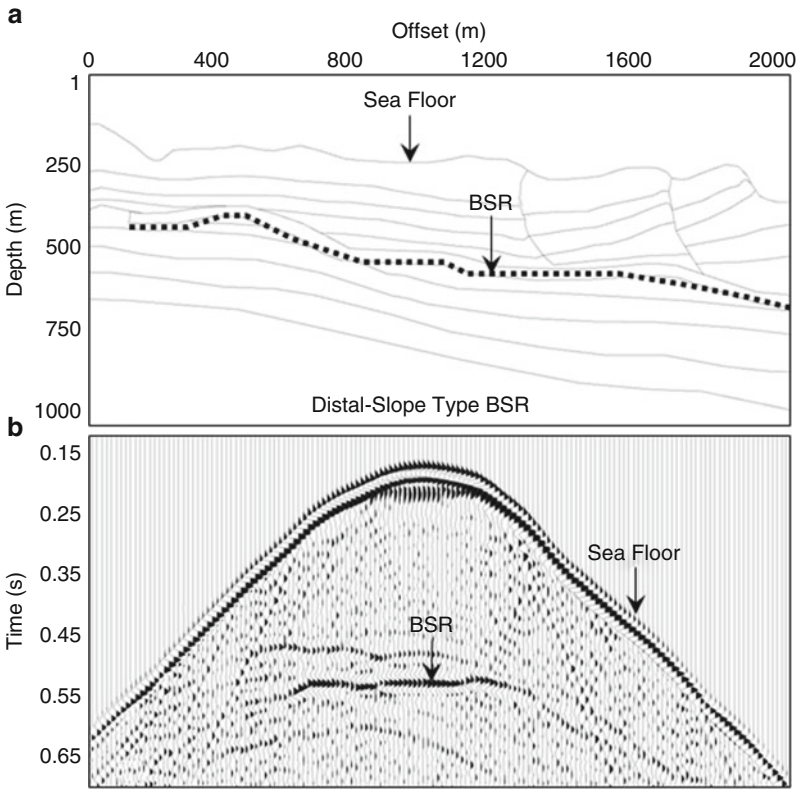

Fig. 5.27 Schematic illustration of Distal-Slope structure and corresponding seismic data simulated with finite difference scheme. (**a**) Distal-Slope structure BSR denoted by black dotted line. (**b**) BSR corresponding to "Fig. 5.27a" is identified as a reverse polarity event on simulated data

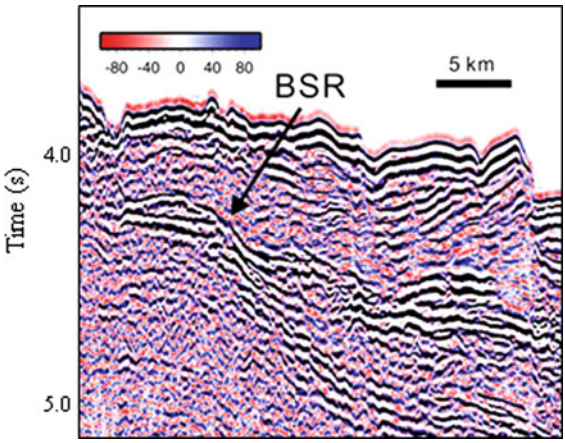

Fig. 5.28 Real data example of Distal-Slope structure BSR from incipient arc-continent collision zone off southwest Taiwan. The *red*-to-*blue* scale denotes the seismic amplitude. (After Lin et al. 2009, reprinted with the permission)

necessary "ingredients" and conditions (water, gas, nucleation sites, temperature and pressure). Bunz et al. (2003) suggested that on the continental slope, the lithology of glacigenic debris flow deposits and pre-glacial basin deposits could prevent gas hydrate formation, because of reduced pore size, reduced water content and fine-grained sediment composition. The formation of BSR and gas hydrates could be dominated by an advection of gas from the strata distinctly beneath the gas-hydrate stability zone (Bunz et al. 2003). Fluids could migrate upward and could be deflected laterally by hydrated sediments and less permeable layers.

The accumulation of sediments could result in creating seismic uplift (Fig. 5.29) and increasing the temperature of deeper sediments which could cause the break down of older sediments containing hydrates and releasing the free gas that could moved though discrete layer of fracture network. There could be other possibility of gas accumulation at relatively impermeable base of hydrate-saturated sediments, as such configuration could act as a trap. In this scenario the gas which is trapped is inferred to have penetrated in the gas hydrate stability zone by diffusion or by network of small compacted faults and fractures. This gas converts to gas hydrates and increases the concentration of gas hydrates.

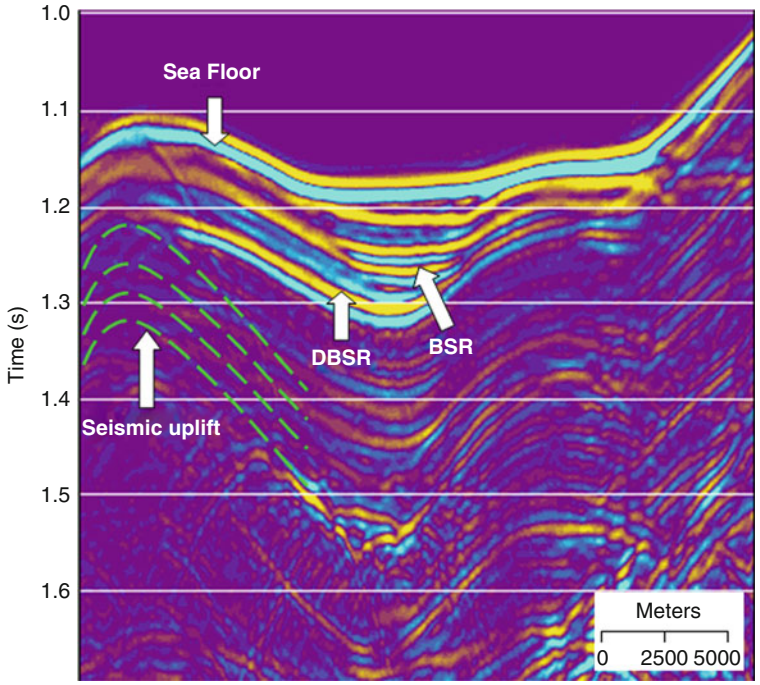

Fig. 5.29 Example of single and double BSR structures from Green Canyon, Gulf of Mexico, offshore, USA. The accumulated sediments in this area are causing a seismic uplift like structure as indicated by *green* dotted lines

5.2.3 Diapirism

Diapirism is a geological phenomenon and the emplacement of diapirs is controlled not only by the physical properties of rising sediments but also the geological events affecting that region. Gas charged mud is a potential source of diapir. In addition to this there are few examples available (Schmuck and Paull 1993; Auzende et al. 2000) related to gas hydrate occurrence in diapir structure. Ginsburg et al. (1984) was first to report the formation of gas hydrates with submarine mud diapirs, and then, mud diapirs and related gas hydrates had been widely identified in the areas of rapid sedimentation, lateral tectonic compression and geologically recent magmatic activity, such as in the Black Sea and Caspian Sea where 10,000 m thick Cenozoic strata were deposited in high rates. At the Norwegian Sea, offshore Nigeria and the Gulf of Mexico, faults played a key role in the formation of mud diapirs, and in the Mediterranean Ridge, Barbados Ridge and the Nankai Trough, most of which are at accretionary wedges lateral overpressure also played a part in creating mud diapirs. (Henry et al. 1996; Higgins and Saunders 1973; Lance et al. 1998; Ludmann and Wong 2003; Milkov 2000; McConnell and Kendall 2003). The Okinawa Trough is an active, initial back-arc rifting basin formed behind the Ryukyu arc-trench system in the West Pacific, where the Philippine Sea Plate is subducting under the Eurasia Plate (Jin and Yu 1987; Lee et al. 1980; Letouzey and Kimura 1986; Sibuet et al. 1998). High heat flow values, intensive earthquake, volcanoes, active faults are very distinct in this region. High sediment deposit rate is favouring the higher organic content and the well developed active faults provide passageway for gas hydrate accumulation in the Okinawa Trough (Guo et al. 2007; Qin et al. 1987; Ning et al. 2009).

Gas may be trapped in landward-dipping strata or in bowed strata that are crosscut and capped at their updip ends by the base of the gas hydrate-cemented sediments. Gas may also be trapped by doming of the gas hydrate-cemented sediment due to diapirism. To understand this phenomenon better, a model has been presented (Fig. 5.30a) and gas hydrate related signatures on seismic section has been observed (Fig. 5.30b). Further penetration of the diapir causes extensional faulting above the diapir and the base of the gas hydrate is depressed above the diapir. Gas collects beneath a hydrate seal. Gas hydrates are concentrated around the diapir and it's structure becomes very complex in the vicinity of the diapirs. Migration of a diapir through the subsurface forms a gas trap which could result from the breakdown of hydrate above the diapir and accumulation of the gas from surrounding area (Fig. 5.30a, b). This process causes the development of extension fault above the diapir, which could be extended through the base of hydrate stability field.

The thermal conductivity of a salt diapir is greater than that of the surrounding sediments, resulting in a local increase in heat flow above the diapir and a compression of the isotherms (MacLeod 1982). Increased heat flow from a salt diapir and the migration of salt ions into the surrounding sediments cause the base of the gas hydrate to move up from the diapir, creating a dome in the base of the

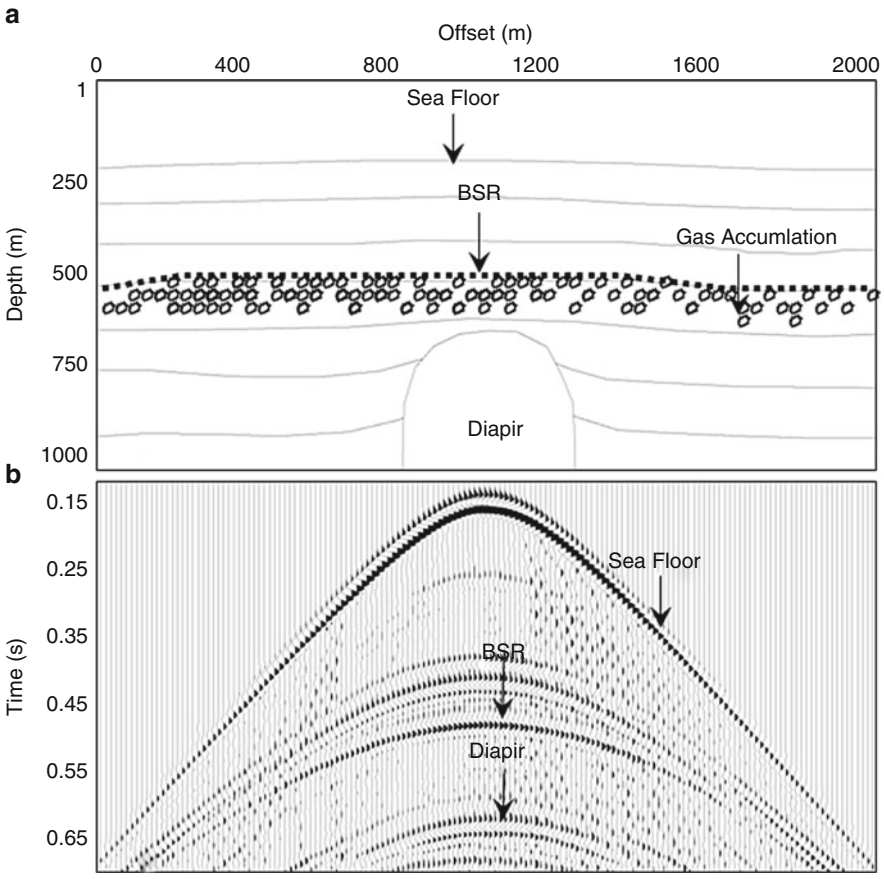

Fig. 5.30 Diapir model for gas hydrates. Schematic illustration of gas trapped due to diaprism and corresponding seismic data simulated with finite difference scheme. (**a**) Schematic representation of Gas hydrates related diaper model. Gas is trapped by doming of gas hydrate cemented sediments. (**b**) Identified BSR on the simulated data corresponding to "Fig. 5.30a". The gas hydrate feature is identified as a reverse polarity event

hydrate-cemented sediment (Dillon et al. 1980; Macleod 1982). This process, in conjunction with the doming of the surrounding strata by the diapir, forms a trap for gas released by disintegrating gas hydrate above the diapir and gas migrating up dip from strata surrounding the diapir. A good example of mud diapir is discussed by Ning et al. (2009) and the stacked section of the structure is presented in Fig. 5.31.

5.2.4 Fluid Migration Features

Upward fluid migration is one of the main process in the formation of gas hydrates. Hydrates are formed due to dispersed and focused fluid migration. Vertical zone of

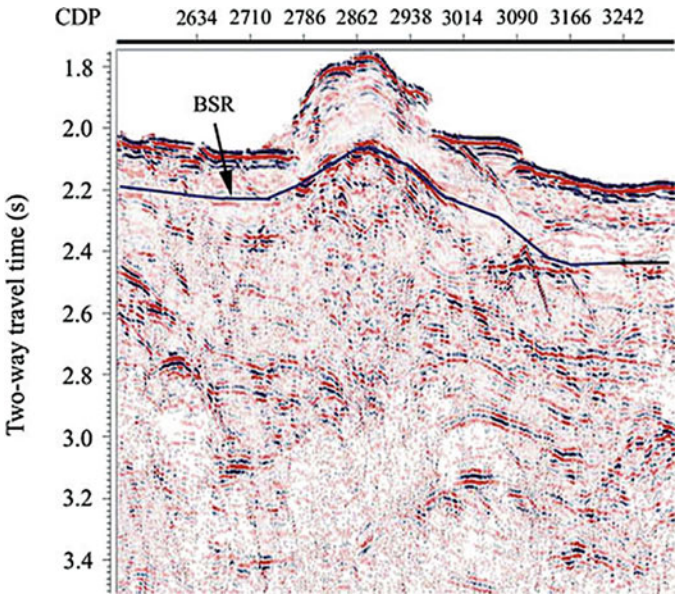

Fig. 5.31 Real data example of a gas hydrate related mud diaper structure from southern Okinawa Trough. The profile is showing mud diaper (After Ning et al. 2009, reprinted with the permission)

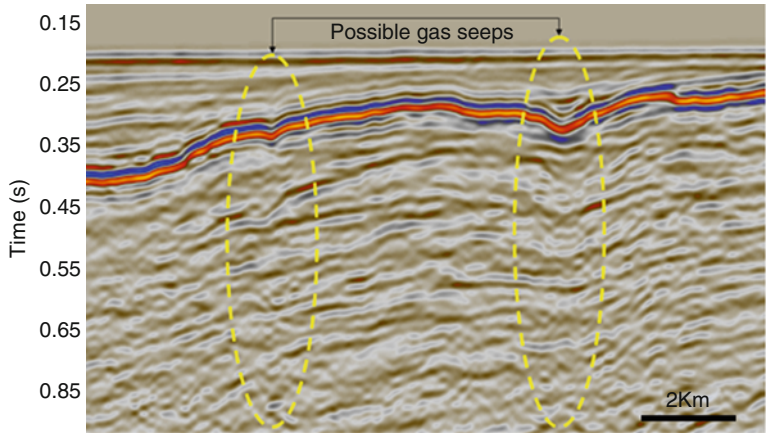

Fig. 5.32 Real data example from Sydney basin. Possible gas seeps are marked on the profile (Courtesy of CSIRO)

acoustic wipe-out which originates at different depths, possibly at the base of hydrate stability zone could be observed at different geological provinces. It is not always necessary that fluid or gas migration features always exist in gas hydrate province. There could be some other source of fluid migration not connected to

formation of gas hydrates as seen in the Sydney basin Australian offshore (Fig. 5.32). These fluid migration features could terminate at different stratigraphic levels within the gas hydrate accumulation region. The source of methane gas, which forms gas hydrate, is mostly derived from microbial degradation of organic matters in shallow sediments as evidenced from studies at other gas hydrate-bearing geo-provinces (e.g., Marchesi et al. 2001; Colwell et al. 2004). As methane gas dissolves in sediment pore water, the gasbearing fluids may migrate upward along dipping permeable sediments (e.g., sand layers) to the GHSZ and form gas hydrates (Hyndman and Davis 1992).

Brittle fault zones are also good migration conduits for deep-seated, gas-bearing fluids (Caine et al. 1996). For example, studies in the Barbados accretionary wedge have shown clear evidence for migration of fluid flows along fault zones and especially along the decollement (Gieskes et al. 1990; Langseth and Moore 1990; Shipley et al. 1995). Similar conditions for fluids migrating along fault zones and decollements have been suggested in the Nankai accretionary wedge (Moore et al. 1990), the Costa Rica accretionary wedge (Shipley et al. 1990), and the Cascadia accretionary wedge (MacKay et al. 1994).The gas-bearing fluids may migrate upward beneath the slope, forming gas hydrates under favorable conditions and resulting in many BSRs that even exist beneath gullies and not only in topographic highs as is usually the case.

5.2.4.1 Pockmarks

The escape of gases or fluids through the sea floor could also be caused by pockmarks, which are known to be the result of fluid expulsion. Pockmarks can be buried and hence relict, or actively venting gas at the seafloor. Buried ones indicate a long term and continuing activity (Hasiotis et al. 1996). A good example of the pockmark is observed at the seabed of the Nyegga region (Hovland and Svendsen 2006) as shown in Fig. 5.33. All these pockmarks have positive topography and they are partly covered in bacterial mat, which indicates ongoing fluid flow. These pockmarks over Nyegga region have distinct corrosion pits on their surface which indicates fluidization and point source corrosion of the covering sediments that is caused by the localized sub-surface gas hydrate dissociation. It can be concluded that these type of features formed by the local accumulation of hydrate in marine sediments.

5.2.4.2 Mud Volcanoes

These are one of the most important geological indicators of fluid or gas migration through sea floor to the surface and are mainly found around subduction zones and orogenic belts where lateral tectonic compressional stress is dominant. These are

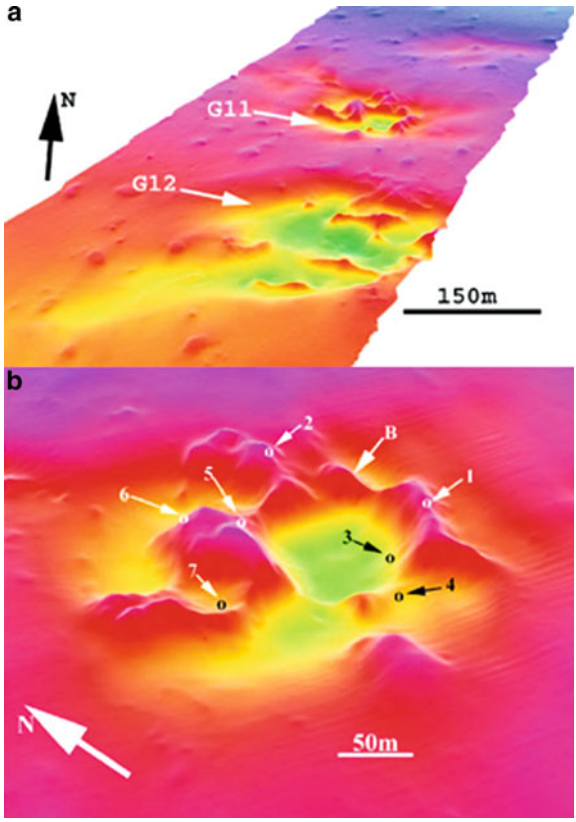

Fig. 5.33 (**a**) Oblique perspective view of the study area, seen from south (based on multibeam echosounder). Two complex pockmarks are shown, G11 and G12. G11 measures about 220 m in diameter and is approx. 12 m deeper than the surrounding general seafloor. The general water depth just north of G11 is 725 m. Just north of G12 the general water depth is 727 m. (**b**) Similar, but closer view of complex pockmark G11, where the hydrate pingoes were discovered. The ridges within the pockmark consist of irregular carbonate blocks (modified from Hovland et al. 2005). The pingoes, visually documented in 2004 during an ROV grid survey are shown as small, numbered circles (1–7). (**b**) Indicates location of sediment sample acquired in 2003, at a bacterial mat. Note that the pingoes and bacterial mat occur adjacent to and on the carbonate ridges. (After Hovland and Svendsen 2006, reprinted with the permission)

also called gas–oil volcano which transport water mixed mud to seep to the surface. Mud volcanoes are the geological formations created by geo-excreted liquids and pressurized gases with mud. Two examples of the mud volcano's are shown in Fig. 5.34a, b. Gas hydrate related mud volcanoes are found around the world, an example from Anaximander mountains (Eastern Mediterranean sea) is studied by Lykousis et al. 2009 and illustrated in Fig. 5.35. Conical sub-bottom reflectors that resemble buried mud volcanoes or eruption centers are identified (Fig. 5.35).

5.2.4.3 Faulting

Fault zones are commonly interpreted as one of the important conduits for the upward flow of fluid (e.g., Moore et al. 1990, 1995). Fluid migration occurred via fault zones, joint and fracture system and other physical discontinuities in rocks and sediments. Field studies suggested that the formation of gas hydrates and associated free gas have a strong structural control on the base of the stability field of gas hydrates (for which the BSR is an indicator) and on the base of the underlying free gas zone. In particular, the BSR shoals along fault lines, and it shoals even more at fault intersections. The free gas layer could be thinner or thicker along faults and fault-bounded sediments.

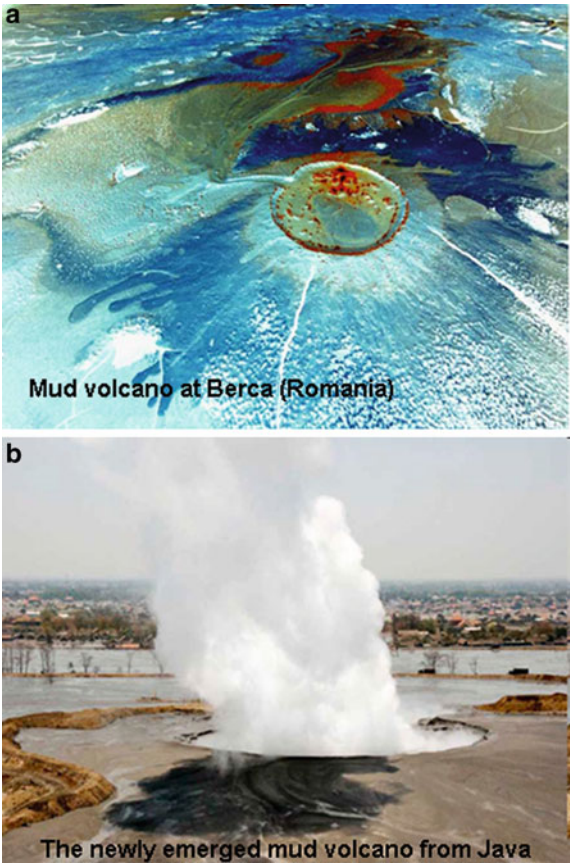

Fig. 5.34 Real example of mud volcano's. (**a**) Mud volcano at Berca (Romania). A sharp feature is observed. (**b**) The newly emerged mud volcano from Java (Courtesy of softpedia news source; http://www.news.softpedia.com/newsImage

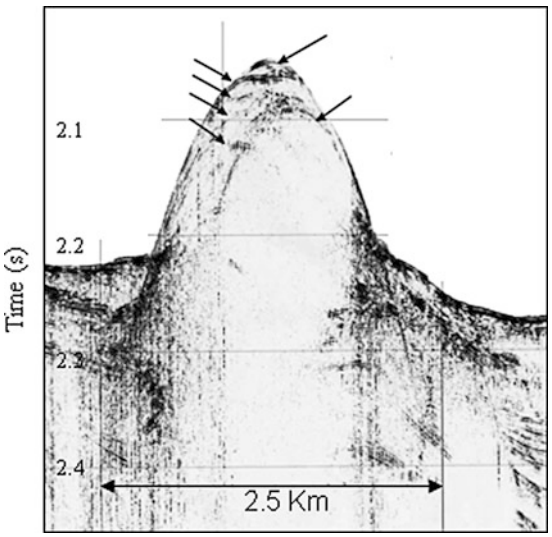

Fig. 5.35 Real seismic data example of mud volcano observed in Eastern Mediterranean Sea (After Lykousis et al. 2009; reprinted with the permission)

References

Auzende, J.M., Van de Beuque, S., Dickens, G., François, C., Lafoy, Y., Voutay, O., Exon, N., 2000. Deep sea diapirs and BSR in Fairway Basin (Southwest Pacific). Marine Geophysical Research 21, 579–587.

Baba, K., Yamada, T., 2004. BSRs and associated reflections as an indicator of gas hydrate and free gas accumulation: an example of accretionary prism and forearc basin system along the Nankai Trough, off central Japan. Resource Geology 54, 11–24.

Barker, P.F., 1982. The Cenozoic subduction history of the Pacific margin of the Antarctic Peninsula: ridge crest–trench interactions. Journal of the Geological Society of London, 139, 787–801.

Barker, D.H.N., Austin, Jr., J.A., 1994. Crustal diaprism in Bransfield Strait, West Antarctica: evidence for distributed extension in marginalbasin formation. Geology 22, 657–660.

Barnes, P.M., et al., 2009. Tectonic and geological framework for gas hydrates and cold seeps on the Hikurangi subduction margin, New Zealand. Marine Geology doi:10.1016/j.margeo.2009.03.012.

Buenz, S., Mienert, J., Vanneste, M., Andreassen, K., 2005. Gas hydrates at the Storegga Slide: constraints from an analysis of multicomponent, wide-angle seismic data. Geophysics 70, B19–B34.

Bunz, S., Mienert, J., Berndt, C., 2003. Geological controls on the Storegga gas-hydrate system of the mid-Norwegian continental margin. Earth and Planetary Science Letters 209, 291–307.

Caine, J.S., Evans, J.P., Forster, C.B., 1996. Fault zone architecture and permeability structure. Geology 24(11), 1025–1028.

Charlou, J.L., Donval, J.P., Zitter, T., Roy, N., Jean-Baptiste, P., Foucher, J.P., Woodside, J., MEDINAUT Scientific Party, 2003. Evidence of methane venting and geochemistry of brines on mud volcanoes of the eastern Mediterranean Sea. Deep-Sea Research, Part I 50, 941–958.

Clennell, M.B., Hovland, M., Booth, J.S., Henry, P., Winters, W.J., 1999. Formation of natural gas hydrates in marine sediments. Part 1: Conceptual model of gas hydrate growth conditioned by host sediment properties. Journal of Geophysical Research B 104, 22985–23003.

Colwell, F., Matsumoto, R., Reed, D., 2004. A review of the gas hydrates, geology, and biology of the Nankai Trough. Chemical Geology 205, 391–404.

Cook, A.E., Goldberg, D., 2007. Gas hydrate filled fracture distribution, eastern Indian continental margin. American Geophysical Union Fall Meeting, San Francisco, CA, AN, OS11C-04.

Dillon, W.P., Grow, J.A., Paull, C.K., 1980. Unconventional gas hydrate seals may trap gas oft southeast US. Oil and Gas Journal 78, 124–130.

Gieskes, J.M., Vrolijk, P., Blanc, G., 1990. Hydrogeochemistry of the Northern Barbados accretionary complex transect: Ocean Drilling Program Leg 110. Journal of Geophysical Research 95(B6), 8809–8818.

Ginsburg, G.D., Ivanov, V.L., Soloviev, V.A., 1984. Natural gas hydrates of the world's oceans. Oil and gas content of the world's oceans. PGO Sevmorgeologia, 141–158.

Guo, J.H., Wu, S.G., Xu, N., Fan, F.X., 2007. Structural characteristics of gas hydrates deposition in the west slope of the Okinawa Trough and its adjacent area. Oceanologia Et Limnologia Sinica 38(5), 432–437.

Haq, B.U., 2003. Climatic impact of natural gas hydrate. in: M.D. Max, (Ed.),Natural Gas Hydrate in Oceanic and Permafrost Environments, Kluwer, The Netherlands, pp. 137–147.

Hasiotis, T., Papatheodorou, G., Kastanos, N., Ferentinos, G., 1996. A pockmark field in the Patras gulf (Greece) and its activation during the 14.7.93 seismic event. Marine Geology 130, 333–344.

Henry, P., Thomas, M., Clennell, M.B., 1999. Formation of natural gas hydrates in marine sediments. Part 2: Thermodynamic calculations of stability conditions in porous sediments. Journal of Geophysical Research B 104, 23005–23022.

Hernry, P., Le Pichon, X., Lallemant, S., Lance, S., Martin, J.B., Foucher, J.P., Fiala-Medioni, A., Rostek, F., Guilhaumou, N., Pranal, V., Castrec, M., 1996. Fluid flow in and around a mud volcano field seaward of the Barbados accretionary wedge: results from Manon cruise. Journal of Geophysical Research 101, 20297–20323.

Higgins, G.E., Saunders, J.B., 1973. Mud volcanoes-their nature and origin: contribution to the geology and paleobiology of the Carribbean and adjacent areas. Verhandlungen der Naturforschenden Gesellschaft in Basel 84, 101–152.

Hovland, M., Svendsen, H., 2006. Submarine pingoes: indicators of shallow gas hydrates in a pockmark at Nyegga, Norwegian Sea. Marine Geology 228, 15–23.

Hovland, M., Svensen, H., Forsberg, C.F., Johansen, H., Fichler, C., Fosså, J.H., Jonsson, R., Rueslåtten, H., 2005. Complex pockmarks with carbonate-ridges off mid-Norway: products of sediment degassing. Marine Geology 218, 191–206.

Hyndman, R., Davis, E., 1992. A mechanism for the formation of methane hydrate and seafloor bottom simulating reflectors by vertical fluid expulsion. Journal of Geophysical Research 97, 7025–7041.

Jin, X.L., Yu, P.Z., 1987. Structural characteristics of Okinawa Trough. Science in China (Ser. B) 17(2), 196–203.

Kennett, J.P., 2002. Methane Hydrates in Quaternary Climate Change: The Clathrate Gun Hypothesis. American Geophysical Union, Washington, DC.

Kvenvolden, K.A., 1993. Gas hydrates — geological perspective and global change. Review of Geophysics 31, 173–187.

Lance, S., Henry, P., Le Pichon, X., Lallemant, S., Chamley, H., Rostek, F., Faugeres, J.C., Gonthier, E., Olu, K., 1998. Submersible study of mud volcanoes seaward of the Barbados accretionary wedge: sedimentology, structure and rheology. Marine Geology 145, 255–292.

Langseth, M.G., Moore, J.C., 1990. Fluids in accretionary prisms, EOS 71, 245–246.

Lee, C.S., Shor, Jr., G.G., Bibee, L.D., Lu, R.S., Hilde, T.W.C., 1980. Okinawa Trough: origin of a back-arc basin. Marine Geology 35, 219–241.

Letouzey, J., Kimura, M., 1986. The Okinawa Trough: genesis of a back-arc basin developing along a continental margin. Tectonophysics 125, 209–230.

Lin, C.-C., Tien-Shun Lin, A., Liu, C.-S., Chen, G.-Y., Liao, W.-Z., Schnurle, P. 2009. Geological controls on BSR occurrences in the incipient arc-continent collision zone off southwest Taiwan. Marine and Petroleum Geology 26(7), 1118–1131.

Long, D., Lovell, M.A., Rees, J.G., Rochelle, C.A., 2009. Sediment-hosted gas hydrates; new insights on natural and synthetic systems (in Sediment-hosted gas hydrates; new insights on natural and synthetic systems). Geological Society Special Publications, 319, 1–9.

Ludmann, T., Wong, H.K., 2003. Characteristics of gas hydrate occurrences associated with mud diapirism and gas escape structures in the north-western Sea of Okhotsk. Marine Geology 201, 269–286.

Lykousis, V., Alexandri, S., Woodside, J., et al., 2009. Mud volcanoes and gas hydrates in the Anaximander mountains (Eastern Mediterranean Sea). Mar Petrol Geol 26, 854–872.

MacKay, M.E., Jarrad, R.D., Westbrook, G.K., Hyndmann, R.D., and the Shipboard Scientific Party of ODP leg 146, 1994, Origin of bottom simulating reflectors: Geophysical Evidence from the Cascadia Accretionary prism, Geology 22, 459–462.

MacLeod, M.K., 1982. Gas hydrates in ocean bottom sediments. American Association Petroleum Geologists Bulletin 66, 2649–2662.

Malone, R., 1985. Gas Hydrates Topical Report, DOE/METC/SP-218 (DE85001986). Department of Energy, Morgantown Energy Technology Center, USA.

Marchesi, J.R., Weightman, A.J., Cragg, B.A., Parkes, R.J. and Fry, J.C., 2001. Methanogen and bacterial diversity and distribution in deep gas hydrate sediments from the Cascadia Margin as revealed by 16S rRNA molecular analysis. FEMS Microbiology Ecology 34, 221–228.

McConnell, D.R., Kendall, B.A., 2003. Images of the base of gas hydrate stability in the deepwater Gulf of Mexico and implications for successful well planning. The Leading Edge 22(4), 361–367.

Mienert, J., Posewang, J., Baumann, M. (1998). Gashydrates along the northeastern Atlantic margin:possible hydrate-bound margin instabilities and possiblerelease of methane. in: J.-P. Henriet, J. Mienert (Eds.), Gas Hydrates: Relevance to World Margin Stability and Climate Change, Geological Society Special Publication, London, 137, pp. 275–291.

Milkov, A.V., 2000. Worldwide distribution of submarine mud volcanoes and associated gas hydrates. Marine Geology 167, 29–42.

Moore, G.F., Shipley, T.H., Stoffa, P.L., Karig, D.E., Taira, A., Kuramoto, S., Tokuyama, H., and Suyehiro, K., 1990, Structure of the Nankai Trough accretionary zone from multichannel seismic reflection data: Journal of Geophysical Research, v. 95, p. 8753–8765.

Moore, G.F., Shipley, T.H., Stoffa, P.L., Karig, D.E., Taira, A., Kuramoto, S., Tokuyama, H., Moore, J.C., Moore, G.F., Cochrane, G.R., Tobin, H.J., 1995. Negative-polarity seismicmultichannel seismic reflection data. Journal of Geophysical Research, 95, 8753–8765.

Ning, X., Shiguo, W., et al., 2009. Gas hydrate associated with mud diapirs in southern Okinawa Trough. Marine and Petroleum Geology 26(8), 1413–1418.

Paull, C.K., Speiss, F.N., Ussler, III, W., Borowski, W.S., 1995. Methane rich plumes on the Caroline continental rise: associations with gas hydrates. Geology 23, 89–92.

Paull, C.K., Ussler, III, W., Dillon, W.P., 2000. Potential role of gas hydrate decomposition in generating submarine slope failures, in: M.D. Max (Ed.), Natural Gas Hydrate in Oceanic Permafrost Environments, Coastal Systems and Continental Margins 5, Kluwer, Dordrecht, pp. 149–156.

Qin, Y.S., Zhao, Y.Y., Chen, L.R., Zhao, S.L., 1987. Geology of the East China Sea. Science Press, Beijing, 290 pp.

Rajput, S., 2008. Analysis of Ocean Bottom Seismometer data for gas hydrate studies and subsurface models. Ph.D Dissertation, Kurukshetra University Kurukshetra.

Schmuck, E.A., Paull, C.K., 1993. Evidence for gas accumulation associated with diapirism and gas hydrates at the head of the Cape Fear slide. Geo-Marine Letters 13, 145–152.

Schnurle, P., Wang, C., 1998. Okinawa Trough back-arc basin: early tectonic and magmatic evolution. Journal of Geophysical Research 103(B12), 30245–30267.

Shipley, T.H., Stoffa, P.L., Dean, D.F., 1990. Underthrust sediments, fluid migration paths, and mud volcanoes associated with the accretionary wedge off Costa Rica: Middle American Trench, Journal of Geophysical Research 95, 8743–8752.

Shipley, T.H., Ogawa, Y., Blum, P., (Eds.) 1995. Proc. Ocean Drilling Prog., Init. Rep., 156, 301 pp.

Sibuet, J.C., Deffontaines, B., Hsu, S.K. et al., Okinawa trough back arc basin: Early tectonic and magnetic evolution, Journal of Geophysical Research, 1998, 103: 30245–30267.

Sloan, E.D., 1998. Clathrate Hydrates of Natural Gases, 2nd ed. Marcel Dekker, Inc., New York, pp. 75–76.

Spence, G.D., Hyndman, R.D., Chapman, N.R., Riedel, M., Edwards, N., Yuan, J., 2003. Cascadia Margin, Northeast Pacific Ocean: hydrate distribution from geophysical investigations. in: M.D. Max (Ed.),Natural Gas Hydrate in Oceanic and Permafrost Environments, Kluwer, The Netherlands, pp. 183–198.

Suyehiro, K., 1990. Structure of the Nankai Trough accretionary zone from reflections along faults of the Oregon accretionary prism: indicators of overpressuring. Journal of Geophysical Research 100, 12895–12906.

Talukder, A.R., Bialas, J., Klaeschen, D., Brueckmann, W., Reston, T., Petersen, J. 2008. Tectonic framework of the mud mounds, associated BSRs and submarine landslides, offshore Nicaragua Pacific margin. Journal of the Geological Society 165, 167–176.

Tucker, P.M., & Yortson, H., J., 1973, Pitfalls in Seismic Interpretation, Soc. Explor. Geophys. Mono. Ser. No. 2

Xu, W., Ruppel, C., 1999. Predicting the occurrence, distribution and evolution of methane gas hydrate in porous sediments. Journal of Geophysical Research 104, 5081–5095.

Chapter 6
Geophysical Indicators

Abstract Gas hydrates are found worldwide and many studies have been carried out to develop an efficient method to identify them using various geophysical as well as other anomalies. The geophysical impact of gas hydrate formations is that, it gives strength to the host sediments and this is a consequence of change in the physical properties which are directly related to the compressional (V_p) and shear velocities (V_s). This chapter presents a review and synthesis of various geophysical indicators which should be used for the identification of gas hydrates on seismic datasets. Synthetic seismic response together with field data from different regions of the world reveal various seismic indicators of gas hydrates and associated free gas, such as the bottom simulating reflector (BSR), double bottom simulating reflector (DBSR), enhanced seismic reflection below the BSR, seismic chimneys and hydrate mounds. Seismic chimneys are characterized by columnar amplitude reduction that terminates at different stratigraphic levels. A few seismic chimneys crop out on the seafloor, forming very small mounds. These seismic chimneys with seafloor expressions probably represent vertical vents for gas, originating from below the GHSZ. Analysis of seismic data from Green canyon area reveal that Gas hydrates are usually confined to permeable sand layers causing large changes in velocity across sedimentary formations. The large impedance contrasts so produced will result in high amplitude anomalies similar to those formed due to the presence of gas in sediments.

6.1 Introduction

Gas hydrates are crystalline minerals composed of water and certain gases. Gas hydrates feature high on energy, wide in distribution and large in size, and are thought to be a vital source of energy for the twenty-first century. It is estimated that 90% of the continental margins is favorable for generation of hydrates (Kvenvolden et al. 1993). As the supply of the available energy sources tends to get non encouraging globally, searching for alternate sources of energy becomes most relevant. The distribution of hydrates has specific characteristics and have been

N.K. Thakur and S. Rajput, *Exploration of Gas Hydrates*,
DOI 10.1007/978-3-642-14234-5_6,

described extensively (Collett 1995, Ecker et al. 1998; Howell 1993; Kvenvolden 1993a, b; Max 2000; Max and Lowrie 1992, 1996) and are known to occur in the Arctic and in sediments underlying the world's margins (Fleischer et al. 2001, Kvenvolden 1993). The presence of hydrates can be inferred from seismic evidence such as bottom simulating reflectors (BSRs) or changes in seismic velocity (e.g., Hovland and Judd 1988, Lowrie et al. 1997). Gas hydrates have also been found where there is no BSR (Holbrook et al. and Shipboard Scientific Party 1996).

The presence of gas hydrate in sediment pore space elevates interval velocity in the gas hydrate stability zone (GHSZ) and may significantly reduce interstratal acoustic impedance contrasts, causing a marked decrease in seismic amplitude above the BSR (Dillon et al. 1993), a seismic anomaly known as amplitude blanking. Gas hydrate-bearing sediments can also create bright spots as seen in the Mallik gas-hydrate field (Bellefleur et al. 2006). Free gas below the GHSZ increases acoustic impedance contrasts between sedimentary layers, enhancing seismic amplitude below the BSR. The free gas can act as a low-frequency filter and thus the BSR often marks a sharp interface between high frequency reflections above and low-frequency reflections below (Vanneste et al. 2002). Seismic chimneys or vertical seismic wipe-outs are also seen in many oceanic gas hydrate provinces. These seismic reflection anomalies are often accompanied by pockmarks or craters (Ginsburg 1998) or mound-like vents (Sager et al. 1999) on the seafloor, suggesting localized expulsion of gas, originating from below the GHSZ (Hyndman et al. 2001; Wood et al. 2002). Modeling synthetic seismic data and it's correlation with the real world data reveals different geophysical indicators related to gas hydrates and associated free-gas. Some examples from different regions of the world (Green Canyon, Hydrate Ridge, offshore USA and Kerala-Konkan basin, offshore India) are presented here which summarizes the identified geophysical indicators for gas hydrates and associated free gas.

6.2 Geophysical Indicators

Assessment of the gas hydrate bearings sediments has been made by various means including geophysical, geological and geochemical investigations. Among those geophysical indicators are the main characteristics for the identification of gas hydrate and associated free gas on seismic datasets. BSR is considered as the principal geophysical indicator for the identification of the gas hydrates. The BSR is thought to correspond to the base of gas-hydrate stability zone (GHSZ) and occurr due to an acoustic impedance contrast between hydrate-bearing sediments and free gas trapped in the sediments underneath gas hydrates (Holbrook et al. 1996; Sassen et al. 2001). In order to study the distribution of gas-hydrates, a detailed assessment of various geophysical indicators e.g., the BSR, the double bottom simulating reflector (DBSR), enhanced seismic reflection below BSR, seismic chimneys, hydrate mounds and amplitude blanking is required. Such anomalous signatures have been presented considering field data and synthetic response of gas hydrate-free gas models.

6.2.1 The Bottom Simulating Reflectors

A sub-class of seismic reflectors is BSR, which originates as per hydrate stability zone depth, which in turn depends on velocity, pressure and temperature within the sediments. The most common BSRs are caused by the occurrence of gas hydrates. On synthetic offset gathers (Fig. 6.1) and on time migrated seismic section from Kerala-Konkan (KK) basin, western continental margin of India (Fig. 6.2), it is identified as a high amplitude and reverse polarity event which is due to high acoustic impedance contrast between gas hydrate and free gas layer. BSR is identified, which principally infers the presence of gas hydrate. In the presence of a low velocity layer (LVL) within the gas hydrate zone two reflectors of high amplitude and reverse polarity, could be observed (Figs. 6.3 and 6.4). The first reverse polarity event is interpreted as primary BSR and the second one is interpreted as secondary or double bottom simulating reflector (DBSR) as shown in Fig. 6.3. While analyzing the seismic data from Green Canyon, Gulf of Mexico, Offshore USA the same type of feature (Fig. 6.4), is interpreted as DBSR. The occurrence of DBSR in Green Canyon area is caused by the underlying free gas and presence of discrete fractured sedimentary layers through which the gas is migrating in upward direction. There could be several reasons for the occurrence of DBSR. The regional uplift, sea-level change, change in bottom-water temperature, or the presence of low velocity layer/contaminated form of hydrocarbons within the hydrate stability zone have been suggested as causes of DBSR (Trehu et al. 1999; Rajput 2008).

6.2.2 Enhanced Seismic Reflections Below BSR

Depending on the concentration of hydrate, enhanced or suppressed seismic reflectance can be observed (Holbrook et al. 2002). At high hydrate saturation hydrate-bearing layers can have velocities significantly greater than the surrounding sediment, thus generating enhanced reflectance. The accumulation of free gas below the GHSZ increases acoustic impedance contrasts between sedimentary layers, and enhance seismic amplitude below the BSR. Enhanced reflections below the BSR are observed, where the gas hydrate is present (Figs. 6.1, 6.3, 6.5 and 6.6). In general, they are not laterally extensive, and fade out rapidly with depth. Termination of enhanced reflections also locally forms the BSR in uplifted sediments. The section below the BSR (Fig. 6.5), including the enhanced reflections, which is considered as bright spot that is a characteristic of gas accumulations, suggesting that the hydrate-bearing sediments in the GHSZ effectively seal the gas-charged layer below. The vertical association of these enhanced seismic reflections below BSR with disruptions in the underlying gas zone reveals that these events represent concentrated hydrate formed by upward migration of methane gas along discrete layers having faults or fractures.

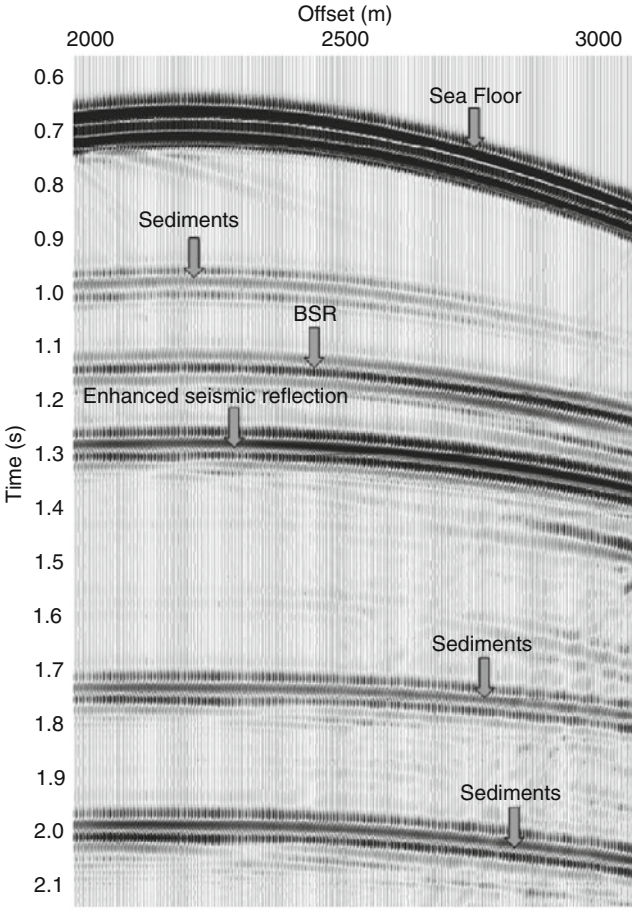

Fig. 6.1 Example of synthetic shot gathers for a layered BSR model. The BSR is identified as a reverse polarity event. Enhanced seismic reflection below BSR is representing the presence of free gas

6.2.3 Seismic Chimney and Amplitude Blanking

Seismic chimneys are the vertical zones of depressed seismic signal and establish spatial link between source rock, reservoir trap, spill-points and shallow-gas anomalies. The presence of gas chimneys have been interpreted as hydrocarbon leakage pathways (Meldahl et al. 2002; Ligtenberg 2003; Heggland 2004). These are important in unravelling the basin's hydrocarbon history, to distinguish between charged and noncharged prospects and to detect geo-hazards (Heggland 1998). Seismic chimneys often form a well-defined column of seismic wipe-outs. Good examples of seismic chimneys are found on Green Canyon offshore USA. Most seismic chimneys in Green Canyon area do not fade out upward but terminate rather abruptly before reaching the

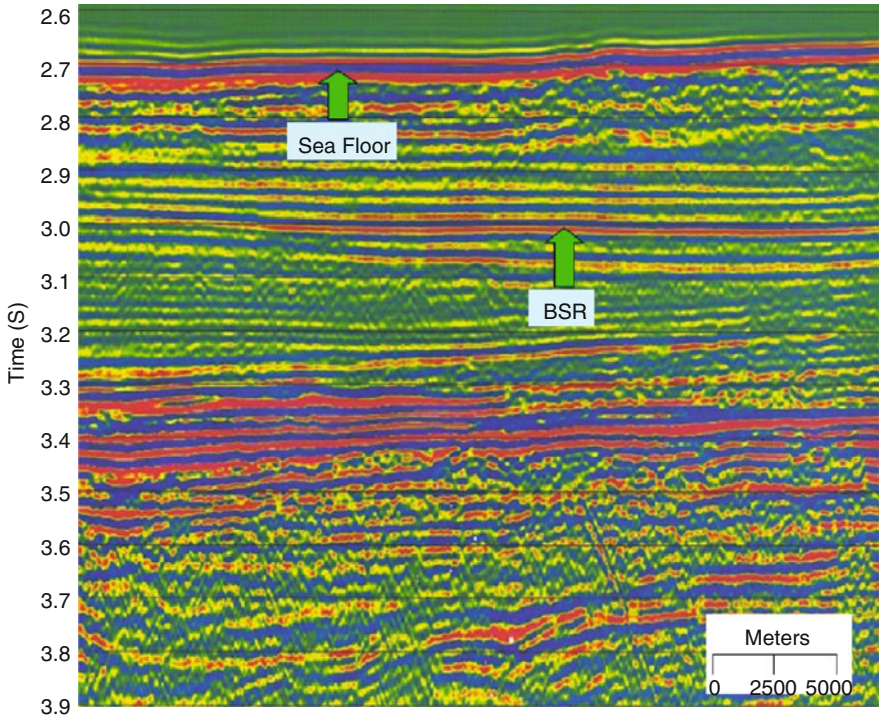

Fig. 6.2 Real data example from Kerala-Konkan (KK) basin, offshore India. The BSR is identified at 3.0 s as a reverse polarity event

seafloor and only a few crop out on the seafloor as shown in Fig. 6.7. The seismic chimneys appear to be wide owing to its lateral exaggeration in seismic profiles and its origin with deep structures. Weak BSRs or BSR-like features are seen below the seismic chimney in sedimentary deposits of Green Canyon area. The seismic chimney observed on Green Canyon seismic data form a well-defined column of seismic wipe-out. The BSR below or within the seismic chimneys is weak but appears to be also upwarped. It can be concluded that these types of seismic chimneys with seafloor expressions as representing vertical vents or focused conduits for gas that originates from below the GHSZ.

6.2.4 Hydrate Mounds

A mound is usually referred as an elevated earthen structure. Generally, the mounds were established in a deeper environment as suggested by the lack of indications for ground-moving waves. Non-photic conditions are indicated by the absence of cyanobacterial activity and calcareous algae. The mounds are reefs in the biological sense which means that they are autochthonous structures with a significant relief

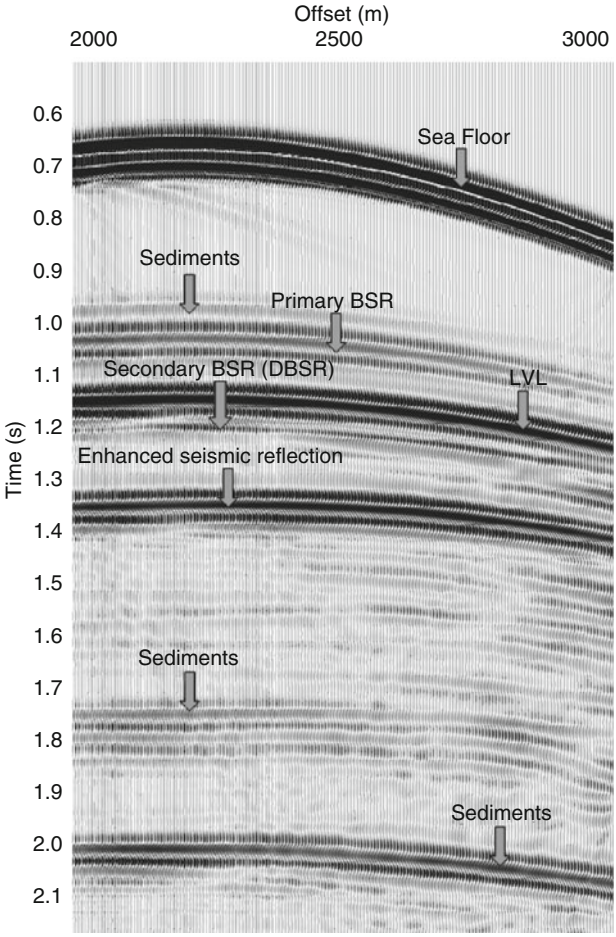

Fig. 6.3 Synthetic data example for the occurrence of DBSR. In the presence of a low velocity layer within the gas hydrate stability zone this sharp DBSR features is observed. Note single and double BSR are of negative polarity as compared to the sea floor. Below these BSRs enhanced seismic reflections are marked

build by organisms. Submarine structures suspected to have originated from the formation and dissociation of sediment-hosted gas hydrates have previously been described as 'hydrate mounds' (Aharon et al. 1992; MacDonald et al. 1994; Ginsburg and Soloviev 1994; Sager et al. 2003; Chapman et al. 2004), 'giant gas mounds' (Kvenvolden 1988; McConnell and Kendall 2002), disruption craters (Prior et al. 1989; Lammers et al. 1995), sediment slides (Schmuck and Paull 1993; Sultan et al. 2003) and large collapse features (Dillon et al. 1998). Synthetic seismic response (Fig. 6.6) from Green Canyon model and field seismic data (Fig. 6.7) indicate the presence of mound in hydrate hosted sediments. Gas Hydrate mounds form when proper temperature, pressure and chemical composition for the gas are met. Typically

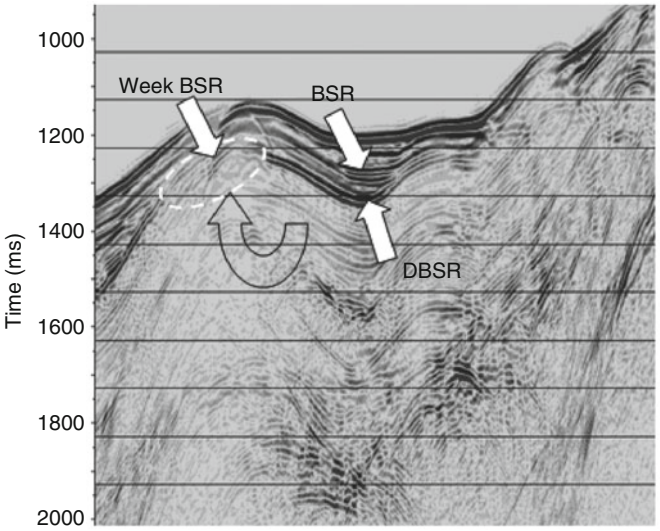

Fig. 6.4 Real data example from offshore Green Canyon Basin (Gulf of Mexico, USA). The single and double BSR are observed on the profile. Week BSR like feature is also observed sue to upward migration of gas through faulted zones (After Rajput 2008, reproduced with permission)

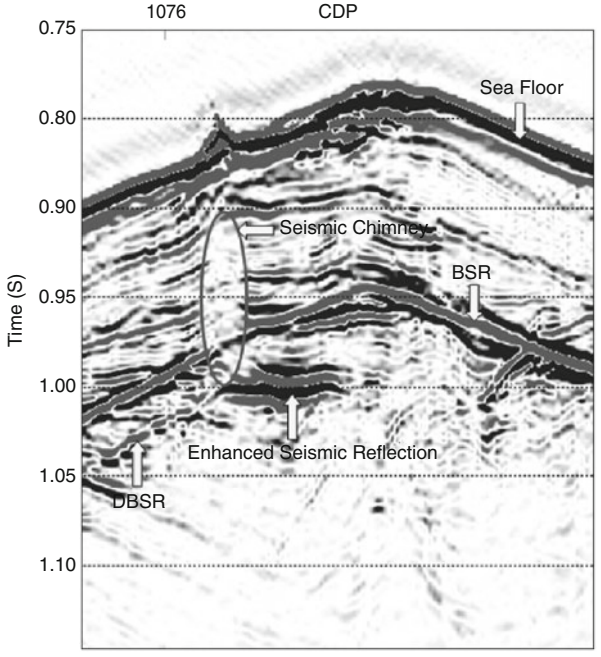

Fig. 6.5 Real data example from offshore Hydrate Ridge offshore USA. BSR and related features such as enhanced seismic reflections and seismic chimneys are marked on the section

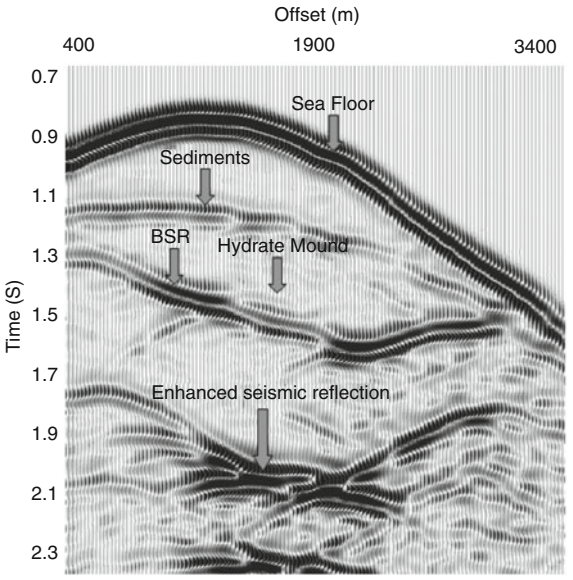

Fig. 6.6 Synthetic data example from a real model (Green Canyon model), hydrate related features such as mound and enhanced seismic reflections are observed on the seismic profile

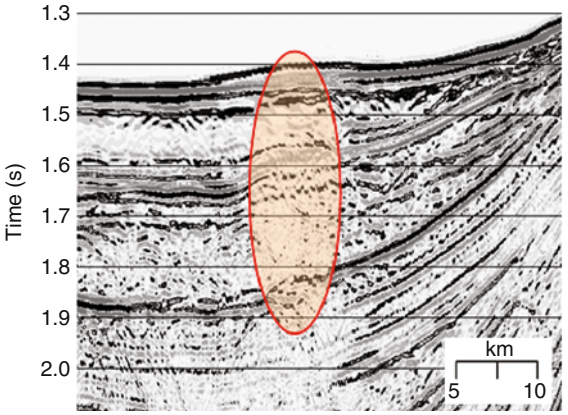

Fig. 6.7 A very good example of seismic chimneys from Gulf of Mexico. This features is terminating near to sea floor

the mounds can be categorized by their shape, surface expression and size. The mounds are assessed based on the environment they exist in order to evaluate whether the mounds are inhabited by hydrates. Analyses of seismic data from Green Canyon show that the hydrate mounds have the indications of the presence of gas hydrate in this region. (Fig. 6.7). The shape of hydrate mound is well-rounded and smooth. The amplitude of the BSRs vary from moderate to high near the mound associated with the accumulation of hydrates feeder structure and it decreases away from them.

6.2.5 Instantaneous Seismic Attributes

Seismic attributes are the information obtained from seismic data. The instantaneous seismic attributes characterize sample-by-sample variability and isolate the individual waveform components that make up the seismic trace. These attributes are considered as one of the important geophysical indicators for the occurrence of Gas. Though their application for gas hydrates are still debated.

6.2.5.1 Reflection Strength

Instantaneous amplitude, or reflection strength, is the square root of the total energy of the seismic signal at an instant of time and can be thought of as amplitude independent of phase. It is the envelope of the seismic trace. Therefore reflection strength is always positive and always in the same order of magnitude as the recorded data. Reflection strength is an effective tool to identify bright and dim spots. It provides information about contrasts in acoustic impedance. Lateral changes in reflection strength are often associated with major lithologic changes or with hydrocarbon accumulations. Gas reservoirs, in particular, appear frequently as high-amplitude "bright spot" reflections. Reflection strength can also be used to distinguish massive reflectors from thin-bed composites. Reflection strength depends on the contrast of acoustic impedance (i.e. product of velocity and density). Only a few percent of free gas in the pore space of sediments decrease seismic compressional (P-) wave velocity drastically (Domenico 1977). Therefore layers that contain trapped free gas often generate strong reflections (bright spots). Free gas is also known to highly attenuate seismic P-wave energy. The reflection strength plot for a complex DBSR model (Fig. 6.8) displays amplitude anomalies corresponding to dark red and blues, respectively. The reflection-strength (Fig. 6.8) was derived based on cross-well seismic reflectivity data for a complex DBSR model which is explained in detail in Chap. 8. It is suggested that such a display would make the locations of energy maxima more obvious in the seismic section. The reflection-strength can be analyzed with standard colour maps and subjected to trace mixing or other data-enhancement processes. In addition, this attribute can be used to map lateral variations of lithology formation.

6.2.5.2 Instantaneous Frequency

One way to describe a signal simultaneously in time and in frequency is to consider its *instantaneous frequency*. This seismic attribute is considered a good tool for lateral seismic character correlation. The instantaneous frequency is a measure of time dependent mean frequency. It may be difficult to interpret, as noise makes it unstable but one finds it useful to look at the high amplitude reflector which is associated with the low frequency anomaly. The value of Instantaneous Frequency

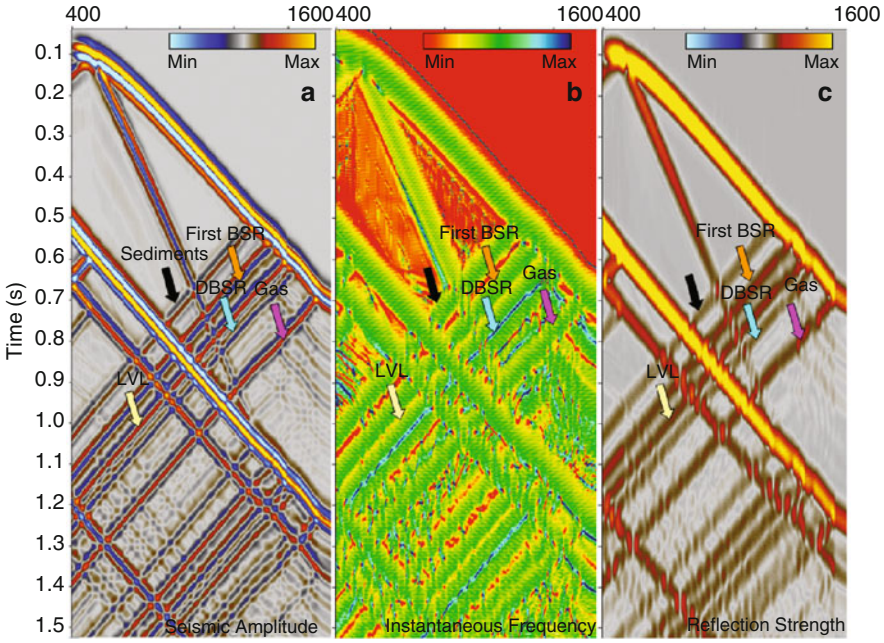

Fig. 6.8 Seismic attributes for a complex BSR model. These instantaneous seismic attributes are helpful in identifying single and multiple BSRs. (**a**) Seismic amplitude (**b**) Instantaneous frequency (**c**) Reflection Strength

lies in that high frequencies are attenuated by gas and condensate in reservoirs. In the past, a low instantaneous frequency anomaly has been used to predict conventional hydrocarbons (oil & gas) accumulations in the oil industry. Instantaneous frequency enables one to detect the regions of high attenuation by absorption of seismic energy due to internal friction. For a particular region of high attenuation high frequency will be preferentially attenuated. This results in a shift towards lower frequencies of reflection below regions of high attenuation. For the present objectives it is expected to visualize a high-frequency anomaly due to the relatively high velocity of the gas hydrates.

The interpretation of instantaneous frequency attribute could provide some meaningful information which may help in identifying the gas zones. The instantaneous frequency attribute responds to both wave propagation effects and depositional characteristics, hence it is a physical attribute and can be used as an effective discriminator. It can be used as hydrocarbon indicator by low frequency anomaly. This effect is sometimes accentuated by unconsolidated sands due to the oil content in the pores. It can also be used as bed thickness indicator. Higher frequencies indicate sharp interfaces such as exhibited by thinly laminated shales, lower frequencies are indicative of more massive bedding geometries, e.g. sand-prone lithologies. Another piece of information we can extract from the seismic data are the locations where instantaneous frequencies jump or exhibit a negative sign.

These sign reversals are caused by closely-arriving reflected wavelets. Therefore, the time derivative of the phase function will contain the indicators for thin beds, in the form of large variations of instantaneous frequency. Its smooth variation will relate to bedding characteristics. BSR has predominantly reversed apparent polarity (Fig. 6.8a) and easily recognized on the seismic section. The occurrence of DBSR like feature is associated with the LVL, which is assumed within the gas hydrate zone. The instantaneous frequency plot of seismic data displays high and low frequencies represented by blues and red respectively. The dominant instantaneous frequency of the seismic data shifts from about 140 Hz above the BSR to 75 Hz for reflections in the zone of free gas. The DBSR can be identified as a strong event in the instantaneous frequency plot (Fig. 6.8b). A shift to lower frequencies occurs beneath the BSR, which indicate high attenuation in the underlying layers. Gas charged sediment cause high absorption in addition to a sharp decrease on compressional wave velocity. Low frequency shadows are therefore commonly associated with the occurrence of free gas, if they occur beneath highly reflective layers indicating strong acoustic impedance contrast (Taner et al. 1979; Yilmaz 1987; Yilmaz et al. 2006 and Taylor et al. 2000).

References

Aharon, P., Roberts, H.H., Snelling, R., 1992. Submarine venting of brines in the deep Gulf of Mexico: observations and geochemistry. Geology 20, 483–486.

Bellefleur, G., Riedel, M., Brent, T., 2006. Seismic characterization and continuity analysis of gas-hydrate horizons near Mallik research wells, Mackenzie Delta, Canada. Lead. Edge 25, 599–604.

Chapman, R., Pohlman, J., Coffin, R., Chanton, J., Lapham, L., 2004. Thermogenic gas hydrates in the northern Cascadia Margin. EOS. Trans. A.G.U. 85(38), 361–365.

Collett, T.S., 1995. Gas hydrate resources of the United States. In: Gautier, D.L., Dolton, G.L., Takahashi, K.I., and Varnes, K.L. (Eds.). National assessment of United States oil and gas resources on CD-ROM: U.S. Geological Survey Digital Data Series 30, 1 CD-ROM.

Dillon, W.P., Danforth, W.W., Hutchinson, D.R., Drury, R.M., Taylor, M.H., Booth, J.S., 1998. Evidence for faulting related to dissociation of gas hydrate and release of methane off the southeastern United States. In: Henriet, J.-P., Mienert, J. (Eds.), Gas Hydrates: Relevance to World Margin Stability and Climate Change, Geological Society Special Publications, London, vol. 137, pp. 275–291.

Dillon, W.P., Lee, M.W., Fehlhaber, K., and Coleman, D.F., 1993. Gas hydrates on the atlantic continental margin of the United States - controls on concentration: The Future of Energy Gases, USGS Professional Paper 1570.

Domenico, S.N., 1977. Elastic properties of unconsolidated porous sand reservoirs. Geophysics 42, 1339–1368.

Ecker, C., Dvorkin, J., and Nur, A., 1998. Sediments with gas hydrates: Internal structure from A YO. Geophysics 63, 1659–1669.

Ginsburg, G.D., Soloviev, V.A., 1994. Mud volcano gas hydrates in the Caspian Sea. Bull. Geol. Soc. Den. 41, 95–100.

Ginsburg, G.D., 1998. Gas hydrate accumulation in deep-water marine sediments. In: Henriet, J.-P., Mienert, J. (Eds.). Gas Hydrates — Relevance to World Margin Stability and Climate Change. The Geological Society Special Publication, vol. 137, pp. 51–62.

Heggland, R., 1998. Gas seepage as an indicator of deeper prospective reservoirs. A study based on exploration 3D seismic data. Mar. Pet. Geol. 15, 1–9.

Heggland, R., 2004. Hydrocarbon migration and accumulation above salt domes – Risking of prospects by the use of gas chimneys: Presented at the 24th Annual Gulf Coast Section, SEPM.

Hovland, M., Judd, A.G., 1988. Seabed pockmarks and seepages. Impact on Geology, Biology and the Marine Environment. Graham & Trotman Ltd., London. 293 pp.

Holbrook, W.S., Hoskins, H., Wood, W.T., Stephen, R.A., Lizarralde, D., and Leg 164 Science Party, 1996. Methane hydrate and free gas on the Blake Ridge from vertical seismic profiling. Science 273, 1840–1843.

Holbrook, W.S., Gorman, A.R., Hornbach, M., Hackwith, K.L., Nealon, J., Lizarralde, D., Pecher, I.A., 2002. Seismic detection of marine methane hydrate. Leading Edge 21(7), 686–689.

Hyndman, R.D., Spence, G.D., Chapman, R., Riedel, M., Edwards, R.N., 2001. Geophysical studies of marine gas hydrate in Northern Cascadia. Natural Gas Hydrates: Occurrence, Distribution, and Detection. AGU Monograph, vol. 124, pp. 273–295.

Kvenvolden, K.A., 1988. Methane hydrate – a major reservoir of carbon in the shallow geosphere. Chem. Geol. 71, 41–51.

Kvenvolden, K.A., 1993a. Gas hydrates as a potential energy resource – a review of their methane content. In: Howell, D.G. (Ed.). The Future of Energy Gases – U.S. Geological Survey Professional Paper 1570: Washington, United States Government Printing Office, p. 555–561.

Kvenvolden, K.A., 1993b. A primer on gas hydrates. In: Howell, D.G. (Ed.). The Future of Energy Gases – U.S. Geological Survey Professional Paper 1570: Washington, United States Government Printing Office, p. 279–291.

Lammers, S., Suess, E., Hovland, M., 1995. A large methane plume east of Bear Island (Barents Sea): implications for the marine methane cycle. Geol. Rundsch. 84, 59–66.

Ligtenberg, J., 2003. Unraveling the petroleum system by enhancing fluid migration paths in seismic data using neural network pattern recognition techniques. Geofluids 3, 255–261.

Lowrie, A., Max, M.D., Hamiter, R., Lerche, I., Bagirow, E., 1997. Hydrate Stability Zone Permanence Along Dynamic Louisiana Offshore. Gulf Coast Association of Geological Societies Transactions, V. 47, pp. 311–315.

MacDonald, I.R., Guinasso, N.L., Sassen, R., Brooks, J.M., Lee, L., Scott, K.T., 1994. Gas hydrates that breaches the sea floor on the continental slope of the Gulf of Mexico. Geology 22, 699–702.

Max, M.D. (Ed). 2000. Natural Gas Hydrate. In: Oceanic and Permafrost environments. Kluwer Academic Publishers, London, Boston, Dordrecht, 414 pp.

Max, M.D., and Lowrie, A., 1992. "Natural Gas Hydrates: Arctic and Nordic Sea Potential," Arctic Geology and Petroleum Potential. In: Vorren, T.O. et al., (Ed.). Norwegian Petroleum Society, 1992.

Max, M.D., and Lowrie, A., 1996. Oceanic methane hydrates: A &&frontier'' gas resource. Journal of Petroleum Geology 19, 41–56.

McConnell, D.R., Kendall, B.A., 2002. Base of gas hydrate stability, northwest Walker Ridge, Gulf of Mexico. Offshore Technology Conference Proceedings. Houston, Texas, OTC paper # 14103.

Meldahl, P., Bril, R.H.R., de Groot, P., Aminzadeh, F., 2002. Identifying seismic objects by their texture, orientation and size:A new interpretation tool. Presented at the AAPG Annual Convention and Exhibition.

Prior, D.B., Doyle, E.H., Kaluza, M.J., 1989. Evidence for sediment eruption on deep sea floor, Gulf of Mexico. Science 243, 517–519.

Rajput S., 2008. Analysis of Ocean Bottom Seismometer data for gas hydrate studies and subsurface models. Ph.D Thesis, Department of Geophysics, Kurukshetra University, Kurukshetra.

Sager, W.W., Lee, C.S., MacDonald, I.R., Schroeder, W.W., 1999. High-frequency nearbottom acoustic reflection signatures of hydrocarbon seeps on the northern Gulf of Mexico continental slope. Geo Mar. Lett. 18, 267–276.

Sager,W.W., MacDonald, I.R., Hou, R., 2003. Geophysical signatures of mud mounds at hydrocarbon seeps on the Louisiana continental slope, northern Gulf of Mexico. Mar. Geol. 198, 97–132.

Sassen, R., Losh, S.L., Cathles, L., III., Roberts, H.H., Whelan, J.K., Milkov, A.V., Sweet, S.T., DeFreitas, D.A., 2001. Massive vein-filling gas hydrate: relation to ongoing gas migration from the deep subsurface of the Gulf of Mexico. Mar. Petr. Geol. 18, 551–560.

Schmuck, E.A., Paull, C.K., 1993. Evidence for gas accumulation associated with diapirism and gas hydrates at the head of the Cape Fear Slide. Geo-Mar. Lett. 13, 145–152.

Sultan, N., Cochanat, P., Foucher, J.-P., Mienert, J., Haflidason, H., Sejrup, H.P., 2003. Effect of gas hydrate dissociation on seafloor slope stability. In: Locat, J., Mienert, J. (Eds.), Submarine Mass Movements and their Consequences. Kluwer Academic, Dordrecht, pp. 103–111.

Taner, M.T., Koehler, F., Sheriff, R.E., 1979. Complex seismic trace analysis, Geophysics 44, 1041–1063.

Taylor, M.H., Dillon, W.P., Pecher, I.A., 2000. Trapping and migration of methane associated with the gas hydrate stability zone at the blake ridge diapir: new insights from seismic data. Mar. Geol. 164, 79–89. doi:10.1016/S0025-3227(99)00128-0.

Trehu, A.M., Torres, M.E., Moore, G.F., Suess, E., and Bohrmann, G., 1999. Temporal and spatial evolution of a gas-hydrate-bearing accretionary ridge on the Oregon continental margin. Geology 27, 939–942.

Vanneste, M., Jeffrey, P., De Batist, M., Klerkx, J., 2002. Atypical heat flow near gas hydrate irregularities and cold seeps in the Baikal Rift Zone. Mar. Pet. Geol. 19, 1257–1274.

Wood, W.T., Gettrust, J.F., Chapman, N.R., Spence, G.D., Hyndman, R.D., 2002. Decreased stability of methane hydrates in marine sediments owing to phase boundary roughness. Nature 420, 656–660.

Yilmaz, O., 1987. Seismic Data Processing, Society of Exploration Geophysicists, Tulsa, OK.

Yilmaz, O., Eser, M., Berilgen, M., 2006. A case study of seismic zonation in municipal areas. Lead. Edge 25(3), 319–330.

Chapter 7
Geophysical Surveys and Data Analysis

Abstract Gas hydrates occur worldwide in marine sediments and can play a major role in contributing world's energy requirements. The identification and assessment of gas hydrate volume can be done by different geophysical techniques including various types of seismic surveys, like (2D/3D conventional, ocean bottom seismic, vertical seismic profiling, cross-well seismic and multi-component), well logging, and control source electromagnetic surveys. This chapter provides a brief of various survey designs and optimal survey parameters for gas hydrate exploration. Reflection seismic profiles are useful to construct the compressional velocity (V_P) model for hydrate bearing formations and to explore its possible lateral variation and thereby provide possible relevant interpretations in terms of the geology/tectonics of the subsurface earth. Ocean bottom seismic surveys are the key to explore deeper structures and to build the shear velocity model for hydrates. The results of various gas hydrate models together with the field data reveals that seismic methods are able to detect the lower stratigraphic bound of the hydrates as there is no seismic reflection from upper bound and there is no seismic signature within the hydrate stability zone. Another technique for hydrate detection includes well logging (electrical resistivity, gamma ray etc.) which, provide point measurements and provide no information into the lateral distribution of hydrates. Electromagnetic methods for hydrate detection are also feasible but require more field attempts and laboratory studies.

7.1 Introduction

The digital revolution in the 1960 profoundly changed seismic acquisition, and made it possible to record more data by increasing the number of channels and fold of coverage. Because of this digital revolution, in 1970s switch over from calculators to computers led to a new era of processing algorithms. In the 1980 seismic industry took an additional step forward which was the beginning of three dimensional seismics that served the oil and gas industry for several decades.

N.K. Thakur and S. Rajput, *Exploration of Gas Hydrates*,
DOI 10.1007/978-3-642-14234-5_7,

Finally in 1990 the geophysicists were able to provide the subsurface images not just in three dimensions in time but also in depth. In twenty first century, with a new development of seismically monitoring the reservoirs gave the time-lapse three dimensional survey data, which constitutes the basis of the four dimensional (4D) seismic method, and one could track the flow paths and fluid distribution in the reservoirs throughout their lifetime. Nowadays not just P-waves but also converted S-waves are recorded for a wide range of targets.

Reflection seismic profiles are useful to reconstruct the compressional velocity (V_P) field and to explore its possible lateral variation applying inversion techniques (e.g. inversion of travel times), and thereby provide possible interpretations in terms of the geology/tectonics of the subsurface earth. Deeper layers are infact difficult to explore using conventional reflection profiling because a horizon which is strongly reflective and high in the stratigraphic column, such as a bottom simulating reflector (BSR), effectively masks signal from the underlying structure (Jarchow et al. 1994). Ocean bottom seismometer data are required to investigate layers below the BSR (from refracted waves) and to assess the shear velocity (V_S) structure.

The transmission of shear waves was impossible in water because of the non-supportive nature for fluid. Under certain conditions, for example, if the conventional energy source is used then the phenomena of conversion of part of compressional (P) wave energy into shear waves, can be utilized the imaging of the subsurface by down-going P waves and up-coming shear (S) waves. These converted shear waves can be recorded by placing a horizontal component geophone on the ocean floor. The reflected P wave can be recorded simultaneously by seismometers and hydrophones. For such an instrument configuration, the term four-component (4C) technology has been introduced. The direct measurement of shear waves in ocean studies has been attempted by several methods, mainly using ocean bottom seismometers (OBSs) and ocean bottom cables (OBCs), which consist of four components, in each case including a three-component geophone (3C) and a hydrophone. There are certain shortcomings in using OBCs, such as distortion of the shear-wave component by the cable, non-coupling of the geophone to the ground in rugged terrain, drifting of the ship in rough seas, and higher expense. Scientific organizations have been using OBS data for the past two decades and have obtained promising results for deep marine environments (Bangs et al. 1993; Christeson et al. 2000; Kim et al. 2000; Kopp 2002; Walther 2003).

OBS receivers also allow the recording of wide azimuth P-wave data, thereby overcoming a major limitation of current 3D practice. Since both the seismic source and the geology create a large variety of wave types, one needs full multicomponent seismic recording and analysis techniques to unravel and use all of the seismic information content. By reducing ambiguities in interpretation, multicomponent data promote an improved and more accurate evaluation of gas hydrate deposits (Digranes et al. 1996; Mikhailov et al. 2001). It has been argued that converted waves generated at different interfaces due to the impedance contrast could be utilized for studying the petrophysical properties of gas hydrates in the marine environment (Gaiser et al. 2001). In practice, the synthetic seismograms are generated for multi-channel seismic data considering the S-wave velocity

information, derived as a weighted compressional velocity for different geological formations (Domenico 1977; Castagna et al. 1985, 1993; Alfaraj 1993; Huffman and Castagna 2001). Since the late 1970s, analyses of multi-channel seismic data have revealed a number of BSRs along the continental margins of different parts of the world, suggesting the presence of gas hydrate in these regions (Shipley et al. 1979a, b; Hyndman and Spence 1992; Katzman et al. 1994; Tinivella 1999; Carcione and Tinivella 2000).

7.2 2D/3D Conventional Seismic Surveys

In present world, conventional seismic surveys are by far the most common form of seismic experiments and are most popular because of detection ability of BSR and its different response in most of the geophysical parameters. In reflection seismic surveys, the survey vessel tows multichannel receiver cable up to several km in length, at a depth of few meters, with the end marked by a tail-buoy and radar sensors. Reflection seismic surveys are usually conducted using specialized vessels that tow very long (approx 10–12) km, up to 18 seismic streamers, with a separation distance of 50–150 m between the streamers. Maintaining the streamer separation and monitoring their position requires a considerable amount of equipment to be towed astern of seismic vessel, including paravanes (or "doors"), mono-wings, dilt floats (located at the head of each cable) and tail buoys which are located at the end of each cable (Fig. 7.1). The seismic energy source is usually an array of air guns mounted below large marker buoys and towed immediately behind the survey vessel. Before launching the field experiment, it is mandatory to plan for ascertaining good response from the subsurface targets.

Two types of seismic surveys are available to the geophysicist: two-dimensional (2D) surveys, or three-dimensional (3D) surveys. 2D is generally used for regional

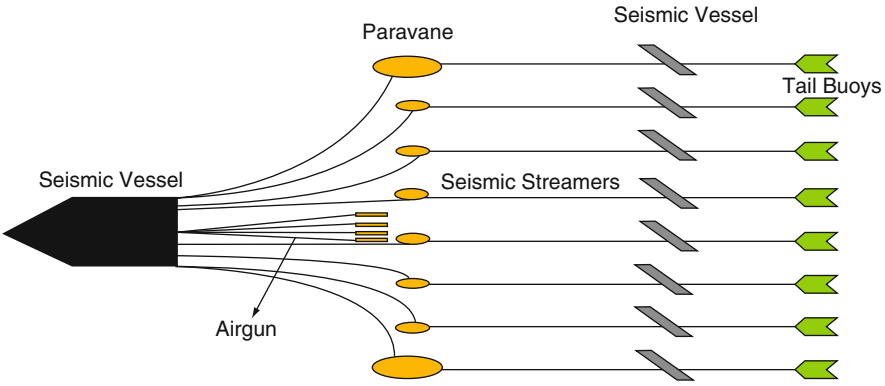

Fig. 7.1 Schematic (not to scale) showing a simplified configuration for a 3D marine seismic vessel towing eight streamers. Airgun is situated in the middle of the seismic streamers

reconnaissance or for detailed exploration work where economics may not support the greater cost of 3D. For gas hydrate detection in marine environment, both (2D and 3D) surveys can be launched. Simple marine seismic data acquisition geometry can be understood with the help of a layered gas hydrate model (Fig. 7.2). The model parameters are given in Table 7.1. In the geological regions where hydrate occurr in shallow sediments, the seismic data can be acquired with 125 Hz source to detect the hydrate response on seismic record (Fig. 7.3). A real data example from a project which was initiated by Korea is shown in Fig. 7.4, showing one of the seismic stack section of a seismic survey conducted in the East Sea of Korea to

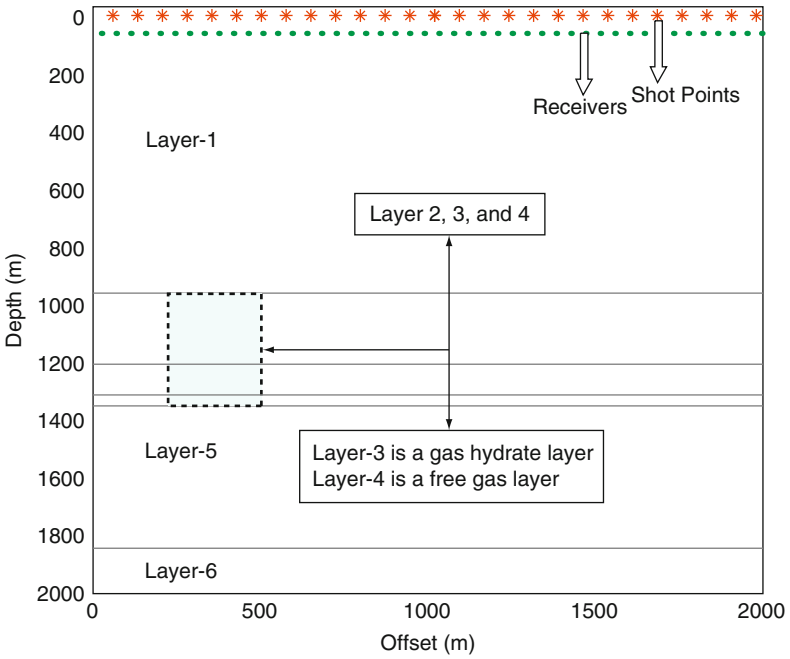

Fig. 7.2 Conventional seismic data acquisition configuration for a region. *Red dots* are the shot points. *Green dots* are the receivers. *Layer-1* is representing the water column, *Layer-2* is representing sediments, *Layer-3* is a gas hydrate layer and *Layer-4* is a free gas layer. The subsequent layers (*5* and *6*) are the sediments. The corresponding parameters are shown in Table 7.1

Table 7.1 Model parameters for a layered gas hydrate structure (Fig. 7.2)

Layer Information		α (m/s)	β (m/s)	ρ (kg/m3)	Gradient
Layer-1	Water	1,500	0	1,000	0.5
Layer-2	Sediments	1,700	819	1,750	0.5
Layer-3	Gas Hydrates	1,875	1,078	1,998	0.5
Layer-4	Free Gas	1,450	865	1,896	0.5
Layer-5	Sediments	2,250	1,300	2,160	0.5
Layer-6	Sediments	2,400	1,390	2,160	0.5

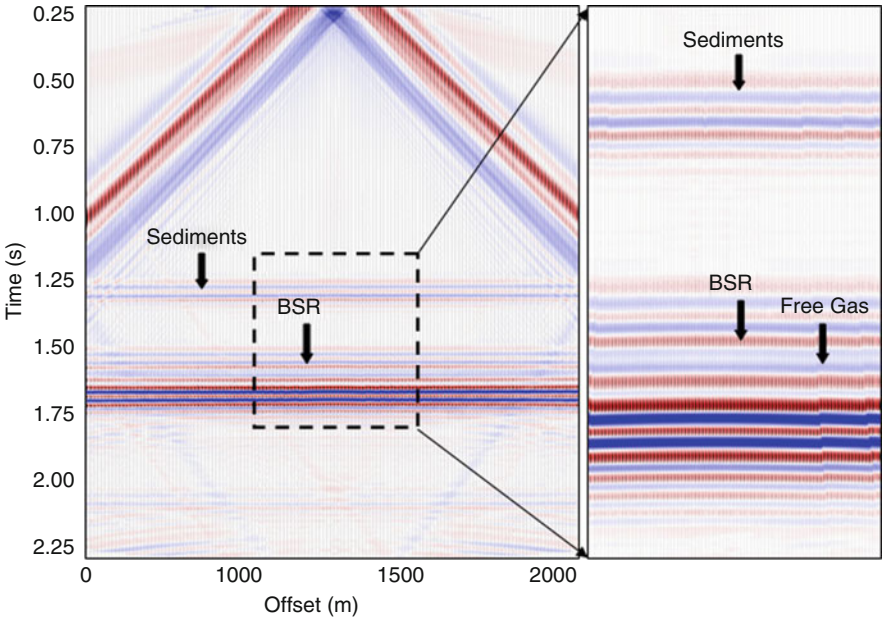

Fig. 7.3 Synthetic data example for the configuration shown in Fig. 7.2. The model parameters are given in Table 7.1. In the post stack migrated section reflections from sediments, BSR and free gas are identified and marked. BSR is showing a clear polarity reversal

quantify the potential magnitude and distribution of natural gas hydrates. Although there is no specific configuration to design the seismic surveys for gas hydrate studies, however, one need to be more careful in planning the receiver spacing, shot interval, source signature, volume of source etc. Receivers should be closely deployed for remote detection of gas hydrates.

7.3 4C Ocean Bottom Seismic Surveys

It's a hybrid marine data acquisition of deploying four component sensors on the ocean bottom and a conventional marine seismic source, particularly an array of air guns, towed by the seismic vessel. Configuration of four component OBS survey is shown in Fig. 7.5. Since 4C seafloor seismics is a new technology, there are many methods and instruments, developed by different geophysical contractors, to accomplish the objectives. Different types of acquisition systems are available today to acquire the 4C seismic data. Cable-based ocean bottom systems and node-based ocean bottom systems are generally used for these operations. In the data acquisition stage, three basic obstacles need to be addressed: positioning of the sensors, orientation of geophones and coupling of the geophones.

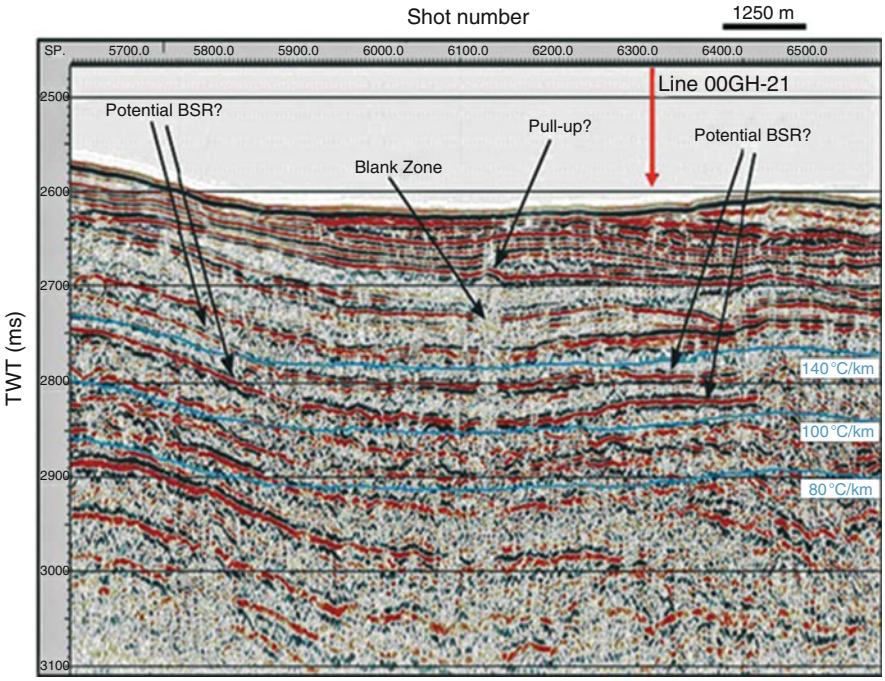

Fig. 7.4 Real data example resulted from a seismic survey over East Sea of Korea. The experiment was conducted for the gas hydrate related studies. Different features associated with the occurrence of gas hydrates such as BSR, blank zone, time pull up are marked. (After Lee et al. 2005, reprinted with permission from Springer)

In the present scenario, the positioning and coupling problems are handled in the OBS system. However, the orientation of the sensors remains the main obstacle in the data acquisition stage. Some algorithms have been proposed to correct the orientation and coupling in the processing stage (Yuan et al. 2001, 1996); Gaiser 1997, 1998; Li and Yuan 1999; Li et al. 1999). The OBS is a modular design four component instrument (Bialas and Flueh 1999; Flueh et al. 2002), which incorporates industrial type standard components can be deployed into a fully autonomous mode with an operational range of 6,000 m water depth. Before deployment each part of the OBS should be checked and then placed in an anchor and tied by a the fine wire. Prior to touch down the instrument at the sea floor, the lever deploys the seismometer about 2.0 m to the side of the system carrier. After deployment, the OBS is no longer mechanically in contact with the carrier. With the help of hydro acoustic unit the data can be recorded and stored in situ on the equipment. In multicomponent data recording, hydrophones record P-waves (pressure sensitive) and three geophones record both P- and S-waves. However, the vertical component geophones primarily record P-waves while the horizontal components record S-waves. The orientation of horizontal receivers are not known and both the

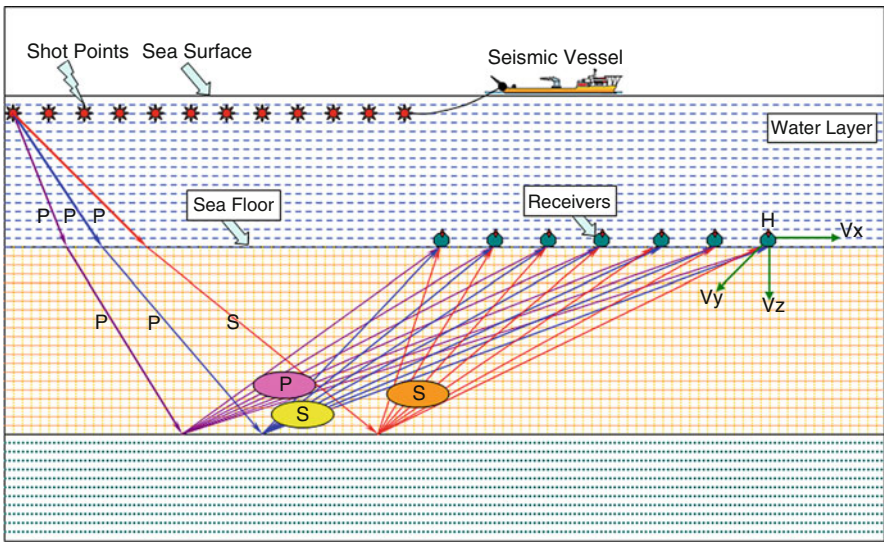

Fig. 7.5 Converted wave survey geometry in marine environment. The *green circles* with *red mark* on the *top* are representing the position of deployed ocean bottom seismometer at the sea bottom. The last OBS indicates all the four components (H, X, Y, Z). Seismic waves (compressional and shear) are represented by *P* and *S* letters. Three possible cases are shown and represented by different colours. In first case (*violet* colour waves) the seismic energy travels as P waves in water then again transmitting as P-waves in sediments and again reflected back to the ocean bottom and recorded by the OBS. In second case (*blue* colour wave) the P-wave is converted to S-wave on the reflector and in the third case (*red* colour wave) the ocean bottom and the reflector are playing as a conversion boundary

receivers record S-waves. The orientation of geophones are rotated to radial and transverse components to maximize the S-wave energy on the radial component.

Different aspects of OBS seismic experiments i.e. pre-survey model studies and post survey data evaluation are discussed to make the data recorded more meaningful. For pre-survey measures, synthetic response of different hydrate and free gas models was obtained to arrive at travel time curve pattern. The validity of observed travel time patterns depends upon the dataset synthesized or acquired. In this context a synthetic data example supports the arguments. For post survey assessment a field data example from Offshore USA, Hydrate ridge has been discussed. The hydrate ridge experiment was conducted exclusively for studying the physical properties of gas hydrates and associated free gas.

7.3.1 Patterns in Travel Time for Ocean Bottom Seismometer Experiments

To study the travel time patterns associated with gas hydrates, a 2D ray tracing technique (Zelt and Smith 1992) is appropriate. This technique proves to be very

useful for studying gas hydrates on regional basis. To demonstrate as an examples, here a modeling study is presented; This example presents different patterns in travel times curves for Ocean Bottom Seismic experiment which are further validated by simulation of seismic data.

A 2D (x,z) isotropic medium is assumed. The velocity model is composed of a sequence of layers separated by boundaries consisting of linked linear segments of arbitrary dip. Ray tracing is performed by numerically solving the ray tracing equations for 2D media using a Runge Kutta method. Travel times are calculated by numerical integration along ray paths using the trapezoidal rule. The travel times correspond to any ray paths which can be traced through the model, being either first or later arrivals. The shear wave velocity (V_S) is calculated from interpolated compressional wave velocity using Poisson's ratios specified for each trapezoid. It has been suggested that V_P is sensitive both to small amounts of free gas in the sediments and to how the free gas is distributed in the pore spaces. Hence the estimation of free gas from seismic velocity can be only approximate (Domenico 1977). To validate the different patterns a finite difference simulation technique (Rajput 2008) is used. This technique takes the complete wave field and structure effect into account and generates the shot gathers instead of the common midpoint (CMP) gathers. To compare with the travel time curves from the ray tracing, the synthetic data were treated as recorded data and taken through a processing sequence to CMP gathers.

2D ray tracing was done for three OBSs, which were located on the sea floor along a 40 km profile at a 10 km separation. Two different sea-floor depths, 1,000 and 2,000 m were considered (Figs. 7.6 and 7.7). In both cases the overburden sedimentary layer above the GHZ has a thickness of 200 m. Based on the available estimates of gas hydrate and free gas layer thicknesses from different locales in the world, GHZ thicknesses of 100, 150, and 200 m and FGZ thicknesses of 50 and 100 m were tested by the modeling. The GHZ and FGZ were restricted to a 10 km zone in the center of the model. In all cases the shooting interval was 100 m.

Reflection and refraction from different interfaces are recorded on the three OBSs. Based on the geological conditions offshore eastern India and through a literature survey, the best was one where the thickness of the GHZ is 150 m. For the model with the sea floor at 1,000 m depth, P-wave velocity increases from 1.7 to 2.0 km/s in the GHZ. Below the GHZ, a 100 m thick low-velocity layer of free gas ($V_P = 1.4–1.5$ km/s) was included in the sedimentary sequence. For the case with the sea floor located at 2,000 m depth, the velocities for the GHZ and the FGZ are varied to account for the greater depth. The P-wave velocity model for this case has an increase from 1.8 to 2.25 km/s in the GHZ. Below it, a low-velocity layer of thickness of 100 m with velocity of 1.45–1.55 km/s is placed, indicating the presence of FGZ in the sedimentary layer (Rajput 2008).

Here the main assumption is that the geometry for S-wave modeling is the same as that for P-wave modeling. In the final S-wave model for a 1,000 m water layer, V_S in the GHZ increases from 0.90 to 1.05 km/s and the FGZ has a V_S of 0.75 km/s. For the model where the seafloor is located at 2,000 m, V_S in the GHZ increases from 0.90 to 1.20 km/s and the FGZ has a Vs of 0.85 km/s. When the velocity gradient of

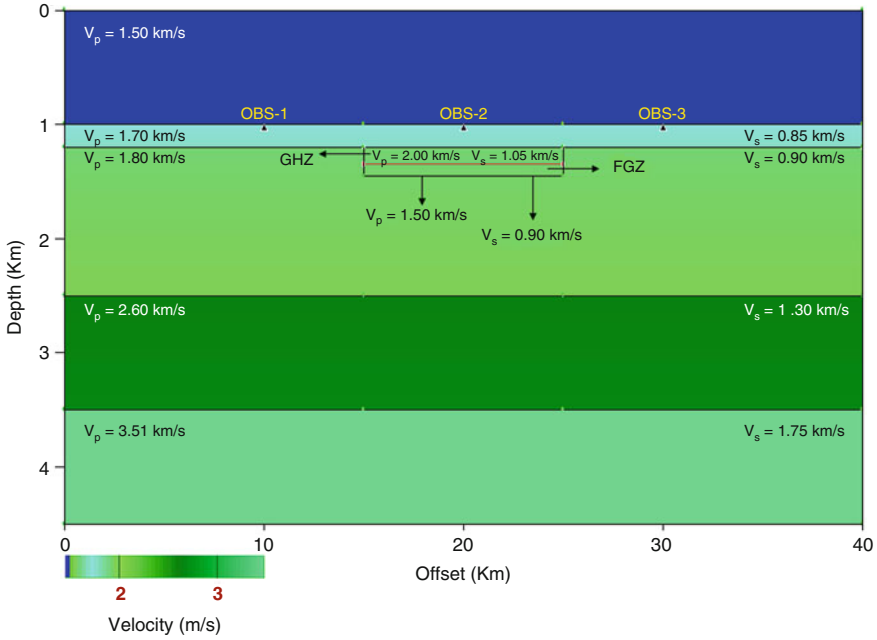

Fig. 7.6 P-wave velocity model with 1,000 m water depth, 150 m thick gas hydrate zone (GHZ) and 50 m thick free gas zone (FGZ)

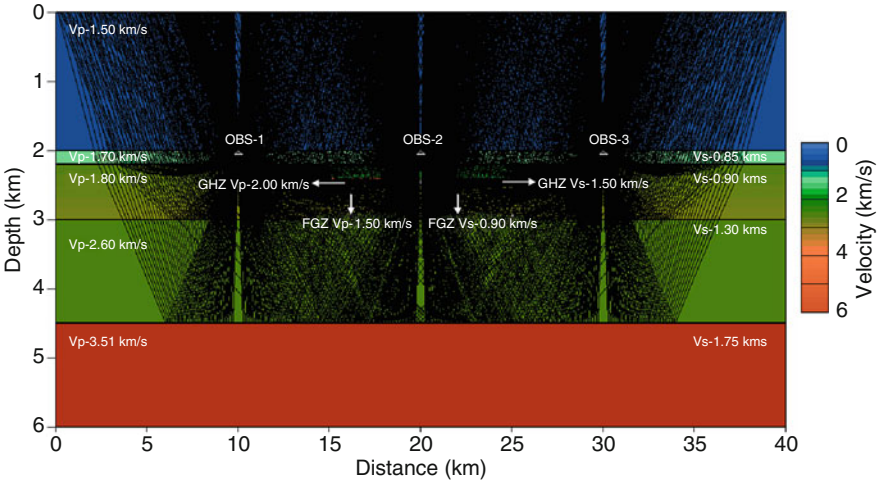

Fig. 7.7 P-wave velocity model with 2,000 m water depth, 150 m thick gas hydrate zone (GHZ) and 50 m thick free gas zone (FGZ) and rays traced for all Ocean Bottom Seismometers

the overlying GHZ layer is sufficiently high the velocity inversion can be identified with the help of travel-time skips, where the first arrival refraction cycle dies out in quick succession, creating a shadow zone (Hirahara 1980; MacLeod 1982).

The diving waves again emerge after encountering the high velocity layer beneath the FGZ, creating the "skip" in the first arrivals. Keeping other parameters fixed an increase/decrease in the thickness of the low-velocity FGZ will lead to a corresponding increase/decrease in the magnitude of the travel-time skip. From the ray paths it is clear that the arrivals at OBS-2 are more influenced by the GHZ and FGZ than OBS-1 and -3 (see Fig. 7.7 for the model with water depth of 2,000 m), hence only the results for OBS-2 are discussed here. Synthetic seismograms are also generated by wave equation modeling for case with a water depth of 1,000 m (see Fig. 7.8). The travel time skips observed in the travel time curves from ray tracing are also identified in the synthetic seismograms from wave equation modeling and shown in Fig. 7.8.

The P-wave ray tracing allows to identify travel time reflections and refractions as P^X and P_X, respectively, where x is the velocity (see Figs. 7.9 and 7.10). The skips in travel times are more prominent in the case of 100 m thick FGZ compared to when the thickness is 50 m. For OBS-2, deployed in the middle of the section above the zone of interest, the reflections from all the layers, including GHZ and FGZ are observed. Travel time curves produce significant ray bending due to the high acoustic impedance contract (see Fig. 7.10). When the depth of the sea floor is 1,000 m, the S-wave modeling allows one to identify the following for an FGZ thickness of 100 m: For OBS-1, the travel time responses are clearly observed from all the layers, except the GHZ and FGZ. For OBS-2, the travel time responses in terms of reflections are clearly observed for all the layers, including GHZ and FGZ (see Fig. 7.11). Based on analysis of travel-time response in terms of reflection and refraction for detection of GHZ and FGZ, constraints on the model can be placed.

- The study suggest that: Detailed study of travel time skips is important for better resolution of hydrate-bearing sediments at shallower sea floor depths. The ray bending observed for deepwater OBS deployments may further need some investigations.
- Results indicate that it's complicated to identify the response from thin sediment layers with low velocity and the spacing considered here. This is valid for both compressional and shear waves.
- This type of modeling exercise is a must before conducting any real experiments.

7.3.2 Example of 4C Seismic Experiment

A seismic experiment was conducted during the summer of 2002 at the Hydrate Ridge (HR) of the Cascadia convergent margin offshore U.S.A. (Fig. 7.12) using a seismic vessel (R/V Maurice Ewing) and a drilling vessel (JOIDES Resolution) in coordination with Ocean Drilling Program Leg 204. This experiment brought

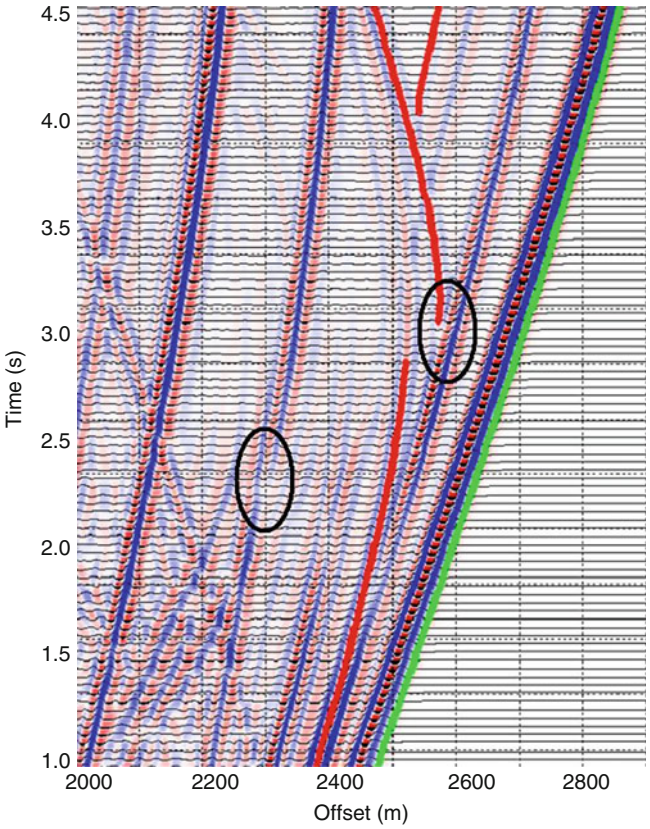

Fig. 7.8 Synthetic seismogram from wave equation modeling for model-1, with observed travel-time skips shown by *black circles*. *Dark red lines* show the picked reflectors. *Green line* shows picked water bottom. *Red wiggle* indicates the maximum amplitude

together multi-disciplinary scientists to understand the origin, formation, distribution, stability, saturation, physical and chemical properties (and proxies), cycle of formation and dissociation, and effects of gas hydrates in an accretionary ridge and adjacent slope basin at Hydrate Ridge. The seismic experiment at Hydrate Ridge was aimed at estimating P- and S-wave velocity profiles in the gas-hydrate-bearing sediments, and calibration of gas-hydrate-bearing sediments with seismic velocities for remote quantification of gas hydrates. Special emphasis was given on S-wave analysis, as from previous studies at Hydrate Ridge no S-wave velocity information was available. This is because the S-wave together with the P-wave velocity is useful in detecting and quantifying gas hydrate and free gas, and inferring paths of fluid migration. An example of the 4C OBS dataset acquired in this experiment is presented in Fig. 7.13. Kumar et al. (2007) presented an example of mapping of P and S wave arrivals in the tau-p domain on the

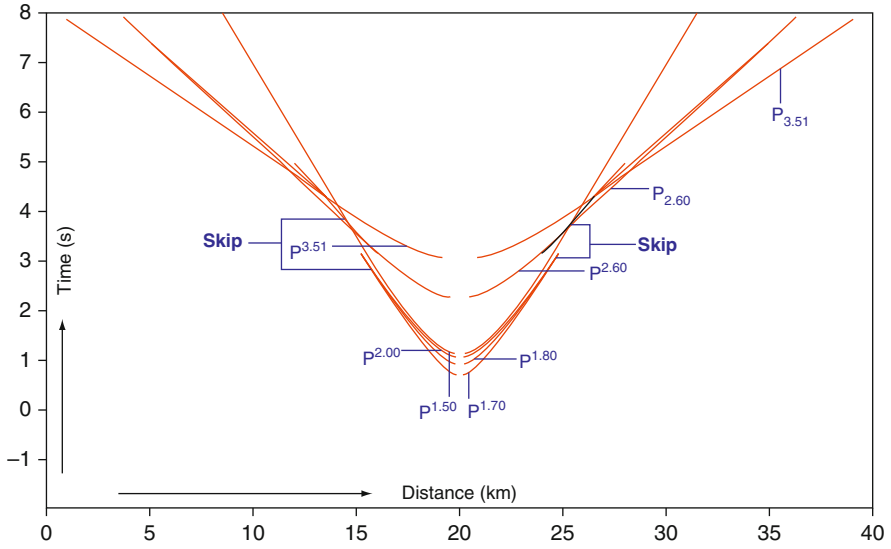

Fig. 7.9 Travel-time response of P-wave velocity (Vp) in terms of reflections (PX) and refractions (PX) for OBS-2 at 1,000 m water depth with a 150 m thick GHZ and 100 m thick FGZ

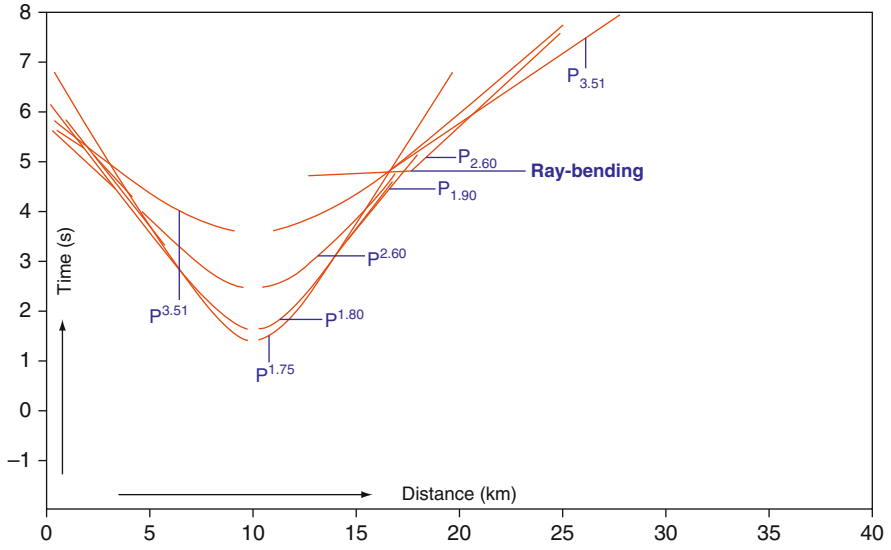

Fig. 7.10 Travel-time responses of P-wave velocity (Vp) in terms of reflections (PX) and refractions (PX) for OBS-1 at 2,000 m water depth with a 150 m thick and 100 m thick FGZ

hydrophone and the radial geophone data for one OBS. In that example the ratio of P to S wave velocities varies from 6.8 near the seafloor to 4.8 near the BSR as shown in Fig. 7.14.

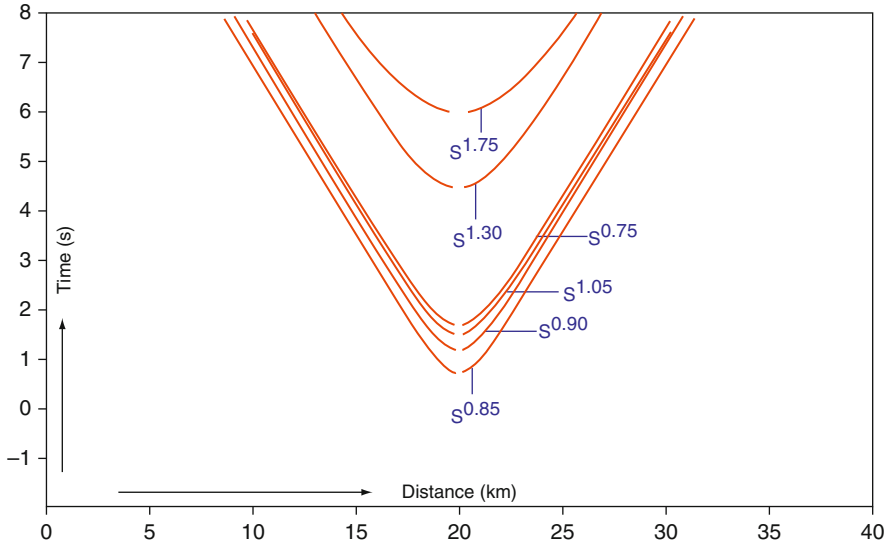

Fig. 7.11 Traveltime responses of S-wave velocity (VS) in terms of reflections (SX) and refractions (SX) for OBS-2 at a 1,000 m water depth with a 150 m thick GHZ and 100 m thick FGZ

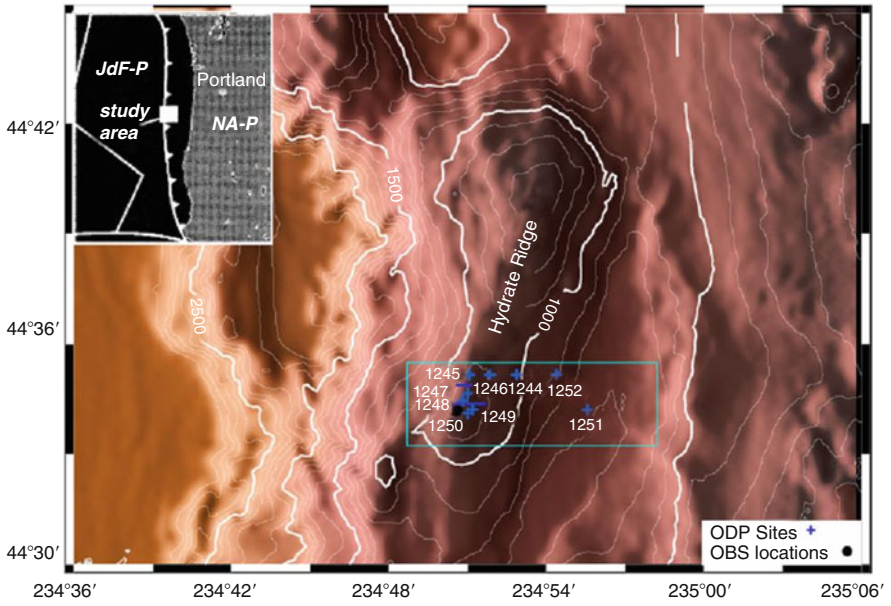

Fig. 7.12 Bathymetry map (contours in m) on the Hydrate Ridge of the Cascadia convergent margin. The ridge is characterized by a northern peak having a minimum water depth of 600 m and a southern peak with a water depth of 800 m. Drilling and seismic experiment (VSP and OBS) are concentrated on the south summit. Inside map shows subduction of the Juan de Fuca plate (JdF-P) beneath the North American plate (After Kumar et al. 2007; reproduced with permission)

7.4 Vertical Seismic Profile Surveys

Conventional VSP data acquisition is considered a non-repeatable effort because it is not practical or cost-effective to re-enter a well after it has been put into production or abandoned. Vertical seismic profiles (VSPs) are commonly used as a densely sampled check-shot survey for sonic velocity calibration and velocity information. In addition, VSP data also are traditionally used to provide the ideal seismic trace at the well for correlation with surface seismics. The checkshot velocity survey is basically a seismic travel time study that measures almost exclusively the downgoing energy traveling from a surface energy source to a downhole geophone tool. The checkshot survey is valuable for velocity control, however, it contains virtually no reflected arrivals and cannot be used to produce an optical reflection seismic image of the subsurface unless it is used to calibrate a sonic log that has been transformed into a hybrid known as a synthetic seismogram. There is a similarity in VSPs and surface-seismic data acquisition, the source is similar at main frequencies (~20–120 Hz). For higher resolution sonic log operates in KHz range, which could be averaged out by up-scaling for time-to-depth conversion of seismic profiles. It's not easy to integrate the surface seismic with sonic data because of possible frequency-dependency issues of seismic velocities. It is also simpler to study seismic attenuation with VSPs than with surface towed data, which may be of particular interest because of recent observations of high

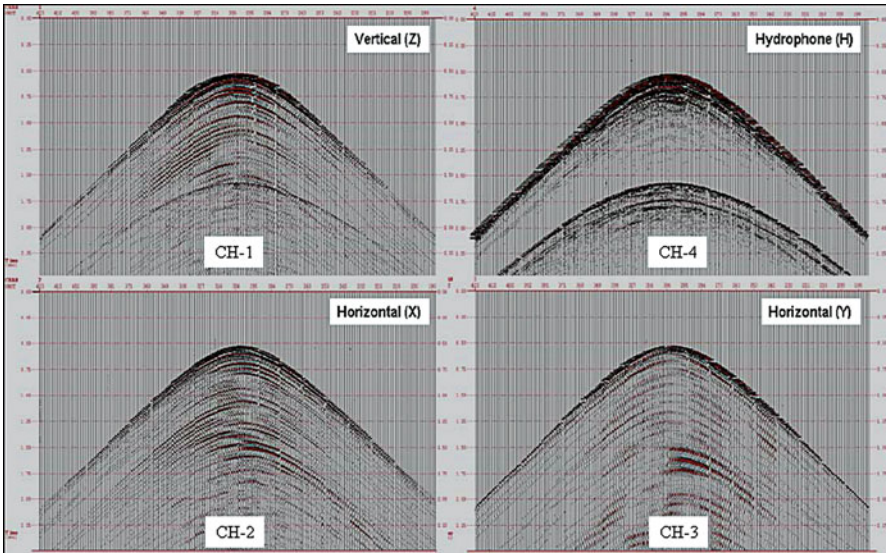

Fig. 7.13 All the four components (two horizontal, one vertical and one hydrophone) of OBS data, acquired over Hydrate Ridge. These components are recorded in different channels, which could be optimized during installation. Here Channel-1 records Vertical (Z) component; Channel-2 records Hydrophone (H) component; Channel-3 records Horizontal (X) component; Channel-4 records Horizontal (Y) component

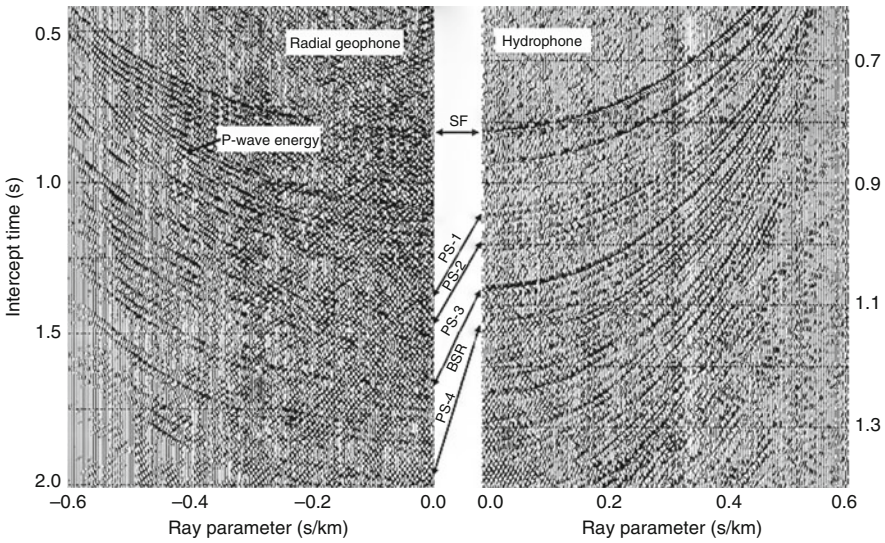

Fig. 7.14 Mapping of P and S wave arrivals in the tau-p domain on the hydrophone and the radial geophone data, respectively, at OBS. The ratio of P to S wave velocities varies from 6.8 near the seafloor to 4.8 near the BSR. Five reflectors are shown by *arrows*, including the response at seafloor (SF, first arrival as P wave), and the four PS wave events. Note that identifying converted S waves near vertical propagation is difficult because P to S wave conversions are weak. Stronger converted S waves are found at far angles (higher absolute ray parameter values). (After Kumar et al. 2007, reprinted with permission)

attenuation in gas-hydrate-bearing sediments (Guerin and Goldberg 2002). For such wide-angle data with near-horizontal rays, knowledge of anisotropy is particularly important (Holbrook 2001), a task that can be achieved with VSPs because receiver depth and vertical velocity are well constrained.

7.4.1 The Beginning Point: Zero Offset VSP

The zero or near offset VSP survey, is defined as a VSP survey where the energy source is positioned as close as logistically possible to the wellhead in an effort to focus downgoing energy in and around the bore hole from near-surface to the target zone and beyond. This geometry favours the recording of reflected arrivals to the downhole geophone tool for about an approximate few meters around the well bore as well as reflected arrivals several hundreds/thousands meters below the target zone of the well. The travel-time of the direct wave from source to receiver gives a travel time-depth function that can be used to convert two-way-travel time sections from surface-reflection profiles to depth, and thus tie events in the reflection data to information from the borehole (Peacher et al. 2010).

Deployment of sources in the water usually limits zero-offset VSPs offshore to recording compressional (P-) waves and hence, offshore zero-offset VSPs usually only yield P-wave velocity (Vp). Onshore, it is possible to use shear (S-) wave sources on the surface together with multi-component geophones in the borehole for acquisition of S-wave VSPs and determination of S-wave velocity (Vs) (Peacher et al. 2010). Zero offset surveys are either run alone or in conjunction with some type of offset vertical seismic profiling. The ZVSP would be used to extract valuable information on seismic propagation to enhance and calibrate surface seismic data processing, including critical information such as attenuation factor (Q), phase differences and identification of multiples. The ZVSP also could be used to predict velocity ahead of the bit, revealing any areas of overpressure, and to enhance the resolution of the 3D seismic cube through the use of matching filters. VSP technology has undergone significant development in recent years, especially with enhanced imaging capabilities (Hornby and Herron 2007, and references therein).

Modern VSP surveys in the hydrocarbon industry often use 3D shooting patterns around long strings of receivers in sometimes deviated boreholes, blurring the boundaries between types of VSPs (Brabdsberg-Dahl et al. 2007). The resulting dense coverage of raypaths and reflection points often allow more accurate analyses than with the "conventional" VSP types listed above. Other survey setups are being used occasionally; e.g., reverse VSPs are sometimes acquired by the industry with shots generated in the borehole (Peacher et al. 2010). ZVSP could serve a very good option for gas hydrate studies because this technique has vertical wavefield propagation, which is known to be zero phase, and has better resolution than surface seismics. Thus far, onshore VSPs have mainly targeted sub-permafrost hydrates. The permafrost layer poses difficulties for seismic imaging further below because it constitutes a significant, highly variable (permafrost sediments are not simply uniformly "frozen", i.e., cemented by ice) seismic high-velocity layer (e.g., Miller et al. 2000). Based on the available information from previous work and recent studies (Peacher et al. 2010; Rajput et al. 2003) key model is selected for simulating ZVSP response. The model parameters are given in Fig. 7.15. The example of ZVSP section at a location is shown in Fig. 7.16. The first arrival is identified and marked on the section, this is check shot. The reflected waves (up-going) from sea floor, sediments and various other reflectors are also identified. Below the sediments a high amplitude and reverse polarity event (with respect to sea floor) is observed which is interpreted as gas hydrate originated bottom simulating reflector (BSR) and marked on the ZVSP section (Fig. 7.16). Below the BSR an enhanced seismic signature is observed which could be interpreted as the gas originated bright spot. One of the key advantages of the synthetic response is that, it's easy to distinguish the up-going and down-going events (Fig. 7.16). If one observes the wavefront propagation for these three ZVSP sections, one is able to identify the reflected (up-going) arrivals as shown in Fig. 7.17. The reflection from sediments, BSR and associated free gas can clearly be distinguished. Fig. 7.17 represents the snapshot recorded at 1.19 s. In the wavefront propagation one is able to recognise

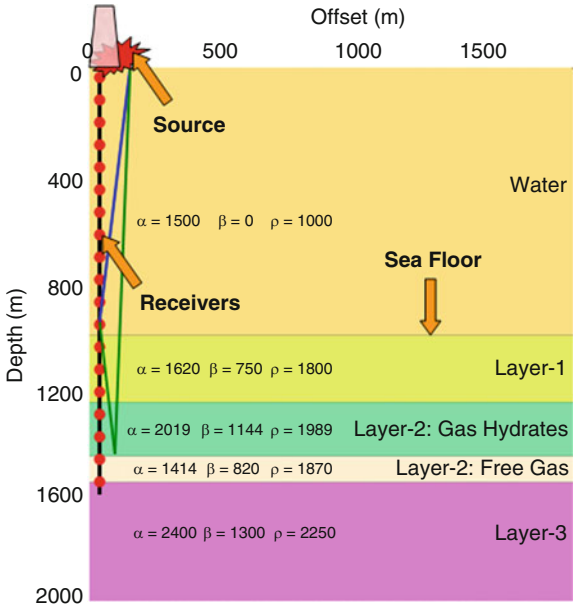

Fig. 7.15 Schematic of layered gas hydrate model for the simulation of zero offset VSP data. The model parameters (compressional (V_p), Shear (V_s) and density (ρ) are given for each layer. Vertical *red dots* are the receivers. The source is located at the surface. The solid *blue line* representing first arrival and solid *green line* represents the reflected wave from the demarcation boundary of gas hydrate and free gas

the reverse polarity and enhanced seismic reflections clearly as indicated in Fig. 7.17. Following are the field examples available for VSP experiments:

- Ocean Drilling Program (ODP) Leg 146 (site 889 off Vancouver island)
- ODP Leg 164 (Blake Ridge)
- ODP Leg 204 (Hydrate Ridge)
- MALLIK gas hydrate campaigns in Mackenzie Delta
- Canada (Mallik 2L-38, 1998; Mallik 3L-38, 2002)
- Nankai Trough Exploratory well (1999–2000)
- Gulf of mexico Joint Industry Project
- IODP Leg 311 (2006)
- Hot Ice (2003–2004)

7.4.2 Walk-Away VSP

WVSP employs a downhole geophone tool assembly and a surface energy source moved along a line extending away from the well. Offsets are designed to image some distance laterally away from the well bore in the direction of the energy source, image a salt dome flank or perhaps a granite intrusive interface. The walk-away

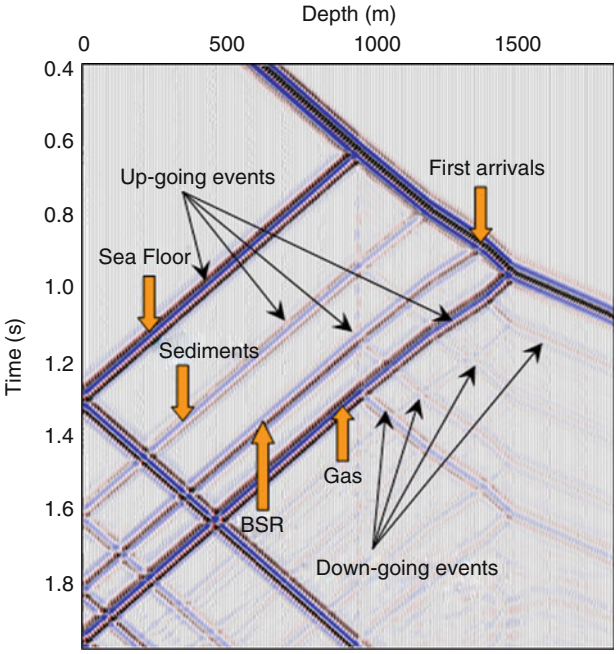

Fig. 7.16 Simulated ZVSP data for the representative model (Fig. 7.15). Both up-going and down-going waves are identified and marked on the profile. BSR is identified as a reverse polarity event. Below the BSR a bright spot like event represents the occurrence of free gas. The arrivals from sea floor and sedimentary layers are also marked

seismic display created from these data can help specify the size, location and fluid saturation levels of a reservoir, defining formation attributes that might otherwise be missed. The reason of choosing WVSP is that it can prove especially in deciding when and where to develop a reservoir or where to optimize the sidetracking of an existing well. It opens the door to multi-fold sampling that increases resolution and improves signal-to noise ratio on images above a specific subsurface point. A walk-away VSP can also help operators to refine their drilling plan and maximize payout possibilities from otherwise marginal reservoirs. The walkaway VSP provide useful information in obtaining a more comprehensive image of geologic complexities in key areas of development and in planning optimal well trajectories through reservoir intervals.

In this case we are able to get some lateral information also, which was not possible in the case of ZVSP because those types of experiments are for vertical imaging. The model which is used for simulation is shown in Fig. 7.15. The synthetic response for Walkaway VSP is shown in Fig. 7.18a. The down-going and up-going events are clearly distinguished. The high amplitude and negative polarity reflector is interpreted as BSR and marked on the Walkaway VSP section. The wavefront propagation for WVSP at 1.16 s is recorded and shown in Fig. 7.18b. Signatures similar to the BSR characteristics can be identified. The down-going

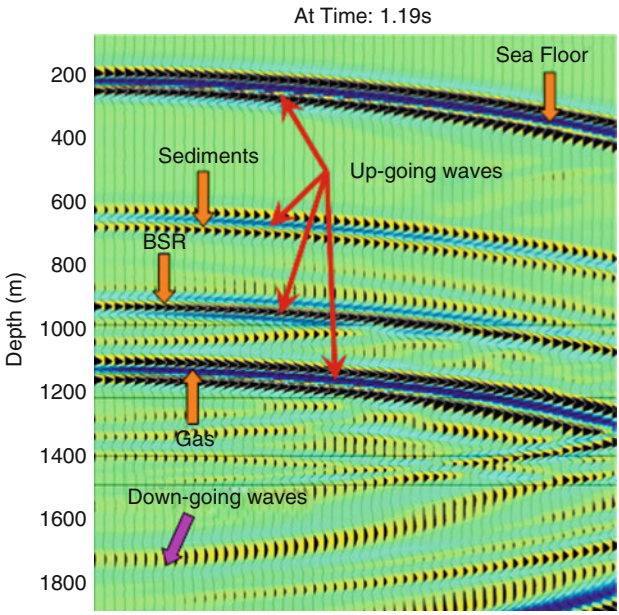

Fig. 7.17 Wavefront propagation (energy propagation) at 1.19 s for corresponding model (Fig. 7.15) and simulated seismic data (Fig. 7.16). Up-going waves and down-going waves are marked. BSR is identified as a reverse polarity event. Below the BSR a bright spot like event represents the occurrence of free gas. The wavefronts from sea floor and sedimentary layers are also marked

and up-going waves are also identified and the reverse polarity characteristics are observed.

7.4.3 Cross-Well Seismic Surveys (CSP)

Crosswell seismic technology has been under development since the early 1980s with many research groups inside major E & P companies involved in early experiments (Lines et al. 1993). Initially researchers focused on tomographic inversion of direct-path travel time data to produce velocity images. Early source technology was limited in reach to about 100 m between wells, and wells had to extend past the reservoir interval for the tomographic image to have full coverage. During the 1990s, researchers at Stanford University demonstrated reflection imaging using crosswell seismic data (Harris et al. 1995). Over the past 15 years, crosswell seismic technology advances have occurred primarily in the area of improved downhole sources and enhanced data processing and analysis methods. In general, characteristics of cross-well records are; (a) cross-well records have higher resolution than surface seismic survey records because the source and

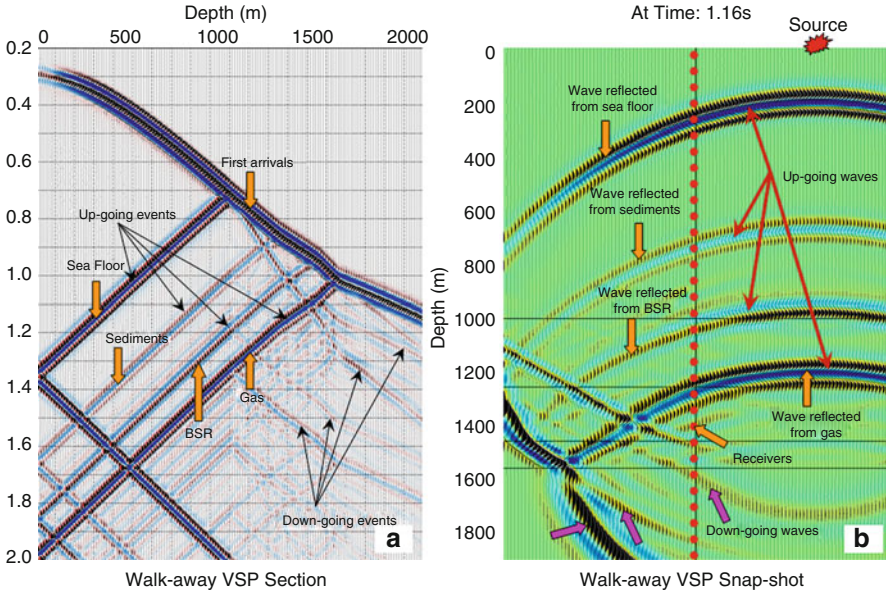

Fig. 7.18 The simulated seismic response for walk-away VSP for the corresponding model (Fig. 7.15). The synthetic seismic data and the wavefront propagation are shown. Both up-going and down-going waves are identified and marked on the profile; (**a**) synthetic walk-away VSP data represents all the identified arrivals from different reflectors. BSR is marked as a reverse polarity reflector. Below the BSR a high amplitude (bright spot) like event represents the occurrence of free gas. The arrivals from sea floor and sedimentary layers are also marked; (**b**) Wavefront propagation (energy propagation) at 1.16 sec. for corresponding model (Fig. 7.15) and simulated seismic data (Fig. 7.18 a). The source is located at top right from the receivers. BSR is representing reverse polarity event. Below the BSR, waves reflected from the free gas zone are identified and marked. The wavefronts from sea floor and sedimentary layers are also marked

receiver layout of cross-well survey is closer to targets, (b) the survey is free from a low velocity layer near surface that attenuates high frequency waves, and (c) the survey is free from surface waves.

Initial model as given in Fig. 7.19 was considered with the distance between the two wells (source and receiver) at the surface of the order of 200 m, which is a good separation for such type of studies. The objective imaging zone was from 1,200 to 1,600 m. During modelling attempt, the downhole seismic source was positioned at depths between 800 and 1,000 m, and the downhole seismic receiver was positioned at depths from 800 to 2,500 m. The synthetic seismic response has been simulated in order to identify major events associated with the occurrence of gas hydrate and free gas. The crosswell seismic P-wave first arrival was identified first. The complexity of the crosswell wavefield sometimes makes it difficult to identify the first arrivals. Reflections from major reflectors (seabed, sedimentary layer, gas hydrate zone and free gas zone) have been identified in the form of upgoing events (Fig. 7.20a). The downgoing waves are also marked on the crosswell seismic

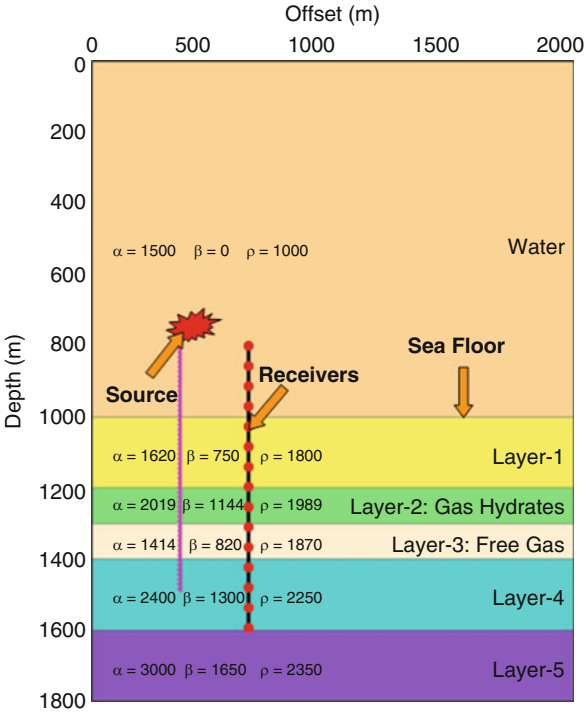

Fig. 7.19 Schematic representation of cross-well VSP survey for a complex gas hydrate model. The model represents six layers including water. The model parameters (compressional (V_p), Shear (V_s) and density (ρ) are given for each layer. The source is located in the other well represented by a *pink line* on left hand side. The *red dots* are receivers located vertically parallel to the other well

section. Refections pertaining to down going wave have a polarity opposite to reflections pertaining to up going wave because of changes in the reflection coefficients during the incidence process of a wave. Additionally the wavefront propagation recorded at 0.47 s and shown in Fig. 7.20b. The reflection from gas hydrate layer is reflecting the reverse polarity and high amplitude, which can also be seen on the snapshot. The enhanced seismic reflection which is observed below the BSR is interpreted as the bright spot.

Secondly one low velocity layer within the gas hydrate zone was considered and simulated seismic response was estimated (Fig. 7.21). This becomes very interesting case as one observed two high amplitude and negative polarity events across the crosswell seismic section. This first event could be interpreted as primary or first BSR and the second event as double bottom simulating reflecting reflector (DBSR) as shown in Fig. 7.22a. The second high amplitude event is observed in real world also (Rajput et al. 2009). The possible cause for the occurrence of this event on field data is explained upward movement of gas through discrete layer of fractures. The reflections from other reflectors are also observed and indicated in the Fig. 7.22a.

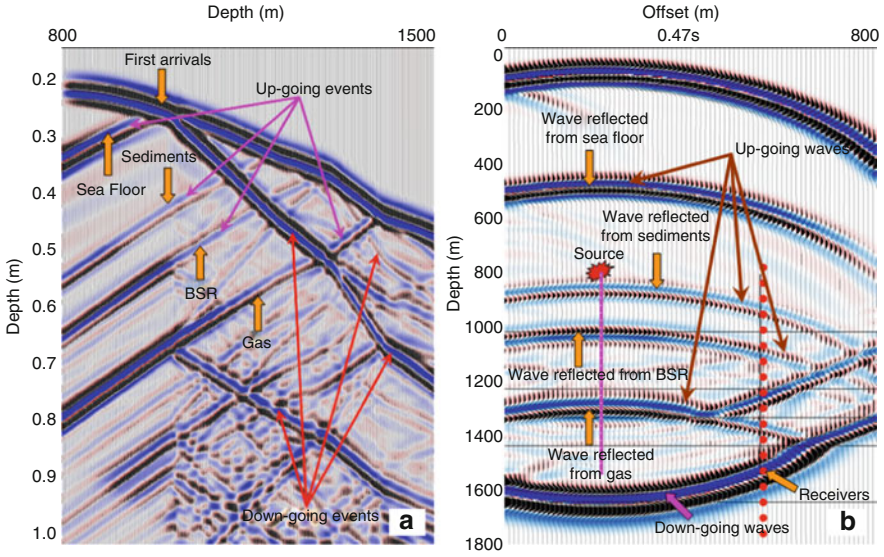

Fig. 7.20 The simulated seismic response for cross-well VSP for the corresponding model (Fig. 7.19). The synthetic seismic data and the wavefront propagation are shown. Both up-going and down-going waves are identified and marked on the profile; (**a**) synthetic cross-well VSP data represents all the identified arrivals from different reflectors. BSR is marked as a reverse polarity reflector. Below the BSR a high amplitude (bright spot) like event represents the occurrence of free gas. The arrivals from sea floor and sedimentary layers are also marked; (**b**) Wavefront propagation (energy propagation) at 0.47 s for corresponding model (Fig. 7.19) and simulated seismic data (Fig. 7.20a). The source is located in the other well represented by a *pink line* on *left* hand side. The red dots are receivers located vertically parallel to the other well. Below the BSR, waves reflected from the free gas zone are identified and marked. The wavefronts from sea floor and sedimentary layers are also marked

The same exercise by with the source at the surface and receivers at the seabed repeated and compared the image with crosswell seismic section. The reflections from sedimentary layers and gas hydrate layers are clearly resolved in ocean bottom seismic experiment results (Fig. 7.22b). Whereas the resolution is better observed in the cross-well seismic image.

7.4.4 Some Remarks

Vertical seismic profiles (VSPs), with seismic sources on the surface and receivers in boreholes, are commonly used in oil and gas exploration to improve the analysis of surface-seismic reflection data using information from boreholes. VSPs have been acquired successfully for studying gas hydrate-related targets in a similar fashion as those for deeper conventional hydrocarbon reservoirs (Peacher et al. 2010). However still challenges are out there, the industry tools needs to be designed for oceanic gas

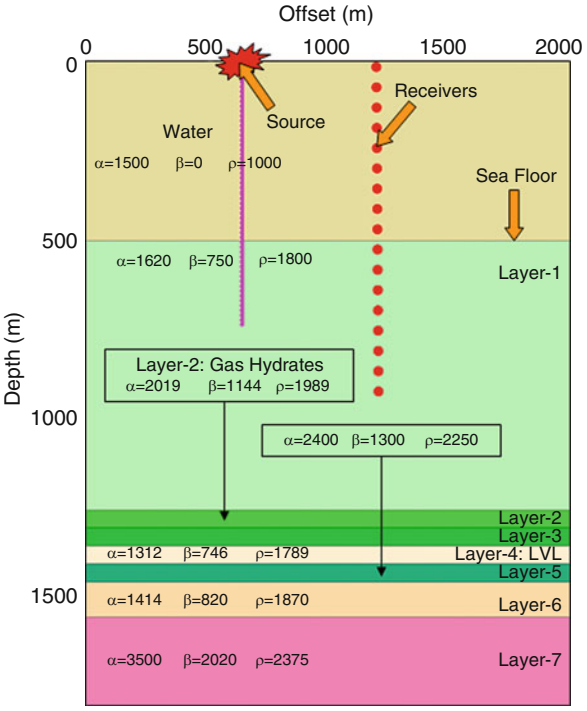

Fig. 7.21 Schematic representation of cross-well VSP survey for a complex DBSR model. A low velocity layer is assumed within the gas hydrate zone. The model represents eight layers including water. The model parameters (compressional (V_p), Shear (V_s) and density (ρ) are given for each layer. The source is located in the other well represented by a *pink line* on *left* hand side. The *red dots* are receivers located vertically parallel to the other well where source is located

hydrates. VSPs through gas hydrate-bearing sediments are may provide constraints for accurate velocity values for P- and S-waves at surface-seismic frequencies, for integrating borehole data with reflection seismic data, and for up-scaling results from higher-frequency sonic data used to characterize gas hydrates in a particular borehole.

7.5 Marine Controlled-Source Electromagnetic Methods (CSEM)

The marine electromagnetic (EM) methods, controlled source electromagnetic (CSEM) and magnetotelluric (MT) techniques, are sensitive to the electrical resistivity of the sediments and the formation porosity, permeability, and resistivity of the pore fluids. The marine CSEM technique was first developed in the academic world to explore mid-ocean ridges (MacGregor et al. 1998; Evans et al. 1994), the

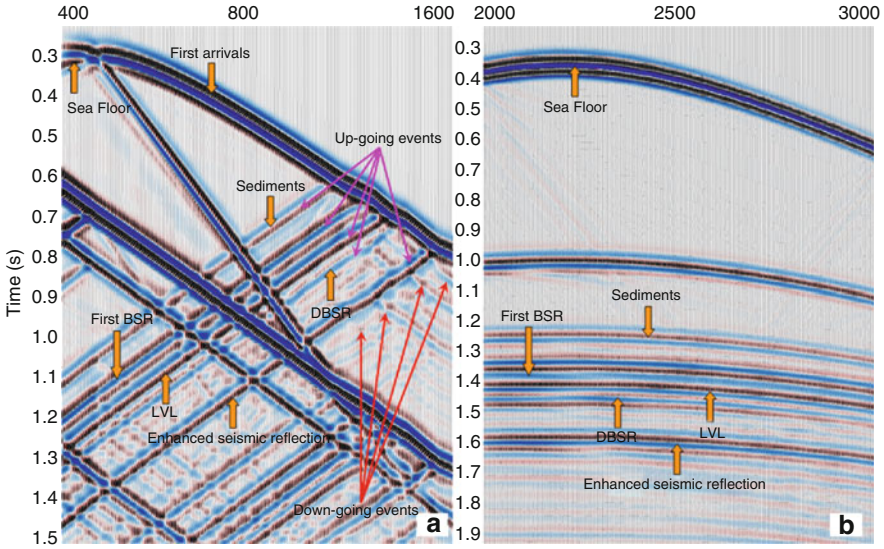

Fig. 7.22 The simulated seismic response for cross-well VSP for the corresponding DBSR model (Fig. 7.21). The synthetic seismic data for cross-well seismic and ocean bottom seismic are shown for the same configuration. The resolution is improved in cross-well seismic section; (**a**) synthetic cross-well VSP data represents all the identified arrivals from different reflectors. In this complex structure BSR and DBSR are identified as a reverse polarity reflector. Below the BSR a high amplitude (bright spot) like event represents the occurrence of free gas. The arrivals from sea floor, sedimentary and low velocity layers are also marked. Both up-going and down-going waves are identified and marked on the section; (**b**) Corresponding Ocean bottom seismic data. The reflections from sedimentary layers and gas hydrate saturated zones are identified. Enhanced seismic reflection from free gas zone is also identified

oceanic lithosphere (Constable and Cox 1996; Chave et al. 1991; Cox et al. 1986) and is becoming commonplace in industry to explore for hydrocarbons (Eidesmo et al. 2002; Hesthammer and Boulaenko 2005; Ellingsrud et al. 2002). Implementation of CSEM to detect gas hydrates has shown great potential (Weitemeyer et al. 2006c; Schwalenberg et al. 2005; Yuan and Edwards 2000) and the CSEM techniques' ability to detect this sometimes subtle electromagnetically resistive target is under active development. Marine controlled-source electromagnetic (CSEM) sounding is a new tool available to geophysicists for offshore hydrocarbon exploration.

Although the technique has been developed for the detection of deep hydrocarbon reservoirs with relatively high resistivities, it also has the potential to be a useful tool for geohazard mitigation via gas hydrate detection (Weitemeyer et al. 2006a, b, c). The hydrate target occurs in the shallow section (hundreds of meters in depth), and is manifested by subtle resistivity contrasts (a few Ω m). This requires modifications to the CSEM technique to extend its capability of imaging the shallower hydrate section (Weitemeyer et al. 2006a, b, c). The marine CSEM method (Fig. 7.23 courtesy of Scripps Institution of Oceanography, source; http://

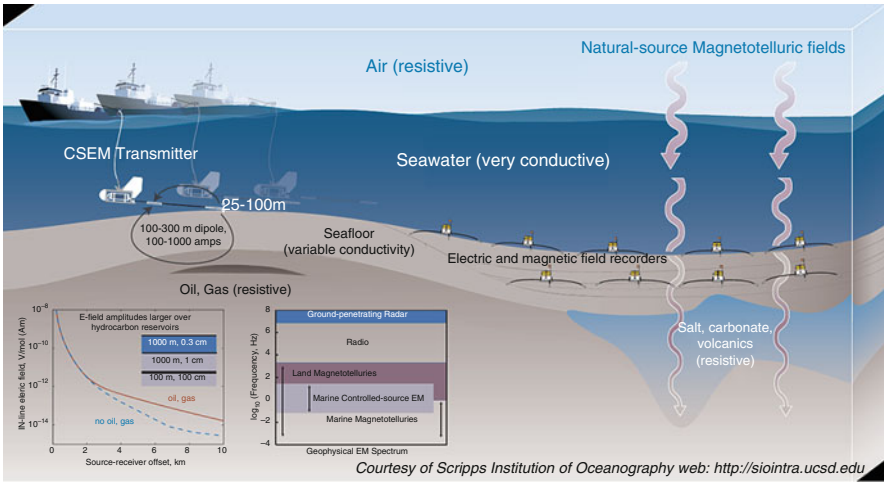

Fig. 7.23 An electric dipole transmitter is towed close the seafloor. EM receivers record the electric field as a function of source–receiver offset. The CSEM method is preferentially sensitive to resistive structure; in conductive environments resolution is limited to a few Km depth (*Courtesy of Scripps Institution of Oceanography web*: http://siointra.ucsd.edu)

siointra.ucsd.edu) uses the same seafloor recorders as the MT method. An electric dipole transmitter is towed close the seafloor. EM receivers record the electric field as a function of source–receiver offset. The CSEM method is preferentially sensitive to resistive structure; in conductive environments resolution is limited to a few kilometers depth. Electric fields recorded at receivers are larger over resistive seafloor structures such as basalt, salt, carbonates, hydrocarbon reservoirs, or gas hydrates (Constable 2006). An example of mapping shallow resistivity for hydrate hazard and resource assessment for 15 Hz and 5 Hz apparent resistivity pseudosections from Hydrate Ridge, Oregon, along with the upper 3 km of a larger magnetotelluric model has been studied by Steven Constable at Scripps Institution of Oceanography (Fig. 7.24).

The application of CSEM methods to hydrate detection was first considered by Edwards (1997). He modeled the transient electric dipole–dipole method as a means of estimating hydrate volume and argued for the usefulness of EM methods in augmenting drilling and seismic techniques. Field studies conducted at the Northern Cascadia margin off the west coast of British Columbia, Canada, demonstrated the merits of CSEM by showing the existence of hydrate where BSR was not identified (Yuan and Edwards 2000), and the existence of hydrate or free gas in seismic blank zones thought to represent hydrate bearing pipes (Schwalenberg et al. 2005). The system employed at Northern Cascadia was a towed horizontal electric dipole–dipole array (Edwards and Chave 1986), made up of a transmitter dipole and reciever dipoles attached at fixed offsets behind the transmitter (Yuan and Edwards 2000). The time–domain system operates by producing a pulse of EM energy and then measuring the diffusion time through the seabed (Cheesman et al. 1986). The

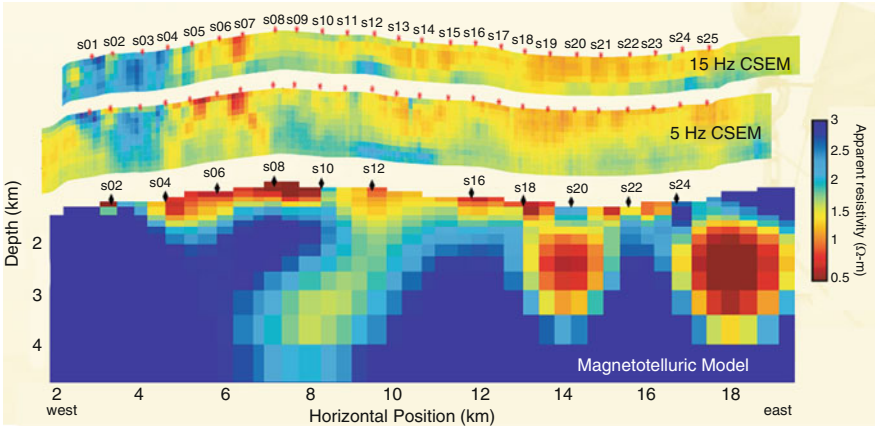

Fig. 7.24 Mapping shallow resistivity for hydrate hazard and resource assessment: 15 Hz and 5 Hz apparent resistivity psuedosections from Hydrate Ridge, Oregon, along with the upper 3 km of a larger magnetotelluric model, plotted on the same linear resistivity scale (Courtesy of Scripps Institution of Oceanography web: http://siointra.ucsd.edu)

travel time is related linearly to the resistivity: the higher the resistivity, the shorter the travel time (Yuan and Edwards 2000). The electric dipole–dipole technique was selected because of its sensitivity to intermediate resistive crustal zones (top 200 m). Hyndman et al. (1999) suggest it is useful, if lateral resistivity changes in sediments are small compared to the lateral changes in hydrate resistivity. A similar towed system, based upon the Geological Survey of Canada's magnetic dipole system, has been used in the Gulf of Mexico as a mapping tool to image hydrate mounds (Evans 2007). It is a frequency-domain towed magnetic dipole system that generates harmonic magnetic fields over a range of frequencies (Hz to kHz) which are recorded by three receivers, each tuned to a specific frequency and towed at a fixed distance behind the transmitter. It is designed to image very shallow sediments – the top 20 m.

The survey conducted at Atwater Valley hydrate mound showed raised porosity (conductivity) as a result of high pore fluid temperatures and salinity beneath the mound (Evans 2007). Since Evans' (2007) EM system is only capable of imaging the top 20 m of sediment, the rest of the hydrate stability zone goes unmapped using such instrument. Edwards' (1997) EM method images the gas hydrate stability zone but is depth-limited by the separation distance of the bipole array. Both lack the ability to image the source of fluid and methane flow migrating into the gas hydrate stability zone. In addition, both methods are mapping tools dragged along the seafloor, limiting their use to undeveloped sedimentary basins (Weitemeyer 2008). The receivers are at fixed geometries and thus are only capable of recording a radial mode (source and receiver are in-line) component of the 3D vector field. This limits resolution and the ability to detect and characterize anistropy or 3D structures. Their data are generally interpreted by only considering 1D inversions to obtain simple subsurface resistivity maps. Two other studies utilizing

electromagnetic methods include a towed DC resistivity survey conducted in the Japan Sea (Goto et al. 2008) and a planned survey at the hydrate observatory site, Mississippi Canyon 118 (Dunbar 2008).

In the Japanese study higher resistivity locales are suggested to be associated with hydrate, although these also appear to correlate with bathymetric effects. The range in resistivities (from 0.3 to 0.8 Ωm) is very small and not suggestive of the significant concentration of hydrate which is expected from the recovery of a massive hydrate sample during the same experiment (Weitemeyer 2008). The Scripps CSEM transmitter system is deep-towed 50–100 m above the seafloor, making it possible to operate in regions with seafloor infrastructure. Because receivers are autonomous almost any geometric arrangement between source and receiver is possible (Weitemeyer 2008). In addition, all components of the electromagnetic field (i.e. *Ex,y,z* and *Bx,y*) are recorded, providing a rich data set compared to the collection a single in-line component. However, navigation of the transmitter becomes very important, unlike the tandem towed systems of Evans and Edwards (above) which are at fixed and known positions (Weitemeyer 2008).

To obtain a quick image of the subsurface structure and heterogeneity across the CSEM profile without a 2D inversion, a pseudosection technique (a method used extensively in land DC resistivity and IP surveys) could be an alternative as used by Weitemeyer, in 2008 for hydrate ridge experiment. This provides a way to look at all of the CSEM data collected at every site in one single image. The midpoint between the source and receiver is plotted at a depth given by a 45° projection from the source and receiver, shown in Fig. 7.25 (Weitemeyer 2008, reprinted with permission).

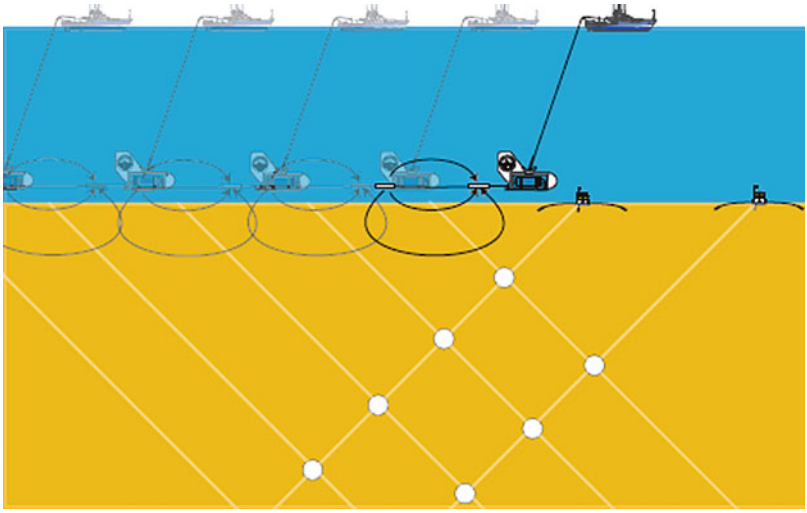

Fig. 7.25 The pseudosection projection technique is created by taking the midpoint between source and receiver and projecting it down at a 45 angle from the horizontal. This imaging technique was used for both the 5 Hz and 15 Hz data (Weitemeyer 2008, reprinted with permission)

Contoured apparent resistivity pseudosections are shown in Fig. 7.26. Reciprocity between the transmitter and receivers creates a twofold redundancy in the data with separate pseudosections from east-side and west-side transmissions. The two pseudosections have different sensitivities and there are subtle differences between them. The pseudosection projection technique causes the west pseudosection to have a striping pattern to the west and vice versa for the east pseudosection (Weitemeyer 2008). This pattern is most obvious for the shallow conductor under site 6. However, the east-side and west-side pseudosections (Fig. 7.26 top and middle panel) are sufficiently similar that an average of the two can be taken (Fig. 7.26 bottom panel) (Weitemeyer 2008). The combination of the east and west averages the striping pattern except under site 6, where a classic pseudosection "pant-leg" feature is present. All three pseudosections display a more conductive basin under sites 18–25 that increases in resistivity with depth (Weitemeyer 2008). This is likely a result of a decrease in porosity due to compaction. The pseudosections also give a resistive anomaly where an anticline is evident in the seismic data under sites 16 and 17. The ridge is more resistive under sites 9–13. Finally there is a large resistor under sites 1–4, particularly evident in the west pseudosection which extends further in this direction (Weitemeyer 2008). The pseudosection projection technique was also applied to the 15 Hz data, shown along with the 5 Hz and 15 Hz data in Fig. 7.27a and (Weitemeyer et al. 2006b, c). The 15 Hz pseudosection is sensitive to shallower

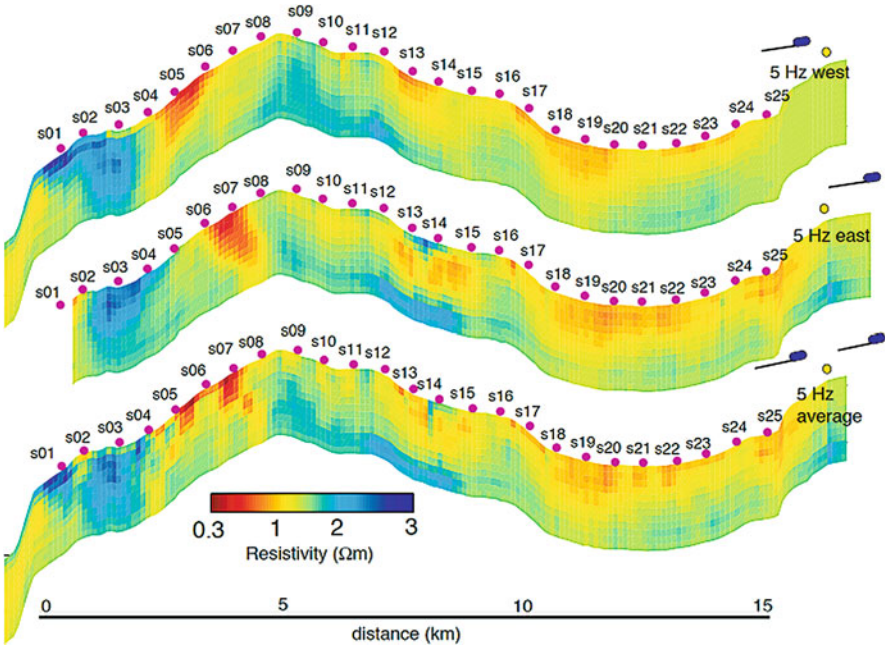

Fig. 7.26 Resistivity pseudosection of 5 Hz data for a transmitter positioned to the west (*top*), east (*middle*), and for combined east and west transmitter positions (*bottom*) (Weitemeyer 2008, reprinted with permission)

sediments because of the shorter EM penetration depths and shorter offsets, and this is reflected by a general agreement with the top of the 5 Hz pseudosection. The pseudosection projection method is better at imaging lateral resistivity variations than those that vary with depth. To obtain a true depth section a 2D inversion is required (Weitemeyer 2008).

7.6 Seismic Data Analysis for Gas Hydrate Characterization

Recent works suggest that the dissociation of gas hydrate can be very important contributor of triggering the submarine landslides at the top edge of the GHSZ as it has been found for example in Hikurangi Margin, New Zealand (Pecher et al. 1997, 2003). However, the occurrence of the shallow gas hydrate is only possible as a result of the focused fluid supply from deep, therefore depending on the regional structural fabrics. The base of the gas-hydrate zone may represent a discontinuity in the strength of the sediment column. The presence of hydrates may inhibit normal sediment consolidation and compaction, and free gas trapped below the hydrate zone may be over-pressured. Any technique proposed for hydrate exploitation would have to succeed without causing additional instability.

Seismic data processing is a critical step towards seismic characterization of gas hydrates. There is no firmed workflow is available for such kind of job as it totally depends on geology and seismic data acquisition parameters. Robust workflow can be developed by amplitude preserved processing, therefore all the technique of seismic noise suppression should not affect the amplitude during processing.

An innovative approach for studying the Gas-Hydrate stability conditions and their impact on environment is to examine the geological, geophysical, and petrophysical conditions towards characterizing tectonics and stratigraphic control on gas hydrate accumulation. Integrating the study of subsurface environments in this way can provide new insights into the entire gas hydrate system and on the hydrocarbon resources they contain (Fig. 7.27). It has been clear that there are no unique seismic attributes that unequivocally resolve the presence of gas hydrates. For example, extensive studies on gas hydrates (Dillon et al. 1994; Hyndman and Spence 1992; Shipley et al. 1979a, b) indicate that a bottom simulating reflector (BSR), shallow amplitude blanking, and high seismic velocity/impedance are the prominent geophysical evidences of natural gas hydrates on seismic data (Fig. 7.28). The data analysis for seismic characterization of gas hydrates is several step processes which consist of the following:

- High resolution reprocessing of the entire seismic data
- Identification of target zones (Stratigraphic evaluation)
- Analyzing seismic attributes
- Seismic inversion
- Rock Physics modeling
- Quantification

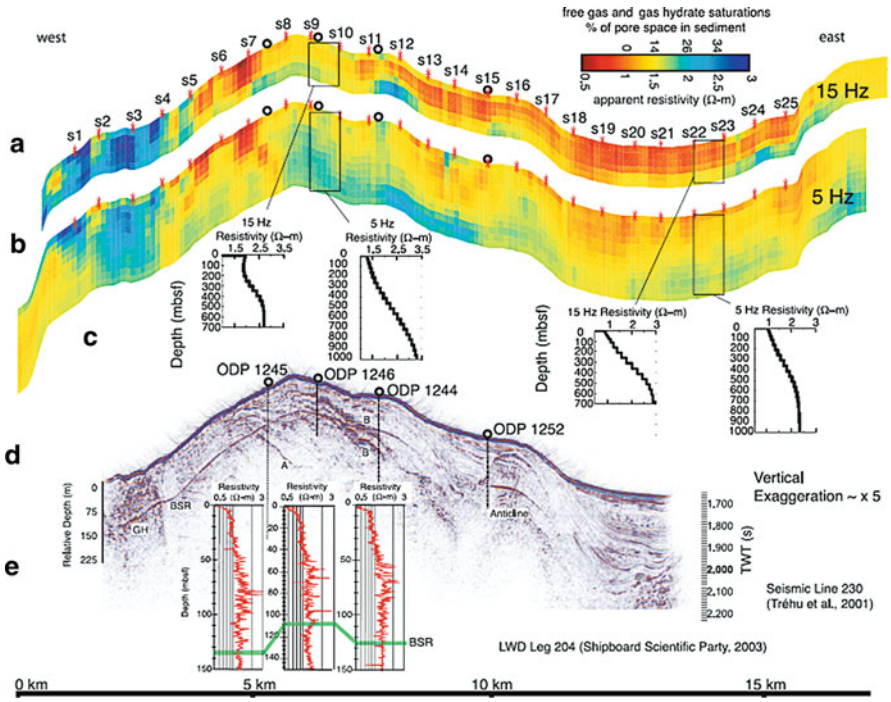

Fig. 7.27 Pseudosection results for (**a**) 15 and (**b**) 5 Hz data, with a combined apparent resistivity and gas hydrate saturation scale; (**c**) 1-D inversions for marked locations; (**d**) seismic line 230, and (**e**) logging-while-drilling (LWD) deep resistivity logs. GH, gas hydrate or free gas inferred from a seismic inversion (Zhang and McMechan 2003); BSR, bottom simulating reflector; A, B, B0, seismic horizons explained in text. ODP Leg 204 sites are marked on seismic section. EM receiver sites are marked by *red asterisk*. (Weitemeyer et al. (2006b, c)

Initial screening of the seismic data should include the identification of seismic indicators (details are provided in Chap. 6) such as, variability in amplitude strength, continuity, lateral consistency within GHSZ, presence of gas and water in near-surface sediments (shallow fluid flow type features), presence of Gas chimneys and Mud volcanoes, "Shingling" of reflectors with increased amplitudes at shallow depths, Seafloor failures and slumping, presence of a BSR, widespread strongly attenuated blanking zones and possible polarity reversals at or near the water bottom interface (Dai et al 2008, Rajput et al 2008). The reprocessing flow necessary to provide the best solution for the inversion and modeling process was not the optimum flow for structural and stratigraphic interpretation. The need for interpretation were optimal imaging and resolution of the faults, hydrate features and other near-surface lithology; need true amplitude recovery (and phase) for seismic inversion to extract meaningful deterministic parameters such as the P- and S-wave velocities (Vp and Vs) and bulk densities (Dai et al. 2008).

A good example of processed data (bathymetric map, water bottom map and seismic data) from the Atwater Valley 14 is centrally located within the Mississippi

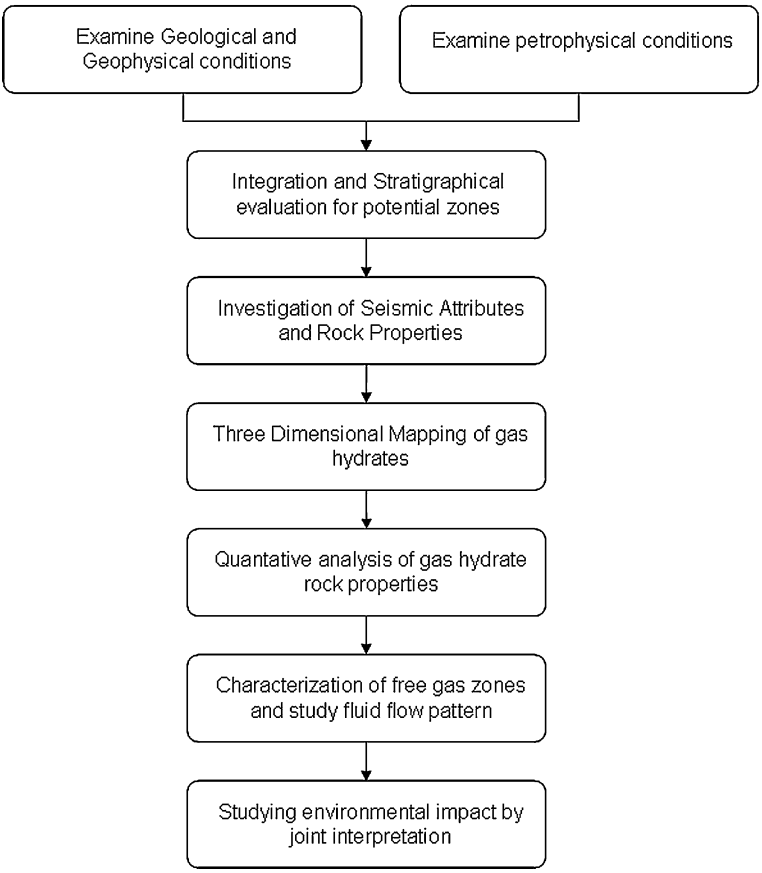

Fig. 7.28 Integrated workflow for stratigraphic controlled gas hydrate and free gas characterization

Valley channel complex in the easternpart of the northern deepwater GoM and has a thick clastic blanket above the salt presented by Dai et al. in 2008 (Figs. 7.29, 7.30, and 7.31). From geological point of view Pleistocene sediments are complex and chaotic, with evidence of many channel levee and slope fan systems. In this are a salt mobilization is responsible for creating the NW–SE trending fault pattern, which also allowed the migration of gas and ultimately the formation of the hydrate deposits. Water depth ranged from about 1,250 m in the western part of the survey to 1,325 m in the eastern part, as shown in Figs. 7.29 and 7.30. The near zero-phased seismic data revealed numerous prominent seafloor features possibly associated with the presence of hydrates. Figure 7.30 shows a series of possible hydrate mounds (A through G) in the western and central area of the survey (Dai et al. 2008). Most of these mounds followed a general NW–SE trend corresponding to the fault fabric. Mound D exhibited a weak amplitude polarity reversal at the water/mound interface amplitude with a chaotic zone and a blanking zone below the mud-

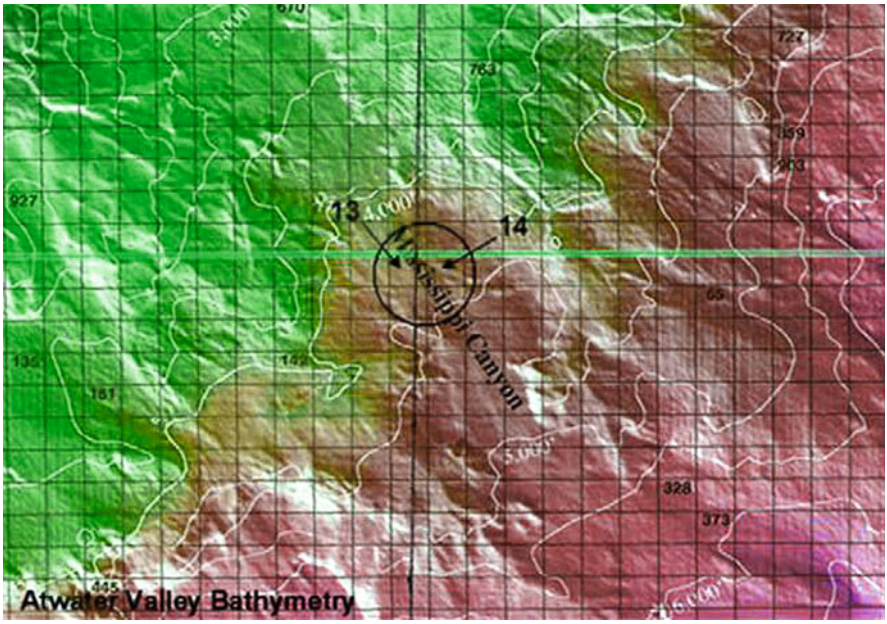

Fig. 7.29 Atwater Valley 14. Bathymetric map showing blocks AT13 and AT14 centrally located in the Mississippi Canyon channel; (Dai et al. 2008; reprinted with permission)

line (BML) (Fig. 7.32). Mound F showed a deeper polarity reversal with a zone of amplitude blanking (Fig. 7.33). An apparent gas chimney is also identified below Mound B (Fig. 7.34). The central region in Fig. 7.30 shows a possible hydrate Mound G and associated slump. Most mounds appeared to be less than 180 m wide. There is no regional BSR evident in the area. Some weak amplitude blanking to about 0.4 s BML suggests possible fluid migration (Dai et al. 2008).

7.6.1 Patterns in Synthetic Seismograms for Gas Hydrates

Most of the seismic reflectors are generally interrelated to geological processes that occur subsequent to the deposition of the sediments. A sub-class of seismic reflectors is the BSR, controlled by to depth of secondary-bed, which in turn depends on velocity, pressure and temperature within the sediments. The most common BSR are caused by the occurrence of gas hydrates. In order to get the optimum processed data for gas hydrate studies, one must study the different gas hydrate related signatures in synthetic seismograms. The marine gas hydrate research both in view of development of prognostic models for gas hydrates, free gas zones, and possible channels of hydrocarbon supply is presented here with

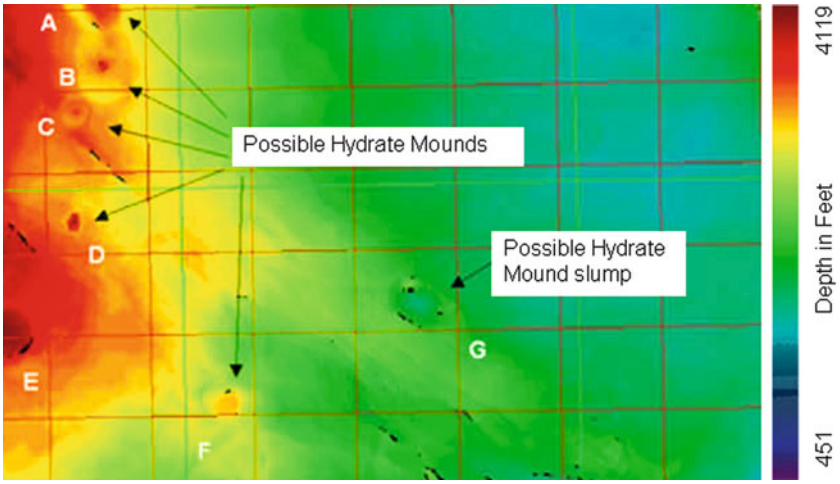

Fig. 7.30 Atwater Valley 14. water bottom map from 3D seismic data, highlighting seafloor mounds indicated by letter labels from Xu et al. (2004) (Dai et al. 2008; reprinted with permission)

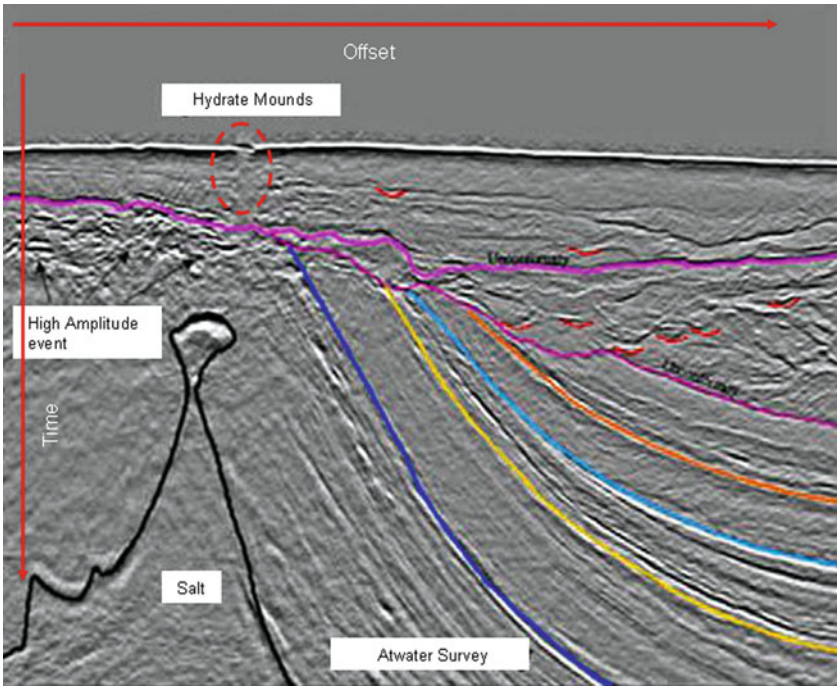

Fig. 7.31 Atwater Valley 14. N–S seismic line showing hydrate Mound D and an interpretation of key seismic events and stratigraphic relationships from Xu et al. (2004). Note the th ick clastic wedge in between the two unconformities on the upper section (Dai et al 2008; reprinted with permission)

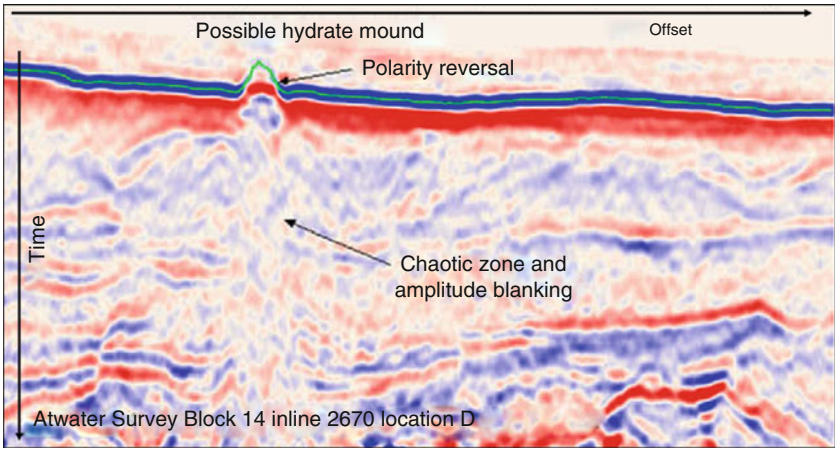

Fig. 7.32 Atwater Valley 14 Inline seismic lines (W–E) showing possible hydrate mounds. Mound D (Fig. 7.30) with polarity reversal at the seafloor and a deeper chaotic zone and amplitude blanking (Dai et al. 2008; reprinted with permission)

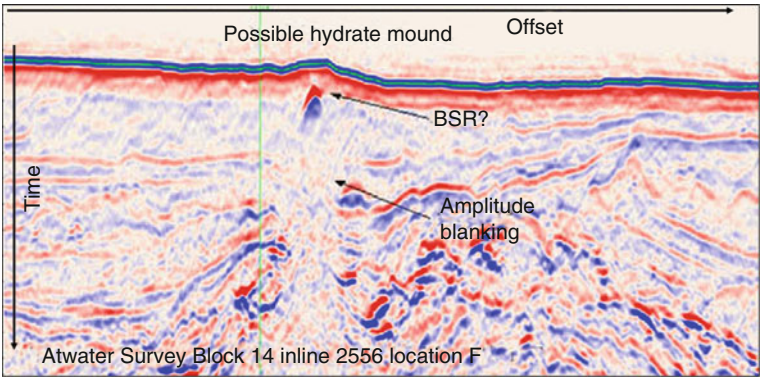

Fig. 7.33 Atwater Valley 14 Inline seismic lines (W–E) showing possible hydrate mounds. Mound F (Fig. 7.30) with amplitude blanking beneath a shallow BSR-like feature (Dai et al. 2008; reprinted with permission)

modeling and field data examples. To study the different aspects of the BSRs, three models are developed and an extensive modeling exercise has been performed using finite difference modeling.

7.6.1.1 Patterns in Synthetic Seismogram for Simple Multilayered Gas Hydrate and Free Gas Model

A large number of models with gradual increasing velocity (both P and S waves) within the gas hydrate are prepared and tested to ascertain the amplitude strength of

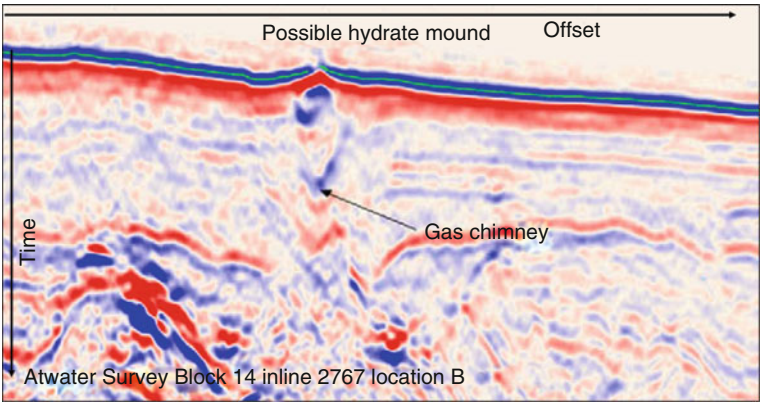

Fig. 7.34 Atwater Valley 14 Inline seismic lines (W–E) showing possible hydrate mounds. Mound B (Fig. 7.30) with amplitude blanking and gas chimneys (Dai et al. 2008; reprinted with permission)

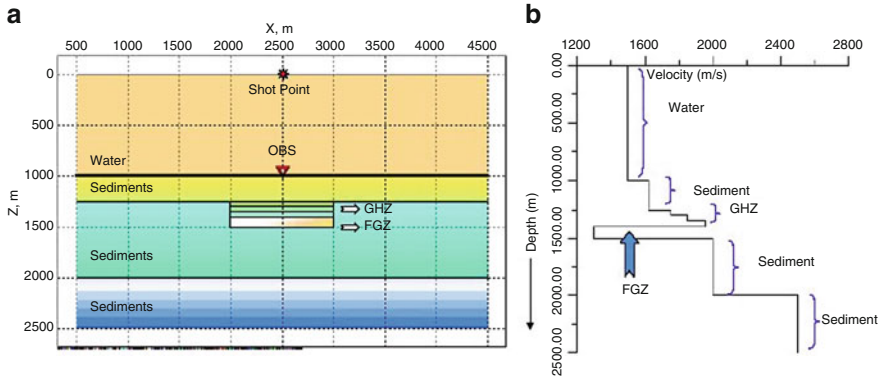

Fig. 7.35 Representative model with a gas hydrate stability zone (GHSZ), and a free gas zone (FGZ) for case-1. Three component OBS are deployed at 50 m separation on the sea floor. A number of 20 kHz shots are fired at 10-m depth from sea surface. (After Rajput et al. 2008 reprinted with permission)

BSR. The best qualitative velocity model for methane gas hydrate deposits in the marine environment is illustrated in Fig. 7.35. Synthetic data contains a number of the seismic (sound) wave field components. They represent a set of dynamic physical parameters, which changes with time. Most of them are basic analogues of ones that can be measured in the field observations; some are product of the basic ones. Several shots are assumed with 25 m interval and multicomponent data are generated using elastic anisotropic modeling technique. The data is processed for independent shot points. It is found that the data for the shot point, which is located just above the GHSZ, demonstrate the best results. It can be said that the gradual increase in the velocity is affecting the amplitude strength of BSR. The vertical

particle velocity component (V-component, together with shear stress and stress shift) is shown in Fig. 7.36a. The strength of BSR increases because of the typical velocity contrast within the gas hydrate zone itself. The reflections from the sedimentary layer are properly resolved on either side of the hydrated zone however at the top of the gas hydrate zone a low amplitude anomaly is observed which

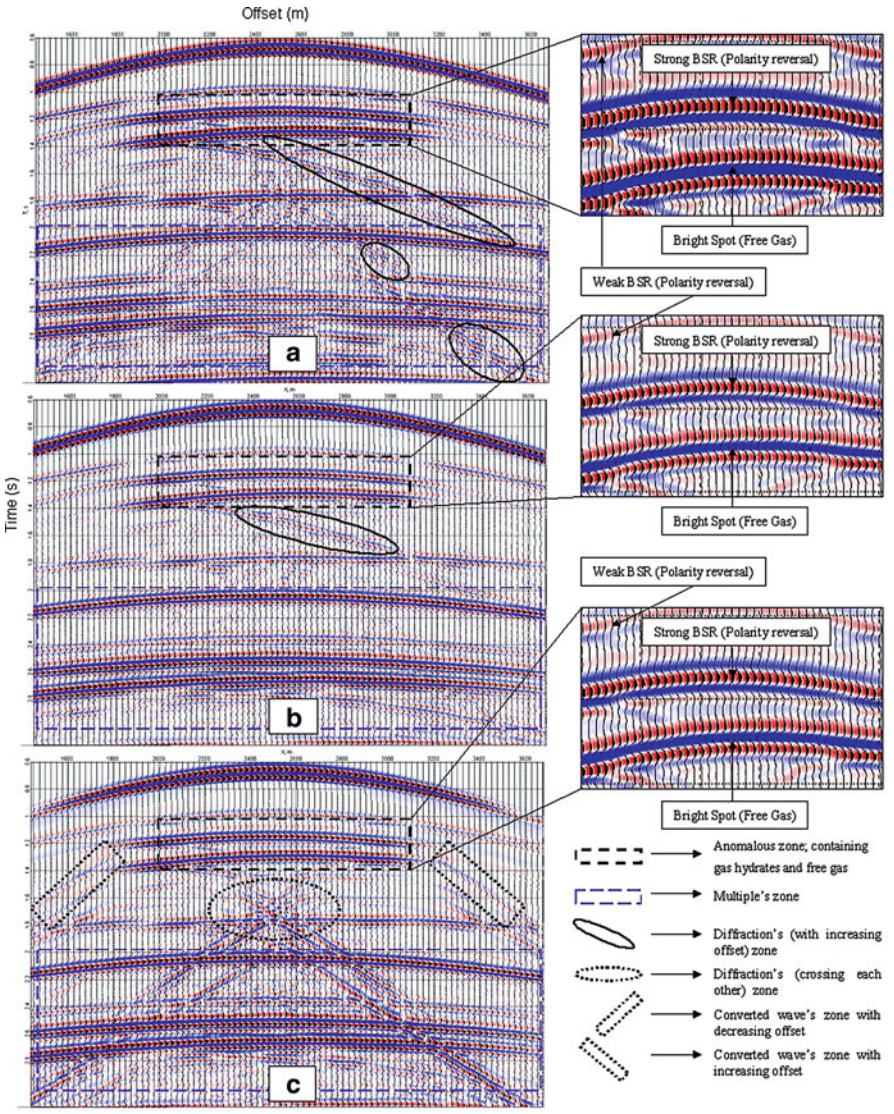

Fig. 7.36 Synthetic seismogram for case-1, calculated by elastic anisotropic modelling technique; (**a**) vertical component of particle velocity component (V- component); (**b**) shear stress component; (**c**) stress shift component. (After Rajput et al. 2008 reprinted with permission)

reflects a weak BSR like feature confirmed by the fragmented polarity reversal. The amplitude strength of BSR increases gradually with depth and as it reaches its maximum value, an abrupt drop in velocity is observed because of the presence of free gas. At the separation point of the GHSZ and FGZ, the BSR record its appreciable amplitude strength and a strong simulating reflection is observed which inveterate by reverse polarity with respect to the sea floor. The multiples from different horizons are observed and are shown on the seismic sections. The diffracted multiples hindered at the base of the target area moved downward with respect to the increasing offset and are indicated in the Fig. 7.36a. The study shows that the shear wave signatures present in the vertical component of particle velocity could be due to some P energy converted from shear in shallow sediments.

Shear stress is one of the dynamic parameters in elastic wave equation. The stress component for this case is shown in Fig. 7.36b. Strong BSR features have been identified at the interfering boundary of GHSZ and FGZ. The amplitude strength of BSR increases with the velocity contrast and confirmed the aforementioned results. The bright spot like features in this component indicate the free gas response underlying the GHSZ. The multiple's (reflected and diffracted) from other reflectors are also recognized in seismic section and have been marked in Fig. 7.36b. Stress shift is normally the difference between the horizontal and the vertical components of stress that exists only in solids i.e. shear velocity is not equal to zero and is taken as wave field component to highlight the sound effects proper to solid medium shown in Fig. 7.36c. The BSR of high amplitude strength is demarcated at the boundary of GHSZ and FGZ. The strong diffractions and principal mode of conversion can be recognized on the seismic section as the observed converted waves (PS) record high amplitude. The down going diffractions from GHSZ crossed each other at half a distance from BSR towards the increasing offset. Apart from that the first order multiples of the ocean bottom reflection, sedimentary layer reflection and other horizons are seen in Fig. 7.36c.

7.6.1.2 Patterns in Synthetic Seismograms for Models Having Brine Saturated Sand Layer Between Gas Hydrates and Free Gas Bearing Sediments

This model represents the consequence of a brine-saturated sand layer, which is sandwiched between the overlying gas hydrate bearing sediments and underlain by the sediments containing free gas (Fig. 7.37). This layer acts as a demarcation boundary of GHSZ and FGZ. The synthetic seismograms, which are shown in Fig. 7.38a, demonstrate the significance of the brine sand layer. A thick BSR like features are produced and have been marked in the Fig. 7.38a. At the top of the GHSZ, the amplitude of the reflected wave is less pronounced while at the base of GHSZ strong amplitude seismic signatures are observed. This is quite evident in the strength of BSR. The thickness of the brine sand layer is 25 m. Diffracted multiples are observed at the either end of the anomalous zone. Apart from that the multiple of ocean bottom reflection and of the other reflectors are observed as well. The

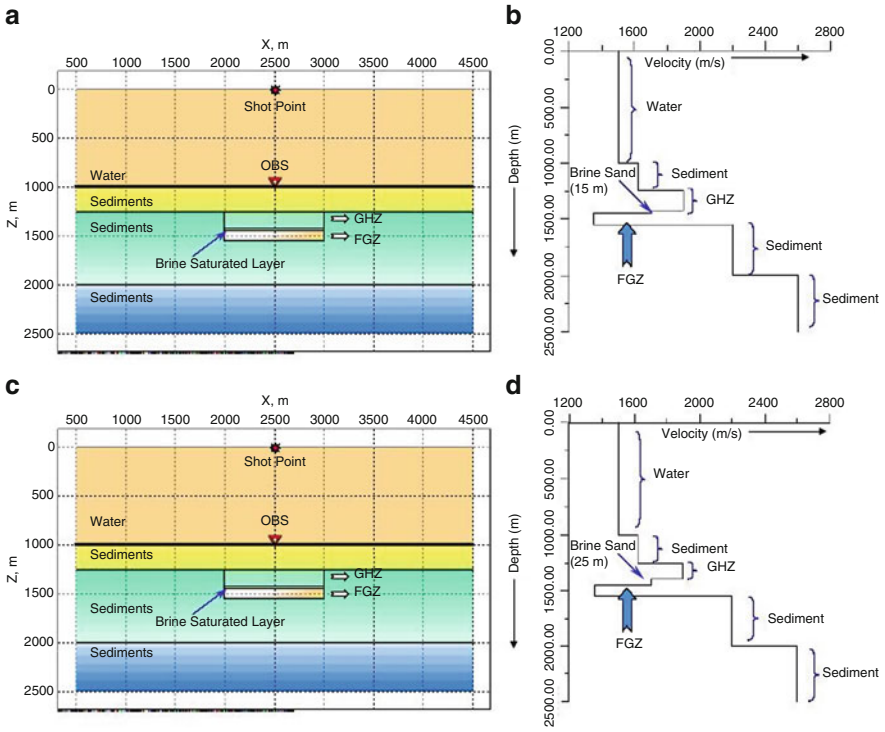

Fig. 7.37 Representative model with brine sand layer, which is sandwiched between the overlying gas hydrate bearing sediments and underlain by the sediments containing free gas. Three component ocean bottom seismometers are deployed at 50-m separation on the sea floor. The shot point is located just above the target zone; (**a**) Two dimensional velocity model for 25-m thick brine sand layer; (**b**) One dimensional velocity model for 25-m thick brine sand layer and the OBS is deployed just above the target area. (**c**) Two dimensional velocity model for 15-m thick brine sand layer; (**d**) One dimensional velocity model for 15-m thick brine sand layer and the OBS is deployed just above the target area. (After Rajput et al. 2008 reprinted with permission)

reflection from the free gas zone is significant on the seismic section. The wavelets are processed with the application of high gain and frequency filtering and shown in Fig. 7.38b. Seismic energy travels downward and reflects in upward direction and is therefore recorded by the multicomponent receivers, which are placed at the ocean bottom.

The seismic energy is partially reflected and partially transmitted as shown in the Fig. 7.38b. Brine sand layer plays an important role to calculate the strength of the BSR in marine sediments. The results show that the amplitude of the BSR is inversely proportional to the thickness of the brine sand layer. A comparison has been made to delineate the nature and strength of BSR. The synthetic seismograms are calculated for both the 25 m thick and 15 m thick brine sand layer. Figure 7.39a represents the case in which the thickness of brine sand layer is 25-m and Fig. 7.39b illustrates the seismogram for the same model with 15-m thick brine sand layer. The

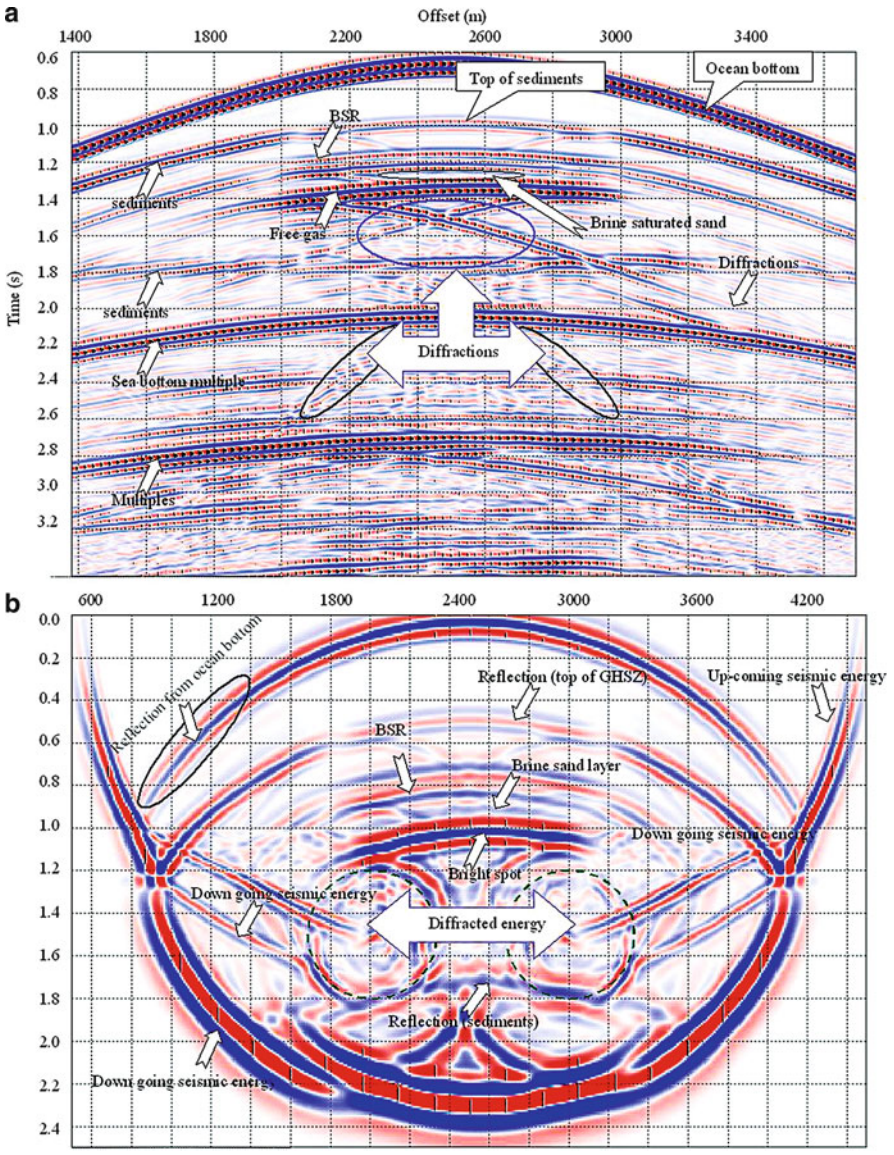

Fig. 7.38 The vertical component of particle velocity component (V- component) for case-2; (**a**) demarcation of the BSRs of different strength by polarity reversal with respect to the sea floor and the reflected arrival from the brine sand layer; (**b**) wavelet propagation at 1.6 s with illustration of diffracted arrivals from either side of the GHSZ and the transmission of seismic energy (down going, reflected and diffracted) for model having brine saturated sand between gas hydrates and free gas. (After Rajput et al. 2008 reprinted with permission)

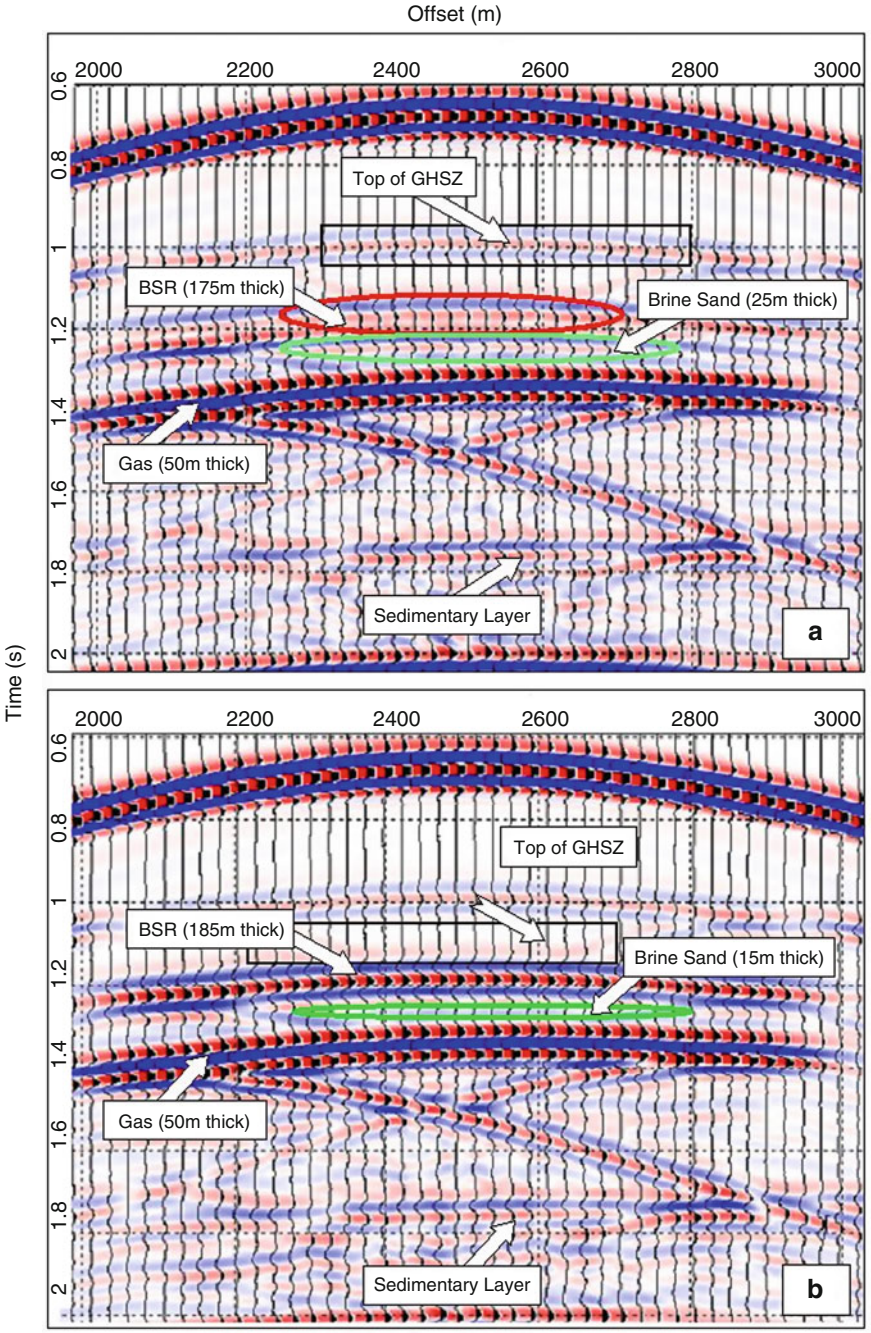

Fig. 7.39 The vertical component of particle velocity components (V- component) for varying thickness of brine sand layer; (**a**) 175 m thick BSR is demarcated with polarity reversal. The thickness of brine sand layer is 25 m; (**b**) 185 m thick BSR of high amplitude strength is shown with a 15 m thick layer of brine sand. (After Rajput et al. 2008 reprinted with permission)

amplitude strength is more realistic in the case of 25-m thick brine sand layer and is clearly evident on the seismic section calculated by elastic anisotropic modeling technique. The reflected arrivals from the top and the base of the GHSZ, brine sand layer and free gas zone and from the sedimentary layer are reliably resolved. The proposed model with co-existence of methane hydrate, free gas and brine is seems to be realistic, as the occurrence of gas hydrate in identical conditions within the regional hydrate stability zone in nature.

The double BSR model is shown in Fig. 7.40. The source of 20 Hz is assumed for generation of synthetic seismic data. The shot points as well as the OBS, which are located just above the target area, produce the best results. The vertical component proves the generation of double BSR in the presence of low velocity layer as shown in Figs. 7.41 and 7.42. A clear polarity reversal with respect to sea floor is observed on both the BSR. The top of the gas hydrate zone exhibits the low amplitude strength. Primary BSR attains its appreciable strength on the demarcation boundary of GHSZ and mixture of gases. Second BSR achieved its appreciable strength in terms of amplitude on the separation boundary of free gas.

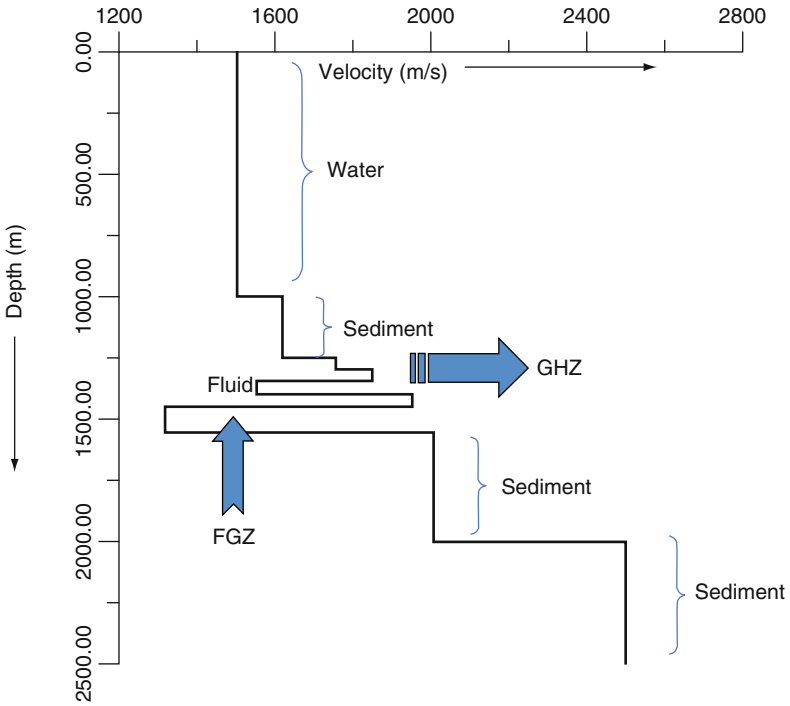

Fig. 7.40 Proposed double BSR model that represent discrete layers of concentrated hydrate formed by upward migration of gas; (**a**) Two dimensional velocity model double BSR; (**b**) One dimensional velocity model double BSR and the OBS is deployed just above the target area. (After Rajput et al. 2008 reprinted with permission)

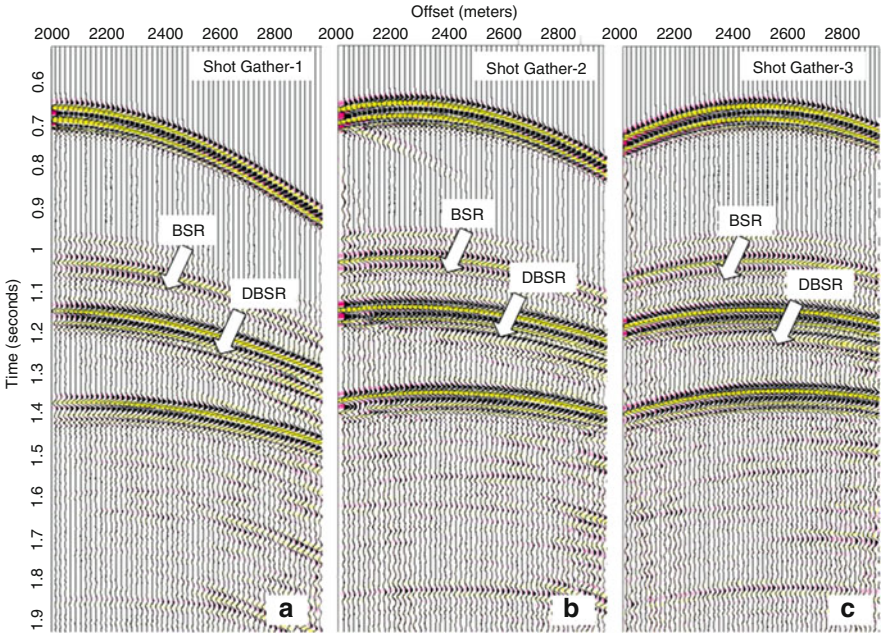

Fig. 7.41 Three different shot gathers for DBSR model. The BSR and DBSR are identified as reverse polarity events and marked on the seismic section (After Rajput et al. 2008 reprinted with permission)

The transmission of seismic energy within the layered media can be shown with the help of wavelet propagation. In case of double BSR the transmission, reflection and diffraction of seismic energy within the structure is considered in this case and is shown in Fig. 7.43. As seismic energy travels within the media, the first reflections from ocean bottom and then sedimentary layer reflection are observed respectively. In the wavelet propagation the strength of BSR in terms of amplitude is demarcated and it favors the aforesaid results.

7.6.1.3 Converted Waves patterns for Complex Bottom Simulating Reflector Model

Seismic wave propagating as elastic wave below the seawater must undergo the transmission, reflection and conversion on each interface of layered media. Theoretical study about the property of various reflections with pressure recording is needed. Since four component (4C) sea bottom surveys use conventional air gun sources, which generate P waves only therefore the shear waves recorded by these 4C sensors on the ocean bottom are mode-converted shear waves. The most common wave-conversion types are shown in Fig. 7.5 (1) P-wave converts to S-wave during transmission at an interface (say, at the seafloor) and then propagates

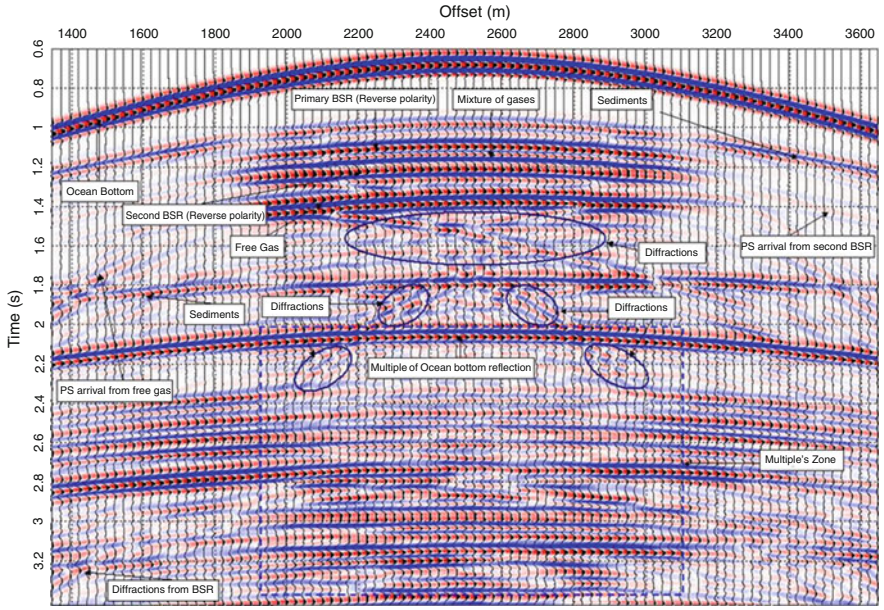

Fig. 7.42 The vertical component of particle velocity component (Z-component) for double BSR case. The *top* part demarcated the double BSR of different strength with polarity reversal with the typical response from the mixture of gases. *Middle* part illustrates the diffractions from either side of the GHSZ and the *lower* part demonstrates the multiples from different horizons(After Rajput et al. 2008 reprinted with permission)

as S-wave (PSS- or SS-wave type. Orange colour line in Fig. 7.5), and (2) P-wave converts to S-wave at a reflector (reflected wave) and then propagates back as S-wave to the receiver (PS-wave type, Blue colour line in Fig. 7.5). There may be many more conversions from P- to S-wave and vice-versa during reflection and transmission at intermediate interfaces, but they are actually too weak to be significant (Stewart et al. 2002). For a layered earth model, SS-wave data can be analyzed in the same manner as the P-wave data (due to its symmetrical ray path). However, P- to S-wave conversion as a transmitted wave at the seafloor (or any other layer interface) depends on the S-wave velocity below the conversion surface (compared to the P-wave velocity above interface). In the shallow subsurface, S-wave velocity at (or near) the seafloor is very low (100–300 m/s) unless there are some high velocity layers (e.g., carbonates and gas hydrates). In such a situation, P- to S-wave conversion during transmission is very weak. The PS-wave is better recorded than the SS-wave since it suffers less attenuation and is faster than the SS-wave. 4C studies allow the application of vector fidelity of seismic wave field (Berg et al. 1994), which used a single OBC deployed by Remote Operating Vehicle in water depth down to about 150 m (Caldwell 1999).

Moreover, cable dimensions lead inevitably to vector infidelity of the seismic cables. As of our knowledge OBCs have not yet been used in water depths

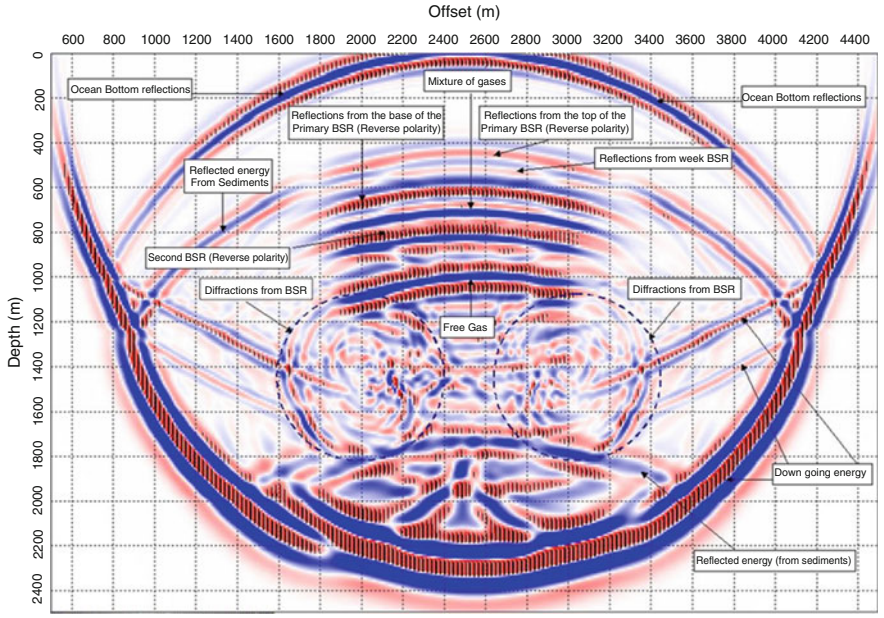

Fig. 7.43 The high gain component of wavelet propagation through the target zone. This component demonstrates the response of seismic energy (down going, reflected and diffracted) traveled through the different zones(After Rajput et al. 2008 reprinted with permission)

exceeding 3,000 m, therefore independent receiver (node) systems have been proposed, consisting of anchors that can be planted by Remote Operating Vehicles and used by connecting a cable to a recording vessel, but their deployment is restricted to the depth at which the Remote Operating Vehicles are capable to operate (Vermeer 2001). Still there are some shortcomings like as, not matching the density of the seabed, affecting the signal to be recorded (Vermeer 2001). These can be better achieved with densely deployed OBS of independent nodes supplied with adopted sensor packages. The 4C OBS includes one hydrophone, one vertical geophone, one inline horizontal geophone and one cross line horizontal geophone. The P- waves generated by the air-gun sources converted to shear waves (PS) at the sea floor, then reflected back at the reflectors and converted to P-waves again at the seafloor, and finally recorded by the sensors near the sea surface. This kind of converted shear wave has a symmetric ray path and can be processed using conventional techniques.

From 4C OBS data, both P-P and P-S sections can be obtained. The OBSs generally record four components, two horizontal (X & Y), one-vertical (Z) and one pressure (H) components. Out of these four components the converted waves are recorded by X and Y component and the P-waves are recorded by Z and H components respectively. The P–S waves recorded by the sensor provide additional information about the target horizons and may provide the better estimate of petrophysical properties, which can't be determined with P-wave data alone. Unlike

the OBC operations, there is no need of specialized operating vessels for the deployment and retrieval of OBS. The instrument placement can be prepared easily for two dimensional (2D) or three dimensional (3D) surveys with optimization of the coupling of the geophones by making a link between the density of sea floor and the sensors for ultra deep environment, respectively making the OBS surveys less expensive than OBC.

The S-wave data analysis is complicated in comparison to P wave (P-wave from the source to the reflector and a converted S-wave from the reflector to the receiver). Unlike the PP- or SS-wave reflection paths, the S-wave reflection point (or conversion point) is not the midpoint between the source and the receiver (Fig. 7.5); it is closer to the receiver, and according to Snell's law, resulting in an asymmetric ray path. For closely spaced receiver data (like in OBC), they may be sorted as common conversion point (CCP) gathers for S-wave analysis (Tessmer and Behle 1988). However, for sparse receivers (like in OBS), common conversion point sorting is not practical and common receiver gathers will be used in the analysis, where each trace corresponds to a different shot.

The sea floor model used here is shown in Fig. 7.44, which has thicker sea water layer, thinner and thicker sedimentary layers with variation in velocities, high velocity layer squeezed in anomalous layers of gas hydrates and free gas deposits. Some assumptions have taken into account: those P-waves are mainly recorded by the pressure component (H) and vertical geophone (Z-component) and converted-waves are recorded by two horizontal geophones (X & Y-Components). It is also

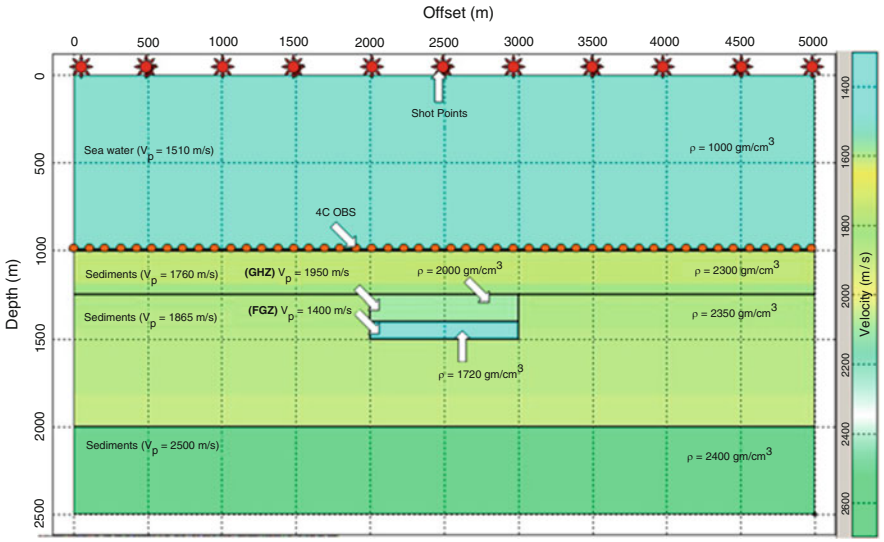

Fig. 7.44 Gas hydrate configuration model for finite difference simulations, Gas Hydrate Zone (GHZ) & Free Gas Zone (FGZ) are located at 1,250-m and 1,400-m depth respectively. Four component Ocean Bottom Seismometers are deployed on the ocean surface. 40 Hz shot are assumed at 10-m depth. (After Rajput et al. 2008 reprinted with permission)

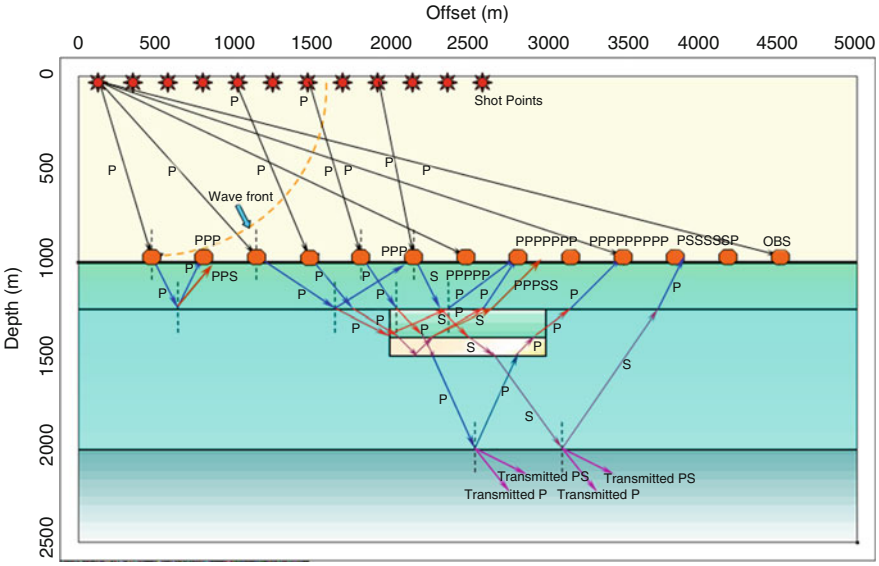

Fig. 7.45 Converted wave ray geometry for the key model. Horizontal component recorded by hydrophone with pragmatic signatures from the different reflectors including the gas hydrates and free gas province. The transmission of the seismic energy within the earth in the form of compressional and converted mode is demonstrated. (After Rajput et al. 2008 reprinted with permission)

assumed that P–S conversions occur at the reflectors. These assumptions are valid for most of the cases (Caldwell 1999). Following the converted mode geometry, the synthetic seismograms have been calculated for all the four components (X, Y, Z, and H). Converted ray geometry for the key model for a number of point sources located 10-m below the sea surface with different receivers deployed at ocean floor is calculated and demonstrated in Fig. 7.45. Reflection recorded by the pressure component for the single point source located in the middle of the seismic profile in seawater is shown in Fig. 7.46. The strong direct wave, and reflected waves from the sea bottom are clearly visible on the seismic section. The order of the arrival time on the profile of seismic reflections with the obvious amplitudes are PPP, PPPPP, PPPPPPP, PPPPPPPPP, PPS, PPPSS, PPPPSSS, and PPPPPSSSS. The letter P and S represent P-wave and shear-wave propagating in each layer respectively. PPP represents down-going P-wave in water, then down-going P-wave in layer-1, and then up-going P-wave recorded by receivers, which are placed at ocean bottom and finally reflected back in the sea water.

Most of the reflections (e.g. PPS, PPPSS etc.) have partial shear wave ray paths and experienced multi conversions at the reflectors except some of the reflections (e.g. PPP etc.). Some of the seismic reflections are due to transmitted mode-conversion on the solid–gas interface. These reflections could be of larger amplitudes than that of the P-wave path reflections on the other components. These results

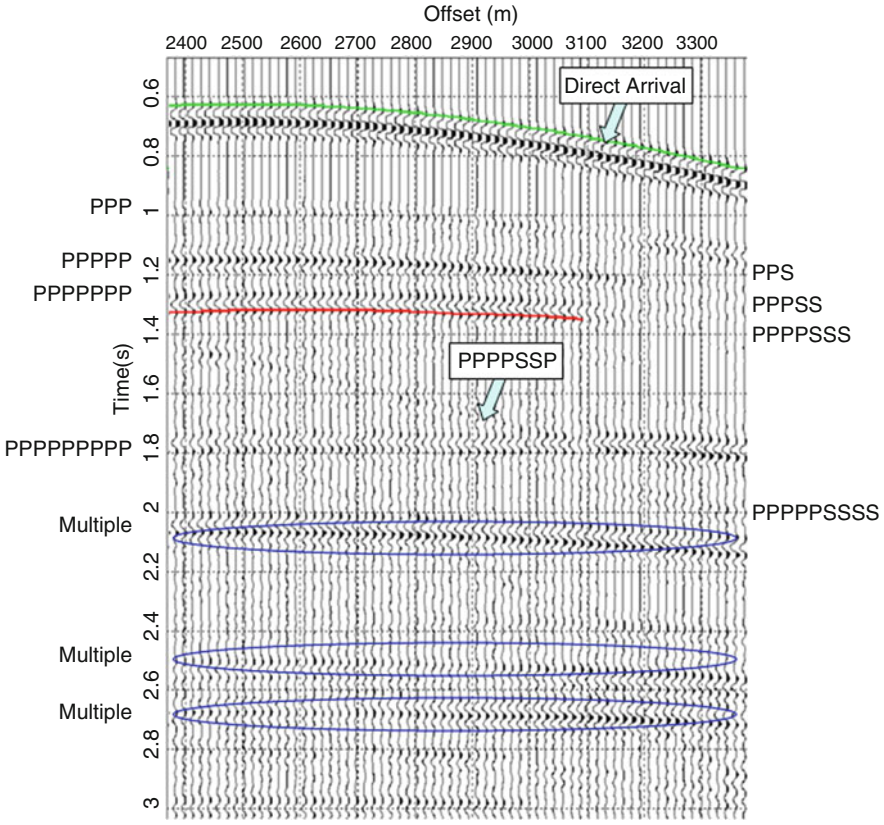

Fig. 7.46 Reflection recorded by hydraulic pressure component in seawater with obvious amplitudes PPP, PPPPP, PPPPPPP, PPPPPPPPP, PPS, PPPSS, PPPPSSS, and PPPPPSSSS. The wave type letter P and S represent compressional wave (P- wave) and S wave (S-wave) propagation respectively. *Green line* represents the direct arrival and the *red line* represents reflected wave. (After Rajput et al. 2008 reprinted with permission)

should be paid more attention for seismic data processing and interpretations. The other characteristics of the reflection section are the order of the arrival time of all reflections does not correspond to the depth order of the seismic interface. While starting the survey, reflections recorded by the hydrophone for the first shot point in the ocean water are shown in Fig. 7.47. Although dominate reflections and wave type numbers (PPP and PPS etc.) the reflection properties on the seismic section can be easily identified. Multi-converted diffractions with multiples are also identified. Figure 7.47b show wavefront propagation at inside the earth structures; transmission of seismic energy inside the earth as well as in the sea water, diffracted wavelets while propagation through a typical acoustic impedance contrast zone and converted wavelets are easily identified and demarcated on the profile.

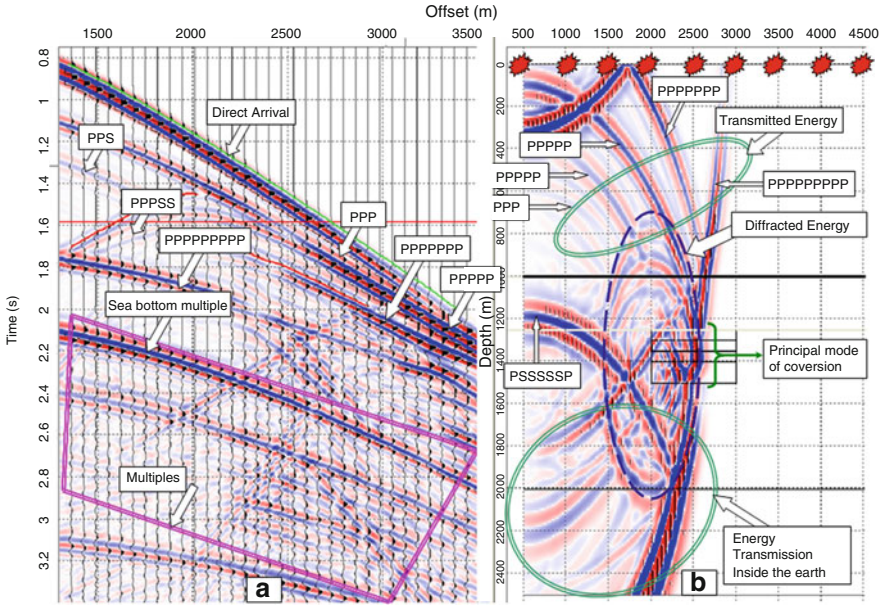

Fig. 7.47 Reflection recorded by pressure component in seawater with obvious amplitudes PPP, PPPPP, PPPPPPP, PPPPPPPPP, PPS, PPPSS, PPPPSSS, and PPPPPSSSS. The wave type letter P and S represent compressional wave (P- wave) and Shear wave (S-wav H component) recorded by hydrophone with some observed multiples and energy transmission inside the earth. (**a**); Pressure wave field including reflections with obvious amplitudes PPP, PPPPP, PPPPPPP, PPPPPPPPP, PPS, PPPSS, *Green line* indicates direct arrival and the *red line* indicates some reflected arrivals. This figure corresponds to Fig. 7.46. (**b**) The energy transmission by wavelet propagation inside the earth. Principal mode of conversion observed at the typical velocity contrast. (After Rajput et al. 2008 reprinted with permission)

Some Remarks

Here we discussed various patterns in synthetic data observed in gas hydrate studies. The modeling results provide "a priori" information, which allows unique determination of parameters of seismic models for the design of ocean bottom seismometer experiments over continental margins for the purpose of gas hydrate exploration. Bottom simulating reflectors (BSRs), are the high amplitude and negative polarity reflectors which occur due to the strong acoustic impedance contrast between the hydrate bearing sediments and underlying low velocity deposits and often used as a principal geophysical indicator of gas hydrate in a region. Using synthetic multi-channel seismic data, significant attempts have been made to study the nature and formation of BSR and its relevance to gas hydrate. The information gained through P wave data lacks in arriving an appropriate model and quantification of gas hydrates reserves. Multicomponent Ocean Bottom Seismometer (OBS) or Ocean Bottom Cable (OBC) studies are particularly the significant way to study the enigma of the nature and strength of the BSR.

We may conclude that the amplitude of BSR is strong enough to be recognized in all the components. Occurrence of the double BSR is associated with the presence of a low velocity layer within the gas hydrate zone, representing possible presence of fluids or contamination from other constituents of hydrocarbons. The shear strength of BSR diminishes with increasing thickness of the brine-saturated layer. The typical impedance contrast boundary is usually the strong conversion boundary through which P-wave and shear-wave are converted. The dominant reflections on P-wave profile (pressure and vertical component) may include the contribution of waves once propagated as shear-wave. PS waves from different mode-conversions underneath water layer can be recorded by 4C ocean bottom seismometer (OBS) operations at sea basement.

7.6.2 Converted Wave Velocity Model for Gas Hydrate Studies

Converted mode (P–S) exploration is complex in nature as it requires sophisticated technologies. Different seismic experiments composed of multichannel streamers, Ocean Bottom Seismometers (OBS); Vertical Seismic Profiles (VSP) were carried out in 2002 at the Hydrate Ridge, offshore Oregon continental margin to map the gas hydrate distribution, and to study the converted wave properties within the hydrate stability zone. Gas Hydrates in sea floor sediments can be identified though a geophysical indicator known as Bottom Simulating Reflector (BSR). Over the study area, the BSR covers an area of approximately 44 km^2.

7.6.2.1 Geologic Settings of Hydrate Ridge

Hydrate Ridge is located offshore the northwestern United States, and is the consequence of the subduction of the Juan de Fuca plate beneath the North American plate, The plate is subducting at a rate of about 4.5 cm/year (Fig. 7.48). Sediments on the subducting plate contain large volumes of sandy and silty turbidites. At present most of this sediment is accreted onto the continental margin either by off-scraping at the deformation front or by underplating beneath the accretionary complex (MacKay 1995). Sediments on the ridge are Pliocene in age. The ridge is characterized by a northern peak having a minimum water depth of 600 m and a southern peak with a water depth of 800 m (Fig. 7.12).

Subducting sediments and fluids will experience compressive force and as the anticlines in the accretionary prism (ridge) forms and sediments on the top of the ridge will move away from the ridge (extensional force) which will in turn would lead to formation of normal faults. Methane-rich fluids will migrate up towards the seafloor, and they form gas hydrates in favorable thermodynamic conditions. Methane gas is primarily of biogenic origin (inferred from carbon-isotope composition, methane has $\delta^{13}C$ lighter than -60%) (Kvenvolden 1988) but higher order hydrocarbons of thermogenic origin are also present. If gas saturation is in excess compared to water saturation or if the water salinity is high (≈ 105 gkg^{-1}) then

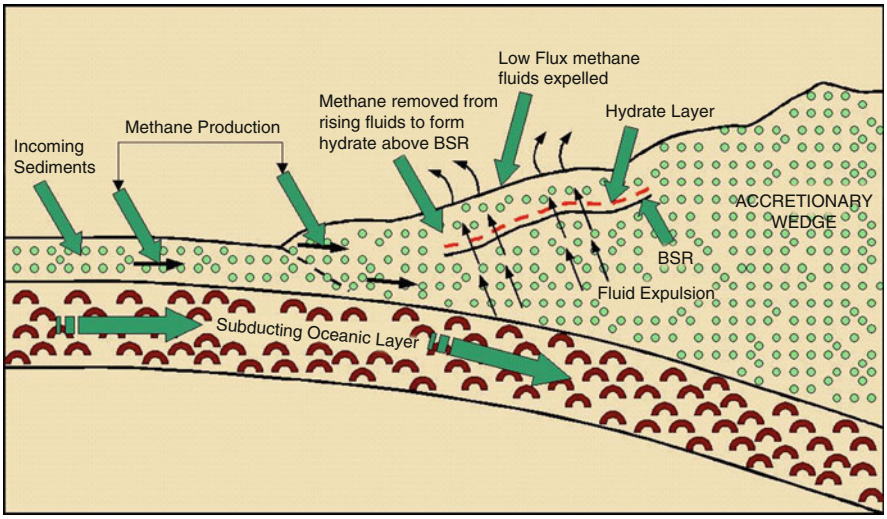

Fig. 7.48 Subduction of Juan de Fuca plate beneath North American plate (modified from Riedel et al. 2001)

free-gas can be present together with the gas-hydrate (e.g., Milkov et al. 2004). Gas hydrates and methane gas have been observed on the sea floor by submersible and deep-towed video surveys (Suess et al. 2001).

7.6.2.2 Velocity Analysis

Traditionally, a root mean square (rms) P-wave velocity is estimated from the normal move out analysis of hydrophone common mid-point (CMP) gathers in offset-time domain (Yilmaz 2001). The output is the P-wave rms velocity versus two-way zero-offset travel time and then Dix's (1955) equation is used to estimate interval velocity. In the case of VSP and OBS recording, the data are the receiver gathers (CMP gathers are not feasible), and the objective here is to find the interval velocity in depth. For this purpose velocity analysis in the τ-p domain (intercept time – ray parameters) is preferred. The interval velocity analysis has been performed in the τ-p domain assuming a locally 1D earth model resulting in interval layer velocities as a function of depth. Recently Kumar (2005) presented the application of interactive interval P-wave velocity analysis. The τ-p trajectory of a reflected P-wave (PP-wave) and PS-wave in an isotropic medium (Bessonova et al. 1974) is given by;

$$\tau_P(p) = 2\tau_P^0 \sqrt{1 - p^2 v_P^2}, \tag{7.1}$$

$$\tau_S(p) = \tau_P^0 \sqrt{1 - p^2 v_P^2} + \tau_S^0 \sqrt{1 - p^2 v_S^2} \tag{7.2}$$

where τ_P^0 and τ_S^0 is one-way vertical travel times and v_P v_S are the P and S-wave velocities for a layer. This formulation requires the data in the τ-p domain. The steps for the interactive interval P-wave velocity analysis assuming locally 1D isotropic media are as follows:

1. Convert the P-wave data (hydrophone or vertical component data) from offset-time to τ-p domain using plane wave decomposition (Stoffa et al. 1981; Treitel and Lines 1982).
2. Identify the P and S-wave reflection events between which velocity is desired.
3. Interactively pick a velocity (v_P) and v_S for a reflection event.
4. Final output is a 1D interval velocity model in depth.

The 1D velocity models estimated at each OBS location were interpolated to produce a smooth 2D P-wave velocity profile (W–E) across south ridge from summit to the slope basin side (Fig. 7.49). The P-wave velocity profile has been superimposed on the stack section derived from the streamer data. Note the higher velocity above BSR level suggesting the presence of gas hydrates, and lower velocity below BSR towards ridge due to the presence of free gas. There is no lowering of velocity below BSR level towards slope basin (covering four rightmost OBSs) suggesting an absence of free gas (marked by dashed elliptic shape), which is also evident due to discontinuous (or absence of a strong) BSR reflection. However, BSR is locally present in the basin (east) near anticlinal structures

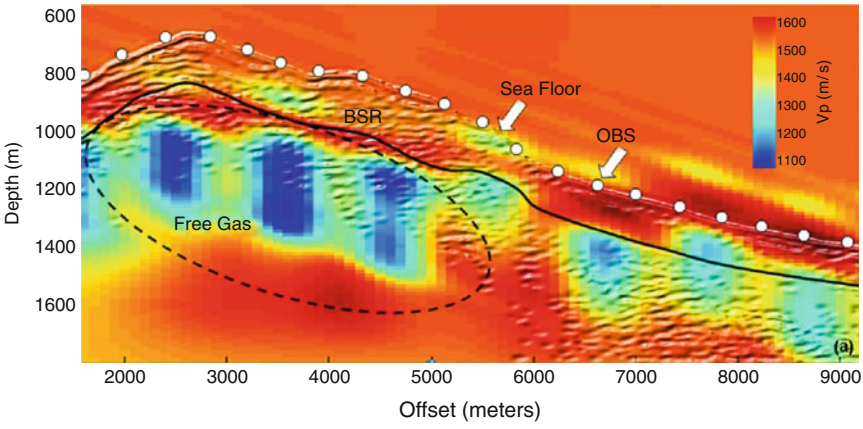

Fig. 7.49 The P-wave velocity profile derived from a velocity analysis using OBS data (about 0.5 km spacing) across south ridge from the south summit (W) to the slope basin side (E). Velocity data have been superimposed on the streamer data along OBS locations. Seafloor and BSR reflections are marked on the section. (After Rajput et al. 2008 reprinted with permission)

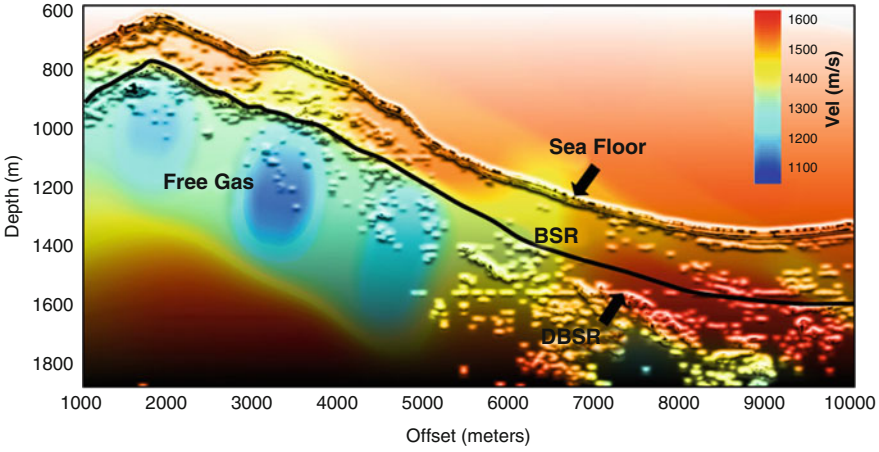

Fig. 7.50 The P-wave velocity profile derived from a velocity analysis using OBS data (about 0.5 km spacing) across south ridge from the south summit (W) to the slope basin side (E). Velocity data have been superimposed with more interpolation on the streamer data along OBS locations. Seafloor and BSR reflections are marked on the section. Free gas is present in the faulted zones beneath the BSR. The double BSR is also marked on the seismic section. (After Rajput et al. 2008 reprinted with permission)

suggesting presence of free gas. The presence of Double BSR is prominent on both the location and indicated on the profile.

There is no lowering of velocity observed below BSR level towards slope basin (between the ODP sites 1250 & 1251), suggesting an absence of free gas, which is also evident due to discontinuous (or absence of a strong) BSR reflection where as free gas is present on the 7OBS profile as the low velocity is observed and marked on the profile. Again the aforementioned process is applied with more smoothing and finally the P-wave velocity profile has been superimposed on the stack section derived from the streamer data (Fig. 7.50). Interval P-wave velocity analysis is performed in the τ-p domain from south summit to slope basin side at the Hydrate Ridge. Velocity is higher above BSR and lower below the BSR, indicating the presence of gas hydrates and free gas, respectively. Free gas is concentrated towards the summit and is absent towards basin, which is also evident from the presence or absence of a continuous BSR. Near the summit from sea floor down to about 50 m, lower P-wave velocity is observed which is interpreted to be caused by the presence of free gas along with gas hydrates. The BSR reflects different amplitude strength at different locations. The low velocity zone in the immediate vicinity of the first BSR, could be interpreted as brine saturated layer or a gas layer or some form of the hydrocarbons is causing the double BSR signature on the seismic section. The converted wave velocity mode for 20 OBS (WE profile) is shown in Fig. 7.51. For the other profile (WE Line) which contain 7 OBS data the velocities obtained from OBS are superimposed on MCS section (Figs. 7.52 and 7.53).

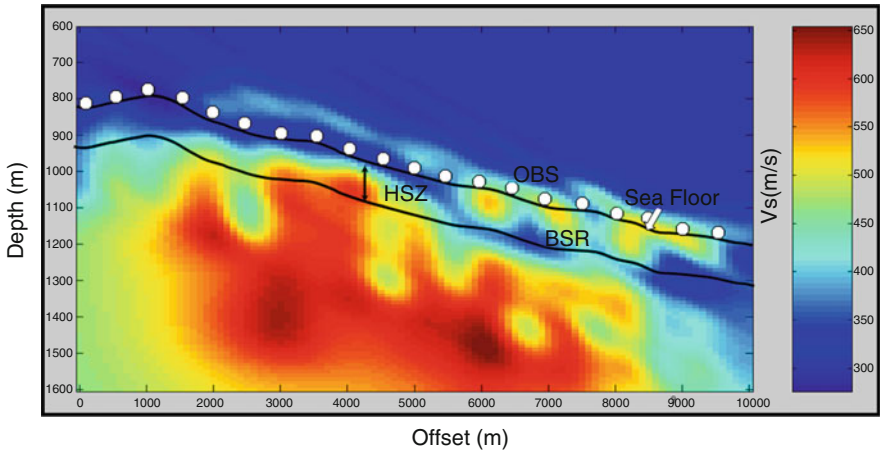

Fig. 7.51 The PS-wave velocity profile derived from a velocity analysis using OBS data (about 0.5 km spacing) across south ridge from the south summit (W) to the slope basin side (E). Velocity data have been superimposed with more interpolation on the streamer data along OBS locations. Seafloor and BSR reflections are marked on the section. Free gas is present in the faulted zones beneath the BSR. The double BSR is also marked on the seismic section. (After Rajput et al. 2008 reprinted with permission)

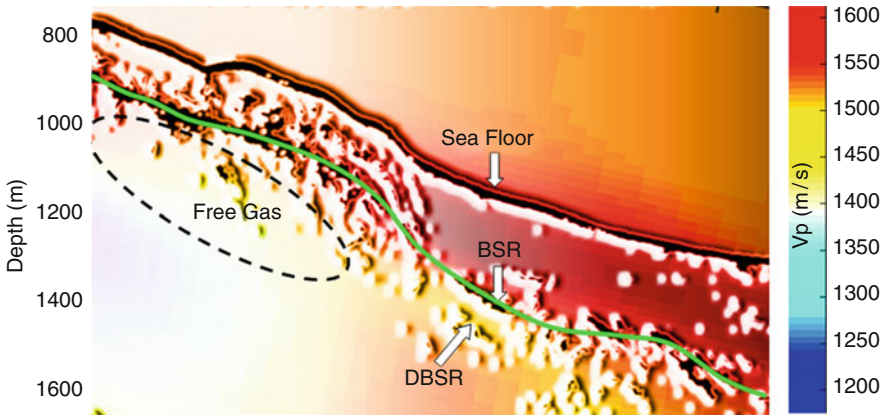

Fig. 7.52 The P-wave velocity profile derived from a velocity analysis using 7 OBS data across south ridge from the south summit (W) to the slope basin side (E). Velocity data have been superimposed with more interpolation on the streamer data along OBS locations. Seafloor and BSR reflections are marked on the section. Free gas is present in the faulted zones beneath the BSR. The double BSR is also marked on the seismic section. (After Rajput et al. 2008 reprinted with permission)

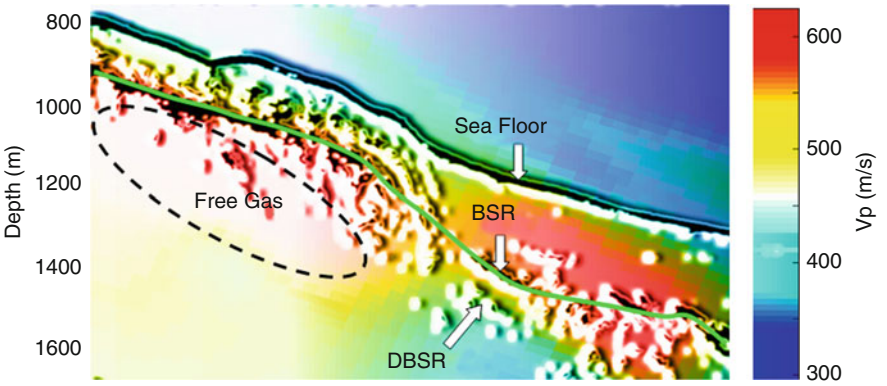

Fig. 7.53 The PS-wave velocity profile derived from a velocity analysis using 7 OBS data across south ridge from the south summit (W) to the slope basin side (E). Velocity data have been superimposed with more interpolation on the streamer data along OBS locations. Seafloor and BSR reflections are marked on the section. Free gas is present in the faulted zones beneath the BSR. The double BSR is also marked on the seismic section. (After Rajput et al. 2008 reprinted with permission)

Some Remarks

In this example we have extend the work done by Kumar et al. (2005) and follow the same approach. The data from two lines (20 Ocean Bottom Seismometer along the ODP sites 1250 and 1251 and the 7 Ocean Bottom Seismometer along the ODP sites 1244 and 1245) was utilized to study the PS mode properties and to investigate the sensitivity of the seismic velocities to the presence of gas hydrate and associated free gas in the sediments. The study area is shown in Fig. 7.12. The data have been processed for individual receiver gathers and the seismic velocities have been estimated for all the 27 Ocean Bottom Seismometers. As the accurate estimation of the distribution and concentration of gas hydrates and free gas from seismic velocities depends on the interval velocities of P- and S-waves, the method is based on an interactive velocity analysis of P and converted S waves in the tau-p domain (Kumar et al. 2007) applied to the 4C Ocean Bottom Seismometer data. The results reveal a complex velocity structure (Figs. 7.49–7.53) along specific sedimentary strata. We may conclude that the converted wave velocity does not show velocity anomaly in the hydrate-bearing sediments. The results indicate that the gas hydrate likely to occur at the HR on offshore Oregon Continental margin in an approximately 150-m thick zone directly above the BSR. The gas in the strata significantly increases the impedance contrast, causing enhanced reflections on the seismic reflection data. The reflection enhancement terminates at the level of the HSZ, where gas hydrate overlies and possible trap gas causing BSR to be observed as an envelop of those terminations rather than a distinct reflection. The data also illustrate that the origin of the BSR is largely the result of the trapped gas underneath.

7.6.3 *Processing of 4C OBS Data for Gas Hydrate Studies*

In multi-component data recording, we have hydrophone which records P-waves (pressure sensitive) and three geophones that record both P- and S-waves. However, the vertical component geophones primarily record P-waves and the horizontal components record S-waves. During data recording the orientation of horizontal receivers are not known and both the receivers record S-waves. They are trigonometrically rotated to radial and transverse components to maximize the S-wave energy on the radial component. After preprocessing of the Ocean Bottom Seismometer data the final four component (4C) data file in SEGY format (Fig. 7.13) have been utilized for further processing. Following are the main steps for processing of multi-component seismic data.

1. Transfer the Raw data from instrument (OBS) to an internal hard disk.
2. Apply frequency filtering.
3. Merge with navigation data.
4. Apply clock correction and location of vessel.
5. Convert into SEGY format.
6. Locate different component of OBS instrument.
7. Extract 4C file.
8. Extract four components from this single file.
9. Rotate two components into radial and transverse component (e.g. Gaiser 1999 and Brown et al. 2002).
10. Perform velocity analysis (preferably in an interactive way e.g. Kumar et al. 2007) for compressional and shear waves.
11. Crosscheck with MCS velocities by superimposing of calculating correlation coefficient.
12. Validate by the direct information (if available) e.g. log data.

An example of cross check for above mentioned steps has been illustrated in Fig. 7.53. To match the reflectors identified on the OBS data with the reflectors on the streamer data, the P- and S-wave OBS data (Fig. 7.53) has been superimposed on the streamer data in depth domain. While analyzing the OBS data, 1D velocity depth section at every OBS location have been created for BSR identification. An example of this has been presented in Fig. 7.54. BSR reflection event has been marked on the streamer data to match with that on OBS data. Similarly, S-wave velocity analysis at other OBS stations have been performed which gives the S-wave section (radial component data) and the one dimensional S-wave velocity models in depth at the corresponding OBS sites (Fig. 7.55).

7.7 Log Responses for Gas Hydrates

In addition to the seismic data, geophysical information from logs can be used in combination with each other. This could add value in the detection and evaluation of gas hydrates. There are a variety of logs available which can detect the response

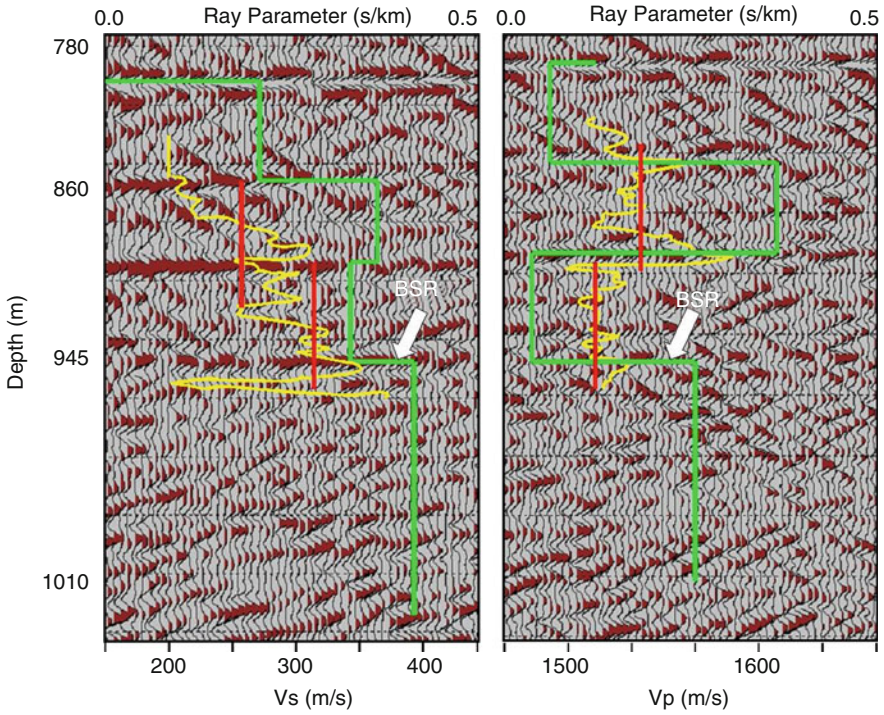

Fig. 7.54 Radial geophone (*left*) and hydrophone (*right*) data (in the τ-p domain) from one instrument (Hydrate ridge experiment) after NMO correction in time and converted to depth. Seismic velocities are overlaid on the seismic section (Vs on radial geophone and Vp on hydrophone data). Seismic velocities estimated from velocity analysis (in *red*) are compared with velocities derived from sonic (Vp) and dipole sonic (Vs) logs (in *yellow*). Vertical *blue* lines represent rms velocity from sonic logs (marked in two depth layers). All the reflectors (marked with *arrows*) are matching well in depth. (**a**); Vs profile (**b**): Vp profile (After Rajput et al. 2008 reprinted with permission)

of gas hydrates. Here we discuss the response for different logs in the presence of gas hydrates

7.7.1 Electrical Resistivity Log Response

Gas hydrate, like ice, acts as an electrical insulator. The presence of gas hydrate (or free gas) increases the resistivity of rock. *If we compare gas hydrate zones with water saturated horizons high resistivity deflections indicate the presence of gas hydrates in the region*. A very good example of resistivity log response is illustrated by Kumar et al. (2009) (Fig. 7.56). This example is from BP-DOE-USA consortium

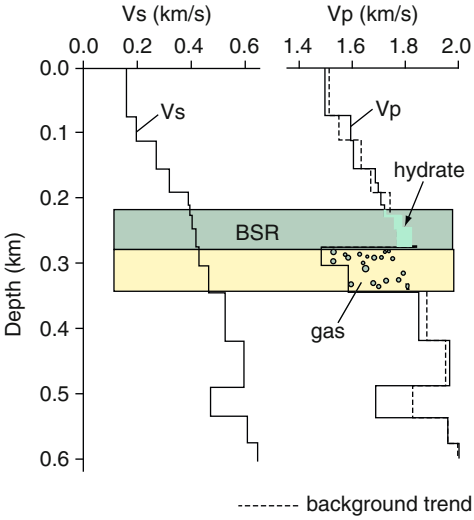

Fig. 7.55 One-dimensional velocity depth section for OBS (#4). Gas Hydrate zone (*light green*) and free gas zone (*light yellow*) are separately marked on the model

well test in 2007 called "Mount Elbert test" to study the feasibility of hydrate exploration and exploitation in Alaska (Inks and Agena 2008; Boswell et al. 2008).

7.7.2 Spontaneous Potential Log Response

The spontaneous potential log (SP) measures the natural or spontaneous potential difference (sometimes called self-potential) that exists between the borehole and the surface in the absence of any artificially applied current. It is a very simple log that requires only an electrode in the borehole and a reference electrode at the surface. These spontaneous potentials arise from the different access that different formations provide for charge carriers in the borehole and formation fluids, which lead to a spontaneous current flow, and hence to a spontaneous potential difference. The spontaneous potential log is given the generic acronym SP. Spontaneous potentials are usually caused by charge separation in clay or other minerals, by the presence of a semipermeable interface impeding the diffusion of ions through the pore space of rocks, or by natural flow of a conducting fluid (salty water) through the rocks. Variations in SP can be measured in the field and in wellbores to determine variations of ionic concentration in pore fluids of rocks (oilfield glossary from Schlumberger website; www.glossary.oilfield.slb.com). *For gas hydrate zones SP log shows relatively lower (less negative) deflection compared to that associated with free-gas zone.*

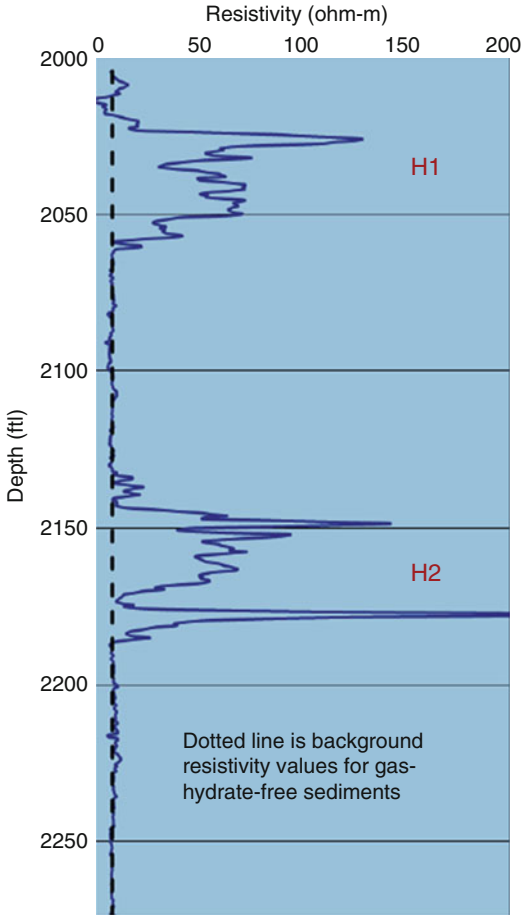

Fig. 7.56 Response of resistivity well log from Mount Elbert. Two possible gas hydrate zones are marked as H1 and H2. (After Kumar et al 2009, reprinted with permission)

7.7.3 Caliper Log Response

The caliper probe provides a "first look" at borehole conditions in preparation for additional logging. The log is used to measure borehole diameter and rugosity, locate fracture zones, assess borehole quality and stability, and for calculation of bore volume for pile construction. *The caliper log in gas hydrate zone usually indicates an oversized borehole resulting from spalling associated with gas hydrate decomposition*. A very good example of caliper log is illustrated in the Ocean Drilling Program (ODP) Leg 204 report (open literature) on drilling gas hydrates over Hydrate Ridge, Cancadia Continental Margin, offshore Oregon. The differential caliper log, which gives the distance between the tool sensor and the borehole wall, is the best indicator of borehole conditions. Differential caliper values are generally <1 in. over 90% of the total section in all the Holes, indicating an

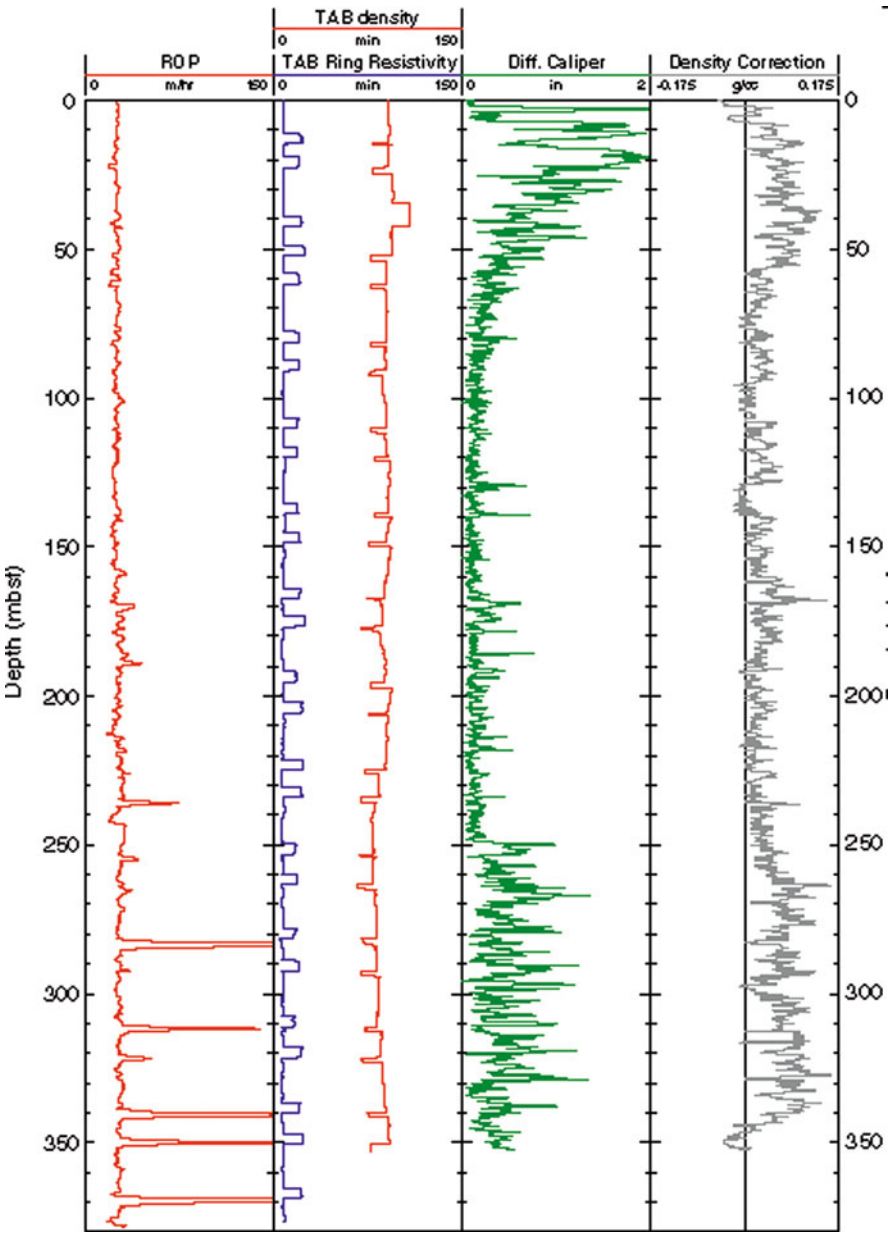

Fig. 7.57 Plots of quality control LWD logs: A, Hole 1244D drilling gas hydrates over Hydrate Ridge, Cancadia Continental Margin, offshore Oregon source http://www.ldeo.columbia.edu/BRG/ODP/ODP/LEG_SUMM/204/leg204.html.

accuracy of $\pm$ 0.015 g/cm^3 for the density measurements. Only the uppermost 30–40 mbsf of the holes show washouts greater than 1 in. In Hole 1244D the interval below 250 mbsf shows minor washouts due to borehole breakouts in the accretionary complex sediments, with differential caliper measurements up to 1 in. (Fig. 7.57 from ODP Leg 204 report).

7.7.4 Sonic Log Response

The sonic or acoustic log measures the travel time of an elastic wave through the formation. This Information can also be used to derive the velocity of elastic waves through the formation. Its main use is to provide information to support and calibrate seismic data and to derive the porosity of a formation. *Gas hydrate zone*

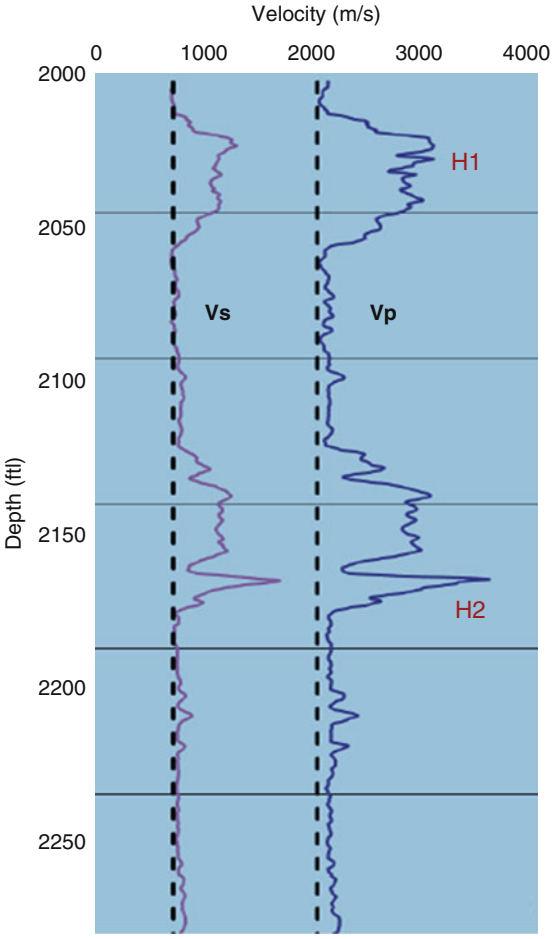

Fig. 7.58 Response of Vp and Vs logs with corresponding background values plotted by *black* dotted vertical lines from Mount Elbert. Two possible gas hydrate zones are marked as H1 and H2. (After Kumar et al. 2009, reprinted with permission)

shows a decrease in acoustic transit time compared with water saturated or gas zone. A very good example from Mount Elbert is illustrated by Kumar et al. (2009) (Fig. 7.58).

7.7.5 Neutron Log Response

The Neutron Log can be summarized as the continuous measurement of the induced radiation produced by the bombardment of that formation with a neutron source contained in the logging tool which sources emit fast neutrons that are eventually slowed by collisions with hydrogen atoms until they are captured (think of a billiard ball metaphor where the similar size of the particles is a factor). The Neutron Log is primarily used to evaluate formation porosity. It is used to detect gas in certain situations. *Gas hydrate zone shows slight increase in neutron porosity in contrast to an apparent reduction in neutron porosity in free gas zone*. A very good example is illustrated by Collett et al. 2010 from Northwest Eileen State-2 well.

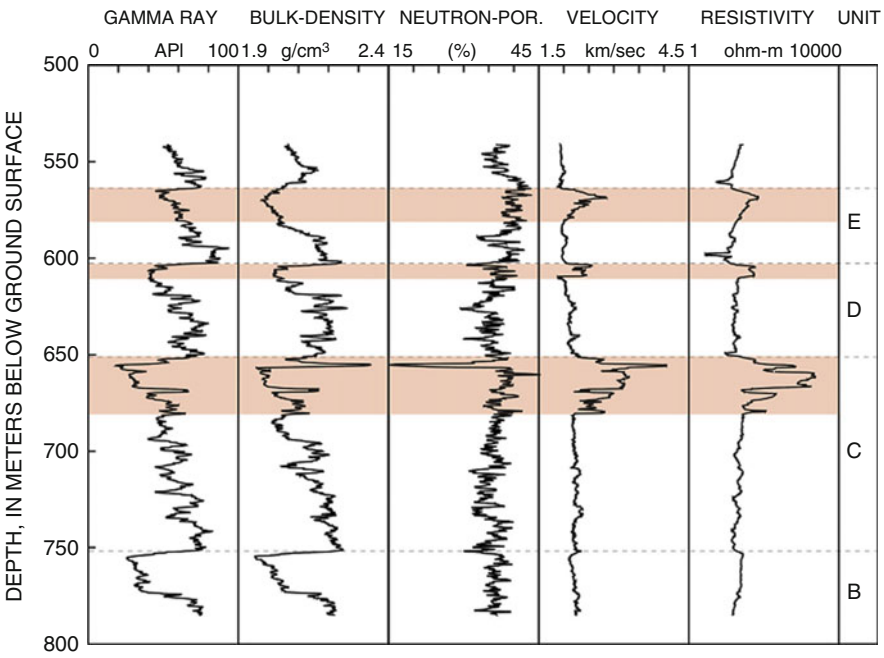

Fig. 7.59 Downhole logs from the Northwest Eileen State-2 well depicting the depth of units B, C, D, and E. Data shown include the natural gamma ray log, bulk-density, neutron porosity, acoustic velocity, and electrical resistivity data (Collett et al. 2010 reprinted with permission)

7.7.6 Density Log Response

Density log records the density of rocks. Gas hydrate zone shows slight decrease in density compared to a unit saturates with water. A very good example from Northwest Eileen State-2 well is illustrated in Fig. 7.59.

7.7.7 Some Remarks

The confirmed gas hydrate occurrence in the Northwest Eileen State-2 well provided an ideal starting point for the development of gas hydrate well log evaluation techniques (Figs. 7.59 and 7.60) (Collett et al. 2010). Collett (1993) and numerous studies since this early work have shown that in most cases only two well logging devices are used to identify potential gas hydrates: they are the electrical resistivity and acoustic transit time logs. For the most part, a gas hydrate-bearing sand reservoir is characterized by relatively high electrical resistivities and rapid acoustic transit times in comparison to water-saturated sands. However, resistivity and acoustic logs behave similarly within a sedimentary section that is saturated with either gas hydrate or ice. Hence, the occurrence of gas shows on the mud log produced from decomposing hydrate often provides the only means of conclusively differentiating a gas hydrate from ice in Arctic

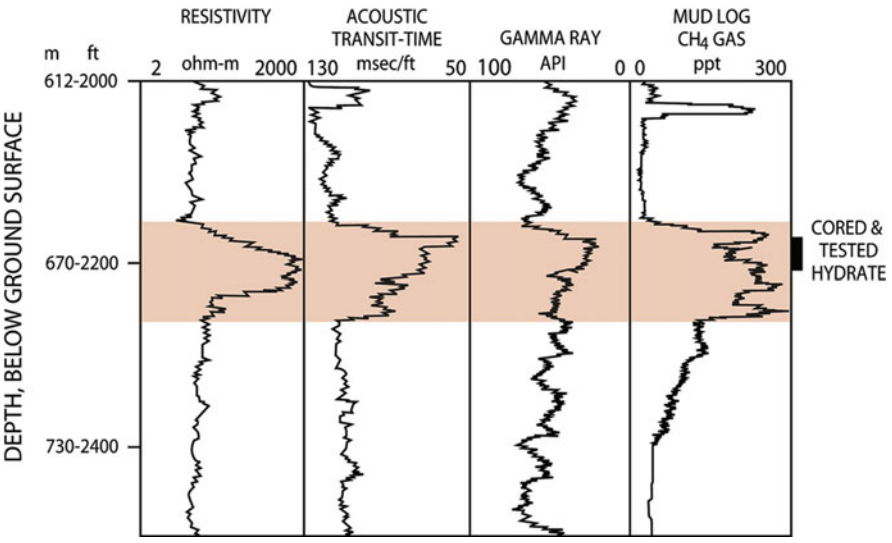

Fig. 7.60 Downhole logs from the Northwest Eileen State-2 well depicting the depth of units B, C, D, and E Insert of well logs from the cored (664–667 m) gas hydrate interval (unit C) in the Northwest Eileen State-2 well. Data shown include well logs and methane (CH_4) mud log curve. See Fig. 7.8 for well location (Collett et al. 2010 reprinted with permission)

permafrost regions (Collett et al. 2010). It has been speculated that the first commercial production of gas from gas hydrates is likely to occur in northern Alaska, where gas from gas hydrates could be used to support local oil and gas field operations, or be available for commercial sale if and when suitable gas pipelines are constructed (Collett et al. 2010). The Alaskan North Slope has been and will continue to be a focal point for gas hydrate research studies.

References

Alfaraj, M., 1993, Transformation to zero offset for mode-converted waves: PhD Thesis, Colorado School of Mines, Colorado.

Bangs et al, 1993, Brandsberg-Dahl et al. 2007 and Rajput et al. 2003; have been cited in the text, remaining others have been deleted.

Bangs, N. L., Sawyer, D. S., and Golovchenko, X., 1993, Free gas at the base of the gas hydrate zone in the vicinity of the Chile Triple Junction: Geology, **21**, 905–908.

Berg, E., Svenning, B., Martin, J., 1994, SUMIC: Multicomponent sea-bottom seismic surveying in the North Sea – data interpretation and application. 64th Annual International Meeting of the Society of Exploration Geophysicists, Expanded Abstracts, 477–480.

Bessonova, E. N., Fishman, V. M., Ryaboyi, V. Z., and Stinikova, G. A., 1974, The Tau method for inversion of travel times-I. Deep seismic sounding data: Geophysical Journal of The Royal Astronomical Society, **36**, 377–398.

Bialas, J., and Flueh, E. R., 1999, Ocean bottom seismometers: Sea Technology, **40**(4), 41–46.

Boswell, R., Hunter, R., Collett, T., Digert, S.,Hancock, S., Weeks, M., and Mount Elbert Science Team, 2008, Investigation of gas hydrate-bearing sandstone reservoirs at the "Mount Elbert" Stratigraphic test well, Milne Point, Alaska: Proceedings of the 6th International Conference on Gas Hydrates, Vancouver, BC, Canada, July 6–10.

Brandsberg-Dahl, S., Hornby, B., and Xiao, X., 2007, Migration of surface seismic data with VSP Green's functions: The Leading Edge, **26**, 778–780.

Brown, L.T., T.L. Davis, and M. Batzle, 2002, Integration of rock physics, reservoir simulation, and timelapse seismic data for reservoir characterization at Weyburn Field, Saskatchewan Society of Exploration Geophysicists. SEG Expanded Abstracts 21, pp. 1708–1711

Caldwell, J., 1999, Marine multicomponent seismology: The Leading Edge, **11**, 1274–1282.

Carcione, J. M., and Tinivella, U., 2000, Bottom simulating reflectors: seismic velocities and AVO effects: Geophysics, **65**(1), 54–67

Castagna, J. P., Batzle, M. L., and Eastwood, R. L., 1985, Relationship between compressional-wave and shear wave velocities in elastic silicate rocks: Geophysics, **50**, 571–581.

Castagna, J. P., Batzle, M. L., Tubman, K. M., Gaiser, J. E., and Burnett, M. D., 1993, Offset-dependent reflectivity – theory and practice of AVO analysis. In: Castagna, J.P., Backus, M.M. (Eds.), Investigations in Geophysics. SEG Publication, USA, pp. 115–135.

Chave, A. D., Constable, S. C., and Edwards, R. N., 1991. Electrical exploration methods for the seafloor, in Electromagnetic Methods in Applied Geophysics, edited by M. Nabighian, chap. 12, pp. 931– 966, Soc. of Explor. Geophys., Tulsa, Okla.

Cheesman, S., Edwards, R., and Chave, A., 1986, On the theory of sea-floor conductivity mapping using transient electromagnetic systems: Geophysics, **52**(2), 204–217.

Christeson, G. L., McIntosh, K. D., Shipley, T. H., 2000, Seismic attenuation in the Costa Rica margin wedge: amplitude modelling of ocean bottom hydrophone data: Earth and Planetary Science Letters, **179**, 391–405.

Collett, T. S., 1993, Natural gas hydrates of the Prudhoe Bay and Kuparuk River area, North Slope, Alaska: American Association of Petroleum Geologists Bulletin, **77**(5), 793–812.

Collett, T. S., et al., 2010, Permafrost associated natural gas hydrate occurrences on the Alaska North Slope: Marine and Petroleum Geology, doi:10.1016/j.marpetgeo.2009.12.001.

Constable, S., 2006, Marine electromagnetic methods – A new tool for offshore exploration: The Leading Edge, **25**(4), 438–444.

Constable, S., and Cox, C. S., 1996, Marine controlled-source electromagnetic sounding 2. The PEGASUS experiment: Journal of Geophysical Research, **101**(B3), 5519–5530.

Cox, C., Constable, S., and Chave, A., 1986, Controlled-source electromagnetic sounding of the oceanic lithosphere: Nature, **320**(6), 52–54.

Dai, J.C., Snyder Fred, Gillespie, D., Koesoemadinata, A., Dutta, N., 2008, Exploration for gas hydrates in the deepwater Northern Gulf of Mexico: part I. A seismic approach based on geologic model, inversion, and rock physics principles. Marine and Petroleum Geology, **25**, 830–44.

Digranes, P., Mjelde, R., Kodaria, S., Shimamura, H., Kanasawa, T., Shiobara, H., and Berg, E. W., 1996, Modelling shear waves in OBS data from the Voring Basin (northern Norway) by 2D ray tracing. Pure and Applied Geophysics, **147**(4), 611–629.

Dillon, W. P., Lee, M. W., and Coleman, D. F., 1994, Identification of marine hydrates in situ and their distribution off the Atlantic Coast of the United States: Annals of the New York Academy of Sciences, **715**, 364–380.

Dix, C. H., 1955, Seismic velocities from surface measurements: Geophysics, **20**, 68–86.

Domenico, S. N., 1977, Effect of brine-gas mixture on velocity in an unconsolidated sand reservoir: Geophysics, **42**, 1339–1368.

Dunbar, J., 2008, Electrical resistivity investigation of gas hydrate distribution in Mississippi Canyon Block 118, Gulf of Mexico. De-fc26-06nt42959, DOE/NETL Methane Hydrate Projects.

Edwards, R. N., 1997, On the resource evaluation of marine gas hydrate deposits using sea-floor transcient electric dipole-dipole methods: Geophysics, **62**(1), 63–74.

Edwards, R. N., and Chave, A. D., 1986, A transient electric dipole-dipole method for mapping the conductivity of the sea floor: Geophysics, **51**(4), 984–987.

Eidesmo, T., Ellingsrud, S., MacGregor, L. M., Constable, S., Sinha, M. C., Johansen, S., Kong, F. N., and Westerdahl, H., 2002, Sea bed logging (SBL), a new method for remote and direct identification of hydrocarbon filled layers in deepwater areas: First Break, **20**, 144–152.

Ellingsrud, S., Eidesmo, T., Johansen, S., Sinha, M., MacGregor, L., and Constable, S., 2002, Remote sensing of hydrocarbon layers by seabed logging (SBL): Results from a cruise offshore Angola: The Leading Edge, **21**(10), 972–982.

Evans, R. L., 2007, Using CSEM techniques to map the shallow section of seafloor: From coastline to the edges of the continental slope: Geophysics, **72**(2), WA105–WA116.

Evans, R., Constable, S., Sinha, M., and Unsworth, M., 1994, On the electrical nature of the axial melt zone at 13° N on the East Pacific Rise: Journal of Geophysical Research, **99**, 577–588.

Flueh, E. R., Klaeschen, D., and Bialas, J., 2002, Options for multi-component seismic data acquisition in deep water: First Break, **20**(12), 764–769.

Gaiser, J. E., 1997, 3-D converted shear-wave rotation with layer stripping: Western Atlas Internat. Inc., Houston, Tex., U.S. Patent Number 5,610,875.

Gaiser, J. E., 1998, Method for improving the coupling response of a water-bottom seismic sensor: Western Atlas Internat. Inc., Houston, Tex., U.S. Patent Number 5,724,307.

Gaiser, J. E., 1999, Applications for vector coordinate systems of 3-D converted-wave data. The Leading Edge, **18**, 1290.

Gaiser, J., Moldoveanu, N., Macbeth, C., Michelena, R., and Spitz, S., 2001, Multicomponent technology: the players, problems, applications, and trends: summary of the workshop sessions: The Leading Edge, **20**(9), 1042–1047.

Goto, T.-N., Kasaya, T., Machiyama, H., Takagi, R., Matsumoto, R., Okuda, Y., Satoh, M., Watanabe, T., Seama, N., Mikada, H., Sanada, Y., and Kinoshita, M., 2008, A marine deep-towed DC resistivity survey in a methane hydrate area, Japan Sea. Exploration: Geophysics, **39**, 52–59.

Guerin, G., and Goldberg, D., 2002, Sonic waveform attenuation in the gas hydrate-bearing sediments from the Mallik 2L-38 research well, Mackenzie Delta, Canada: Journal of Geophysical Research, **107**, 2088.

Harris, J. M., Nokn-Hoeksema, R. C., Langan, R. T., Van Schaack, M., Lazarator, S. K., and Rector, J. W., III., 1995, High resolution imaging of a west Texas carbonate reservoir: Pan 1 – Project summary and interpretation: Geophysics, **60**(3), 667–681.

Hesthammer, J., and Boulaenko, M., 2005, The offshore EM challenge: First Break, **23**, 59–66.

Hirahara, K., 1980, Three-dimensional P-wave velocity distribution in southwestern Japan. Annual Meeting of the Seismological Society of Japan, no. 2.

Holbrook, W. S., 2001, Seismic studies of the Blake Ridge: Implications for hydrate distribution, methane expulsion, and free gas dynamics. In: Paull, C. K., and Dillon, W. P. (Eds.), Natural Gas Hydrates, Occurrence, Distribution, and Detection. American Geophysical Union, **124**, 235–256.

Hornby, B. E., and D. Herron, 2007, Introduction to this special session: Borehole geophysics/ VSP: The Leading Edge, **26**, 731.

Huffman, A. R., and Castagna, J. P., 2001, Petrophysical basis for shallow-water flow prediction using multicomponent seismic data: The Leading Edge, **20**(9), 1030–1035.

Hyndman, R. D., and Spence, G. D., 1992, A seismic study of methane hydrate marine bottom simulating reflectors: Journal of Geophysical Research, **97**, 6683–6698.

Hyndman, R. D., Yuan, T., and Moran, K., 1999, The concentration of deep sea gas hydrates from downhole electrical resistivity logs and laboratory data: Earth and Planetary Science Letters, **172**, 167–177.

Inks, T. L., and Agena, W. F., 2008, Successful gas hydrate prospecting using 3D seismic-a case study for the Mt. Elbert prospect, Milne Point, North Slope Alaska: SEG expanded abstract, 27, 473–477.

Jarchow, C.M., Catchings, R.D. and Lutter, W.J., 1994. Large explosive source, wide recording aperture, seismic profiling on the Columbia Plateau, Washington. Geophysics, **59**, 259–271.

Katzman, R., Holbrook, W.S., and Paull, C.K., 1994, A combined vertical incidence and wide-angle seismic study of a gas hydrate zone, Blake Outer Ridge: Journal of Geophysical Research, **99**, 17975–17995.

Kim, S. D., Nagihara, S., and Nakamura, Y., 2000, P- and S-wave velocity structures of the Sigbee abyssal plain of the Gulf of Mexico from ocean bottom seismometer data: Gulf Coast Association of Geological Societies (GCAGS) Transactions, **50**, 475–484.

Kopp, H., 2002, BSR occurrence along the Sunda margin: evidence from seismic data: Earth and Planetary Science Letters, **197**, 225–235.

Kumar, D., Dash, R., and Dewangan, P., 2009, Methods of gas hydrate concentration estimation with field examples: Geohorizons, 76–86

Kumar, D., Sen, M. K., and Bangs, N. L., 2005, Estimation of gas-hydrate saturation using multicomponent seismic data: SEG Expanded Abstracts 24, 1542; doi:10.1190/1.2147985

Kumar, D., Sen, M. K., Bangs, N. L., 2007, Gas hydrate concentration and characteristics within Hydrate Ridge inferred from multicomponent seismic reflection data. J Geophys Res, **112**, B12306. doi: 10.1029/2007JB004993.

Kumar, D., 2005, Analysis of multicomponent seismic data from the hydrate ridge, offshore Oregon: PhD thesis, The University of Texas, Austin.

Kvenvolden, K. A., 1988, Methane hydrate – a major reservoir of carbon in the shallow geosphere?: Chemical Geology, **71**, 41–51.

Lee, H., Lee, J.-W., Kim, D.Y., Park, J., Seo, Y.-T., Zeng, H., Moudrakovskr, I.L., Ratcliffe, C.I., and Ripmeester, J.A., 2005, Tuning clathrate hydrates for hydrogen storage. Nature, **434**, 743–746.

Li, X. Y., and Yuan, L, 1999, Compiling defeasible networks to general logic programs: Artificial Intelligence, **113**(1–2), 247–268.

Li, X., Kind, R., Priestley, K., Sobolev, S. V., Tilmann, F., Yuan, X., and Weber, M. 1999, Mapping the Hawaiian Plume Conduit with Converted Seismic Waves: AGU 1999 Fall Meeting (San Francisco, USA 1999).

Lines, L. R., Miller, M., Tan, H., Chambers, R., and Treitel, S., 1993, Integrated interpretation of borehole and crosswell data from a west Texas field: The Leading Edge, **12**, 13–16.

MacGregor, L., Constable, S., and Sinha, M., 1998, The ramesses experiment iii: Controlled source electromagnetic sounding of the reykjanes ridge at 57°45'n: Geophysics Journal International, **135**, 772–789.

MacKay, M. E., 1995, Structural variation and landward vergence at the toe of the Oregon accretionary prism: Tectonics, **14**, 1309–1320.

MacLeod, M. K., 1982, Gas hydrates in ocean bottom sediments. AAPG Bulletin, **6**, 2649–2662.

Mikhailov, O., Johnson, J., Shoshitaishvili, E., Frasier, C., 2001, Practical approach to joint imaging of multicomponent data: The Leading Edge, **20**(9), 1016–1021.

Milkov, A., et al., 2004, Co-existence of gas hydrate, free gas, and brine within the regional gas hydrate stability zone at Hydrate Ridge (Oregon margin): evidence from prolonged degassing of a pressurized core: Earth and Planetary Science Letters, **222**, 829–843.

Miller, R. D., Hunter, J. A., Doll, W. E., Carr, B. J., Burns, R. A., Good, R. L., Laflen, D. R., and Douma, M., 2000, Imaging permafrost with shallow P- and S-wave reflections: SEG Expanded Abstracts, **19**, 1339.

Peacher, I. A., Milkereit, B., Sakai, A., Sen, M. K., Bangs, N. L., Huang, J. -W., 2010, Vertical Seismic Profiles through Gas-Hydrate-Bearing Sediments (In Press with SEG).

Pecher, I. A., Holbrook, W. S., Stephen, R. A., Hoskins, H., Lizarralde, D., Hutchinson, D. R., and Wood, W. T., 1997, Offset-vertical seismic profiling for marine gas hydrate exploration – is it a suitable technique? First results from ODP Leg 164, Proc. 29th Offshore Technology Conference, 193–200.

Pecher, I. A., Holbrook, W. S., Sen, M. K., Lizarralde, D., Wood, W. T., Hutchinson, D. R., Dillon, W. P., Hoskins, H., and Stephen, R. A., 2003, Seismic anisotropy in gas-hydrate and gas-bearing sediments on the Blake Ridge, from a walkaway vertical seismic profile: Geophysical Research Letters, **30**, 1733.

Rajput, S., 2008, Analysis of Ocean Bottom Seismometer data for gas hydrate studies and subsurface models. Ph.D Dissertation, Kurukshetra University, Kurukshetra.

Rajput S., Sen M. K., and Chopra S., 2009 Seismic indicators of gas hydrates and associated free gas, SEG Expanded Abstracts, **28**, 2622; doi:10.1190/1.3255391

Rajput, S., Rao, P. P., and Thakur, N. K., 2003, Traveltime modeling for the occurrence of the gas hydrates over the continental margins of India, Gas Hydrate Group Report, NGRI (Confidential).

Riedel, M., Spence, G. D., Chapman, N. R., and Hyndman, R. D., 2001, Deep-sea gas hydrates on the northern Cascadia margin: The Leading Edge, **20**, 87–92.

Rajput S, 2008. Analysis of Ocean Bottom Seismometer data for gas hydrate studies and subsurface models. Ph.D Dissertation, Kurukshetra University Kurukshetra.

Schwalenberg, K., Willoughby, E., Mir, R., and Edwards, R. N., 2005, Marine gas hydrate electromagnetic signatures in Cascadia and their correlation with seismic blank zones: First break, **23**, 57–63.

Shipley, T. H. et al., 1979, Seismic evidence for widespread possible gas hydrate horizons on continental slopes and rises: AAPG Bulletin, **63**, 2204–2213.

Shipley, T. H., Houston, M. H., Buffler, R. T., Shaub, F. J., McMillen, K. J., Ladd, J. W., Worzel, J. L., 1979, Seismic evidence for widespread possible gas hydrate horizons on continental slopes and rises: AAPG Bulletin, **12**, 2204–2213.

Stewart, R. R., Gaiser, J. E., Brown, R. J., and Lawton, D. C., 2002, Converted-wave seismic exploration: Methods: Geophysics, **67**, 1348–1363.

Stoffa, P. L., Buhl, P., Diebold, J. B., and Wenzel, F., 1981, Direct mapping of seismic data to the domain of intercept time and ray parameter– A planewave decomposition: Geophysics, **46**, 410–421.

Suess, E., et al., 2001, Sea floor methane hydrates at Hydrate Ridge, Cascadia Margin. In: Paull, C. K., and Dillon, W. P. (Eds.), Natural gas hydrates: Occurrence, distribution, and detection: AGU monograph 124, Washington, DC.

Tessmer, G., and Behle, A., 1988, Common reflection point data-stacking technique for converted waves: Geophysical Prospecting, **36**, 671–688.

Tinivella, U., A method or estimating gas hydrate and free gas concentrations in marine sediments: Bollettino di Geofisica Teorica ed Applicata, **40**, 19–30.

Treitel, S., and Lines, L., 1982, Linear inverse theory and deconvolution: Geophysics, **47**, 1153–1159.

Vermeer, G. J. O., 2001, Seismic data acquisition developments in the last decade and in the next – a biased view: CSEG Recorder, **26**(3), 13–16, June.

Walther, C.H.E., 2003, The crustal structure of the Cocos ridge off Costa Rica. Journal of Geophysical Research, **108**(B3):2136.

Weitemeyer, K. A., 2008, Marine electromagnetic methods for gas hydrate characterization: Scripps Institution of Oceanography, UC San Diego. Retrieved from: http://escholarship.org/uc/item/61x1136v.

Weitemeyer, K., Constable, S., and Key, K., 2006a, Marine EM studies of Hydrate Ridge, Oregon, USA-imaging hydrates and the accretionary complex. EM Workshop, El Vendrell, Spain.

Weitemeyer, K., Constable, S., Key, K., 2006b, Marine EM techniques for gas-hydrate detection and hazard mitigation: The Leading Edge, **25**, 629–632.

Weitemeyer, K., Constable, S., Key, K., and Behrens, J., 2006c, First results from a marine controlled-source electromagnetic survey to detect gas hydrates offshore Oregon: Geophysical Research Letters, 33, L03304, doi:10.1029/2005GL024896

Xu, H., Dai, J., Snyder, F., and Dutta, N., 2004, Seismic detection and quantification of gas hydrates using rock physics and inversion. In: Taylor, C.E., Kwan, J.T. (Eds.), Advances in Gas Hydrates Research. Kluwer, New York, pp. 117–139.

Yilmaz, O., 2001, Seismic Data Analysis: Processing, Inversion, and Interpretation of Seismic Data: 2nd Edn., Society of Exploration Geophysicists, Tulsa.

Yuan, J., and Edwards, R. N., 2000, The assessment of marine gas hydrates through electronic remote sounding: Hydrate without a BSR? Geophysical Research Letters, **27**(16), 2397–2400.

Yuan, J., and Edwards, N., 2001. Towed seafloor electromagnetics and assessment of gas hydrate deposits: Geophysical Research Letters, **27**(16), 2397–2400.

Yuan, T., Hyndman, R. D., Spence, G. D., and Desmons, B., 1996, Seismic velocity increase and deep-sea gas hydrate concentration above a bottom-simulating reflector on the northern Cascadia continental slope: Journal of Geophysical Research, **101**, 13655–13671.

Zhang, Z., and McMechan, G. A., 2003, Elastic Inversion and interpretation of seismic data from Hydrate Ridge, offshore Oregon, with emphasis on structural controls of the distribution and concentration of gas hydrate and free gas. Masters thesis, Center for Lithospheric Studies, The University of Texas at Dallas, PO Box 830688, Richardson, TX 75083-0688, USA.

Zelt, C. A., and Smith, R. B., 1992, Seismic travel time inversion for 2D crystal velocity structure: Geophysical Journal International, **108**, 16–74.

Chapter 8
Identification to Quantification of Gas Hydrates

Abstract In order to meet the world's energy requirements, identification to quantification of potential energy resources such as gas hydrates is of prime importance. Here we present details of different interpretation techniques and seismic characteristics for drawing inference about the presence of gas hydrates in a region of investigations. The regional identification of gas hydrates could be achieved by travel time inversion schemes. Full waveform modeling is useful in studying the different characteristics, including finer velocity and density estimates of gas hydrates and associated free gas. Seismic attributes are necessary in the direction of predicting gas hydrate saturation. The calculation of seismic attributes can be achieved by the integrated workflows of seismic, geology, pertophysics and rock physics techniques. Modeling for estimating BSR strength in terms of thickness of hydrate/free gas layers with information contained in the velocity estimation is a useful tool for estimating the reflection coefficients, Poisson's ratios and quantification of gas hydrate resources. This chapter summarizes the prevalent techniques for regional to local mapping of gas hydrates. To this end few synthetic and real data examples of gas hydrate characterizations from different regions of the world are discussed.

8.1 Introduction

The abundance of methane gas hydrate in the earth, if extracted, promises to solve the world's energy needs for many centuries. If we could produce on 17–20% of this resource it can be a sufficient supply of energy for 200 years (Makogon 2010). Up to now over 230 Gas Hydrate Deposits (GHD) have been found around the globe (Makogon 2010). The presence of gas hydrates in the subsurface earth cements the sediment grains by stiffing, which results in increasing acoustic velocity (Rajput et al. 2010). The sediments below the hydrate cemented zone; if saturated with water/free gas will have velocities appreciably lower compared to the hydrated layer.On regional scale the occurrence of marine gas hydrates are

N.K. Thakur and S. Rajput, *Exploration of Gas Hydrates*,
DOI 10.1007/978-3-642-14234-5_8,

usually identified by the demarcation of a high amplitude and negative polarity reflector which is known as Bottom Simulating Reflector (BSR) (e.g. Crutchley et al. 2010; Chand and Minshull 2003; Chapman et al. 2005; Davis 1992).

The BSR marks the base of gas hydrate stability (BGHS), above which conditions are generally favourable for gas hydrate formation, and below which they are not (Pecher et al. 2004; De Mets et al. 1994; Gei and Carcione 2003; Jakobsen 2000). The BSR is the response to a decrease in seismic velocity and/or density, which is usually attributed to free gas underlying gas hydrate (Bangs et al. 1993). Free gas associated with the gas hydrate system can potentially intersect the seafloor at BSR pinch-outs, where the BGHS coincides with the seafloor (e.g. Crutchley et al. 2010; Kostyukevych et al. 2001; Kvenvolden 1993; Lee 2008; Lee et al. 2009; Lynch 2000; Shipley et al. 1979; Sloan 1998). BSR also can form where there is only a small volume of the hydrates and only small quantity of free gas in the underlying layer because even a small amount of gas reduces velocity significantly. On the other hand, in some cases, BSRs are not traceable even where there are proven gas hydrate deposits. Addition to this the presence of BSR like feature doesn't confirm the presence of gas hydrates. A example of this type of geological environment is seen offshore Sydney, where one could observe BSR like feature but geological environment and Pressure/Temperature conditions are not favourable for gas hydrate accumulation (Fig. 8.1).

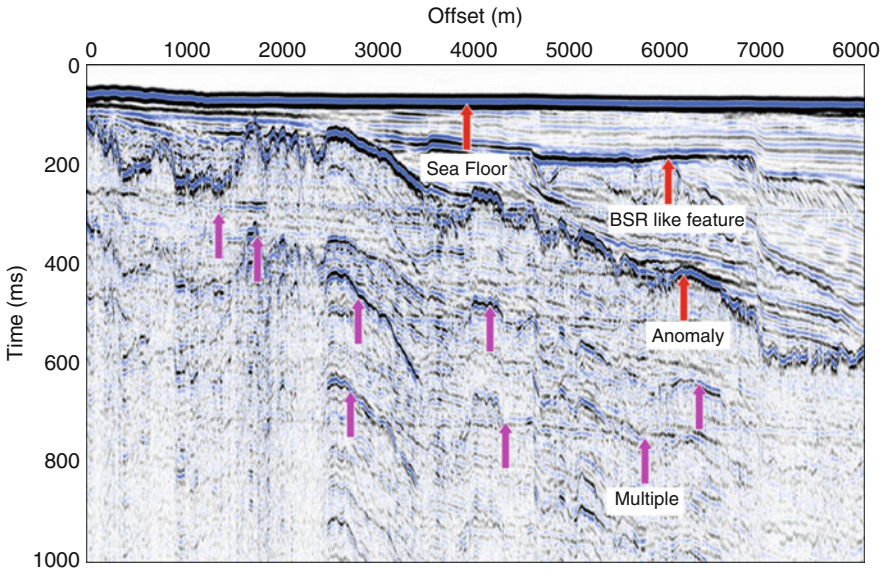

Fig. 8.1 Post Stack seismic section from offshore Australia (Sydney Basin). BSR like feature is identified and marked on the seismic section. *Pink arrows* are representing Multiples (Courtesy of CSIRO)

The presence of gas hydrates in the host rock appreciably enhances acoustics velocity with reference to velocity of unsaturated host rock and such enhancement can be utilized to estimate hydrate concentration (Kumar et al. 2009). The presence of methane gas exceeding its solubility in the deeper waters may uprise through advection of fluids in GHSZ for the formation of gas hydrates and free gas may likely to escape through the sea floor (Ginsburg and Soloviev 1997; Wood et al. 2002; Liu and Flemings 2006, 2007). The localised accumulation of free gas in marine sediments often yields anomalous seismic signatures, making seismic methods a useful tool for identification and characterisation of the sub-seafloor 'plumbing' beneath seep sites. Amplitude enhancement of sedimentary or structural features (i.e. "bright spots") can occur when gas preferentially accumulates in high porosity layers or structural voids such as faults (e.g. Taylor et al. 2000; Tréhu et al. 2004; Crutchley et al. 2010).

In order to evaluate the commercial potential of gas present within the gas hydrate, specific quantification procedure have to be adopted. There are numerous techniques dealing with quantification of gas hydrate reserves (Lee et al. 1996; Tinivella 1999; Ecker et al. 2000; Lu and McMechan 2002; Carcione and Gei 2004; Kumar et al. 2007, 2009; Westbrook et al. 2008; Collett 1998; Collett et al. 2010; Collett and Lee 2005; Kleinberg et al. 2005 etc.). The hydrate concentration estimation procedure then requires formulating an appropriate relationship to describe the change in mechanical properties of the sediment with gas hydrate concentration (Kumar et al. 2009). However, the accuracy of the estimation will depend on the sensitivity of these physical properties to the presence of gas hydrate e.g., higher the sensitivity of property more reliable is the estimation of hydrate concentration (Kumar et al. 2009). Physical parameters such as velocities, Poisson's ratio, resistivity, density and temperature are important and commonly used for quantitatively estimation of the gas hydrates. In this chapter, we describe various seismic tools of studying gas hydrates.

8.2 Regional Mapping of Gas Hydrates

There are various applications (e.g. seismic, rock physics, pertophysics etc.) available for quantitatively estimating of gas hydrates reserves. Here we discuss the most robust techniques from identification to quantification (Regional to local) as clean energy resource.

Hydrates have been found to occur in localized regions which may produce, lateral and vertical velocity variations (Pecher and Holbrook 2003). Detailed velocity analysis of seismic data constrains the quantitative estimates of gas hydrates volume, as well as the presence and volume of the underlying free gas (Hyndman et al. 1992). Dasgupta et al. (2006) pointed out the presence of gas hydrate without BSR. In order to get reliable estimates of gas hydrate resources one should start analyzing the available data and narrow down the search to quantify hydrate reserves in presence/absence of BSR (Fig. 8.1). The best reliable approach for

regional identification of gas hydrate provinces is the ray inversion method developed by Zelt and Smith (1992). This inversion algorithm requires a starting velocity model for the subsurface. The velocity field model is described by two types of model parameters, velocity nodes and boundary nodes, the latter specifying the depth of interface points between layers. Examination of the seismic data provides an assessment of the number of layers and nodes to be utilized in order to generate the starting model. The nodes are connected linearly to generate the layers. The velocity field for each layer is defined so that this varies linearly across upper and lower interfaces of the layers in the vertical direction. The difference between the observed and computed travel time curves is minimized by changing the velocity and the depth. Changes in the velocity leads to changes in the slope of the travel time curve. By changing the depth node the position of the estimated arrival travel time may made slower or faster. Velocities and depths are then modified until a satisfactory match between observed and computed depths was attained.

The advantage of using the inversion technique is that it provides an estimate of model parameter and an assurance that the data has been fit according to a specified norm. The technique is able to significantly increase the vertical resolution of the velocity structure because (1) the picking of seismic reflections of distinct continuous reflections without interference from adjoining reflections, transforms them into practically instantaneous events (the method assumes that the reflection event occurs in correspondence to the amplitude maximum), and (2) each event preserves its individual contribution to the velocity estimate during the whole inversion procedure. As a first step in the inversion process, rays are traced through the starting model and travel times were predicted, and then compared with the observed travel-times picked from the seismograms. The difference, in the form of a χ^2 error, is used to update the starting model. The model parameters of the boundary mode either of velocity or vertical coordinate (depth), or both, are modified after each iteration. The updated model serves as the starting model for the next iteration, and the process is repeated until the updated model predicts seismic travel-times that agree with the observed values to a degree determined by the assigned pick uncertainties, which is of the order of 10 ms (~50 Hz) (Zelt and Smith, 1992).

8.2.1 An Example from Kerala-Konkan (KK) Basin Offshore India

The Kerala-Konkan (KK) basin located at South of 16°N latitude. Kerala-Konkan offshore basin forms the southern part of the western continental margin of India and extends from Goa in the north to Cape Comorin in the south. Westward, the basin extends to Arabian Abyssal plain (DGH India web http://www.dghindia.org). On the eastern side it is bounded by peninsular shield. The basin evolved through early rift and post rift phases and contains more than 5 km of Cretaceous to Recent sediments. Post-rift mature sediments with sufficient organic carbon content are

present in the basin. Drilling results and adsorbed gas anomalies confirm generation of hydrocarbons in the basin.

The sedimentary sequence is comprised of Mesozoic and Tertiary sediments. Western continental margin basin of India evolved through the break-up of eastern Gondwanaland from western Gondwanaland in the Late Triassic/Early Jurassic and the subsequent spreading history of the eastern Indian Ocean. The western margin evolved through early rift and post rift phases of divergent margin development (DGH India web http://www.dghindia.org). A series of regional and local horsts and grabens resulted in response to rifting along the dominant basement tectonic trends. The northernmost part of the western continental margin was the first to be subjected to continental rifting and crustal subsidence in the Late Triassic. The process of rifting gradually advanced towards south and by Cretaceous time almost all the rift-related horsts and grabens came into existence. The source rock is mainly Paleocene to Eocene shales (DGH India web http://www.dghindia.org).

The Karwar Formation (Eocene) has rich organic matter (TOC upto 29%) and Kasargod Formation (Late Paleocene) has fair to good source potential. Shelfal Depressions & Lakshadweep Depression are considered to be kitchens for hydrocarbon generation. Eocene to Middle-Miocene Carbonates & Paleocene to Middle Miocene Sandstones are the possible reservoirs of Kerala-Konkan. Extensive carbonate platforms and shelf margin reefal bodies developed during Eocene to early Middle Miocene post rift phase over almost the entire western part of the shelfal horst-graben complex which serves as the reservoirs. The slope basin transition zone, particularly in front of the major shelfal depressions, is favorable for development of turbidite reservoirs in deep-sea fan complexes. There is a possibility of extension of turbidite reservoir facies locally into the Laccadive Depression through submarine canyons. Carbonate platforms around Laccadive Islands are likely to provide abundant reservoir bodies in the region of Laccadive Ridge (DGH India web http://www.dghindia.org).

The Indian subcontinent is surrounded by a passive margin. Because of this the sedimentary strata (bedding plane) are mostly horizontal in the deep sea. In such a situation the characteristic cross cutting property of the BSR relative to the bedding plane is generally missing. In this example we attempt to build up a velocity field model for a part of a seismic reflection line from the Kerala-Konkan (KK) bains of the western continental margin of India (Fig. 8.2 from DGH India web http://www.dghindia.org/15.aspx#) using 2D travel time inversion (Zelt and Smith 1992). This exercise maps the vertical extent, as well as the lateral anomalous velocity distribution and thereby infers the extent of gas hydrate and free-gas present in this basin.

The arrival times at every tenth shot gather of 96 channels with equal spacing of 250 m were analyzed from a seismic line in the KK region covering a distance of 7,500m. Spectral analysis of MCS data in this region indicates that the spectral band covering frequency range from 20 to 60 Hz (with the dominant peak at 35 Hz) contributes mainly to the amplitude (NGRI 2001). The corresponding vertical resolvable thickness ($\lambda/4$, where λ is the spatial wavelength) with acoustic velocity 2,000 m/s for this dominant frequency is about 15 m. Under these constraints one may not be able to distinctly resolve the thickness of very thin layers, because

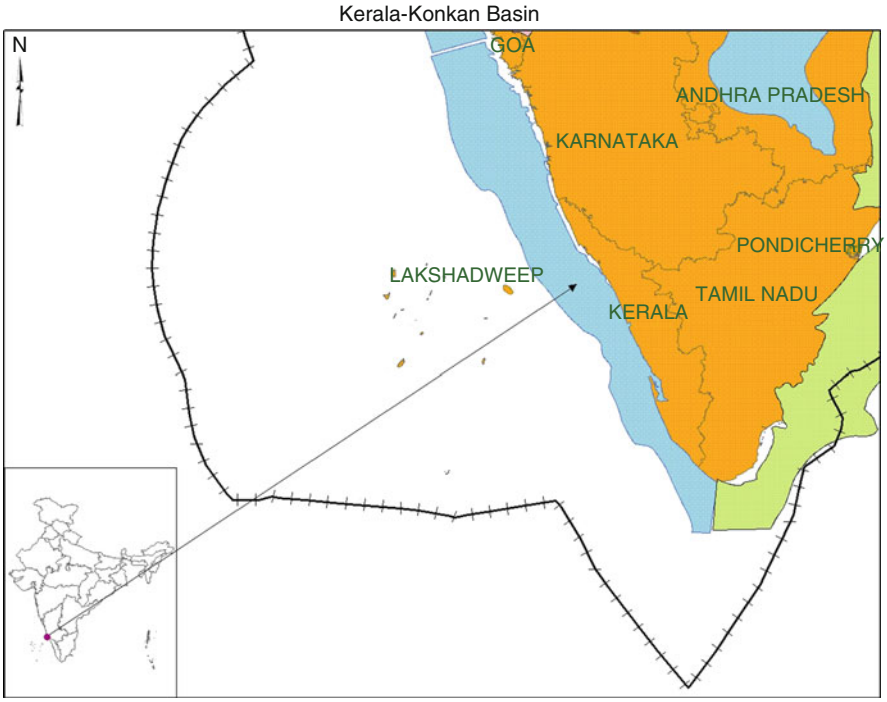

Fig. 8.2 Location of Kerala-Konkan (KK) basin offshore India. Adopted from Directorate General of India website
Source: http://www.dghindia.org

interference from thinner layers may impede signal resolution in the seismic sections. Travel-times were provided by picking seismic reflections in common-shot and common-offset gathers. Six events were picked from common shot gathers including direct arrivals. The event marked as 'D' is the direct arrival, H1 is the sea floor, H4 is a BSR-like feature, and the remaining events are reflections from different sedimentary sequences that were picked in order to determine the velocity distribution in the shallow layers under the region of investigation. Figure 8.3 shows the picking of events on shot gathers. The criteria selected was that the trace spacing must be constant within a shot gather because the selected traces provide the optimum reflectivity and amplitude response on contiguous shot gathers. This choice has also been conditioned as a result of the amplitude enhancement (AVO) for gas-bearing far offset traces (Rutherford and Williams 1989).

The resulted forward model (Fig. 8.4) was inverted in order to arrive at the finer velocity field, i.e. which fits best to the travel time data for KK. Considering the sediment velocity of 2,000 m/s the probable error in estimating the thickness for each layer of the sediments would be about 10 m. A few cycles were repeated until all possible picks were made at all receiver locations. The final model had the following the characteristics (a) A minimum number of velocity and depth nodes

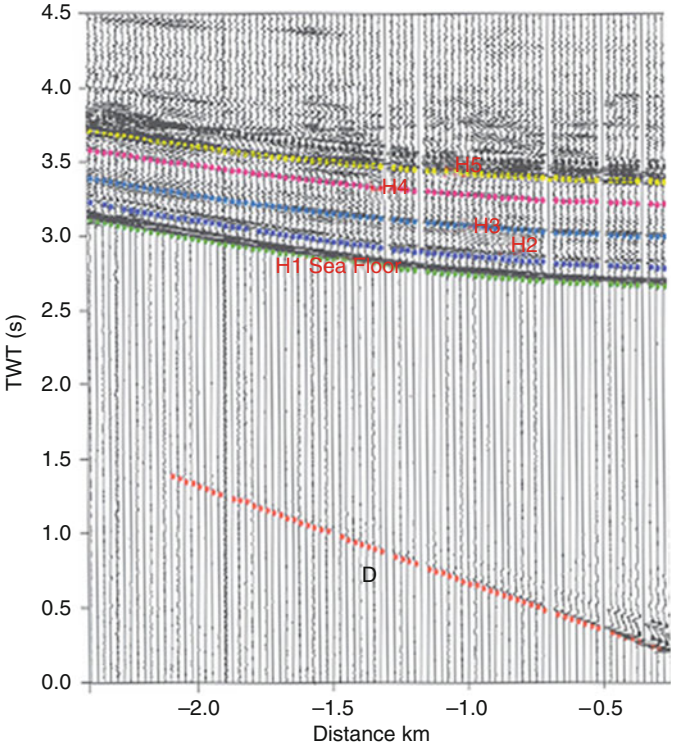

Fig. 8.3 Six events picked from common shot gathers. The event marked as '*D*' is the direct arrival. *H1* is the sea floor, *H4* is a BSR; *H2*, *H3*, and *H5* are the reflections from different sedimentary sequences (modified from Rajput et al. 2009)

needed to match the predicted travel times to the observed travel-times with their associated uncertainties, (b) the model allows rays to be traced to the maximum possible number of observation points and (c) the model contains only those features that are required by the initial models, and the dominant frequency of the seismic data. The final velocity field model after the inversion process is shown in Fig. 8.5. The χ^2 error for the fitted model is less than 2.0. The identified BSR in this region is shown in Fig. 8.6.

8.2.2 Some Remarks

P-wave velocities estimated of hydrated sediments for different regions of the world shows a large variation. Waveform inversion of data offshore Vancouver Island has produced a value of 1,700 m/s for the hydrated layer (Singh et al. 1993). In the region of Blake Ridge a velocity of 2,500 m/s was obtained (Rowe and

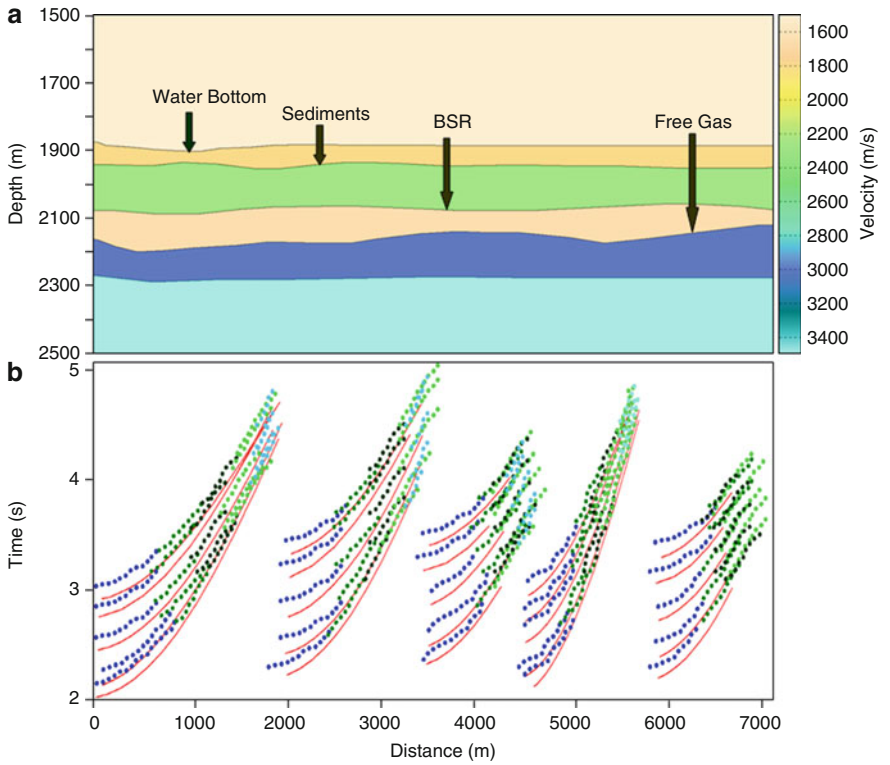

Fig. 8.4 Forward modeling results. (**a**) Obtained forward model for estimating the travel time arrivals. (**b**) The estimated travel time fit for the observed data. Solid red line indicates the observed travel time and dots with different colors indicate the estimated travel time for different horizons picked for analysis (Modified from Rajput et al. 2009)

Gettrust 1993). Similarly, for the free-gas layer the velocities estimated also shows appreciable variation ranging from as high as 1,850 m/s for the Indian region (Satyavani et al. 2002) to as low as 1,240 m/s for the Cascadian margin (Mackay et al. 1994). The 2D travel time inversion results of KK basin reveal a 50–60 m thick sedimentary layer with velocities ranging from 1,770 to 1,850 m/s. A layer with high P-wave velocities in the range of 1,980–2,100 m/s below the uppermost sedimentary layer is interpreted as the hydrated layer. The thickness of this hydrated layer varies from 110 to 140 m. The hydrated layer is underlain by a low-velocity layer having velocity in the range 1,660–1,720 m/s. This may represent a free–gas layer, whose thickness varies in the range 50–100 m. The low-velocity layer is underlain by sedimentary sequences with a normal velocity-depth structure.

Earlier P-wave velocities obtained from the westernmost part of this seismic line (Satyavani et al. 2002) suggest the probable presence of a thin zone of free gas

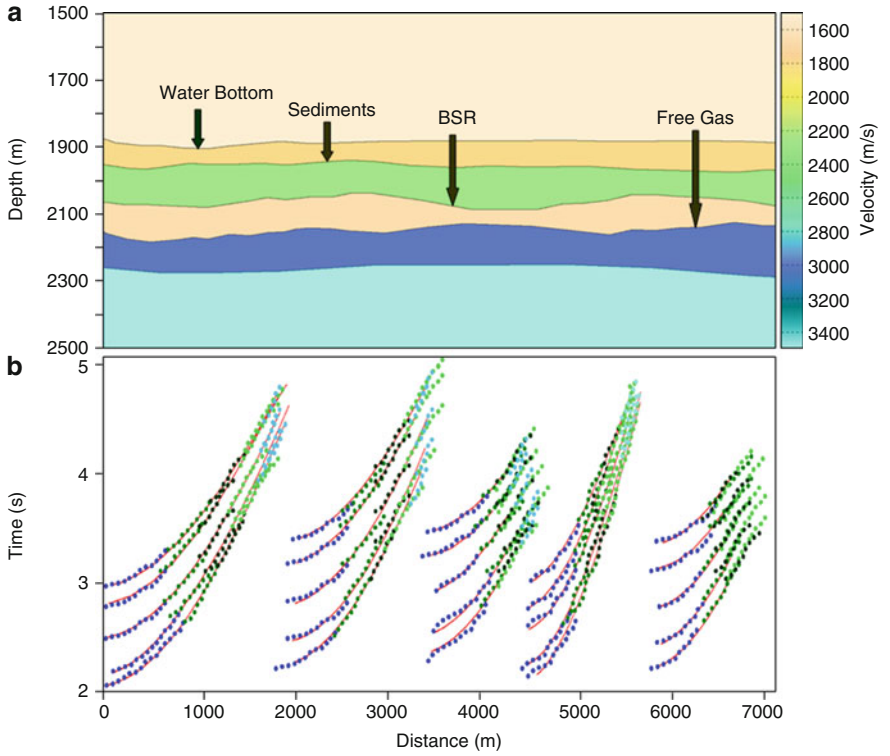

Fig. 8.5 Tomographic Inversion results. (**a**) Finer scale final model obtained through 2D travel time inversion of seismic data; (**b**) Best possible fit for the observed travel time after the inversion. Most of the travel time data is fitted quite well. Solid *red line* indicates the observed travel time and *dots* with different colors indicate the estimated travel time for different horizons picked for analysis (Modified from Rajput et al. 2009)

under the gas hydrate layer. The study indicates a sharp velocity increase to 2,050 m/s followed by a sudden decrease in velocity deeper in the section. The interval velocity falls to 1,850 m/s and this drop in velocity suggests the presence of gas-bearing sediment. The thickness of free-gas layer is very thin, around 20 m (Satyavani et al. 2002). The earlier results give a representative 1-D velocity model without lateral variation in the hydrated and free gas layer. Uma Shankar et al. (2006) utilized the fluid flow phenomena, such as venting through the seafloor, pock-marks, seafloor collapse and the presence of transparent, gas-charged sediments to evaluate the probable hydrate location in this region.

Travel time inversion results indicate that the increase in velocity of gas hydrate-bearing sediment varies laterally (From 1,975 to 2,150 m/s), probably due to changes in the saturation of gas hydrate in the sediments. Obtained vertical velocity variation ranges from 1,980–2,100 m/s for hydrated layers and 1,660–1,720 m/s for the free gas layers. The estimated velocity values for hydrate

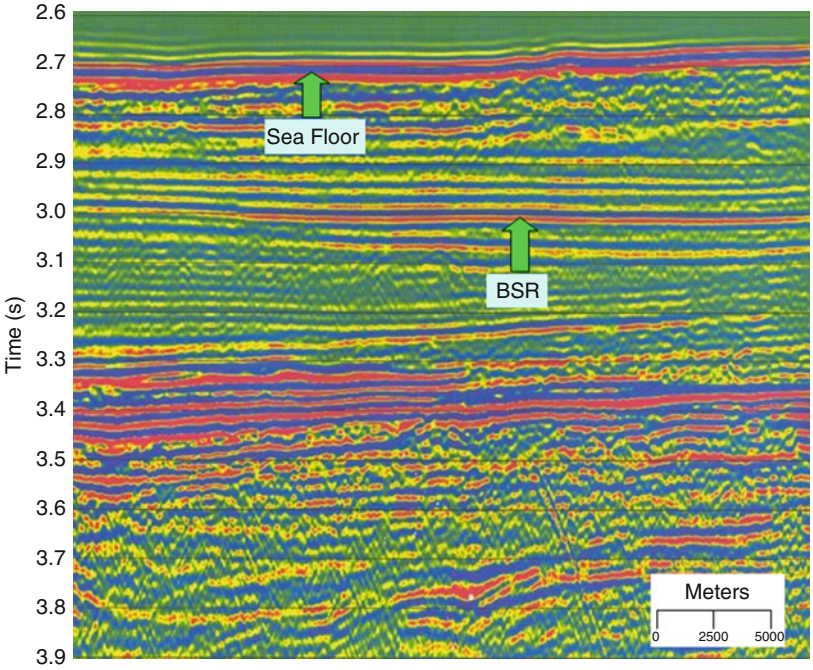

Fig. 8.6 Multi-channel seismic stack section of the eastern segment of seismic line under study (Modified from Rajput et al. 2009)

and free gas are in the range obtained for other hydrate regions of the world. The thickness of hydrated layer varies from 100 to 140 m and that of the free gas layer is in the range of 50–100 m. Initial drilling results from JOIDES Resolution at only one site 70.6°E and 15.3°N in the KK Basin have not encountered the gas hydrate layer (NGHP 2006). This drilling site was selected on the basis of high-resolution seismic proxies and other geological parameters, and is located to the northwest of the region of the present study. It has been observed that most potential gas hydrate sites, such as Blake Ridge in the Atlantic Ocean (Holbrook et al. 1996) and initial results from the Krishna–Godavari and Mahanadi Basins in the Bay of Bengal (NGHP 2006) have not encountered the presence of hydrate throughout the entire region. The absence of gas hydrate at only one site in KK Basin, does not rule out the possible occurrence of gas hydrate other parts of the basin, including the area of study here.

A 2D travel time inversion (Zelt and Smith 1992) on multichannel seismic data of Kerala-Konkan basin, western continental margin of India showed that the gas hydrates and free gas configuration could be modeled. The inversion results tend to show that 2D travel time inversion is well suited for mapping gas hydrates and free gas on regional basis and a reliable map of the P velocities that enables to delineate horizontal and vertical extent of the hydrates.

8.3 Amplitude Strength

The BSRs are caused by the negative impedance contrast between sediments containing high velocity hydrates and the low velocity free gas underneath the gas hydrate stability zone (GHSZ), and produce the reverse polarity. The occurrence of double BSRs has been interpreted that it could be a paleo BSR formed when methane gas froze into methane hydrate. The BSR, however, is a composite hydrate/gas reflection, and its amplitude is principally sensitive to the presence of free gas at the hydrate phase boundary. Numerous authors have been reported the worldwide occurrence of gas hydrates and the free gas at the base of the gas hydrate reservoir (Lee et al. 1996; Pecher and Henrys 2003; Pecher et al. 2004, 2005, 2007, 2008; Bangs et al. 1993; Barnes et al. 2010; Behrens 1988; Bialas et al. 2007; Caine et al. 1996; Dillon and Max 2000).

The observation of the multiple BSRs is unusual and rare. As of yet, very few published data about multiple BSRs exists and only a few scientists have reported the occurrence of multiple BSR (e.g. Posewang and Minert 1999). A BSR can appear without free gas below the GHSZ if the gas hydrate fills more than 30% of the pore space. Theoretically, the lateral changes of the BSR reflection characteristics may result from significant lateral and vertical changes in sedimentation history or vertical tectonism. Free methane gas that exists as bubbles in pore space, occurs under most known hydrate deposits. Available estimates of the volume of hydrate free gas are very speculative. The aerial extent of free gas would ideally be calculated from a global BSR survey, which does not currently exist. To reveal the concept of multiple BSR, nature and the strength of BSR a detailed model studies are needed and the synthetic data needs to be treated as recorded data and should be taken through a processing sequence.

Exploration-oriented seismic modelling requires accurate and efficient methods. There are a variety of seismic modelling algorithms incorporating analytical methods, semi-analytical methods (e.g. reflectivity method), raygeometric methods (e.g. ray tracing method) and direct methods (finite-difference and finite-element methods). Ray tracing modelling has the advantage of being fast and easy in identifying primary reflections. It is also very efficient for obtaining travel time information but the amplitudes determined with this method are not always reliable. On the other hand, elastic wave equation modelling accounts for direct waves, primary and multiple reflection waves, converted waves, head waves as well as diffraction waves. It therefore overcomes the shortcomings of the ray tracing approach, which fails in many cases, for example, at the edges where the calculated amplitude is infinite or in the shadow zone where the amplitude is zero. (Rajput et al. 2005a, b); and Rajput (2008) discussed that the elastic anisotropic and amplitude vs. offset modelling (AVOM) are very effective techniques for gas hydrate studies as their success relies on not only the quality of seismic data but also data processing and understanding of the rock's physical properties. In order to study the amplitude strength related characteristics of BSR finite difference technique is appropriate. There are various tools available which uses finite

difference solution of the wave equations and generate the synthetic data (e.g. Tesseral 2D and Norsar 2D and 3D).

All sound/seismic full-wave modelling schemes are deduced from the differential wave equation and the mechanical formula for the particle motion. They imply dependence of the wave propagation on a number of physical parameters distributed in space. Some of them are static, such as local wave velocity and density; the others are dynamic, such as the instant particle movement, pressure, etc. Static parameters do not vary with time and are prior to computations of the dynamic ones. Here we present a modeling study that reveals the amplitude strength related characteristics of BSR.

By trial and error method and based on the past experience different models have been tested and a key model is selected for further studies. Here we are presenting three cases for different models. Synthetic seismic response has been generated for all and the amplitude characteristics of single and multiple BSR have been studied. For first case the model utilized is presented in Fig. 8.7 (After Rajput 2008). Synthetic seismic response is generated by assuming several shots with 25-m interval. It is found that the shot point which is located just above the GHSZ, demonstrates the best results as shown in Fig. 8.8 (After Rajput 2008). The reflections from the sediments are properly resolved on either side of the hydrated zone. The amplitude strength of BSR increases gradually with depth. At the demarcation boundary of the GHSZ and FGZ the BSR record its noticeable amplitude strength and a strong simulating reflection is observed, which is confirmed by reverse polarity. The amplitude strength of BSR increases with the velocity contrast and confirmed the aforementioned results.

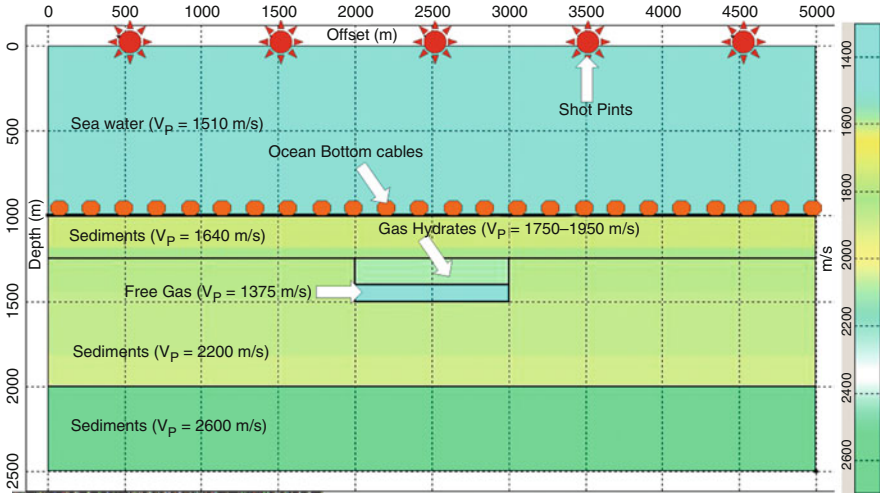

Fig. 8.7 Key model for the occurrence of BSR. Few shot points are shown in figure. Ocean bottom cables are assumed on the sea floor (Modified from Rajput et al. 2009)

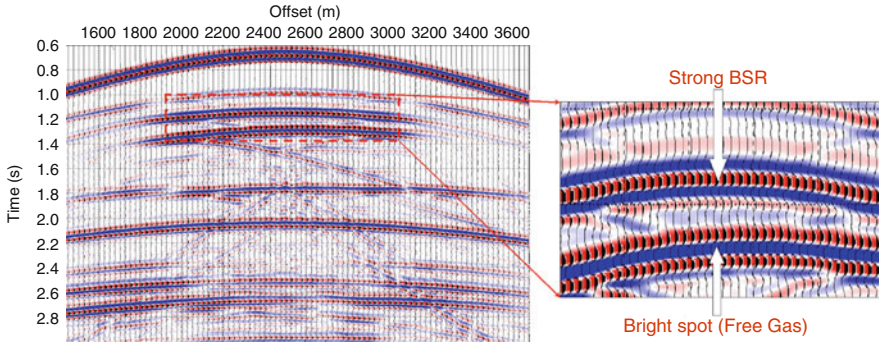

Fig. 8.8 Synthetic seismic response for the shot point located just above the target zone. Strong BSR for the occurrence of gas hydrate and a bright spot like feature, which indicate the presence of free gas is marked (After Rajput 2008)

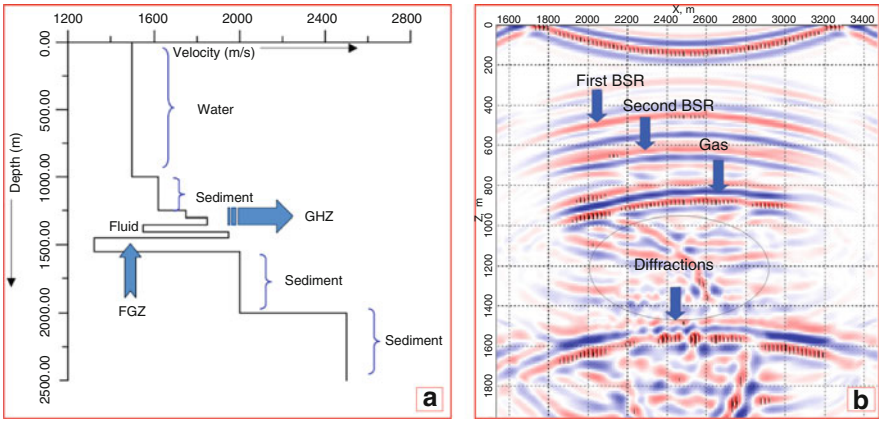

Fig. 8.9 Synthetic response of the model for the occurrence of DBSR; (**a**) Represents the velocity-depth curve. (**b**) Represents the energy propagation for DBSR model. First and second BSRs with the indication of the presence of Gas are marked on the section. Diffractions are also observed as indicated (After Rajput 2008)

In second case a low velocity layer (LVL) is assumed within the GHSZ. The vertical component proves the occurrence of double BSR (Fig. 8.9) in the presence of LVL 7 (After Rajput 2008). A clear polarity reversal with respect to sea floor is observed on both the BSR. The top of the gas hydrate zone exhibits the low amplitude strength but the polarity reversal seems realistic. First BSR attains its noticeable strength on the demarcation boundary of GHSZ and LVL while second BSR achieved its amplitude strength on the separation boundary of free gas. The reflections from the base of each sedimentary layer, diffracted multiples with increasing offset as well as from BSR with decreasing offset, multiples of ocean bottom reflection and of other layers are observed. Figure 8.9a represents one dimensional velocity depth curve for the model. Figure 8.9b is showing the

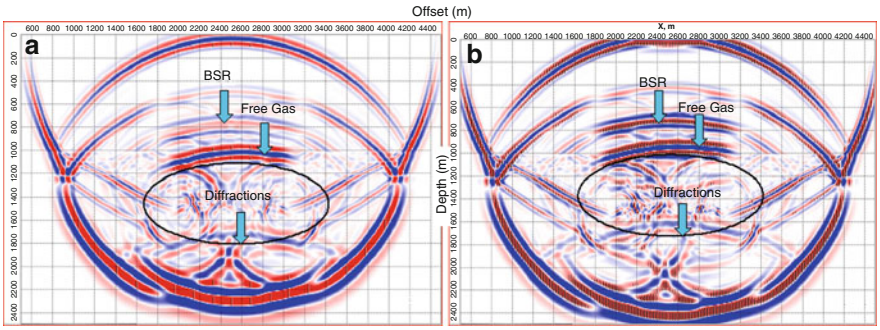

Fig. 8.10 Energy propagation for case −3; (**a**) Represents the 25 m thick brine saturated sand layer; (**b**) Represents 15 m thick brine saturated sand layer (After Rajput 2008)

wavefront propagation. Both the BSRs with the presence of gas are observed. The third case represents the consequence of a brine-saturated sand layer, which is sandwiched between the gas hydrate and free gas layers. The energy propagation for this case are showing in Fig. 8.10a. A comparison has been made to delineate the amplitude strength of BSR. The synthetic seismograms are calculated for both the 25 m thick and 15 m thick brine sand layer (Fig. 8.10a, b). The amplitude strength is more realistic in the case of 15 m thick brine sand layer. The proposed model with co-existence of methane hydrate, free gas and brine is authentic, as the occurrence of gas hydrate in identical conditions within the regional hydrate stability zone exists in nature (Rajput 2008).

8.3.1 Some Remarks

When seismic energy impacts on a boundary, fraction of the energy is reflected while fraction is transmitted. If the angle of incidence is not zero, P wave energy is translates further into reflected and transmitted (P and S components). The amplitudes of the reflected and transmitted energy depend on the contrast in physical properties transversely the boundary. The important physical properties in subject are compressional wave velocity (v_p); shear wave velocity (v_s) and density (ρ). The reflection amplitudes also depend on the angle-of-incidence of the original ray. So if one knows the amplitudes of a reflector with angle-of-incidence, one can figure out some concrete explanation about how the physical properties of the reservoir rocks are changing transversely the boundary. This example clearly demonstrates that the nature of the BSR mainly depends upon the physical properties of surrounding rocks and their apparent polarity. BSR is the exist evidence for a clear phase reversal with respect to the sea floor due to the occurrence of free gas underneath gas hydrates. The velocity contrast within the GHSZ reflects the amplitude strength of the BSR and produce noticeable strength BSR at the demarcation boundary of a low velocity layer underlying the GHSZ. However, the

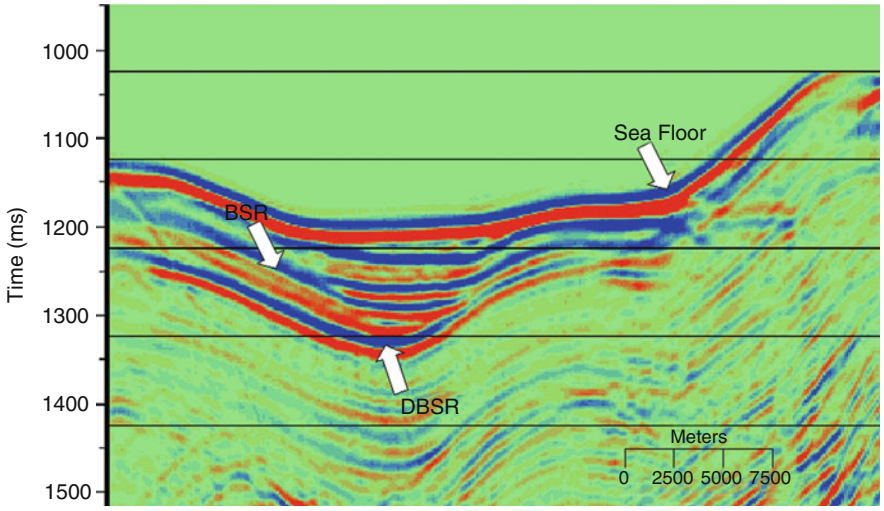

Fig. 8.11 Real data example from green canyon area. BSR and DBSR are clearly observed and marked on the seismic section (Modified from Rajput et al. 2010)

presence of LVL indicates the double BSR like features on the seismic sections. The qualitative velocity model for the occurrence of DBSR is proposed (Fig. 8.9), and validated by the real data example from green canyon area of Gulf of Mexico (Fig. 8.11). DBSR can be interpreted in terms of the discrete reflectors of concentrated hydrated formed by the upward migration of gas. The authenticity of the proposed velocity models for gas hydrates depends on the quality of seismic data, surrounding geological environment and competence of computer simulations.

8.4 Amplitude vs. Offset Characteristics

The inference of about the presence of oceanic natural gas hydrates is drawn from the identification of BSRs on seismic reflection data. Presently, our knowledge of BSRs includes two aspects: one is the direct characteristics of BSR which can be identified from the seismic profiles and is called the first characteristics; the other is the Amplitude vs. Offset (AVO) characteristic extended from the former and is called the second characteristics (Gong 1999; Niu et al. 2004). A theoretical analysis shows that the increase of free-gas saturation causes an increase in the magnitude/reflection coefficient with the offset. For a given gas saturation, however, it is difficult to evaluate the amount of gas hydrate at low concentration. The AVO technique is one of the methods which can be used to identify and predict lithologic characteristics and fluid properties by using the relationship between Amplitude and Offset (Huaishan et al. 2009). Not only the P-wave characteristics, but also the S-wave characteristics are considered when seismic waves propagate

through the strata (Huaishan et al. 2009). In order to demonstrate the AVO effects on BSR structure a modelling study is conducted as presented here under;

8.4.1 *Calculation of Synthetic Seismogram and Reflection Coefficient*

Using the estimated interval velocities, the effects of different impedance structures on the BSR AVO response was examined in an attempt to reproduce the seismic data. Several models were constructed which were constrained to preserve the average interval velocity of each macro layer. The key model used in this example is illustrated in Fig. 8.12. The model parameters are given in Table 8.1. Gas hydrate reservoir divided into three different discrete layers of thicknesses of 100 m, 50 m and 50 m with compressional and shear velocity (α, β) and density (ρ) variation. We focused our analysis on gas hydrate reservoir where a high concentration of hydrate is assumed in the DBSR model (Fig. 8.12). The model parameters have been adopted after a careful consideration of different geological environment review and are comparable with worldwide estimates of physical properties of gas hydrates. The synthetic seismograms generated by the use of finite difference solution of elastic wave equation for a complex multilayered DBSR model are illustrated in Fig. 8.13; this indicates the single and double BSR features.

Computation of reflection coefficient for single and double bottom simulating reflector (DBSR) configurations, using Haskell-Thomson method (Haskell 1953,

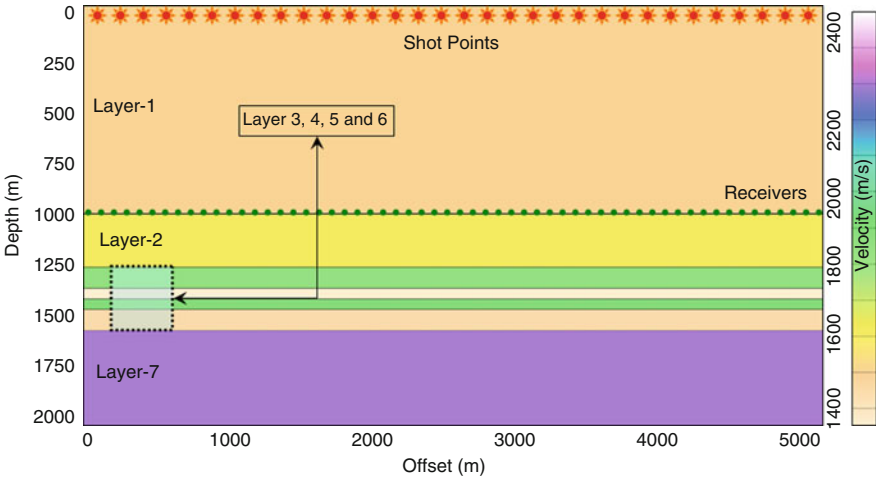

Fig. 8.12 Gas hydrate model configuration for double bottom simulating reflector (DBSR). The model is constructed with 7 layers of different properties (Table 8.1). Gas hydrate zone is divided into three different layers (layer3, 4, and 5). Layer-4 is assumed to be a low velocity layer. Layer-1 is water. Layer 2, and 7 are considered as sedimentary layers (After Rajput et al. 2010)

Table 8.1 Model parameters

Layer information		α (m/s)	β (m/s)	ρ (kg/m3)	Gradient
Layer-1	Water	1,500	0	1,000	0.5
Layer-2	Sediments	1,700	819	1,750	0.5
Layer-3	Gas hydrates	1,875	1,078	1,998	0.5
Layer-4	Low velocity layer	1,350	700	1,856	0.5
Layer-5	Gas hydrates	1,980	1,130	2,016	0.5
Layer-6	Free gas	1,450	865	1,896	0.5
Layer-7	Sediments	2,350	1,400	2,160	0.5

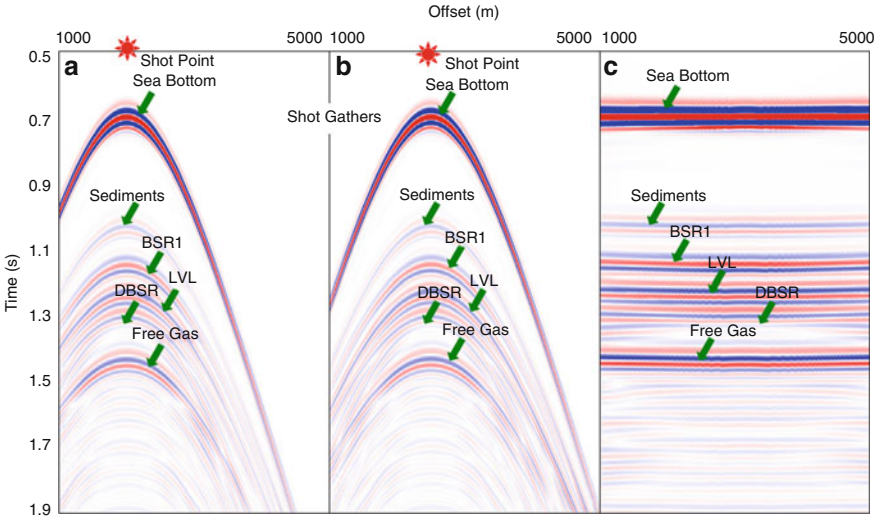

Fig. 8.13 Synthetic seismograms for multilayer complex gas hydrate model. (**a**) Example of a shot gather with identification of single and double BSR and low velocity layer situated within the gas hydrate zone. (**b**) Example of shot gather with identification of single and double BSR and low velocity layer situated within the gas hydrate zone. (**c**) Processed seismic section indicating all the modelled layers (After Rajput et al. 2010)

1960, 1962; Thomson 1950; Aki and Richards 1978), was utilized to demonstrate the Amplitude verses Offset (AVO) effect in porous gas-saturated sandstones. This computation was carried out in two steps. At the first step scattering matrices for a set of plane waves with different frequencies was determined. Then reflection coefficients from the scattering matrices were convolved with a Ricker wavelet of a chosen frequency. This approach allows stability of the reflection and transmission coefficient vs. plane wave dip angle dependency. This fact is well illustrated with the linearized formula (Shuey 1985) for P-wave reflection coefficient. This formula also permits estimation of the magnitude of change in the effective Poisson ratio ($\Delta\sigma$), using the least-squares method.

Following this reflection coefficients were estimated for both the BSRs to perform frequency depending AVO effect on the isotropic and anisotropic DBSR

model. The values of anisotropic parameters ($\varepsilon = 0.05$ and $\delta = 0.04$; for gas hydrate layer, and $\varepsilon = 0.16$ and $\delta = 0.19$ for free gas layer) were adopted from Pecher et al. 2003. Receivers have been assumed at a depth of 1,000 m at the ocean bottom which is not too far from the target interface in order to record AVO-curves. This permitted recording of both incident and reflected waves, estimations of the slowness vector direction for each of the waves and a numerical computation of the AVO-curve.

The offsets were converted into angles by using the reflection angles at the BSR. Furthermore these effects can produce different apparent AVO trends in varying offset range so it is necessary to have significant apertures in AVO measurements for sedimentary rocks and to take into account all the effect of overburden, including random heterogeneities and thin-beds. Properties of the target zone control the AVO trends on all offsets and shows clearly increasingly negative amplitudes with increasing angle. To illustrate the specific AVO response of a DBSR model the reflection coefficient of BSR and DBSR for the model have been calculated as shown in Fig. 8.14. Both of the simulating reflectors (single BSR and DBSR) result in increasingly negative amplitude with increasing offset. Using higher aperture helps to effectively model the observed AVO behavior within gas hydrate reservoir. At zero offset the interference or the tuning is the function of dominant frequency (wavelength) and the thickness of the layer. For conventional seismic prospecting the data is collected with the dominant period of pulse in the range of 10–100 m/s.

The nature of frequency response depends strongly on the AVO behaviour at an interface and the effect of the frequency dependent reflection amplitude is essentially instantaneous in character. Within the context of a standard AVO analysis, it is found that the reflections from hydrate saturated zone appear to display frequency

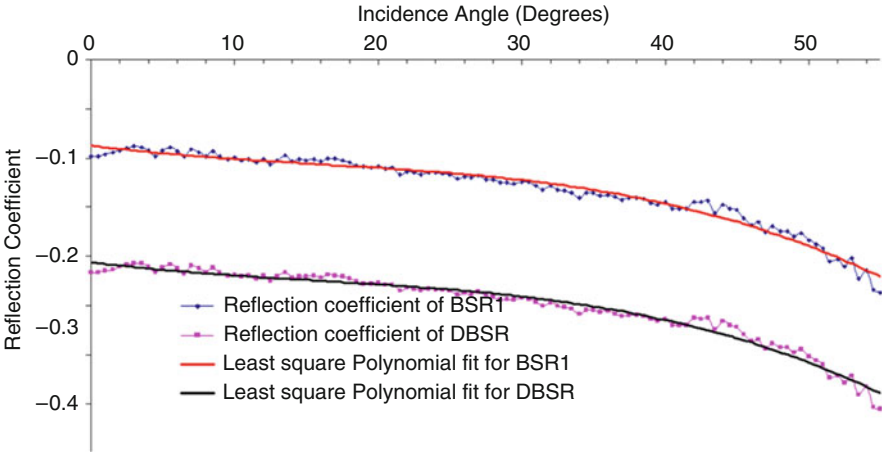

Fig. 8.14 Reflection coefficients of BSR and DBSR. BSR-1 denotes single BSR and DBSR is double bottom simulating reflector. The reflection coefficient is showing the negative trend with increasing incidence angle (After Rajput et al. 2010)

range. Figure 8.15a, b shows the comparison of AVO curves for lower (10 and 20 Hz) and higher (50 Hz) frequencies for a thin-layered isotropic DBSR model. In the case of isotropic medium increasing the frequency the tuning effect for thin beds emerges out clearly. Transverse isotropy (TI) with a vertical symmetry axis was assumed in the gas hydrate bearing sediments. To study the same phenomenon in anisotropic medium, Thomson anisotropic parameters $\varepsilon = 0.05$, $\delta = 0.04$, were adopted (Pecher et al. 2003) for modeling. The reflection amplitude for a thin layer DBSR model is plotted as shown in Fig. 8.16a, b. Transition to a high frequency seismic range changes the AVO response of a DBSR model. The AVO curves vary with the change of frequency as the variation of the reflection amplitude depends on three major factors, interference, impedance ratio, and Poisson's coefficient in the layers.

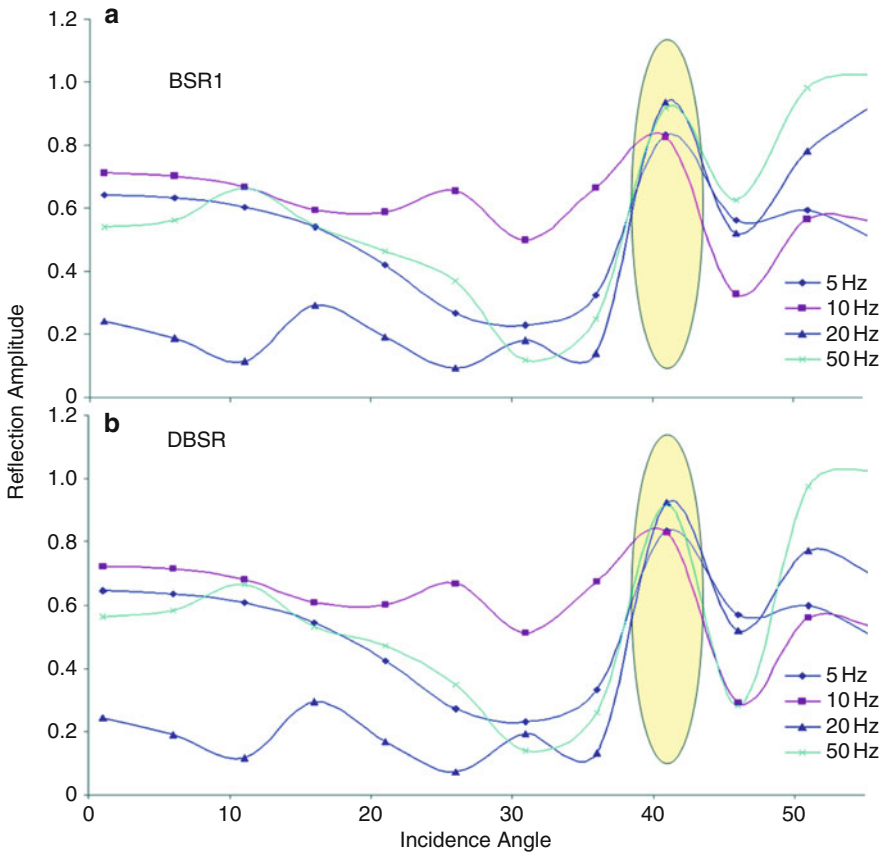

Fig. 8.15 Comparison of AVO curves produced from lower (10 and 20 Hz) and higher frequency (50 Hz) for a multi-layered isotropic DBSR model. The behaviour of reflection amplitude is relatively different with increasing incidence angle. (**a**) The reflection amplitude of single BSR. (**b**) the reflection amplitude of DBSR (After Rajput et al. 2010)

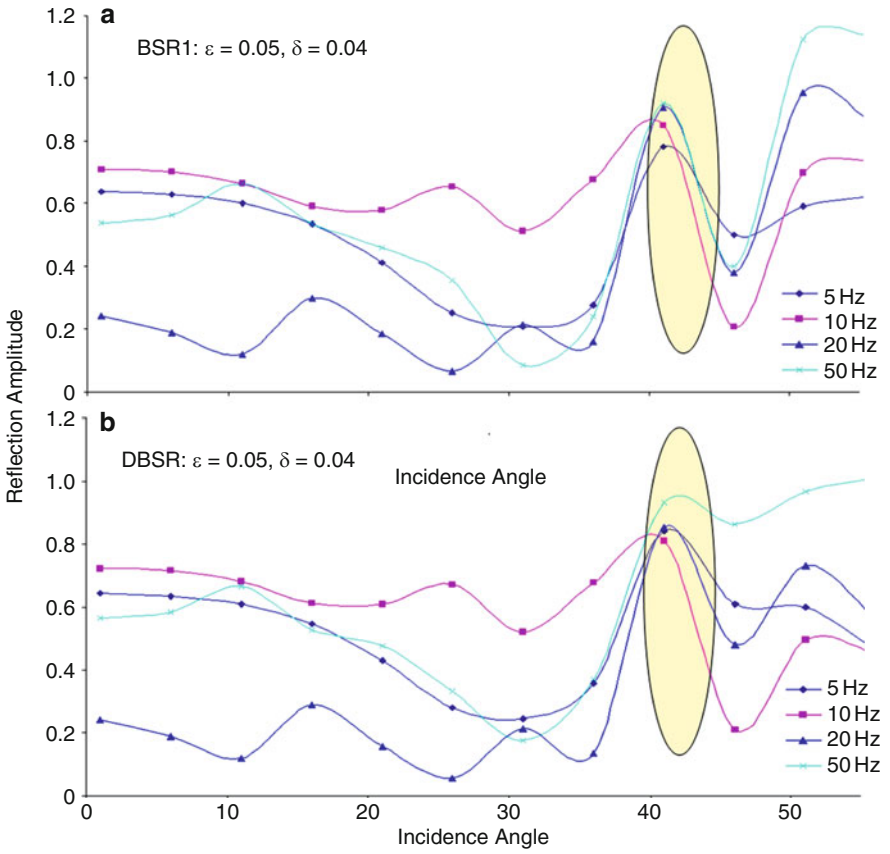

Fig. 8.16 Comparison of AVO curves produced from lower (10 and 20 Hz) and higher frequency (50 Hz) for a multi-layered anisotropic DBSR model (Thomson anisotropic parameters $\varepsilon = 0.05$, $\delta = 0.04$). DBSR model showing the tuning effect. The anisotropic parameters are same for both the gas hydrate layers i.e. BSR1 and DBSR. (**a**) The reflection amplitude of single BSR. (**b**) the reflection amplitude of DBSR (After Rajput et al. 2010)

8.4.2 Some Remarks

Dealing with more than one layer makes the AVO behavior complex. The seismic energy gets attenuated in the presence low velocity layers and the reflection coefficients in general exhibits frequency dependent phase shift. However, there is not much significant change in reflective characteristics for low and high frequencies for small angle of incidence. It has been shown that the top of gas saturated layer is more reflective for low frequency range when compared to high frequency range. In this regard the obtained AVO behaviour from the present modelling studies shows no significant changes for smaller angle of incidence (Figs. 8.15 and 8.16). This pattern is seen for both the cases of BSR and DBSR. However, for

higher angle of incidence the tuning effect produces a complex AVO behaviour. The frequency dependent response for the isotropic medium indicates that tuning effect dominates for lower frequency range.

Anisotropy becomes quite important for the interpretation of processed data and sometimes without its consideration it may lead wrong information about the causative source (Thomsen 1986; Thomson 1999). This aspect is very important when the resource target is confined to fractured and faulted medium. The AVO response for anisotropic medium for different frequency range shows relatively different pattern. In this regard it is advisable to study the characteristics response for different frequency and for the estimating the true behavior of AVO trend. In relevance to above mechanism of formation of DBSR, it is interpreted that the DBSR identified in the Green Canyon in Gulf of Mexico, might have formed either due to the presence of fluids in the hydrated stability zone or may due upward migration of free gas from lower layers and getting trapped in the hydrated layer producing a thin low velocity layer in the hydrate stability zone. Based on the above example one could conclude that:

- DBSR can be generated if the sediments and hydrate matrix has the presence of low velocity fluids in hydrate stability zone even without incorporating higher order hydrocarbons.
- Amplitude strength differs for both the BSRs and also depends on the properties of the LVL, which is situated within the gas hydrate zone.
- Within the frequency range close to the resonant frequency (tuning thickness) for a given DBSR model, favorable conditions occur for predicting multi BSR gas hydrate reservoir from AVO analysis.
- Anisotropy increases the local variation in reflection amplitudes, which become significant for the sedimentary DBSR models with week reflections.

8.5 Seismic Attributes

Seismic attributes are simply defined as the best information extraction from seismic data. There are several categories of seismic attributes such as P-wave and S-wave; Pre-Stack and Post-Stack, Single and Multi Trace, 2D, 3D and time lapse (4D) seismic attributes (Sheline 2005).

- Quality of seismic data
- Processing workflow
- Frequency content
- True amplitude
- Phase

For gas hydrates related studies one considers a seismic attribute as any seismically derived property such as acoustic impedance, poisson's ratio and density (derived from pre stack inversion). Many attributes such as bi-variate scatter plots of amplitude variance, average energy, RMS amplitude, reflection strength, and

average absolute amplitude may duplicate information content because of the nature of the computations but all these attributes contain the same information (Barnes 2001). The velocity and density of the hydrates formation is higher than that of depositional formations filled with free-gas or water. Therefore, the reflection from the bottom interface of the hydrates formation will show positive polarity if the wavelet polarity from seismic data is negative or negative polarity if the wavelet polarity is positive (Yanhun et al. 2008). This interface is the BSR discussed above. Based on this feature, instantaneous amplitude can be used to identify the BSR (Yanhun et al. 2008; Satyavani et al. 2008). The basic definition of these instantaneous seismic attributes (reflection strength and instantaneous frequency) has already been described in Chap. 6.

8.5.1 Reflection Strength

The reflection strength display is a phase independent view of the amplitudes (Lynch and Lines 2004). It is the square root of the trace's energy and thus can show where, in a wavelet, the maximum energy occurs (Taner et al. 1979). It can be used for a number of things, including looking for gas related bright spots. Reflection strength is sensitive to changing acoustic impedance and this to lithology, porosity, hydrocarbons, and thin bed tuning.

Because of the complexities of the model (Fig. 6.8) assumed in the simulation, it's not easy to interpret this attribute. Therefore to investigate this instantaneous attribute related to the characteristics of gas hydrate and associated free gas, further models based on the tuning thickness of gas hydrate and free gas layers were developed. Initially we started with 50 m free gas layer (Fig. 8.17) and then subsequently decrease this thickness to 40 m, 30 m, 20 m, 10 m and 5 m and keep a constant thickness of gas hydrate layer. Next we assume the decreasing thickness of gas hydrate layer in the same fashion as free gas layer models with constant thickness of free gas layer. The simulated response was analyzed for gas hydrate layer with thicknesses of 50 m (Fig. 8.18), 40 m, 30 m, 20 m, 10 m, and 5 m. For all the models only thicknesses of layers (gas hydrate and free gas) was changed, whereas other physical properties (compressional velocity, shear velocity and density) remain unchanged. For micro analysis of the events associated with gas hydrates and free gas we extracted one CDP (500 in this case) for each model (gas hydrate and free gas models) and displayed.

8.5.2 Reflection Strength for Constant Thickness of Hydrate Layer with Different Thickness of Free Gas Layers

The simulated response for crosswell seismic profile for all the free gas models with decreasing thickness from 50 to 5 m (CDP 500) are shown in Fig. 8.19a–f.

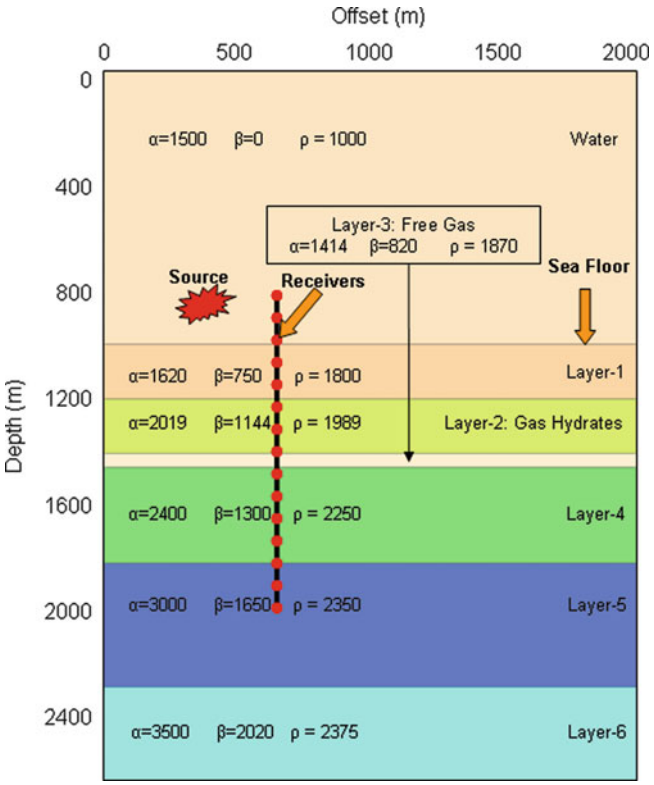

Fig. 8.17 Seven layer gas hydrate configuration model. Solid *red dots* are receivers. Source is assumed at another well location. The model parameters (compressional (*Vp*), Shear (*Vs*) and density (ρ) are given for each layer. In this case the thickness of free gas layer is 50 m and the thickness of gas hydrate (layer-2) is constant (After Rajput et al. 2010)

The BSR is observed as a reverse polarity event and clearly identified on the cross-well seismic image. Thinning gas layer doesn't affect on the amplitude of BSR and one is able to identify for as thin as 5 m free gas layer (Fig. 8.19). A series of trace transform steps were performed starting from frequency filtering with a reasonably band pass filter (10 and 100 Hz) and further processing to improve the image of structure, while preserving the frequency and amplitude of wavelet. The instantaneous attribute (reflection strength) for each model (CDP 500) are displayed in colour (Fig. 8.20). The colour coded image of reflection strength indicates that with this attribute it's possible to even distinguish 10 m free gas layer, whereas it seems to have a mix response for 5 m thick free gas layer. Interpreting the tuning thickness of 5 m we should not look this attribute may be misleading.

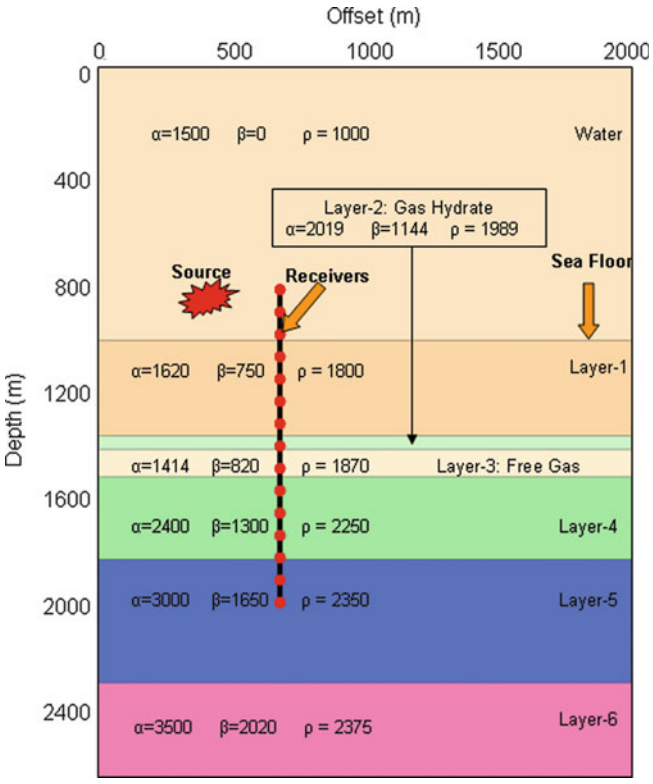

Fig. 8.18 Seven layer gas hydrate configuration model. Solid *red dots* are receivers. Source is assumed at another well location. The model parameters (compressional (*Vp*), Shear (*Vs*) and density (ρ) are given for each layer. In this case the thickness of free gas hydrate (layer-2) is 50 m and the thickness of free gas (Layer-3) is constant (After Rajput et al. 2010)

8.5.3 Reflection Strength for Constant Thickness of Free Gas Layer with Different Thickness of Gas Hydrate Layers

The seismic response for gas hydrate models with decreasing thickness from 50 to 5 m is shown in Fig. 8.21a–f. In these models the thickness of free gas layer doesn't change. Analysis of the seismic data suggests that seismic amplitude of BSR doesn't alter much with the thickness of gas hydrate layer. The high amplitude polarity reversal can be observed for the layer as thin as 5 m (Fig. 8.18f). The seismic amplitude of free gas layer remains unaffected. Following this the investigation for the reflection strength for all the models of varying thickness of gas hydrate zone has been attempted. This instantaneous seismic attribute is very useful in identifying the changes in the seismic impedance contrast and is often associated with the lithologic changes between adjacent rocks such as unconformities and other stratigraphic boundaries associated with sharp changes in sea level or

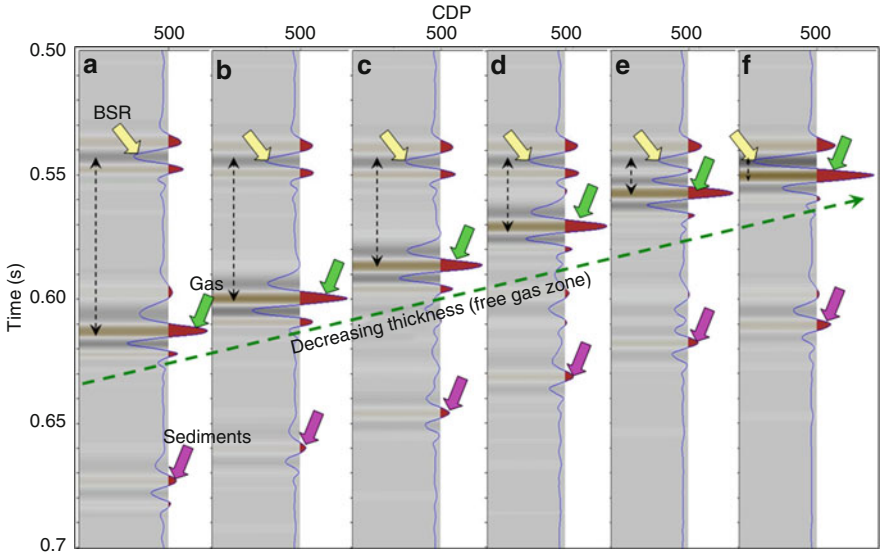

Fig. 8.19 The simulated seismic response for seven gas hydrate configuration models corresponding to the key model Fig. 8.17; the thickness of free gas layer is decreasing from 'a' to 'f'. BSR (*yellow arrows*) is identified as a reverse polarity event and free gas (*green arrows*) is identified as a bright spot. Pink arrows are representing reflections from sedimentary layer; (**a**) The thickness of free gas layer is 50 m. (**b**) The thickness of free gas layer is 40 m. (**c**) The thickness of free gas layer is 30 m. (**d**) The thickness of free gas layer is 20 m. (**e**) The thickness of free gas layer is 10 m. (**f**) The thickness of free gas layer is 5 (After Rajput et al. 2010)

depositional environments. Furthermore, lateral variations in bed thickness change the interference of the reflections, thereby causing lateral changes in the reflection strength. Similar signatures as for free gas layers (Fig. 8.20) were observed but in such case it seems difficult to distinguish 5 m thick gas hydrate layer within sediments (Fig. 8.22f). High reflection strength corresponds to the free gas present underneath gas hydrate zone.

8.5.4 Example from Andaman Offshore Region, India

The Andaman offshore region is a part of the major island arc trench system in the northeast Indian Ocean. During National Gas Hydrate Program, India (NGHP) Expedition-01 Drilling and coring was carried out during 2006. The initial report (Collett et al. 2008) confirms the presence of large sediment thicknesses (260–600 mbsf) with 4.4% saturation of gas hydrates deposits in 62% porous volcanic ash in the Andaman offshore. Satyavani et al. (2008) analysed the seismic data (Fig. 8.23) and performed complex trace analysis for instantaneous seismic attribute calculations. The reflection strength plot corresponding to the seismic data

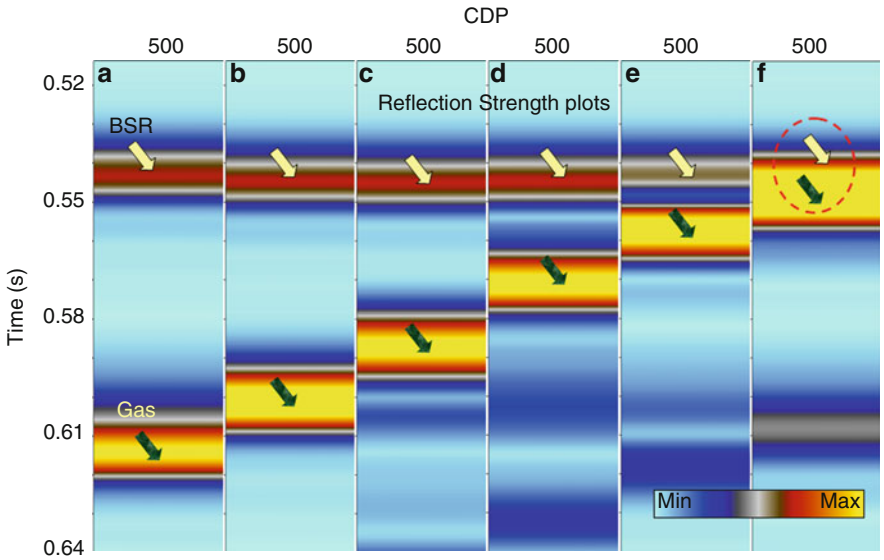

Fig. 8.20 The reflection strength plots for seven gas hydrate configuration models corresponding to the key model Fig. 8.17; the thickness of free gas layer is decreasing from 'a' to 'f'. The thickness of gas hydrate layer is constant. The corresponding seismic data is shown in Fig. 8.19. The gas hydrates (*yellow arrow*) and free gas (*green arrow*) characteristics are identified; (**a**) Reflection strength plot for 50 m thick free gas layer. (**b**) Reflection strength plot for 40 m thick free gas layer. (**c**) Reflection strength plot for 30 m thick free gas layer. (**d**) Reflection strength plot for 20 m thick free gas layer. (**e**) Reflection strength plot for 10 m thick free gas layer (**f**) Reflection strength plot for 5 m thick free gas layer (After Rajput et al. 2010)

(Fig. 8.23) shows the amplitude anomalies in colour with high and low amplitudes representing reds and greens, respectively. The regions of reduced amplitudes are identified (bright red colour in Fig. 8.24), while on the eastern segment of the study area (between CDPs 991 and 386), a bright reflector is identified, which is parallel to the seafloor and cuts across the stratigraphic horizons. This strong reflection occurring around 2,600 ms TWT is interpreted as the BSR.

8.5.5 Example from Offshore Australia

Another example of reflection strength attribute is from offshore Sydney basin, which is located between latitudes 32°30′S and 34°30′S between the coastal cities of Newcastle in the north and Wollongong in the south. The offshore part of the Sydney basin covers a total area of approximately 15,000 km^2. In the absence of any direct control, the stratigraphy of the offshore basin is based on that of the adjacent onshore basin (Alder et al. 1998). Sediments of the Sydney Basin appear to extend beneath the shelf between 32° and 35°S. These sediments consist of at least

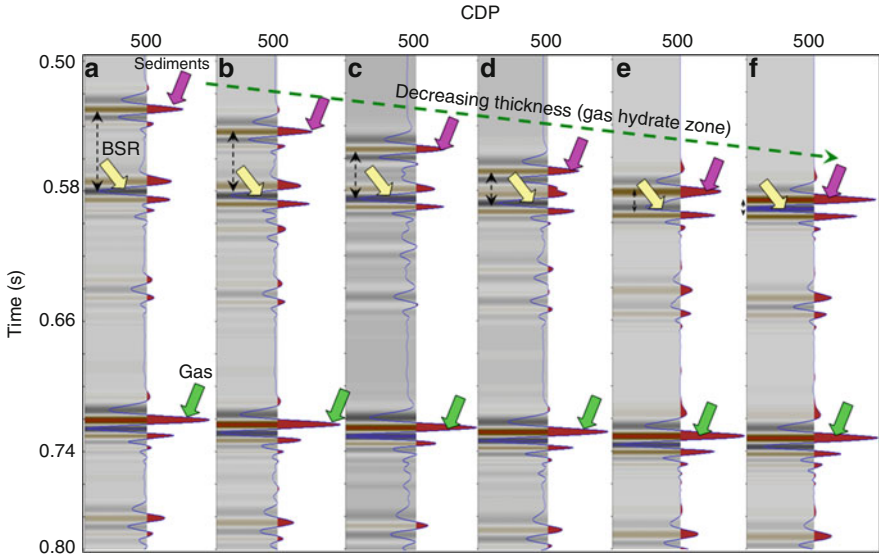

Fig. 8.21 The simulated seismic response for seven gas hydrate configuration models corresponding to the key model Fig. 8.18; the thickness of gas hydrate layer is decreasing from 'a' to 'f'. BSR (*yellow arrows*) is identified as a reverse polarity event and free gas (*green arrows*) is identified as a bright spot. *Pink arrows* are representing reflections from sedimentary layer; (**a**) The thickness of gas hydrate layer is 50 m. (**b**) The thickness of gas hydrate layer is 40 m. (**c**) The thickness of gas hydrate layer is 30 m. (**d**) The thickness of gas hydrate layer is 20 m. (**e**) The thickness of gas hydrate layer is 10 m. (**f**) The thickness of free gas layer is 5 (After Rajput et al. 2010)

6 km (and possibly up to 9 km) of Permo-Triassic marine and non-marine sequences of sandstone, mudstone, shale, coal and basalt (Stewart and Alder 2001). The Early Permian sequences are derived from marine sedimentation, with fluvial sediments and coal measures thereafter. It is generally agreed that sedimentation continued through the Jurassic and Early Cretaceous, but uplift in the Late Cretaceous associated with the opening of the Tasman Sea led to massive erosion which removed these sequences from the onshore sections (Alder et al. 1998).

The seismic data example from this region is illustrated in Fig. 8.25. To study more for the high amplitude reflector (Fig. 8.26) which is identified on a seismic line, first the continuity of the event present on seismic section has been analysed (Fig. 8.26) and then calculated some seismic attributes. The first attributes to be investigated have been the instantaneous seismic attributes, which characterize sample-by-sample variability and isolate the individual waveform components that make up the seismic trace. For the time window range (1.3–2.0 s) the investigated seismic anomaly is marked on the figure (Fig. 8.27). To look into detail two CDP; one within the anomaly (950) and other from without anomaly (434) have been selected, which clearly shows the difference in amplitude of high reflection strength event (Fig. 8.28). These signatures are highly encouraging for the prospectively of the basin.

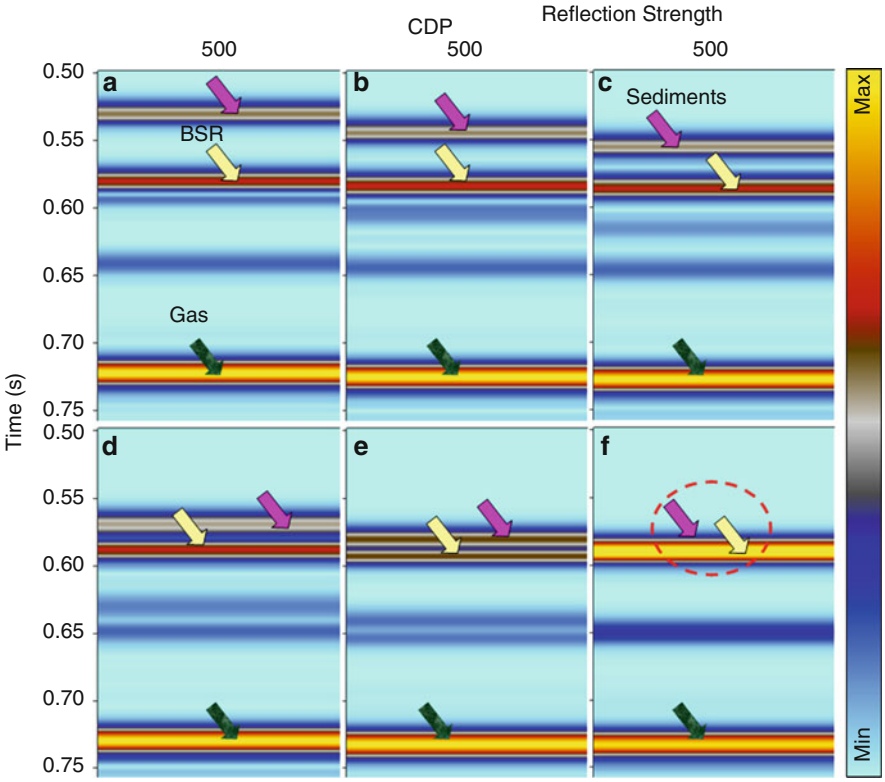

Fig. 8.22 The reflection strength plots for seven gas hydrate configuration models corresponding to the key model Fig. 8.18; the thickness of gas hydrate layer is decreasing from 'a' to 'f'. The thickness of free gas layer is constant. The corresponding seismic data is shown in Fig. 8.21. The gas hydrates (*yellow arrow*) and free gas (*green arrow*) characteristics are identified; (**a**) Reflection strength plot for 50 m thick gas hydrate layer. (**b**) Reflection strength plot for 40 m thick gas hydrate layer. (**c**) Reflection strength plot for 30 m thick gas hydrate layer. (**d**) Reflection strength plot for 20 m thick gas hydrae layer. (**e**) Reflection strength plot for 10 m thick gas hydrate layer (**f**) Reflection strength plot for 5 m thick gas hydrate layer (After Rajput et al. 2010)

8.5.6 Instantaneous Frequency

Instantaneous frequency is useful in identifying abnormal attenuation and thin bed tuning it corresponds to the average frequency (centroid) of the amplitude spectrum of the seismic wavelet. This seismic attributes is a seismic character correlator, which indicates the edges of low impedance thin beds. It also acts as a hydrocarbon indicator by showing the low frequency anomaly which sometimes accentuated by the unconsolidated sands due to oil contents of the pores. This is an important attribute in identifying fractures as these zones exhibits lower frequency moreover instantaneous frequency is a bed thickness indicator as higher frequency indicates

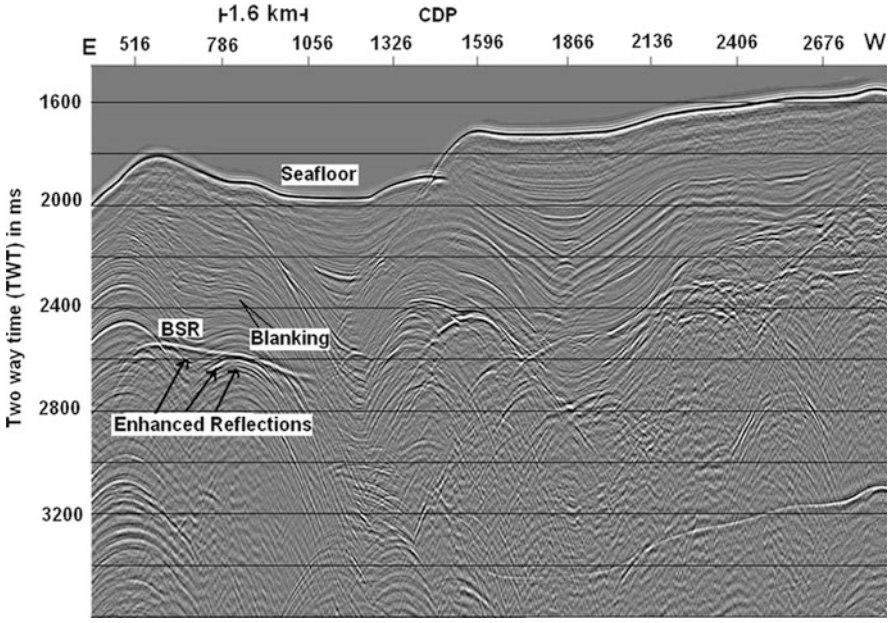

Fig. 8.23 Migrated multi-channel seismic stack section from Andaman offshore region (After Satyavani et al. 2008, reprinted with permission)

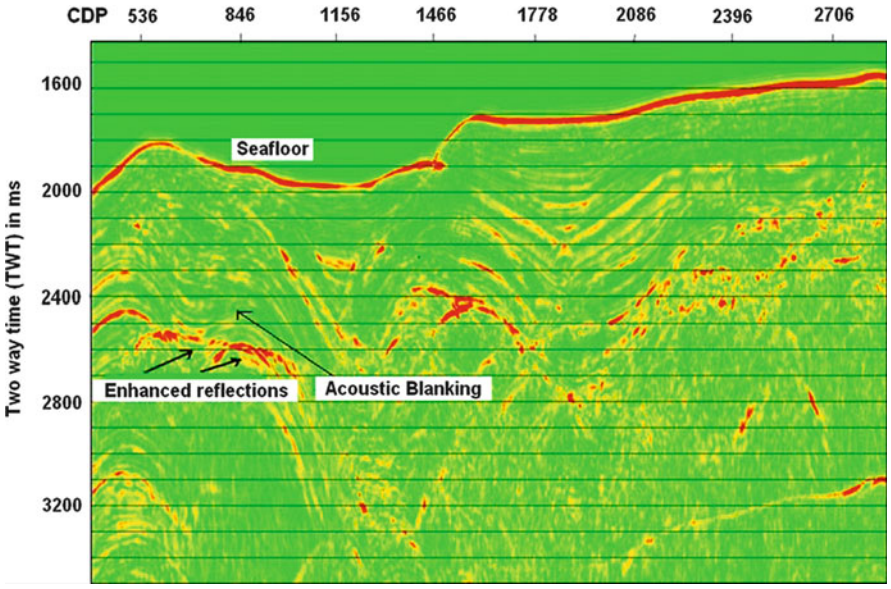

Fig. 8.24 Reflection strength plot for the line, showing loss of amplitude in a specific pattern, just above the BSR, which can be related to the blanking phenomena. The figure also depicts the enhanced reflection patterns. (After Satyavani et al. 2008, reprinted with permission)

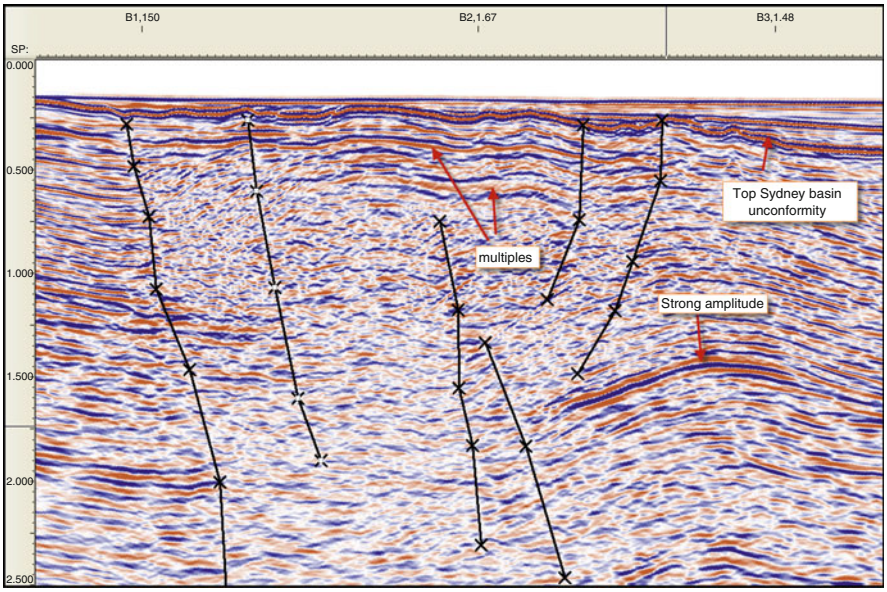

Fig. 8.25 Processed seismic section of a line from Sydney basin, offshore Australia. Top Sydney basin unconformity, multiples and strong amplitude reflector are marked on the section (Courtesy of CSIRO Australia)

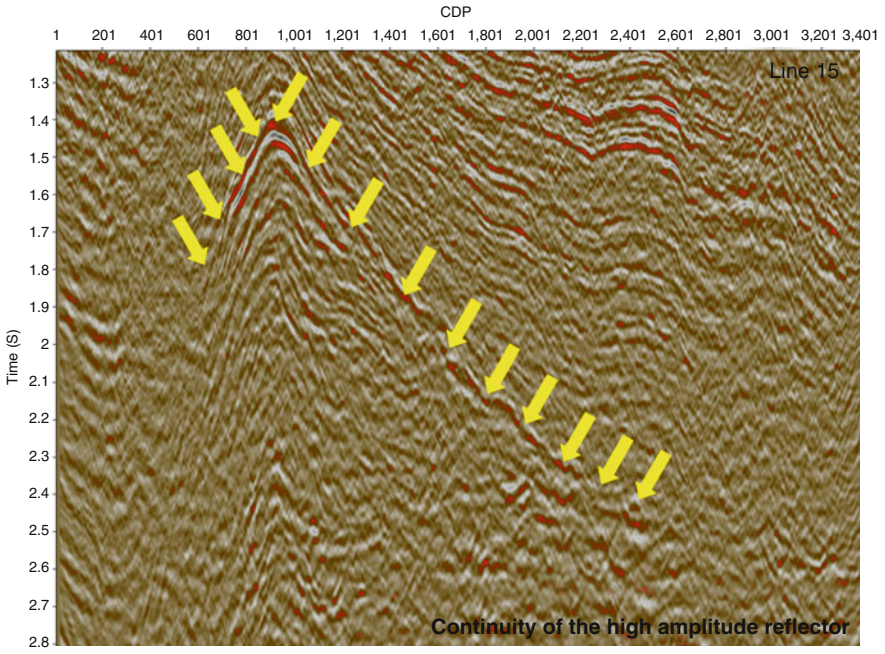

Fig. 8.26 Continuity of a high amplitude reflector from Sydney basin, offshore Australia (Courtesy of CSIRO Australia)

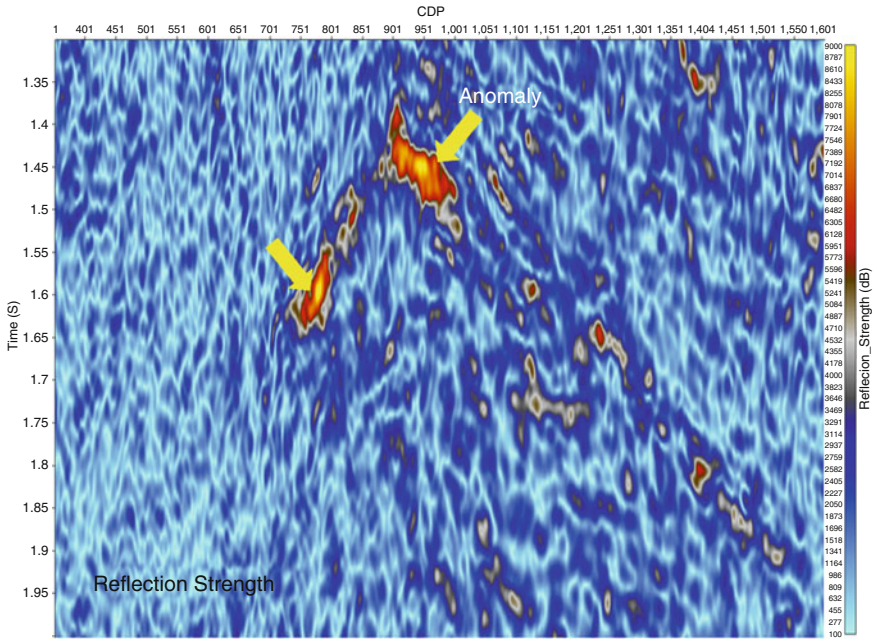

Fig. 8.27 Reflection Strength plot of the high amplitude reflector (Courtesy of CSIRO Australia)

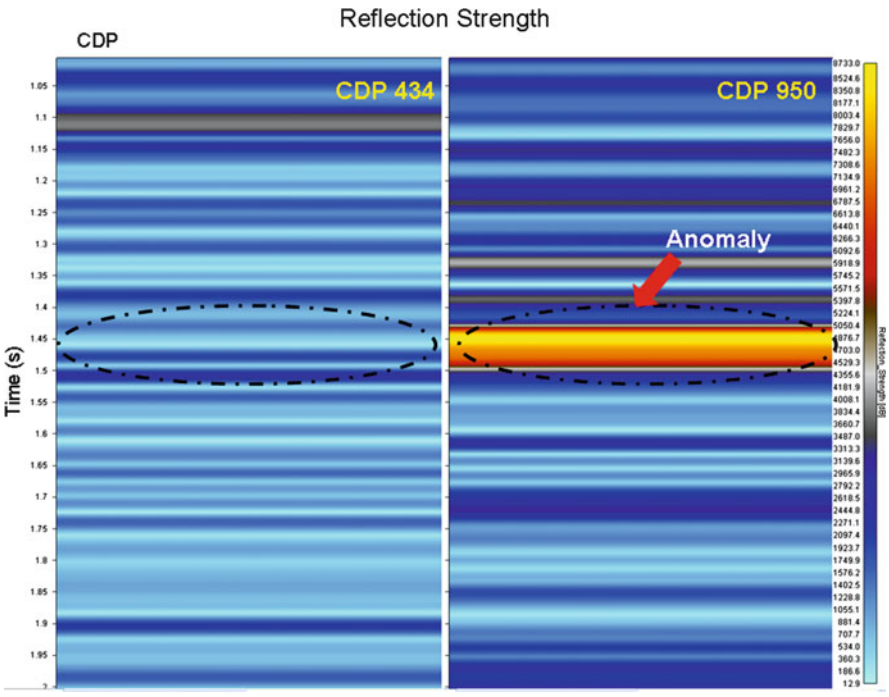

Fig. 8.28 Reflection Strength plot of CDP 434, where we don't have the anomaly and CDP 950 where we the high amplitude reflector is observed (Fig. 8.26) (Courtesy of CSIRO Australia)

sharp interfaces. Synthetic and real example of studying Instantaneous frequency response for gas hydrate configuration is presented. The models used for the calculation of Instantaneous frequency response are given in Figs. 8.17 and 8.18. Two cases were considered; for the first case the thickness of free gas layer was made to decrease from 50 to 5 m (Fig. 8.19) with no change in gas hydrate layer thickness and for the second case the thickness of gas hydrate layer decreased from 50 to 5 m (Fig. 8.21) with no change in the thickness of free gas layer.

8.5.7 Instantaneous Frequency for Constant Thickness of Hydrate Layer with Different Thickness of Free Gas Layers

Gas reservoirs attenuate high frequencies more than do rocks without gas saturation. The interpretation of this instantaneous seismic attributes may yield ambiguous results because of noisy character. However we studied low instantaneous frequency anomalies for several models of decreasing thickness of gas layer (from 50 to 5 m) with constant thickness of gas hydrate layer. The lowering of frequency can often be observed as a simple broadening of the gas reservoir reflections which is well illustrated in Fig. 8.29a–f. The high frequency events correspond to the gas hydrate layer (Fig. 8.29a–f yellow arrow) and low frequency event correspond to the gas layer (Fig. 8.29a green arrow). Ambiguous character of this attribute makes the interpretation difficult. One is not able to differentiate the low and high frequency anomalies for 5 m thick gas layer.

8.5.8 Instantaneous Frequency for Constant Thickness of Free Gas Layer with Different Thickness of Gas Hydrate Layers

The effect of Instantaneous frequency on a constant thick gas layer and decreasing thickness of gas hydrate layer (from 50 to 5 m) are examined. The interpretation of this type of model is more difficult but if analyzed carefully one can differentiate between high and low frequencies up to 10 m thick gas hydrate layer (Fig. 8.30a–f). Lowering this thickness makes interpretation unrealistic therefore this attribute doesn't provide reliable information for 5 m thick gas hydrate zone.

8.5.9 Example from Andaman Offshore Region, India

Satyavani et al. (2008) presented an example of Instantaneous frequency attribute from Andaman offshore region, India. The instantaneous frequency plot in Fig. 8.31, shows the high frequencies in red and lower frequencies in yellow. The

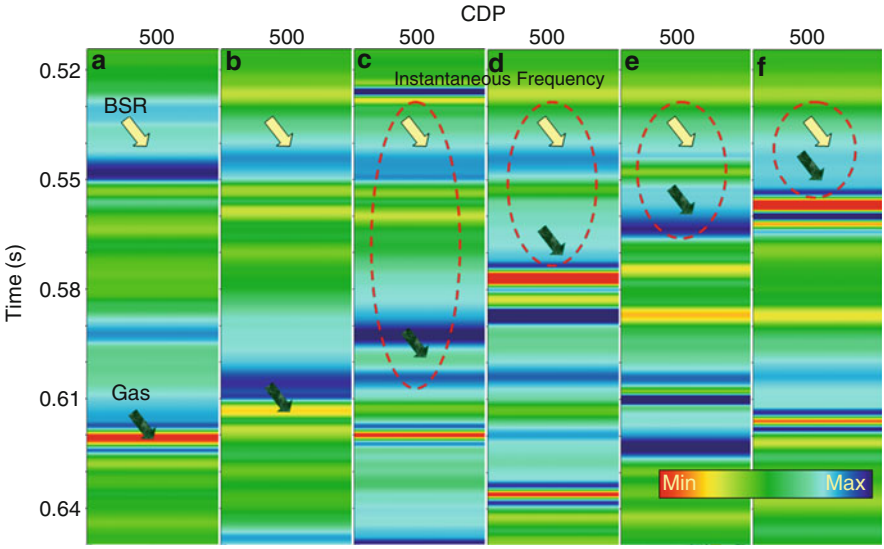

Fig. 8.29 The instantaneous frequency plots for seven gas hydrate configuration models corresponding to the key model Fig. 8.17; the thickness of free gas layer is decreasing from 'a' to 'f'. The thickness of gas hydrate layer is constant. The corresponding seismic data is shown in Fig. 8.19. The gas hydrates (*yellow arrow*) and free gas (*green arrow*) characteristics are identified; (**a**) Instantaneous Frequency plot for 50 m thick free gas layer. (**b**) Instantaneous Frequency plot for 40 m thick free gas layer. (**c**) Instantaneous Frequency plot for 30 m thick free gas layer. (**d**) Instantaneous Frequency plot for 20 m thick free gas layer. (**e**) Instantaneous Frequency plot for 10 m thick free gas layer (**f**) Reflection strength plot for 5 m thick free gas layer 5 (After Rajput et al. 2010)

strong reflection seen between CDPs 991 and 386 in the reflection strength plot (bright red in Fig. 8.24) is now totally missing in the instantaneous frequency plot, implying considerable absorption of higher frequencies. This result corroborates our observation that the strong reflector is a BSR and ascertains the presence of free gas underneath it. Furthermore, the seismic data from Andaman offshore region, India (Fig. 8.23) show an increase in seismic amplitudes with the increase in offset, coupled with the velocity inversion, suggesting the presence of free gas.

8.5.10 Example from Offshore Australia

The structural framework of the offshore portion of the Sydney basin comprises four principal elements; the offshore Syncline, an offshore extension of the New England Fold Belt, an offshore extension of the Newcastle syncline and the offshore uplift (e.g. Alder et al. 1998). The present easterly extent of the basin is the result of the Cretaceous rifting and commencement of seafloor spreading in the adjacent Tasman Sea. Destructive interference caused by seismic processing artifacts such as incorrect NMO or statics corrections (prior to stacking) can artificially reduce the

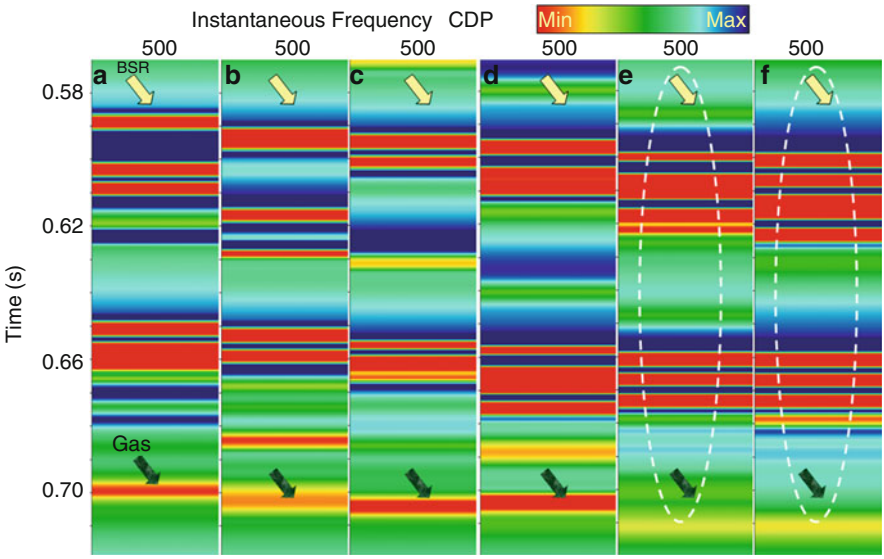

Fig. 8.30 The Instantaneous Frequency plots for seven gas hydrate configuration models corresponding to the key model Fig. 8.18; the thickness of gas hydrate layer is decreasing from 'a' to 'f'. The thickness of free gas layer is constant. The corresponding seismic data is shown in Fig. 8.21. The gas hydrates (*yellow arrow*) and free gas (*green arrow*) characteristics are identified; (**a**) Instantaneous Frequency plot for 50 m thick gas hydrate layer. (**b**) Instantaneous Frequency plot for 40 m thick gas hydrate layer. (**c**) Instantaneous Frequency plot for 30 m thick gas hydrate layer. (**d**) Instantaneous Frequency plot for 20 m thick gas hydrate layer. (**e**) Instantaneous Frequency plot for 10 m thick gas hydrate layer (**f**) Instantaneous Frequency plot for 5 m thick gas hydrate layer (After Rajput et al. 2010)

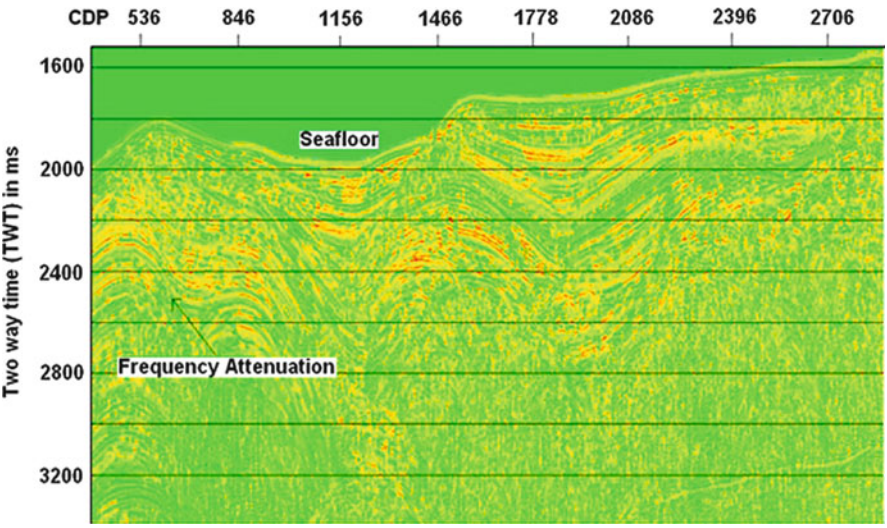

Fig. 8.31 Instantaneous frequency plot for the same line showing the regions of attenuation of high frequencies. (After Satyavani et al. 2008, Reprinted with permission)

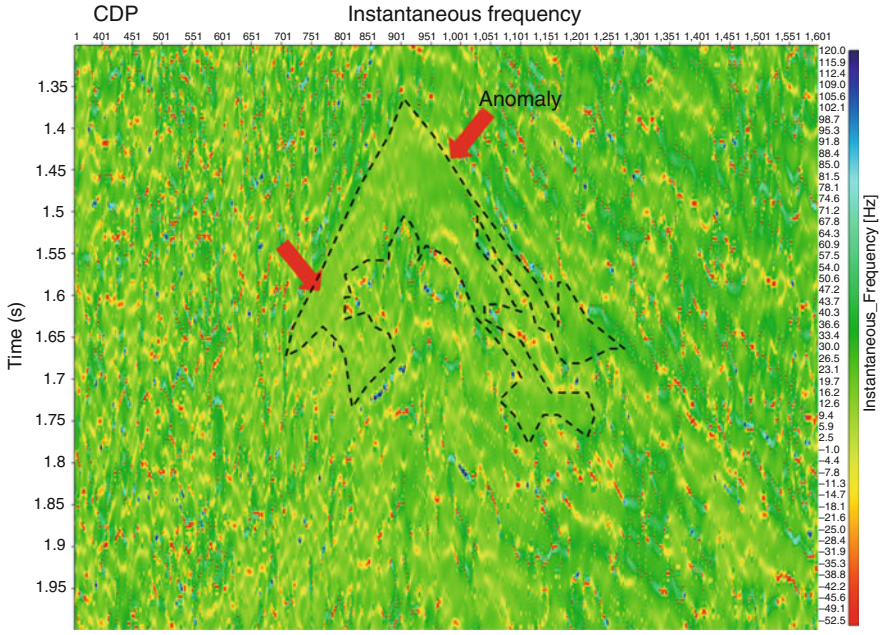

Fig. 8.32 Instantaneous frequency plot for the high amplitude reflector (Fig. 8.26). It is showing low frequency anomaly (Courtesy of CSIRO Australia)

frequency content. The instantaneous frequency plot for the high amplitude reflector is shown in Fig. 8.32. To look into detail we selected two CDPs were selected; one within the anomaly (950) and other from without anomaly (434), which clearly shows the difference in low frequency anomaly (Fig. 8.33).

8.5.11 Some Remarks

Instantaneous seismic attributes become an important tool for detecting the presence of gas hydrate and associated free gas anomalies. Strong instantaneous frequency event could be interpreted as gas hydrate and low frequency anomalies are useful in identifying the gas bearing zone. These seismic attributes are interpreted to establish the presence of free gas accumulations below the BSR.

8.6 Quantification Methods

Global estimates of the methane gas stored in gas hydrates varied from 10^{18} to 10^{15} m^3 over the last few decades (Henke et al. 2008). While the world demand for fossil fuel is ever-increasing and the supply is dwindling, it is essential to have a

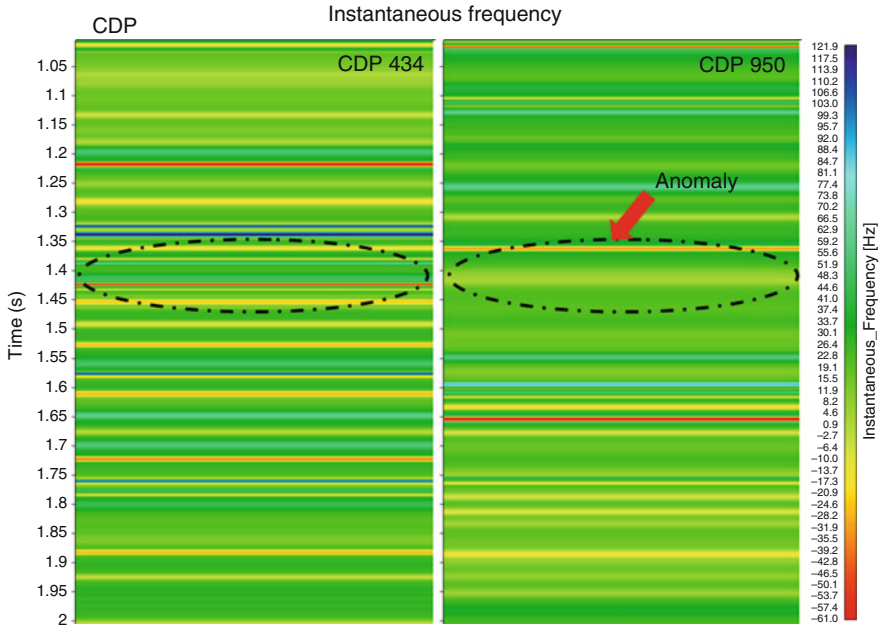

Fig. 8.33 Instantaneous frequency plot of CDP 434, where we don't have the anomaly and CDP 950 where we have the high amplitude reflector. The low frequency anomaly is shown (Courtesy of CSIRO Australia)

methodology for reliable assessment of gas hydrates accumulation in worldwide deepwater basins (Dai et al. 2008a, b, c). Understanding hydrates as a methane reservoir and exploiting hydrates efficiently as an energy resource requires knowledge of gas hydrate characteristics such as concentration (Kumar et al. 2007). There are a variety of quantification methods are available. Recently Kumar et al. (2009) presented a summary of several methods for gas hydrate concentration estimation that make use of data from the measurements of the seismic properties, electrical resistivity, chlorinity, porosity, density, and temperature. Here we discuss methods described by Kumar et al. (2009) with other methods and try to make use of the geophysical and geochemical approach to combine the advantages and to reduce the disadvantages of each technique for characterization of the gas hydrates;

8.6.1 Detection and Estimation of Gas Hydrates by Rock Physics and Inversion

The detection and estimation of gas hydrates prior to drilling can be achieved by an integrated workflow (e.g. Dai et al. 2004). Following are the main steps;

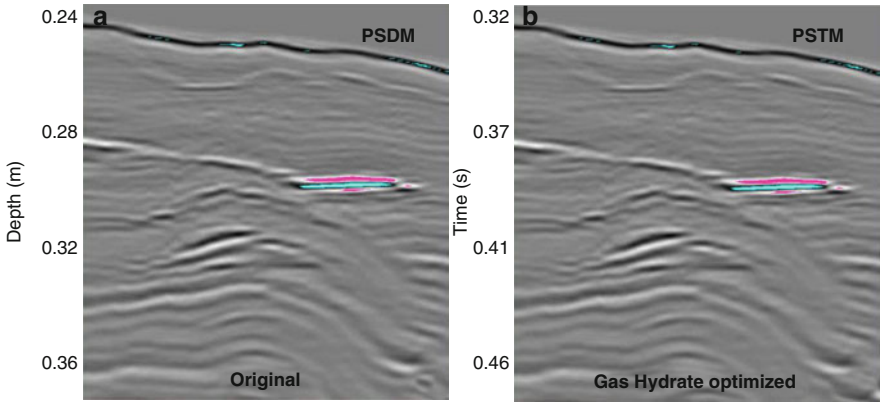

Fig. 8.34 Comparison between PSDM stack (*left*) and the newly-processed PSTM stack (*right*). The spatial continuity and high resolutions are clearly seen in the newly-processed data. (After Dai et al. 2008a, b, c reprinted with permission)

- Screening of the available data.
- Gas hydrates optimized (amplitude preserved) processing (Dai et al. 2004).
- Integration and Stratigraphic evaluation for target zones.
- Investigation of seismic attributes.
- Estimation of elastic properties by inversion (Kumar et al. 2006, 2007, 2009).
- Quantification of gas hydrates saturation using rock physics models (Dai et al. 2004; Kumar et al. 2006, 2007, 2009).
- Characterization of free gas zones and study the fluid flow patterns.

A very good example of the gas hydrate optimized processed seismic section is presented by Dai et al. (2008a, b, c) and illustrated in Fig. 8.34. Higher resolution and more lateral continuity are manifest in the newly-processed result. Seismic inversion provides the estimate of elastic properties of gas hydrates. Dai et al. (2008a, b, c) applied Prestack Full Waveform Inversion (PSWI) which was developed by Mallick (1995, 1999). PSWI is a statistical optimization technique that operates much like biological evolution and derives P- and S-wave velocities and density profiles from a given CMP seismic gather. An example of PSWI run at a key well location was shown in Fig. 8.35 (Dai et al. 2008a, b, c). The left three curves on the left are inverted Vp, Poisson's ratio (PR), and density respectively. The curves in green are the values of elastic properties and the yellow bands show the range of possible errors corresponding to the individual properties. The middle and right panels display the observed seismic angle gather and the synthetic angle gather after convergence during the iteration process. Note that the correlation coefficient between the two gathers is over 0.90, signifying a good match (Dai et al. 2008a, b, c).

The local highs and lows in the derived Vp reflect possible lithology or fluid variations although there are uncertainties associated with noise accumulated during the inversion process due to the lack of full bandwidth frequencies in the input gather and the noise in the gather that corrupts the inversion results. The

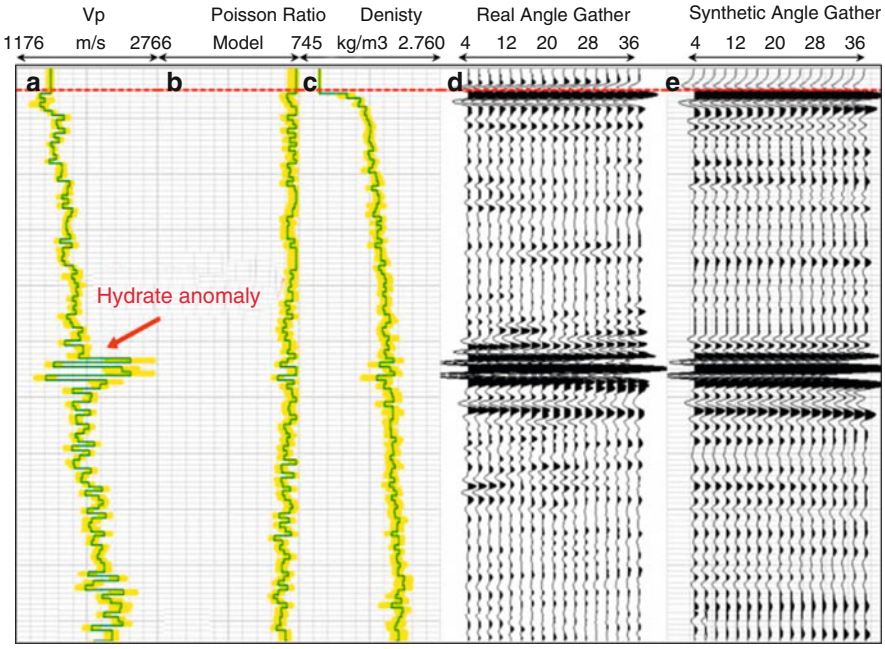

Fig. 8.35 PSWI result at the key well location. (**a**);Compressional velocity (*Vp*); (**b**) Poisson Ratio; (**c**) Density; (**d**) Real seismic data (Angle gathers); (**e**) Synthetic seismic data (Angle gathers) (After Dai et al. 2008a, b, c reprinted with permission)

extreme high Vp event indicated by the red arrow reveals a very likely, high-concentration gas hydrate anomaly. This high Vp anomaly was later confirmed by the acoustic logging result at the actual well location (Dai et al. 2008a, b, c).

For elastic impedance and density volumes Dai et al. (2008a, b, c) applied simultaneous inversion (Rasmussen et al. 2004). In this inversion scheme preconditioned seismic data are input as multiple angle stacks. Prior models for P-Impedance (PI), S-Impedance (SI) (or PR), and density are the initial low frequency models of the elastic parameters that form a basis for the objective and the cost functions of the inversion. A simulated annealing method is used to generate and update model parameters. The forward modeling is done by convolving reflection coefficient series (linearized Zoeppritz equation-based) with wavelets. The wavelets may vary spatially and temporally for each angle stack in order to generate optimal results (Dai et al. 2008a, b, c).

Having generated 3D elastic property volumes, hydrate estimation/quantification was done by mapping the elastic property to hydrate saturation through gas hydrate rock physics modeling and inversion. Readers are referred to Dai et al. (2004, 2007), and Xu et al. (2004) for a detailed discussion of the technique. Hydrate saturations are mapped both deterministically and statistically, using P-wave and S-wave independently and jointly. Figure 8.36 (Dai et al. 2008a, b, c)

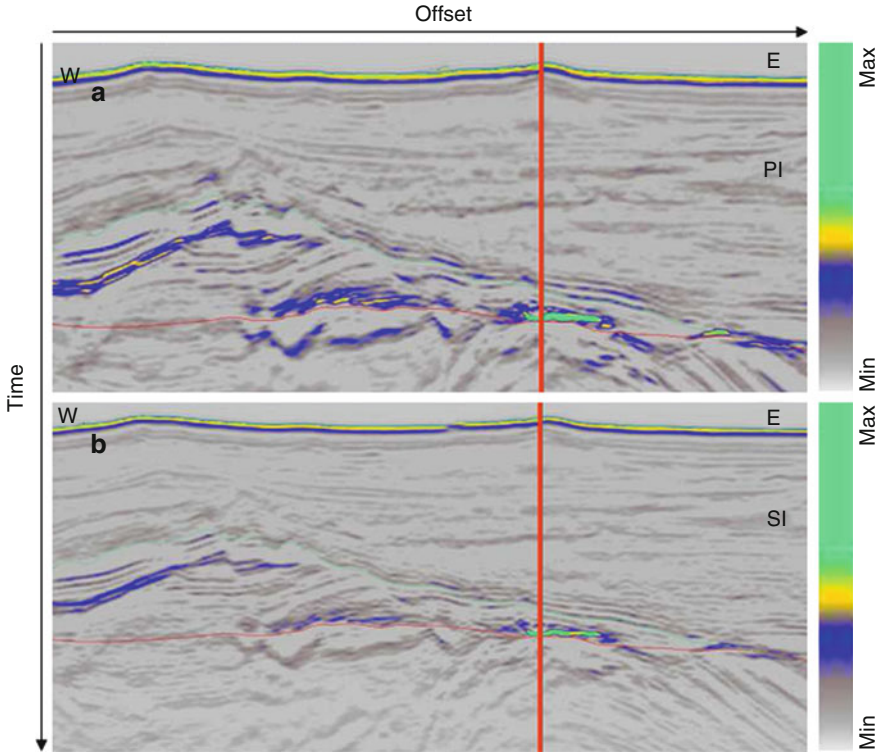

Fig. 8.36 Gas hydrate saturations calculated from P and S impedances. The *red line* shows the location of the well; (**a**) Saturation from PI; (**b**) Saturation from SI (After Dai et al. 2008a, b, c reprinted with permission)

shows the saturations estimated from PI and SI of the same inline as shown in Fig. 8.37 (Dai et al. 2008a, b, c).

8.6.2 Estimating Volumetric Concentration of Gas Hydrates by Modified Wood Equation

Kumar et al. (2009) described a combination of several methods for characterisation of gas hydrates. Here we are discussing about the modified wood equation (Kumar et al. 2007) for gas hydrate quantification.

Several authors have presented relationships between seismic velocities and gas hydrate concentration (Chand et al. 2004), which can be broadly grouped into two categories (1) empirical relations (Lee et al. 1996) and (2) rock physics based effective medium theory (Helgerud et al. 1999). While the presence of hydrates in the pore space always increases the P-wave velocity of the host sediments, the

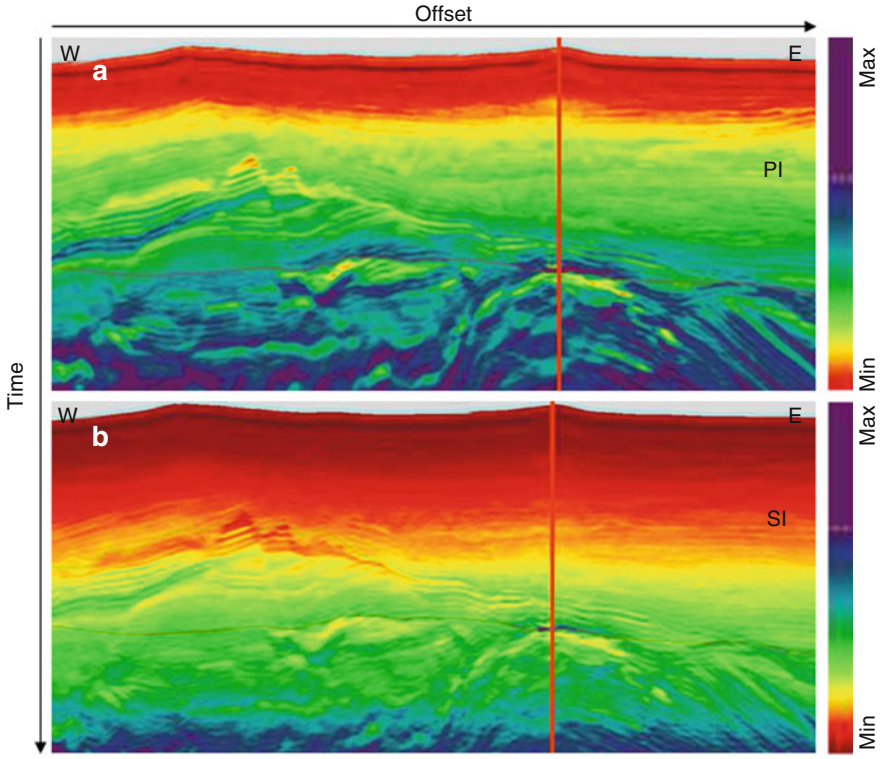

Fig. 8.37 Simultaneous inversion results. The *red line* shows location of the well. (**a**) P impedance (*PI*); (**b**) S impedance (*SI*). (After Dai et al. 2008a, b, c reprinted with permission)

effect on S-wave velocity depends on the nature and concentration of hydrates within the sediment. Commonly used empirical relationships between Vp and saturations (called four-phase relations involving water, gas, gas hydrate and rock matrix) are:

$$\frac{1}{V_P^2} = \frac{\phi S_w}{V_w} + \frac{\phi S_g}{V_g} + \frac{\phi S_h}{V_{hP}} + \frac{1-\phi}{V_{mP}} \tag{8.1}$$

Four-phase (water, gas, hydrate, and matrix) Wood equation for hydrated sediments can be expressed as (Lee et al. 1996),

$$\frac{1}{\rho V_P^2} = \frac{\phi S_w}{\rho_w V_w^2} + \frac{\phi S_g}{\rho_g V_g^2} + \frac{\phi S_h}{\rho_h V_h^2} + \frac{1-\phi}{\rho_m V_m^2} \tag{8.2}$$

where V_P, V_w, V_g, V_h, and V_m are the P-wave velocity in the hydrated sediments, water, free-gas, pure hydrate, and matrix, respectively, ϕ is total porosity (as a fraction of rock volume), S_w, S_g, and S_h are the saturations of water, gas, and

Table 8.2 Parameters used in gas hydrate saturation estimation [data are derived from Helgerud et al. (1999) and Lee et al. (1996)]. Mineral properties in the KG basin are estimated assuming 90% clay and 10% quartz mineral constituents

Mineral/fluid	K (GPa)	G (GPa)	ρ (g/cm^3)	Vp (m/s)	Vs (m/s)	Poisson's ratio
Clay	20.9	6.85	2.58	6,038	4,121	0.06
Quartz	36.6	45.0	2.65	3,412	1,629	0.35
Gas hydrate	7.9	3.3	0.90	3,697	1,915	0.32
Water	2.25	0	1.0	1,500	0	0.50
Methane gas	0.11	0	0.23	692	0	0.50
KG basin (90% clay + 10% quartz)	22.15	9.07	2.59	3,639	1,873	0.32

hydrate in the pore space, respectively ($S_w + S_g + S_h = 1$), and ρ_w, ρ_g, ρ_h, ρ_m, and ρ are density of water, free gas (methane), hydrate, matrix, and bulk sediment, respectively (Table 8.2 from Kumar et al. 2007).

Kumar et al. (2007) modified the Wood equation with an effective medium based rock physics relationship that is appropriate for the Hydrate Ridge (offshore Oregon, USA). This effective medium theory assumes that gas hydrate formation reduces the original porosity and becomes part of the solid matrix. The Vp from Modified Wood equation is;

$$\frac{1}{\rho V_P^2} = \frac{\phi_m S_w}{\rho_w V_w^2} + \frac{\phi_m S_g}{\rho_g V_g^2} + \frac{\phi_m S_h}{\rho_h V_h^2} + \frac{1-\phi_m}{\rho_m V_m^2} \tag{8.3}$$

where $\phi_m = \phi - S_{hyd}$ is porosity after gas hydrate formation, S_{hyd} is the volumetric concentration of gas hydrates in the rock that is now part of the solid matrix, and now gas and water constitute the fluid part in pores ($S_w + S_g = 1$). The S-wave velocity can be empirically derived. Following hydrate formation model of Kumar et al. (2007), Vs can be derived from Vp as follows

$$V_S = V_P(1-\phi)\left(\frac{V_S}{V_P}\right)_m \tag{8.4}$$

where $\left(\frac{V_S}{V_P}\right)_m$ is the ratio of S- to P-wave velocity in the solid matrix and is equal to $\left(\sqrt{\frac{G_m}{K_m + \frac{4}{3}G_m}}\right)$.

G m and *K m* are shear modulus and bulk modulus of solid mineral (hydrate and sand/shale minerals). If the gas hydrate formation model is pore filling (not affecting rock framework), then V_S can be estimated according to Lee et al. (1996) as

$$V_S = V_P\left[\left((1-\phi)\frac{V_{mS}}{V_{mP}}\right) + \phi S_h \frac{V_{hS}}{V_{hP}}\right] \tag{8.5}$$

where, $\frac{V_{hS}}{V_{hP}}$ is the ratio of S to P-wave velocity in the pure gas hydrate (which is about 0.46), and solid matrix includes only sand/shale minerals.

An example from offshore southern Hydrate Ridge, offshore Oregon show a comparison (Fig. 8.38) of estimated gas hydrate concentration, where the P wave velocity is computed by two different methods, the Wood equation (8.1) and the Modified Wood equation (8.3) (Kumar et al. 2007). Figure 8.39 (Kumar et al. 2007) shows predicted P and S wave velocities (using 8.3 and 8.4) as a function of gas and gas hydrate concentration. V_s is dependent on V_p (8.4), which is evident in Fig. 8.39 as V_s is varying (weakly sensitive) in the presence of free gas. Modeled seismic velocities Fig. 8.39 for free gas saturations up to 2% of pore space, the maximum reported (Lee and Collett 2006)], and for gas hydrate concentration up to 10% of the rock volume are comparable to the estimated velocities (for details see Chap. 7). The best estimate gas hydrate concentration corresponds to the minimum error value. This analysis is done for each depth. Furthermore, there are an array of combinations of gas and gas hydrate concentration that match the imperfectly calculated V_p (Fig. 8.40a), but with both V_p and V_s data the gas hydrate concentration is much more constrained (Fig. 8.40b adopted from Kumar et al. 2007).

The gas hydrates concentration has been estimated (Fig. 8.41 from Rajput 2008) from V_p and V_s using the model depicted in Fig. 8.39 for the E–W transect across the south summit. We interpolated and smoothed the 1-D concentration values at OBS sites to produce a 2-D profile of gas hydrate concentration, where maximum hydrate concentration is about 7.4% of the bulk sediment volume (Fig. 8.41).

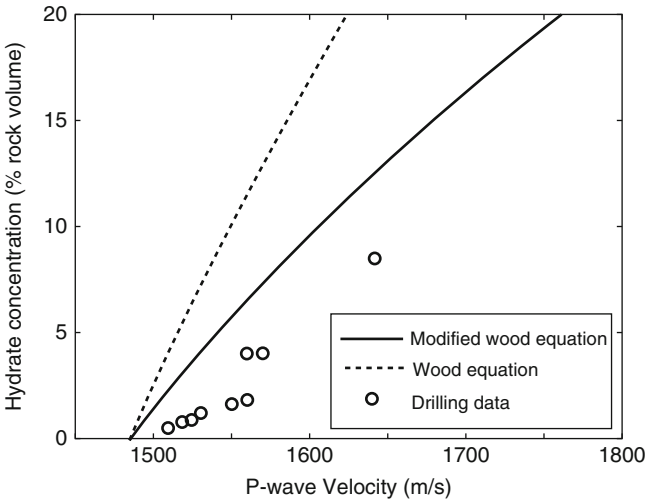

Fig. 8.38 Hydrate concentration estimated using P wave velocity calculated with two methods: the modified Wood equation (8.3) and Wood equation (8.1). The hydrate concentrations estimated with the modified Wood equation are a closer match to the drilling data than those estimated with the Wood equation. The modified Wood equation seems more suitable at Hydrate Ridge. The velocity and gas hydrate concentration of the drilling data are derived from sonic and chloride measurements, respectively (adopted from Kumar et al. 2007 reprinted with permission)

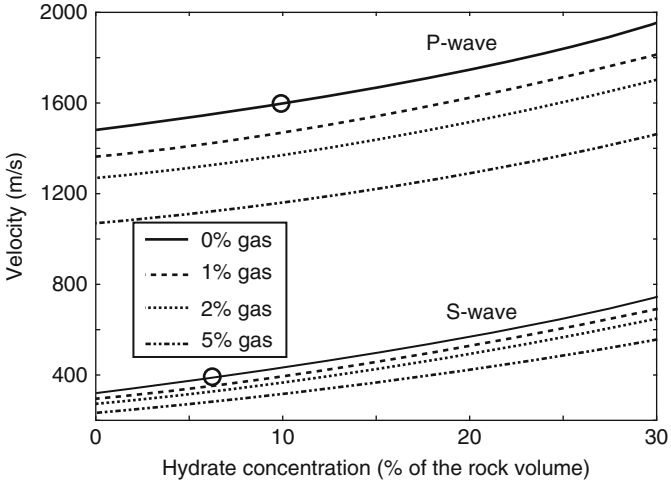

Fig. 8.39 VP and VS profiles as a function of hydrate concentration and gas saturation (% of pore space), estimated using equations (8.3) and (8.5), respectively. Input model parameters are given in Table 8.1 with 60% porosity. Velocity increases in the presence of gas hydrate. The change in Vs in the presence of free gas is due to its dependence on Vp (8.5). The Vp and Vs above the BSR at OBS 3 are marked by open circles on the 0% gas saturation curve. Individually, Vp and Vs predicts different gas hydrate concentration, but simultaneously, they predict result close to drilling result (adopted from Kumar et al. 2007 reprinted with permission)

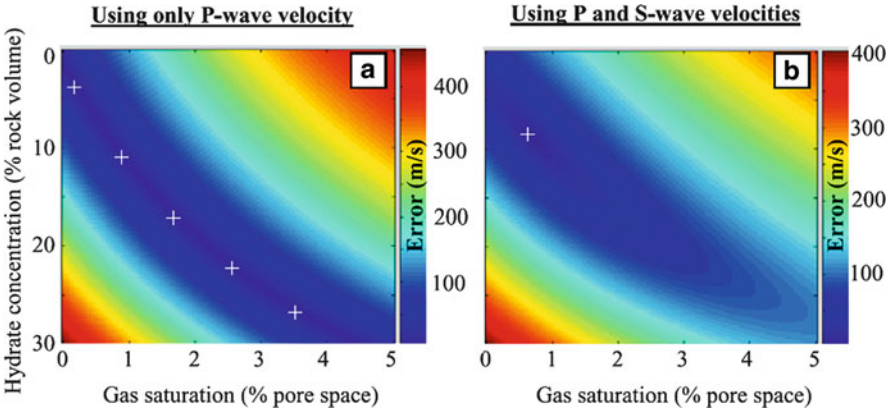

Fig. 8.40 Importance of including the S wave velocity along with the P wave velocity in the estimation of gas hydrates concentration in the presence of free gas is illustrated. (**a**) In the presence of free gas, hydrate concentration is very poorly estimated using only Vp. (**b**) It is better resolved with both the P and S wave velocities. The plus in Fig. 8.37a shows equally likely predictions of gas and gas hydrate content, and the plus in Fig. 8.37b shows the best match between the estimated seismic velocity and modeled seismic velocity, which corresponds to the best estimates of hydrate concentration and free gas saturation (adopted from Kumar et al. 2007 reprinted with permission)

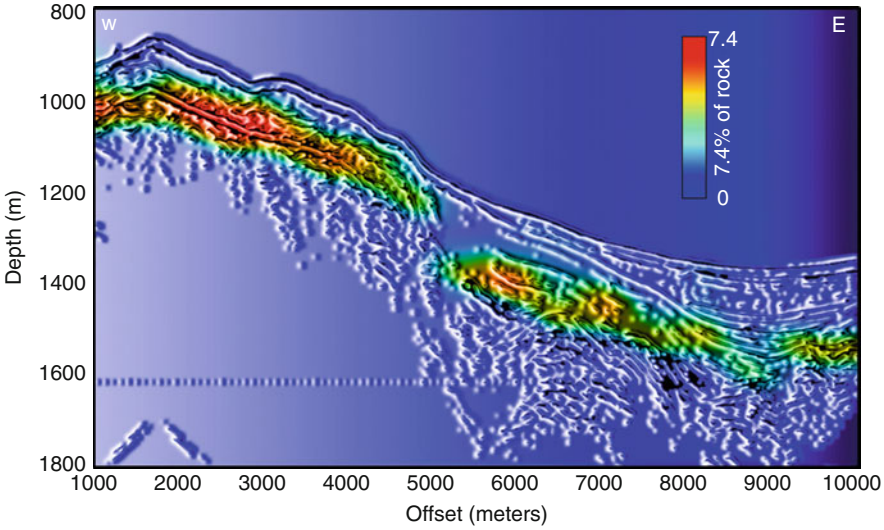

Fig. 8.41 Gas hydrate saturation (volumetric fraction of total rock) across the south summit (W–E) on the Hydrate Ridge. Saturation estimation is performed by matching the observed velocities with the calculated velocities using a "Modified Wood equation" (After Rajput 2008 reprinted with permission)

8.6.3 Example from KG Basin India (NGHP Expedition-01)

The Government of India started the National Gas Hydrate Program (NGHP) in 1997 to explore gas hydrate resources in India. The presence of gas-hydrate in the Indian continental margin was confirmed during drilling/coring onboard JOIDES Resolution between 28th April 2006 and 19th August 2006 (Collett et al. 2008). This is known as NGHP Expedition 01 which is resulted from collaboration between the Directorate General of Hydrocarbons (DGH) and the United States Geological Survey (USGS). During Expedition NGHP-01 there were 494 cores cut with 2,847.01 m of core recovered reflecting 78.7% of the interval cored. The coring system recovered 125 cores with 1,116.74 m of core recovery or 101.6% of the formation penetrated. The XCB coring system recovered 272 cores with 1,661.79 m of core recovery or 68.6% of the formation penetrated. In addition, 97 pressure coring attempts were made with 49 recovering core under pressure. Three different pressure coring systems were used and the criteria for success, was defined as "measurable core" recovered under "measurable" pressure. Actual recoveries and pressures can be found in the referenced data sheets. The number of cores recovered under pressure vs. the number attempted reflected an overall success rate of 50.5%.

Kumar et al. (2009) illustrate the methods of hydrate saturation estimation from well logs acquired in Krishna Godwari (KG) offshore basin during NGHP Expedition-01. Figure 8.42 show gas hydrate saturation estimated at this well location from resistivity (Fig. 8.42 a) and seismic velocities (sonic logs) data (Fig. 8.42 b and c).

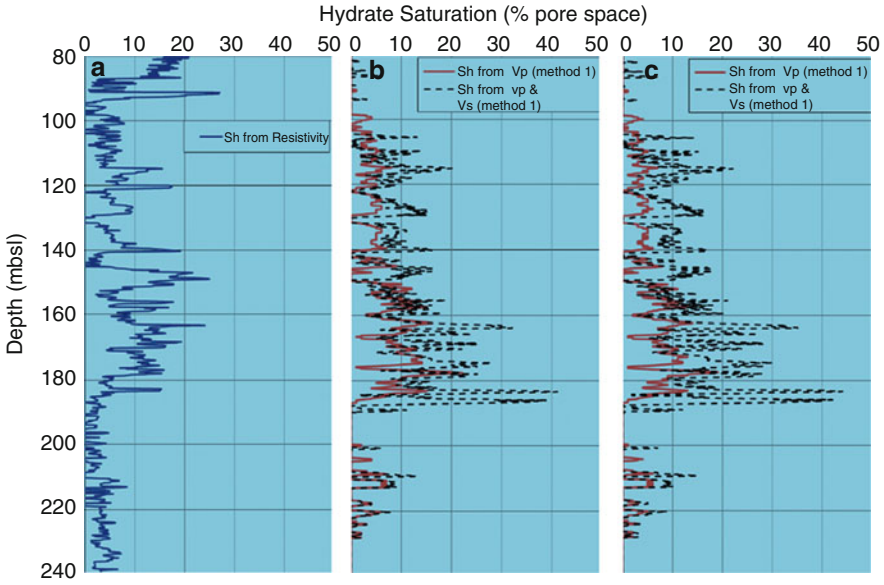

Fig. 8.42 Gas hydrate saturation estimated from well logs in KG basin. On the *left* (**a**) is hydrate saturation estimated using resistivity log with 1.08 Ω m as the background resistivity value. The *middle* panel (**b**) and the *right* panel (**c**) show gas hydrate saturations estimated from VP alone (*red solid curve*) and VP and VS combined (*black dotted curve*) using method 1, with linear background velocities [Vp(m/s) = depth(mbsf) × 0.6 + 1,546.67, and Vs(m/s) = depth(mbsf) × 0.492 + 210.67]. Seismic velocities were modeled assuming 90% clay and 10% quartz as mineral composition in Fig. 8.42a and 100% quartz as mineral composition in Fig. 8.42c. Note the differences in hydrate saturation due to differences in mineral compositions (Fig. 8.42b and c). In this example, Vp is modeled using 8.1 and Vs is modeled using 8.5. A linear increase in the hydrate concentration is observed from 100 to 185 mbsf. The base of the hydrate stability zone is clearly demarcated in the hydrate saturation plot at about 185 mbsf. (After Kumar et al. 2009; reprinted with permission)

Hydrate saturation is different if 100% quartz is assumed as mineral composition compared to 90% clay and 10% quartz as mineral composition (Kumar et al. 2009). The base of hydrate stability zone is clearly demarcated in the hydrate saturation plots at about 185 mbsf. This data example emphasizes the importance of knowing the correct mineral composition. Hydrate saturation varies from 5 to 40% of pore space in the GHSZ (Kumar et al. 2009).

8.6.4 Integrating Geochemical and Geophysical Methods for Gas Hydrates Characterization

Henke et al. (2008) presented an integrated approach for gas hydrate characterization. The technique (Henke et al. 2008) uses geochemical reactive-transport models

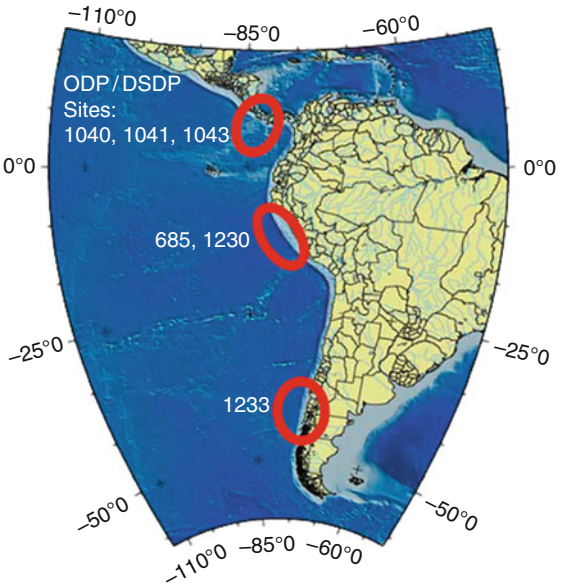

Fig. 8.43 DSDS/ODP drill sites used to develop the transfer function to quantify gas hydrate concentration (After Henke et al. 2008 reprinted with permission)

and geophysical rock physics models to quantify gas hydrate inventories. Several geochemical transport-reaction models constrained on the DSDP/ ODP drill sites 685, 1,230, 1,233, 1,040, 1,041 and 1,043 (Costa Rica, Peru and Chile) have been developed to obtain the natural variance of the different parameters and the resulting gas hydrate concentrations (Fig. 8.43 from Henke et al. 2008). In order to derive the general simplified transfer function, the three control parameters [sulphate penetration depth (SPD), sedimentation rate and thickness of the gas hydrate stability zone (GHSZ)] and the pertinent resulting gas hydrate concentrations from different models have been used to set up a non-linear equation system (Henke et al. 2008). Solving that equation system by iteration results in the following function (8.6) to estimate the potential amount of gas hydrate (depth integrated in g/cm^2 seafloor) (Henke et al. 2008):

$$GHpotential = -a * SPD * \ln(SPD) + b * SedRate * SDP + c * SedRate^2 * SDP + d * GHDZ * SDP + e * SDP \quad (8.6)$$

The GH potential is the maximum potential of GH occurrence in g/cm^2 seafloor. SPD, SedRate, GHSZ are the regional parameters and a, b, c, d, e are the respective determined coefficients (Henke et al. 2008). The input parameters for the application in the transfer function to quantify gas hydrate concentration are illustrated in Fig. 8.44.

Henke et al. 2008 uses a geophysical approach which is based on rock physics modelling incorporating the Effective Medium Theory (Helgerud et al. 1999). Helgerud calculates the elastic bulk and shear moduli from petrophysical

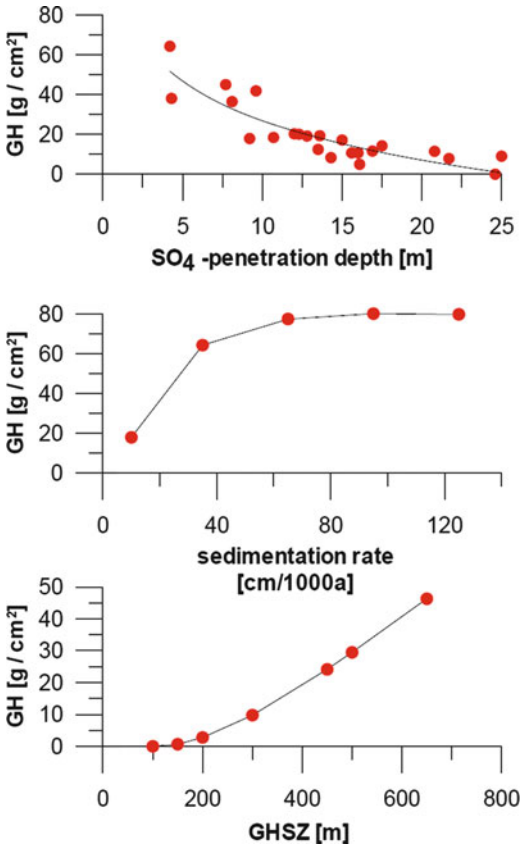

Fig. 8.44 Input parameters for the application in the transfer function to quantify gas hydrate concentration (After Henke et al. 2008 reprinted with permission)

parameters in combination with a gas hydrate formation model. Another good point is that if porosity samples do not represent the in-situ conditions of the slope sediments the calibration of porosity should be done by geochemical approach (Henke et al. 2008). The gas hydrate concentration (Fig. 8.45) is calculated by the transfer function (8.6) and confirmed the details of gas hydrate concentration across the slope sediments by subdividing them along a seismic line. It can be seen that the gas hydrate concentration varies between 0 and 3 vol.% of pore space (Henke et al. 2008).

8.6.5 Waveform Inversion for Gas Hydrates

Prediction of Gas hydrates properties depends on a velocity model that should represents the geology of hydrate province. Commonly the velocity can be derived by analysing the travel-times of the seismic signals which could be achieved by

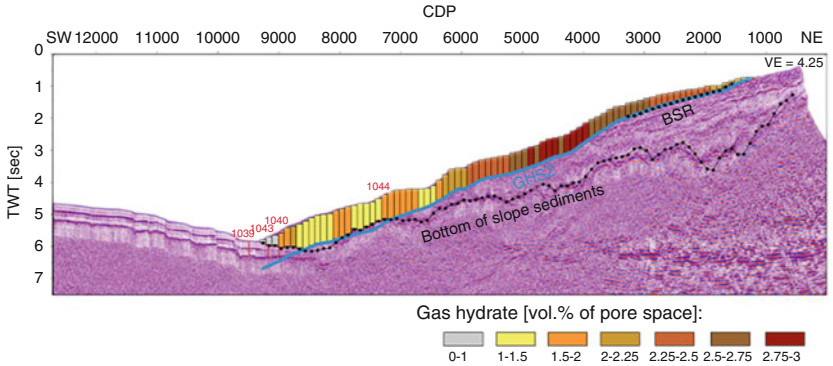

Fig. 8.45 Time migrated section of BGR99-44 with color coded gas hydrate concentration as result of the application of the transfer function (1). The *blue line* which is partly dotted (BSR) describes the base of the gas hydrate stability zone (GHSZ). *The black dotted line* marks the bottom of the slope sediments (After Henke et al. 2008 reprinted with permission)

travel-time tomography. However in the case of gas hydrates we need to better understand the petrophysical properties of rocks and the usefulness of travel-time tomography is limited because of the lack of resolution. This could be achieved by full waveform inversion (e.g. Sen and Stoffa 1991; Sen 2006), which is an alternative travel-time tomography scheme. Full waveform inversion can provide better resolution of the physical properties of rocks (Sen and Stoffa 1991; Kormendi and Dietrich 1991; Minkoff and Symes 1997; Zhou et al. 1997; Plessix and Bork 1998; Pratt 1990, 1999a, b).

AVO inversion is a prerequisite to carryout full waveform inversion. The prior velocity models can be obtained by AVO inversion and full waveform elastic modelling (that includes all multiples and converted waves) can be used in full waveform inversion (Sen 2006). There are several techniques for pre-stack full waveform inversion such as genetic algorithm, simulated annealing, and Markov Chain Monte Carlo schemes. Genetic algorithm (GA) based full waveform inversion utilizes wave equation–based forward modeling that can be run in both the angle or tau-p domains. Wave equation modeling is more accurate than convolutional modeling, thus enabling more accurate prediction of reservoir properties.

Simulated Annealing (SA) is utilizes a global optimization algorithm with a nonlinear cost function to simultaneously invert a number of input stacks to an earth model. The inversion process is based on a convolutional model, generating synthetic seismic data via an iterative process which seeks to reduce the error between observed and modeled seismic. The modeled reflectivity is then used to predict acoustic impedance, Vp/Vs and density using the Aki Richards reflectivity approximation.

Markov Chain Monte Carlo (MCMC), based geostatistical inversion addresses the vertical scaling problem by creating seismic derived rock properties with vertical sampling compatible to geologic models. All field data is incorporated into the geostatistical inversion process through the use of probability distribution

functions (PDFs). Each PDF describes a particular input data in geostatistical terms using histograms and variograms, which identify the odds of a given value at a specific place and the overall expected scale and texture based on geologic insight.

All these above methods could be used in the direction of predicting gas hydrate reservoir properties. Explaining the methods are beyond the scope of this book but there is enough literature available.

References

Aki, K., and Richards, P.G., 1978, Quantitative seismology: Theory and methods. W.H. Freeman and Sons, San Francisco.

Alder, J.D., Hawley, S., Maung, T., Scott, J., Shaw, R.D., and Kouzmina, G., 1998, Prospectivity of the offshore Sydney basin: a new perspective. APPEA, 38, 68–92.

Bangs, N.L.B., Sawyer, D.S., and Golovchenko, X., 1993, Free gas at the base of the gas hydrate zone in the vicinity of the Chile triple junction. Geology, 21, 905–908.

Barnes, A.E., 2001, Seismic attributes in your facies. CSEG Recorder, 26, 41–47.

Barnes, P.M., Lamarche, G., Bialas, J., Henrys, S., Pecher, I., Netzeband, G.L., Greinert, J., Mountjoy, J.J., Pedley, K., and Crutchley, G., 2010, Tectonic and geological framework for gas hydrates and cold seeps on the Hikurangi subduction margin, New Zealand. Marine Geology, 272, 26–48.

Behrens, E.W., 1988, Geology of a continental slope oil seep, northern Gulf of Mexico. AAPG Bulletin, 72, 105–114.

Bialas, J., Greinert, J., Linke, P., and Pfannkuche, O., 2007, FS Sonne Fahrtbericht/Cruise Report SO 191 New Vents, IFM-GEOMAR, Leibniz-Institut für Meereswissenschaften, Kiel, Germany.

Caine, J.S., Evans, J.P., and Forster, C.B., 1996, Fault zone architecture and permeability structure. Geology, 24 (11), 1025–1028.

Carcione, J.M., and Gei, D., 2004, Gas-hydrate concentration estimated from P- and S-wave velocities at the mallik 2L-38 research well, Mackenzie Delta. Canada Journal of Applied Geophysics, 56, 73–78.

Chand, S., and Minshull, T.A., 2003, Seismic constraints on the effects of gas hydrate on sediment physical properties and fluid flow: a review. Geofluids, 3, 275–289.

Chand, S., Minshull, T.A., Gei D., and Carcione, J.M., 2004, Elastic velocity models for gas-hydrate-bearing sediments a comparison. Geophysical Journal International, 159, 573–590.

Chapman, M., Liu, E., and Li X.Y., 2005, Modelling the effect of frequency dependent anisotropy on azimuthal AVO analysis, Proc. EAGE 67th Conference and Exhibition, Madrid, Spain, June 13–16, 2005.

Collett, T.S., 1998, Well log characterization of sediment porosities in gas-hydratebearing reservoirs, Proceedings of the 1998 Annual Technical Conference and Exhibition of the Society of Petroleum Engineers, September 27–30, 1998, New Orleans, Louisiana, USA. Society of Petroleum Engineers, Houston, Texas, 12 p.

Collett, T.S., and Lee, M., 2005, Electrical resistivity well-log analysis of gas hydrate saturations in the JAPEX/JNOC/GSC et al. Mallik 5L-38 well. In: Dallimore, S.R., and Collett, T.S., (Eds.), Scientific results from the Mallik 2002 gas hydrate production research well program, Mackenzie Delta, Northwest Territories, Canada. Geological Survey of Canada Bulletin, 585, 8.p. two CD-ROM set.

Collett T.S., Johnson A., Knapp C., and Boswell R., 2008, Natural gas hydrates—a review Natural Gas Hydrates—Energy Resource Potential and Associated Geologic Hazards. Collett et al., T.S., (Ed) (Tulsa, OK: American Association of Petroleum Geologists)

Collett, T.S., Lewis, R.E., Winters, W.J., Lee, M.W., Rose, K., and Boswell, R. 2010, Downhole well log and core montages from the Mount Elbert gas hydrate stratigraphic test well, Alaska north slope. Marine and Petroleum Geology, doi: 10.1016/j.marpetgeo.2010.03.016.

Crutchley, G.J., Pecher, I.A., et al., 2010, Seismic imaging of gas conduits beneath seafloor seep sites in a shallow marine gas hydrate province, Hikurangi Margin, New Zealand. Marine Geology 272(1–4), 114–126.

Dai, J., Xu, H., Snyder, F., and Dutta, N., 2004, Detection and estimation of gas hydrates using rock physics and seismic inversion: Examples from the northern deepwater Gulf of Mexico, The Leading Edge, 23, 60–66.

Dai J., Banik N., Shelander D., Bunge G., and Dutta N., 2008, Seismic detection and quantification of gas hydrates in Alaminos Canyon, Gulf of Mexico. Proceedings of the 6th International Conference on Gas Hydrates (ICGH 2008), Vancouver, British Columbia, CANADA, July 6–10, 2008.

Dai, J., Banik, N., Gillespie, D., and Dutta, N., 2008, Exploration for gas hydrates in the deepwater, northern Gulf of Mexico: Part II. Model validation by drilling. Marine and Petroleum Geology, 25, 830–844.

Dai, J., Snyder, F., Gillespie, D., Koesoemadinata, A., and Dutta, N., 2008, Exploration for gas hydrates in the deepwater northern Gulf of Mexico: Part I. A seismic approach based on geologic model, inversion and rock physics principles. Marine and Petroleum Geology, 25, 845–859.

Dasgupta, R., Singh, P.K., Bhattacharya, T., and Jaiswal, P., 2006, Possible gas hydrates without distinctive BSR - A case study: 76th Annual International Meeting, SEG, Expanded Abstracts, 26, 676–679.

Davis, A.M., 1992, Shallow gas: an overview. Continental Shelf Research, 12 (10), 1077–1079.

De Mets, G., Gordon, R.G., Argus, D.F., and Stein, S., 1994, Effect of recent revisions to the geomagnetic time scale on estimates of current plate motions. Geophysical Research Letters, 21, 2191–2194.

Dillon, W.P., and Max, M.D., 2000, Oceanic gas hydrate. In: Max, M.D. (Ed.), Natural gas hydrate in oceanic and permafrost environments. Kluwer Academic, Dordrecht, The Netherlands.

Ecker, C., Dvorkin, J., and Nur, A., 2000, Estimating the amount of gas hydrate and free gas from marine seismic data. Geophysics, 65, 565–573.

Gei, D, and Carcione, J.M., 2003, Acoustic properties of sediments saturated with gas hydrate, free gas and water. Geophysical Prospecting, 51, 141–157.

Ginsburg, G.D., and Soloviev, V.A., 1997, Methane migration within the submarine gashydrate stability zone under deep-water conditions. Marine Geology, 137, 49–57.

Gong, J. M., 1999, Natural gas hydrate and its BSR. Ocean Geology Dynamics, 15(4), 4–6.

Haskell, N.A., 1953, The dispersion of surface waves on multilayered media. Bulletin of the Seismological Society of America, 43(1), 17–34.

Haskell, N.A., 1960, Crustal reflection of plane SH waves. Journal of Geophysical Research, 76, 4147–4150.

Haskell, N.A., 1962, Crustal reflection of P and SV waves. Journal of Geophysical Research, 76, 4751–4767

Helgerud, M.B., Dvorkin, J., Nur, A., Sakai, A., and Collett, T., 1999, Elastic wave velocity in marine sediments with gas hydrates: Effective medium modeling. Geophysical Research Letters, 26, 2021–2024.

Henke T., Muller C., Marquardt M., Hensen C., et al., 2008, Integrated gas hydrate quantification off Nicoya Peninsula- Coasta Rica. Proceedings of the 6th International Conference on Gas Hydrates (ICGH 2008), Vancouver, British Columbia, CANADA, July 6–10, 2008.

Holbrook, W.S., Hoskins, H., Wood, W.T., Stephen, R.A., and Lizarralde, D., 1996, Methane hydrate and free gas on the Blake Ridge from vertical seismic profiling. Science, 273, 1840–1843.

Huaishan, L., Guangnan, H.Y., Siyou, T., et al., 2009, AVO character research of natural gas hydrates in the East China Sea. Journal of Ocean University of China, 8(3), 270–276, doi:10.1007/s11802-009-0270-y.

Hyndman, R.D., Foucher, J.P., Yamano, M., and Fisher, A., 1992, Deep sea bottom-simulating-reflectors: Calibration of the base of the hydrate stability field as used for heat flow estimates. Earth and Planet Science Letters, 109, 289–301.

Jakobsen, M., Hudson, J.A., Minshull, T.A., and Singh, S.C., 2000, Elastic properties of hydrate bearing sediments using effective medium theory. Journal of Geophysical Research, 105, 561–577.

Kleinberg, R.L., Flaum, C., and Collett, T.S., 2005, Magnetic resonance log of JAPEX/JNOC/GSC et al. Mallik 5L-38 gas hydrate production research well: gas hydrate saturation, growth habit, and relative permeability. In: Dallimore, S.R., and Collett, T.S., (Eds.), Scientific results from the Mallik 2002 gas hydrate production research well program, Mackenzie Delta, Northwest Territories, Canada. Geological Survey of Canada Bulletin, 585, 10.p. two CD-ROM set.

Kormendi, F., and Dietrich, M., 1991, Nonlinear waveform inversion of plane-wave seismograms in stratified elastic media. Geophysics, 56, 664–674.

Kostyukevych, A.S., Marmalevsky, N.Y., Gornyak, Z.V., Roganov, Y.V., and Mershchiy, V.V., 2001, Finite-difference modelling of duplex waves reflected from sub vertical boundaries. Geophysical Journal (Ukraine), 23, 110–115.

Kumar, D., Sen, M. K., Bangs, N. L., Wang, C., and Pecher, I., 2006, Seismic anisotropy at Hydrate Ridge. Geophysical Research Letters, 33, L01306, doi:10.1029/2005GL023945.

Kumar, D., Sen, M. K., and Bangs, N. L., 2007, Gas hydrate concentration and characteristics within Hydrate Ridge inferred from multicomponent seismic reflection data. Journal of Geophysical Research, 112, B12306, doi:10.1029/2007JB004993.

Kumar, D., Dash, R., and Dewangan, P., 2009, Methods of gas hydrate concentration estimation with field examples. Geohorizons, 14, 76–86.

Kvenvolden, K. A., 1993, Gas hydrates – geological perspective and global change. Review of Geophysics, 31, 173–187.

Lee, M. W., 2008, Models for gas hydrate-bearing sediments inferred from hydraulic permeability and elastic velocities. USGS Scientific Investigations Report 2008-5219, 14.p, online at http://pubs.usgs.gov/sir/2008/5219/pdf/SIR08- 5219_508.pdf.

Lee, M. W., and Collett, T.S., 2006, Gas hydrate and free gas saturations estimated from velocity logs on Hydrate Ridge, offshore Oregon, USA, Proc. Ocean Drill. Program Sci. Results, 204. (Available at http://wwwodp.tamu.edu/ publications/204_SR/ VOLUME/CHAPTERS/ 103. PDF).

Lee, M. W., Hutchinson, D. R., Collett, T. S., and Dillon, W. P., 1996, Seismic velocities for hydrate-bearing sediments using weighted equation. Journal of Geophysical Research, 101, 20347–20358.

Lee, M., Agena, W., Collett, T., and Inks, T., 2009, Pre- and post-drill comparison of the Mount Elbert gas hydrate prospect at the Milne Point area, Alaska North Slope. In: Boswell, R., Collett, T., Anderson, B., and Hunter, R., (Eds.), Scientific results of the BPXA-USDOE-USGS Mount Elbert gas hydrate stratigraphic test well, Milne Point Unit, Alaska North Slope. Marine and Petroleum Geology, doi:10.1016/j.marpetgeo.2010.02.015.

Liu, X., and Flemings, P.B., 2006, Passing gas through the hydrate stability zone at southern Hydrate Ridge, offshore Oregon. Earth Planetary Science Letters 241 (1–2), 211–226.

Liu, X., and Flemings, P.B., 2007, Dynamic multiphase flow model of hydrate formation in marine sediments. Journal of Geophysical Research, 112, B03101.

Lu, S., and McMechan, G.A., 2002, Estimation of gas hydrate and free gas saturation, concentration, and distribution from seismic data. Geophysics, 67, 582–593.

Lynch, S., 2000, Ancient evenings, seismic visualization using very old techniques. CSEG Recorder, 25(8), 5–6.

Lynch, S., and Lines, L., 2004, Combined attribute displays. SEG 2004 source; http://www.crewes.com.

Mackay, M.E., Jarrad, R.D., Westbrook, G.K., and Hyndmann, R.D., 1994, Origin of bottom simulating reflectors: Geophysical evidence from the Cascadia accretionary prism. Geology, 22, 459–462.

Makogon, Y.F., 2010, Natural gas hydrates – A promising source of energy. Journal of Natural Gas Science and Engineering, 2(1), 49–59, doi:10.1016/j.jngse.2009.12.004.
Mallick, S., 1995, Model-based inversion of amplitude-variations-with-offset data using a genetic algorithm. Geophysics, 60, 939–954.
Mallick, S., 1999, Some practical aspects of prestack waveform inversion using a genetic algorithm: An example from East Texas Woodbine gas sand. Geophysics, 64, 326–336.
Minkoff, S.E., and Symes, W.W., 1997, Full waveform inversion of marine reflection data in the plane-wave domain. Geophysics, 62, 540–553.
NGHP, Scientific Party, 2006, National gas hydrate program expedition-1. NGHP, EXP-1, 25–27.
NGRI, 2001, Reprocessing of multi-channel seismic data of ONGCL for gas hydrate exploration in offshore Goa, National Geophysical Research Institute. NGRI-2001-expl-307, 25–35.
Niu, B.H., Wen, P.F., Wen, N., Fu, X., Sun, C.Y., Li, J., et al., 2004, The estimation methods of hydrate content based on BSR's AVO forward model. Geophysics, 49(1), 143–152.
Pecher, I.A., Henrys, S.A., 2003, Potential gas reserves in gas hydrate sweet spots on the Hikurangi Margin, New Zealand, Institute of Geological and Nuclear Sciences Science Report. Lower Hutt, New Zealand.
Pecher, I.A., and Holbrook, W.S., 2003, Seismic methods for detecting and quantifying marine methane hydrate/free gas reservoirs. Kluwer Academic, Dordrecht, pp. 275–294.
Pecher, I.A., Holbrook, W.A., Sen, M.K., Lizarralde, D., Wood, W.T., Hutchinson, D.R., Dillon, W.P., Hoskins, H., and Stephen, R.A., 2003, Seismic anisotropy in gas-hydrate and gasbearing sediments on the Blake Ridge, from a walkaway vertical seismic profile. Geophysical Research Letters, 30(14), 1733, doi:10.1029/2003GL017477.
Pecher, I.A., Henrys, S.A., and Zhu, H., 2004, Seismic images of gas conduits beneath vents and gas hydrates on Ritchie Ridge, Hikurangi Margin, New Zealand. New Zealand Journal of Geology and Geophysics, 47(2), 275–279.
Pecher, I.A., Henrys, S.A., Ellis, S., Chiswell, S.M., and Kukowski, N., 2005, Erosion of the seafloor at the top of the gas hydrate stability zone on the Hikurangi Margin, New Zealand. Geophysical Research Letters, 32, L24603.
Pecher, I., Coffin, R., Henrys, S., and CHARMNZ Working Group, 2007, Tangaroa TAN0607 Cruise report: gas hydrate exploration on the East Coast, North Island, New Zealand, GNS Science Report. Lower Hutt, New Zealand.
Pecher, I.A., et al., 2008, Erosion of seafloor ridges at the top of the gas hydrate stability zone. Hikurangi Margin, New Zealand – New insights from research cruises between 2005 and 2007, 6th International Conference on Gas Hydrates, Vancouver, British Columbia, Canada.
Plessix, R.-E., and Bork, J., 1998, A full waveform inversion example in VTI media. 68th Ann. Internat. Mtg., Soc. Expl. Geophys., Expanded Abstracts, 1562–1565.
Posewang, J., and Mienert, J., 1999, The enigma of double BSRs: Indicators for changes in the hydrate stability field. Geo-Marine Letters, 19, 157–163.
Pratt, R.G., 1990, Inverse theory applied to multi-source cross-hole tomography, Part II: Elastic wave-equation method. Geophysical Prospecting, 38, 311–330.
Pratt, R.G., 1999a, Seismic waveform inversion in frequency domain, Part 1: Theory and verification in physical scale model. Geophysics, 64, 888–901.
Pratt, R.G., 1999b, Seismic waveform inversion in frequency domain, Part 2: Fault delineation in sediments using crosshole data. Geophysics, 64, 902–914.
Rajput, S., 2008, Analysis of ocean bottom seismometer data for gas hydrate studies and subsurface models. Ph.D thesis, Kurukshetra University, Kurukshetra.
Rajput, S., Rao, P.P., and Thakur, N.K., 2005a, Amplitude strength of simulating reflectors by full waveform modeling, 75th SEG Expanded Abstract, 24, 1787–1790.
Rajput, S., Rao, P.P., and Thakur, N.K., 2005b, Two-dimensional elastic anisotropic/AVO modeling for the identification of BSRs in marine sediments using multi-component receivers, Geo-Marine Letters, 25, 241–247.
Rajput S., Sen M.K., and Chopra S., 2009, Seismic indicators of gas hydrates and associated free gas, SEG Expanded Abstracts 28, 2622; doi:10.1190/1.3255391

Rajput S., Thakur N.K., Rao P.P., and Joshi A., 2010, AVO response for a complex double bottom simulating reflectors model, Current Science, 98(10–25), 1354–1358

Rasmussen, K.B., Bruun, A., and Pedersen, J.M., 2004, Simultaneous seismic inversion, 66th Mtg.: Eur. Assn. Geosci. Eng., 165.p.

Rowe, M.M., and Gettrust, J.F., 1993, Fine structure of methane hydrate-bearing sediments on the Blake Outer Ridge as determined from deep-tow multi-channel seismic data. Journal of Geophysical Research, 98, 463–473.

Rutherford, S.R., and Williams, R.H., 1989, Amplitude-versus-Offset variations in gas sands. Geophysics, 54, 680–688.

Satyavani, N., Uma, S., Thakur, N.K., and Reddi, S.I., 2002, Probable gas hydrate/free gas model over western continental margin of India. Marine Geophysical Research, 23, 423–430.

Satyavani, N., Sain, K., Lall, M., Kumar, B.J.P., 2008, Seismic attribute study for gas hydrates in the Andaman Offshore India. Marine and Geophysical Research, 29, 167–175, doi:10.1007/s11001-008-9053-x.

Sen, M.K., 2006, Seismic inversion. SPE Publications, Dallas, USA.

Sen, M.K., and Stoffa, P.L., 1991, Nonlinear one-dimensional seismic waveform inversion using simulated annealing. Geophysics, 56, 1624–1638.

Sheline, H.E., 2005, The use and abuse of seismic attributes. search and discovery article #40143 source; http://www.searchanddiscovery.net.

Shipley, T.H., Houston, M.H., Buffer, T.T., Shaub, F.J., McMillen, K.J., Ladd, J.W., and Worzel, J.L., 1979, Seismic reflection evidence for widespread occurrence of possible gas-hydrate horizons on continental slopes and rises. AAPG Bulletin, 63, 2204–2213.

Shuey, R.T., 1985, A simplification of the Zoeppritz-equations. Geophysics 50(4), 609–614.

Singh, S.C., Minshull, T.A., and Spence, G.D., 1993, Velocity structure of a gas hydrate reflector. Science, 260, 204–207.

Sloan, Jr., E.D., 1998, Gas hydrates: Reviews of physical/chemical properies. Energy and Fuels, 12, 191–196.

Stewart, R., and Alder, D., 2001, (Ed.) New South Wales petroleum potential bulletin. Coal and Petroleum Geology Branch, New South Wales.

Taner, M.T., Koehler, F., and Sheriff, R.E., 1979, Complex seismic trace analysis. Geophysics, 44(6), 1041–1063.

Taylor, M.H., Dillon, W.P., and Pecher, I.A., 2000, Trapping and migration of methane associated with the gas hydrate stability zone at the Blake Ridge Diapir: new insights from seismic data. Marine Geology, 164, 79–89.

Thomsen, L., 1986, Weak elastic anisotropy. Geophysics 51, 1954–1966.

Thomson, W.T., 1950, Transmission of elastic waves through a stratified solid medium. Journal of Applied Physics, 21, 89.

Thomson, L., 1999, Converted-wave reflection seismology over inhomogeneous anisotropic media. Geophysics, 64, 678–690.

Tinivella, U., 1999, A method for estimating gas hydrate and free gas concentrations in marine sediments. Bollettino di Geofisica Teorica ed Applicata, 40, 19–30.

Tréhu, A.M., et al., 2004, Feeding methane vents and gas hydrate deposits at south Hydrate Ridge. Geophysical Research Letters, 31 (L23310), 1–4.

Uma, S., Thakur, N.K., and Ashalatha, B., 2006, Fluid flow related features as an indicator of potential gas hydrate zone: Western continental margin of India. Marine Geophysical Research, 27, 217–224.

Westbrook, G., et al., 2008, Estimation of gas hydrate concentration from multi-component seismic data at sites on the continental margins of NW Svalbard and the Storegga region or Norway. Marine and Petroleum Geology, 25, 744–758.

Wood,W.T., Gettrust, J.F., Chapman, N.R., Spence, G.D., and Hyndman, R.D., 2002, Decreased stability of methane hydrates in marine sediments owing to phase-boundary roughness. Nature, 420, 656–660.

Xu, H., et al., 2004, Seismic detection and quantification of gas hydrates using rock physics and inversion. In: Taylor, C.E., and Kwan, J.T., (Eds.), Advances in the study of gas hydrates. Kluwer, New York, pp. 117–139.

Yanhun, L., Xiwa, L, et al., 2008, Application of seismic techniques to gas hydrate prediction. Applied Geophysics, 5(1), 67–73.

Zelt, C.A., and Smith, R.B., 1992, Seismic travel-time inversion for 2-D crustal velocity structure. Geophysical Journal International, 108, 16–34.

Zhou, C., Schuster, G.T., Hassanzadeh, S., and Harris, J.M, 1997, Elastic wave equation traveltime and wavefield inversion of crosswell data. Geophysics, 62, 853–868.

Chapter 9
The Road Ahead

Abstract The formation of gas hydrates in the field is governed by complex biological, physical and geological processes. Each contributing parameter may have quite distinct role depending on the locales and environment under which gas hydrates are being formed. The stability of the gas hydrates in subsurface earth is under delicate natural balance, any perturbation either natural or man made may lead to dissociation of gas hydrates. The zone of gas hydrate stability under the subsurface earth is evaluated based on some assumptions, which may or may not hold good for precisely determining the upper or lower bounds stability zone. We are not certain whether seafloor makes top of the hydrate layer and how distinct is the coincidence of base of the stability zone to the acoustic signature of hydrates the BSR. The presence of hydrates much above the stability zone suggests that estimated stability zone is not the zone of containment for the hydrates. BSR has been proved most characteristic signature of presence of gas hydrates. In recent times its being debated whether acoustic velocity due to hydrate causes the BSR or it is the free-gas below the hydrate stability zone gives rise to BSR. Hydrates have been found in absence of BSR. Its being argued that BSR may not distinctly be observed due to insufficient supply of methane gas or the base hydrate zone is not in contact with top of the free gas zone. Evidences are emerging to indicate that most characteristic signature of BSR i.e. its mimicking the seafloor may not hold for geologically active regions. Warm fluids emerging from deep within may totally distort the signature of BSR. The velocities associated with hydrates or free-gas does not quantify amount of saturation required for generating the amplitude of BSR. The host rock in which hydrate gets formed may have distinct role in controlling the magnitude of velocities. Its being suggested that velocity gradient in thin zone across hydrate-free gas interface is sufficient to account for the strength of BSR. The pattern of amplitude versus distance (offset) has been extensively used to account for hydrate and free gas saturation in sediments. However, the pattern only suggests that what type of impedance contrast occurs across an interface, it does not really quantify the degree of saturation as velocities tend to show appreciable change owing to the formation of hydrates and presence of free gas depend the properties of the host rock. The present chapter makes an attempt in brief to

N.K. Thakur and S. Rajput, *Exploration of Gas Hydrates*,
DOI 10.1007/978-3-642-14234-5_9,

identify the lacunae in the understanding of different signatures utilized for drawing inference about presence of gas hydrates and caution in using this information with bias.

9.1 Introduction

Gas Hydrates with their vast resource potential are likely to compliment and/or emerge as viable alternative to not so encouraging oil and gas scenario, more so for countries like US, Canada, China, India, Korea and petroleum starved countries like Japan. The exploration and exploitation of gas hydrates in the deep-water sediments encompass new opportunities and challenges. The mechanism of hydrate formations in different regions and under complex geological conditions calls for innovation to resolve the complex processes that govern their genesis. Strategies have to be worked out for its exploitation, preserving the delicate natural balance and without hampering environment in terms of climatic and geological hazards. Extensive field investigations with critical support from laboratory experiments, theoretical/numerical modeling have provided us with basic understanding about the processes that govern the formation of gas hydrate at micro and macro levels. Knowledge gained from laboratories and modeling is being validated by field data under some assumed conditions. However, scale factor difference from the laboratories to field, the observation in the field may differ from that obtained in the laboratory. We discuss here briefly different aspects of gas hydrate formation and their geophysical signatures in relevance emerging information.

9.2 Stability

The estimation of gas hydrate stability zone is prelude to searching for presence of gas hydrate in a region. It provides the depth limits under which, if hydrates are present, have to be confined to limits defined by the thermodynamic conditions of the region. The stability of gas hydrate in the subsurface earth is primarily estimated from the sea floor temperature, geothermal gradient and hydrostatic pressures created by the seawater column as well as by pressure exerted by the sediments cover. In the permafrost regions pressure due to the sediment cover and in the tropical and polar regions the hydrostatic pressure due to the water column as well as that of sediments has also to be considered for estimating probable depth up to which gas hydrates can be stable. In most of the cases stability of the hydrates in the earth is estimated considering pure water and methane gas as the main constituent of the gas composition.

However, the stability of gas hydrates is also controlled by other factors such as the ionic strength (salt content) of pore water, the presence of other gases along with methane (gas composition), and subsurface geology (Kvenvolden 1998; Macleod

1982). Due to non-availability of estimates of these parameters and prohibitive costs of acquiring such information, even if they are predicted, their significance is mostly ignored in arriving at the estimates of hydrate stability. Each of the parameters has quite distinct effect in controlling the stability of gas hydrates. Considering NACL as the main constituent of salt, shifts the temperature by about 1.5°C at the base of hydrate stability at about 3,000 m (Booth et al. 1998). On the contrary having ethane and other higher order molecular gases shifts the base of hydrate stability towards higher temperature and make hydrates to be stable at lower pressures. The presence of nitrogen with methane make the hydrate to be stable at higher pressures. Apart from this thermal conductivity of the different geological structures, distort the isotherms making the base the gas hydrates stable either at shallower (case of salt diapir) or deeper (in case of shale diapir) depths owing to higher thermal conductivity in the former case and lower thermal conductivity in the later (Macleod 1982; Taylor et al. 2000; Dillon and Max 2003). It is argued that hydrates are formed under proper physical/chemical stability conditions by the influx of methane rich fluids from deeper parts through the conduits (Ginsburg and Soloviev 1997). The influx of warm fluids also perturbs the thermal configuration and thereby alter the geothermal gradients and making the hydrate stable at shallower levels. The hydrate stability pattern associated with such configurations is quite complex and shows appreciable changes in the regions of investigations for occurrence of gas hydrates.

An estimate about the hydrate stability can be ascertained in the laboratory mainly by dissociation studies of hydrates and theoretical modeling. Thermodynamic modeling provides conditions under which the three-phase boundary for the formation of hydrates can be stable. Beyond these conditions only two phases are likely to be present. By incorporating different gas compositions and ionic strength different approaches and algorithm (Sloan 1998) have been developed and which form the basis for working out reference for establishing the hydrate stability in the field. An inference about the depth of the base of hydrate of stability can be obtained from the depth of occurrence of bottom simulating reflectors (BSRs) in the regions of investigation. BSRs mark the interface between higher impedance gas hydrate layer and low impedance free gas layer and which is likely to coincides with base of hydrate stability zone. Under these assumptions the geothermal gradients have been estimated in some parts of world and the obtained geothermal gradients match quite well with observed ones (Kaul et al. 2000). However, the causative mechanism for the formation of BSR is still being debated and relying on estimates of stability zone from such data sets may lead to erroneous estimates of hydrate stability zone.

On the basis of measured physical parameters, and theoretical considerations, the intersection point where hydrate stability phase boundary cuts across decreasing temperature and increasing pressure regime defines the top of hydrate stability zone (Osegovic and Max 2005). However, the top of the gas hydrate within the sediments has no such precisely defined limit and in many cases the top of hydrate stability zone may exists much above the seafloor (Dillon and Max 2003). In event of absence of clear signature of the upper limit of hydrate stability in remotely sensed

geophysical signature (rarely identified in seismics, Holbrook et al. 1996; Posewang and Mienert 1999), the seafloor is considered as the top of stability zone. In most of the cases the signatures of indicating the upper limit of hydrate occurrence lies couple of tens of meters below the seafloor. Gas hydrate samples collected during the DSDP and ODP expeditions have indicated that in most of the regions hydrates are stable under lower temperature and higher pressures compared to estimated base of gas hydrate zone. The presence of hydrates much above the stability zone suggests that gas hydrate stability zone is not only the unreliable 'containment' zone but also not a convincing criterion for looking for gas hydrates in the sediments (Booth et al. 1998). Estimates of hydrate stability zone only on the consideration of pressure, temperature at the seafloor and assumed geothermal gradient as has been commonly been attempted, may not provide true image of the stability zone as the chemistry and physical conditions and the geological entities may be quite complex in the nature making the estimates not totally pragmatic. A realistic estimate of hydrate stability zone in the earth require 'a priory' knowledge about various parameters such as the profile of methane concentration in the earth, gas composition, ionic strength of pore water, geological configuration as well as fluid flow pattern. Any resource assessment based on the erroneous assessment of hydrate stability zone will propagate to estimates of quantum of hydrates.

9.3 Bottom Simulating Reflector

The identification of reflector with some characteristic features (BSR) as detailed in Chap. 6 primarily in the multi-channel seismic stack section has been utilized for drawing inferences about the occurrence of gas hydrates. BSR is quite distinct in the regions where the sediment beds are folded or inclined (characteristics of accretion on the convergent plate boundary) and the crosscutting characteristic of BSR is quite evident. However, in the regions of well-bedded slope basins and areas of thick sedimentations the identification of BSR is rather difficult. It is suggested that hydrates may not form in well-bedded sediments due to reduced permeability that may impede free flow of methane and fluids (Zuehlsdorff et al. 2000).

The presence of gas hydrates in sufficient quantity strengthens the sediment frame resulting in increase of compressional velocity (Vp) and if hydrates cement the sediment grains, shear velocity Vs also increases (Chand and Minshull 2003). Laboratory studies have shown that Vp increase abruptly beyond critical value of hydrate saturation and the velocity values are not sensitive to lower saturation (Berge et al. 1999). The sediments below the hydrated layer if underlain by sediment layer saturated with lower velocities, the velocities would be still appreciably lower if the sediments are saturated with gas, producing an impedance contrast across the interface. Because the strength of the reflected signal is proportional to the change in acoustic impedance across the interface, the base of hydrate-cemented zone produces a strong reflector (BSR) that has reverse polarity to that of

the seafloor. However, reflectors mimicking the sea floor have been observed in many parts of the world. These reflectors are caused by mineralogical phase changes as in the case of, from opal amorphous silica (opal-A) to opal cristobalite (opal-CT) to quartz, which can cause an abrupt change of acoustic impedance and in turn is responsible for the presence of seismic reflectors (Wilkens et al. 1987). Owing to ambient pressure-temperature dependence of the phase transformation and abrupt increase in the acoustic velocity, reflectors associated with this phenomenon also show parallelism to the seafloor. However, because of increase in the impedance contrast, these reflectors have polarity same as that of seafloor, owing to their presence generally beyond the base of gas hydrate stability zone they can easily distinguished from those BSRs associated with gas hydrates.

The mechanism for the formation of BSR is still being debated. Which are the critical factors that govern the formation of BSR and conditions under which gas hydrates can occur in absence of BSR? The analysis and modeling of remotely sensed seismic data provide vital information about the velocities, pore saturation and some estimates of quantum of gas associated with hydrates and which differ from in situ measurements of sediment properties and resource estimates. To make remote sensed data and information drawn about different properties more meaningful, the obtained results have to be ground truthed. Attempts to validate the seismic data through sampling and well logs have added more confusion to proposed models for the formation of BSR (Hovland et al. 1997). The BSR emerges out as strong reflector in the conventional low frequency seismics (Fink and Spence 1999) but as diffused boundary in high frequency seismic data with higher velocity associated with hydrates confined to couple of meters above the BSR (Vanneste et al. 2001).

Results from the Ocean Drilling Program (Leg 146) over the Cascadian Margin have indicated BSRs with strong amplitude are not associated with significant quantities of free-gas layer (Hovland et al. 1995). Detailed velocity analysis (Yuan et al. 1996), downhole sonic log measurements (Westbrook et al. 1994) and VSP studies (Mackay et al. 1994) in the vicinity of BSR in this same region has suggested BSR is caused by the hydrated layer underlain by free gas layer. Ocean Drilling Program (Leg 164) on the Blake Ridge in the Atlantic region has suggested that the BSR strength appreciably differs from one region to other without much variation in the hydrate and free gas saturation.

Modeling results have suggested that BSR can be generated by either only hydrate layer, only free gas layer or hydrated layer underlain by the free gas layer and strength of BSR is strongest when hydrates are underlain by free gas layer and weakest when BSR is produced by the presence of hydrates only (Prasanti et al. 2009). Gas hydrates have been drilled in the regions where BSR was not distinctly identified (Holbrook et al. 1996; Ashi et al. 2002). It has been suggested that the BSRs may not be distinctly observed in the hydrate regions due to insufficient supply of methane and where base of hydrate zone may not be in contact with top of free gas zone (Xu and Ruppel 1999; Wood and Ruppel 2000). Alternatively, hydrates may be present but tectonic subsidence and sediment deposition in the slope basin results in downward movement of the base of the stability field, so that

the gas layer is transformed to hydrate and the BSR is much weakened (von Huene and Pecher 1999). It has also been observed that strength of BSR depends on its location with respect to other prominent reflectors (Posewang and Mienert 1999), with the pattern of seafloor topography (Minshull et al. 1994) and tectonic regimes (Pecher et al. 1998).

Modeling in terms of saturation of hydrates and free gas in the sediments in different regions has established that varying the saturation percentages can generate BSR. It is argued that about 30% hydrate saturation in the pore spaces in the overlying sediments may account for the formation of BSR in the Cascadian margin. On the contrary, small amount of free gas in the underlain sediments could generate BSR identified in the same region (Singh et al. 1993).

BSRs have been reported from most parts of the world, where proper physical and chemical conditions exist for the formation of gas hydrates and most of regions the presence of gas hydrates has been established based on the occurrence of BSRs. However, the genesis of BSR so far has not been fully understood. What are the factors that control the formation of BSR? Which is the dominant factor, either it is the percentage hydrate saturation in the sediment or percentage free gas saturation in layers underneath the hydrate layer. What is the likely impedance contrast between the layers to form a BSR? The velocity in sediment rocks mainly depends on the mineral content, compactness, porosity and other factors and depending the on the rock characteristics, the host matrix velocities tend to show lot of variations. If hydrate and free gas saturate different rock types, the velocity enhancement in cases of hydrates or reduction in case of free gas may significantly vary and with insignificant contribution from density, the impedance contrast also exhibits variations. The formation of BSR across an interface, representative of change physical/chemical state of matter does not provide any information that whether the phase boundary is sharp or diffused. If its is sharp boundary then question arises whether hydrates work as the trap for underlying gases, thereby making the base of hydrate to coincide with top of the free gas, a scenario unsuitable for the formation of hydrate without BSR. The processes for the formation of BSR seem to be dynamic and depends on the local environment. In this regards it is essential to consider the role of geological and tectonic factors that control in formation of BSR and governing its strength. Some understandings about biological, physical, and chemical processes that govern the formation of hydrates and generation of free-gases have been attained through extensive studies but the role local geological and other factors that may either shore up or offset such processes needs attention in future studies.

9.4 Blanking

Other inference about the presence of gas hydrates is being drawn from suppression of seismic reflectance (blanking) in the hydrated layer. Presence of blanking in seismic data has been observed over Blake Ridge (Lee et al. 1993, 1996; Dillon and

Max 2003), Lake Baikal (Vanneste et al. 2001) and many other regions. Wood and Ruppel (2000) suggest that 'Blank Zone' in seismic data may imply a paucity of horizontal reflectors rather than lack of impedance contrast. Another possible explanation provided is that spherical spreading seismic wave has finite lateral resolution and decreases with decrease in frequency and increase in distance from the reflector. Homogeneities lower than the resolvable spatial wavelengths are averaged out and due to scattering result in lower reflectivity (Clay and Medwin 1977).

The inference about the association of blanking to the hydrate presence over the Blake Ridge was questioned by Holbrook et al. (1996), who contended that blanking in Blake Ridge region could be attributed to the relative homogeneity of the sediments rather than to hydrate cementation and the blanking in the Lake Baikal was also ascribed to the acoustic characteristics of sediment rather than its association with hydrates (Vanneste et al. 2001). It has been observed that blanking increase with increasing frequency and was considered associated with the formation of hydrates in the vicinity of faults (Reidel et al. 2002). Gas hydrate tends to form in the rocks with higher porosity, i.e. medium to lower velocities. Presence of hydrates enhance velocity relative to less porous (high velocity) layers. At low saturations hydrates may reduce the impedance contrast between low and high porous regions and thereby blanking (Holbrook et al. 2002). The modeling results have suggested that blanking increases with increase in the hydrate saturations (Dillon and Max 2003). Extensive blanking in the hydrate stability zone over a wide range the Kerala-Konkan region in India has been attributed due to the lithology in the region (Reddi et al. 2001). It has been suggested that blanking in hydrate stability zone may not be solely considered, support from other parameters is required such as higher velocity to draw inference about the presence of gas hydrates in a region (Holbrook et al. 2002).

The above studies suggest that blanking, as the prime indicator of presence of gas hydrate is not fully validated by the field studies. Future investigations need extensive efforts in the laboratories and as well as in the field to validate inference drawn from blanking as one of the tools for gas hydrate exploration.

9.5 Inferences from Velocities

Acoustic velocities have been used as the tool for drawing inference about the presence and saturation of gas hydrates and free gas in the sediments. The mineral constituents, morphology, compactness, porosity, grain size and other factors, control the velocity of the sediments. Hydrate interaction with the sediment is strongly dependent on morphology, and that natural hydrate may exhibit contrasting seismic signatures depending upon the geological environment in which it forms (Priest et al. 2009). Owing to higher velocity, hydrates with their presence in sediment pores, grain contacts and on the grain surface enhance the velocity of sediments in different ways. Estimated seismic velocities show large variation

(Vp ~ 1.7–3.5, Vs ~ 0.4–1.6, Goldberg et al. 2003) in the hydrate bearing sediments. These variations are ascribed to various factors mentioned above, such as Vp values measured in fine-grained sediments containing gas hydrate were substantially lower (1,970 m/s). The presence of clay in the host rock leads to reduction in the porosity and thereby the acoustic velocity. Attempts have been made to quantify gas hydrates and free gas from the remotely sensed surface data (Yuan et al. 1996, 1999; Lee et al. 1993, 1996; Ecker et al. 2000). Enhancement/reduction in the Vp velocity has been attributed to presence of hydrates/free gas in the sediments. Presence of hydrate in the sediments increases the shear strength of the sediments and thereby also enhances the Vs velocities. The enhancement of velocities with respect to the seismic velocities of sediments without hydrate has been utilized to estimate the hydrate, free gas saturation. However, owing to different factors contributing to enhancement of seismic velocity, the determination of reference velocities may lead to biasing. In clay rich environment like Blake Ridge a small amount of hydrate may stiffen the sediment matrix on the other hand larger amount of hydrates are required in the coarse grained sediments to have same effect (Berge et al. 1999). Owing to dependency on the pore sizes and mode of hydrate formation in the sediments, the enhancement of seismic velocity may differ significantly from place to place. In this regard the data obtained during the drilling either through logs or through cores have been utilized to establish a reference velocity field. However, non availability such data sets in most of identified gas hydrate regimes makes the reference model biased. The significant difference in the scale factor between different data sets may or may not isolate the signature of reference velocity in the different data sets. Remote sensed conventional seismic data may not resolve finer details about thickness of hydrate and free gas layer. Due to the discrepancies in the resolvability, the model of the formation of BSR on the basis of velocity information may also differ from region to region. Information derived from the remotely sensed data requires support from other measurements to make the results more meaningful and quantifiable. It is likely in future Vs studies may be given more emphasis to identify the mode of hydrate occurrence either in the pores or as cement, and Vp studies may be utilized for assessing the quantum of gas bearing layers.

9.6 AVO Modeling

The information content in the Amplitude versus Offset (distance), AVO, is generally utilized to arrive rock properties, which governs the formation of a reflector. The AVO pattern primarily emerges from the Poisson's ratios across the interface, which mainly depends on the ratios of Vp and Vs across an interface, in the case of gas hydrate investigations, the variation in the density is assumed insignificant. The concentration of gas hydrate and underlying free gas will alter the rock properties (changes in the lithology and fluid) affecting the Poisson's ratio and hence the AVO pattern depending on the contribution from layers across the interface. BSR is

considered the most evident identifier for the occurrence of gas hydrates in the sediments. It has been observed that the amplitude increases (negative) with offset in presence of gas below the BSR (Andreassen et al. 1995). To arrive at the possible cause for the AVO pattern extensive modeling has been attempted in many parts of the world (Katzman et al. 1994; Andreassen et al. 1995; Tinivella and Accino 2000). These models primarily considered either a gradational hydrated layer underlain by normal oceanic sediments or free gas layer. Hyndman and Spence (1992) suggested that the pattern of AVO in Cascadian margin does not require free gas layer. On the contrary, studies of Andreassen et al. (1995) suggested that the AVO pattern in the Beaufort region could be accounted in terms of only free gas layer. All these models consider a gradational increase in the hydrate concentration in the hydrated layer and thereby sharp fall in velocity due to the presence of free gas layer. It is argued that the hydrate saturation controls the AVO pattern significantly rather than the free gas below the BSR, once the gas saturation exceeds beyond 1%. In this regard AVO pattern gives little information about the gas saturation below BSR (Andreassen et al. 1995, 1997). AVO behavior of the BSR is found not to be as useful as was earlier thought for determining the amount of free gas below the BSR. This is because Poisson's ratio change, due to free-gas is likely very small in high-porosity unconsolidated sediments. The uncertainty in the models is large, as there is no reliable Vs wave velocity information for the sediments containing hydrate or free-gas (Yuan et al. 1999). Apart from this AVO anomalies are not much affected by the thickness of the layers and thereby no knowledge is gained in the distribution of hydrate and free gas in the sediments. Modeling results of high frequency seismic data have established that BSR is not caused by the sharp impedance contrast across an interface but due to the fall in Vp (negative gradient) across the interface (Spence et al. 2003). Future studies pertaining to gas hydrate exploration may require more integrated efforts to understand the mechanism of formation of BSR in many parts of the world and make BSR more realistic representative for the occurrence of gas hydrates and free gas.

9.7 Seismic Data Acquisition

In most parts of the world the conventional seismic data acquired for the exploration of oil and gas has been utilized for the investigation for the presence of gas hydrates. Over the oceanic regions the specifications of data acquisition is meant for targeting deeper structures in the shallow waters. The seismic sources have high energy with lower frequency content quite contrary to targeting shallow gas hydrate horizons in the deeper parts of the ocean. Apart from this gas hydrate and free gas layers hardly exceed tens of meters in thickness, specifically free gas layer found to be quite thin. BSR main identifier for the presence of gas hydrates emerges out as strong reflector in conventional seismic data indicating sharp impedance contrast across an interface. In the high frequency seismic data BSR is seen as diffused reflector suggesting that steep fall in acoustic velocity across the interface. The

AVO behavior is governed by the Poisson's ratio across the interface and information about shear wave velocity is essential for generating a model for hydrate and free gas in the region of investigations. The information about the shear wave velocity through the deployment of OBS in conventional seismic data is not generally undertaken due to higher cost and complexities in data acquisition and their interpretation. Gas hydrate investigation requires a good knowledge about shear wave velocities in resolving the model for the formation of BSR and the quantification of gas hydrate and free gas reserves. In this regard seismic data acquisition specifications are significantly different from that of conventional seismic data specifications. The specification of seismic data acquisition for gas hydrate investigation require lower energy seismic source, close receiver spacing, longer streamer length, higher rate of sampling and OBS deployment to arrive for complexities associated with gas hydrate formation and quantification of gas hydrate reserves.

References

Andreassen, K., Hart, P.E., and Grantz, A., Seismic studies of a bottom simulating reflector related to gas hydrate beneath the continental margin of Beaufort Sea, Journal of Geophysical Research, 1995, 100, 12659–126732.

Andreassen, K., Hart, P.E., and Mackay, M., Amplitude versus offset modeling of the bottom simulating reflection associated with submarine gas hydrates, Marine Geology, 1997, 137, 25–40.

Ashi, J., Tokuyama, H., and Taira, A., Distribution of methane hydrate BSRs and its implication for prism growth in the Nankai Trough, Marine Geology, 2002, 187, 177–191.

Booth, J.S., Winter, W.J., Dillon, W.P., Clennell, M.B., and Rowe, M.M., Major occurrences and reservoir concepts of marine clathrate hydrates: Implications of field evidence, in: Henriet, J.P., and Mienert, J., (ed.), Gas hydrate: Relevance to world margin stability and climate change, Geological Society Special Publication, London, 1998,137, 113–127.

Berge, L., Jacobsen, K.A., and Solsted, A., Measured acoustic wave velocities of R11 (CCL3F) hydrate samples with and without sand as a function of hydrate concentration, Journal of Geophysical Research, 1999, 104, 15415–15424.

Chand, S., and Minshull, T.A., Seismic constraints on the effects of gas hydrate on sediments physical properties and fluid flow: A review, Geofluids, 2003, 3, 275–289.

Clay, C.S., and Medwin, H., Acoustical oceanography: Principles and applications, Wiley, New York, 1977, 537.

Dillon, W.P., and Max, M.D., Oceanic gas hydrate, in: Max, M.D., (ed.), Natural gas hydrate in oceanic and permafrost environments, Kluwer Academic, London, 2003, 61–76.

Ecker, C., Dvorkin, J., and Nur, A.M., Estimating the amount of gas hydrate and free gas from marine seismic data, Geophysics, 2000, 65, 563–573.

Fink, C.R., and Spence, G.D., Hydrate distribution off Vancouver island from multi-frequency single channel seismic reflection data, Journal of Geophysical Research, 1999, 104, 2909–2922.

Ginsburg, G.D., and Soloviev, V.A., Methane migration within the submarine gas-hydrate stability zone under deep-water conditions, Marine Geology, 1997, 127, 49–57.

Goldberg, D.S., Collett, T.S., and Hyndman, R.D., Ground truth: In-situ properties of hydrates, in: Max, M.D., (ed.), Natural gas hydrate in oceanic and permafrost environments, Kluwer Academic, London, 2003, 295–310.

Holbrook, W.S., Hoskins, W.T., Wood, R.A., Stephen, G.D., and Lizarralde, D., Methane hydrate and free gas on the Blake Ridge from vertical seismic profiling, Science, 1996, 273, 1840–1843.

Holbrook, W.S., Gorman, A.R., Hornbach, M., Hackwith, K.L., Nealon, J., Lizarralde, D., and Pecher, I.A., Seismic detection of marine methane hydrate, The Leading Edge, 2002, 21, 686–689.

Hovland, M., Lysne, D., and Whiticar, M.J., Gas hydrate and sediment gas composition, Hole 892A, in: Carson, B., Westbrook, G.E., Musgrave, R.J., and Suess, E., (eds.), Proceedings of ocean drilling program, scientific results, 1995, 151–161.

Hoveland, M., Gallagher, J.W., Clennell, M.B., and Lokvam, K., Gas hydrates and free-gas volume in the marine sediments: Example from Niger Delta front, Marine and Petroleum Geology, 1997, 14, 245–255.

Hyndman, R.D., and Spence, G.D., A seismic study of methane hydrate marine bottomsimulating reflectors, Journal of Geophysical Research, 1992, 97, 6683–6689.

Katzman, R., Holbrook, W.S., and Paull, C.K., Combined vertical incidence seismic study of gas hydrate zone, Blake Ridge, Journal of Geophysical Research, 1994, 99, 17975–17995.

Kaul, N., Rosenberger, A., and Villinger, H., Comparison of measured and BSR-derived heat flow values, Makran accretionary prism, Pakistan, Marine Geology, 2000, 164, 37–51.

Kvenvolden, K.A., A primer on the geological occurrence of gas hydrates, in: Henriet, J.P., and Mienert, J. (ed.), Relevance to world margin stability and climate change, Geological Society Special Publication, London, 1998, 137, 9–30.

Lee, M.W., Hutchinson, D.R., Dillon, W.P., Miller, J.J., Agena, W.F., and Swift, B.A., Method of estimating the amount of in situ gas hydrate in deep marine sediments, Marine and Petroleum Geology, 1993, 10, 493–506.

Lee, M.W., Hutchinson, D.R., Collett, T.S., and Dillon, W.P., Seismic velocities for hydrate-bearing sediments using weighted equation, Journal of Geophysical Research, 1996, 101, 20347–20358.

Macleod, M.K., Gas hydrates in ocean bottom sediments, AAPG Bulletin, 1982, 66, 2649–2662.

Mackay, M.E., Jarrard R.D., Westbrook G.K., and Hyndman, R.D., Origin of bottom simulating reflectors: Geophysical evidence from the Cascadia accretionary prism, Geology, 1994, 22, 459–462.

Minshull, T.A., Singh, S.C., and Westbrook, G.K., 1994. Seismic velocity structure at a gas hydrate reflector, offshore western Columbia, from full waveform inversion, Journal of Geophysical Research, 99, 4715–4734.

Osegovic, J.P., and Max, M.D., Compound clathrate hydrate on Titan's surface, Journal of Geophysical Research, 2005, 110, E08004, doi: 10.1029/2005JE002435.

Pecher, I.A., Rnero, C.R., von Huene, R., Minshull, T.A., and Sigh, S.C., The nature and distribution of bottom simulating reflectors at the Costa Rican convergent margin, Geophysical Journal International, 1998, 133, 219–229.

Posewang, J., and Mienert, J., The enigma of double BSRs: Indicators of change of in the hydrate stability field? Geo-Marine Letters, 1999, 19, 157–163.

Prasanti, A., Thakur, N.K., Prasada Rao, P., and Rajput, S., Modelling of BSRs as prime indicator of gas hydrates, Current Science, 2009, 96, 1258–1262.

Priest, J.A., Rees, E.V.L., and Clayton, C.R.I., Influence of gas hydrate morphology on the seismic velocities of sands, Journal of Geophysical Research, 114, B11205, doi:10.1029/2009JB006284.

Reddi, S.I., et al., Reprocessing of multi-channel seismic data of ONGC for gas hydrate exploration in offshore Goa, part II, NGRI Technical Report No.–307, 2001, pp 30.

Reidel, M., Spence, G.D., Chapman, N.R., and Hyndman, R.D., Seismic investigations of a vent field associated with gas hydrates, offshore Vancouver island, Journal of Geophysical Research, 2002, 107, 16, DOI:10.1029/2001JB000269

Singh, S.C., Minshull, T.A., and Spence, G.D., Velocity structure of hydrate reflector, Science, 1993, 260, 204–207

Sloan, E.D., Clathrate hydrate of natural gases, Marcel Dekker, New York, 1998, 705.
Spence, G.D., Hyndman, R.D., Chapman, N.R., Reidel, M., Edward, N., and Yuan, J., Cascadia margin, Northeast Pacific Ocean: Hydrate distribution form geophysical investigations, in: Max, M.D., (ed.), Natural gas hydrate in oceanic and permafrost environments, Kluwer Academic Press, London, 2003, 183-198.
Taylor, M.H., Dillon, W.P., and Pecher, I.A., Trapping and migration of methane associated with gas hydrate stability zone at Blake Ridge Diapir: New insights from seismic data, Marine Geology, 2000, 18, 209–221.
Tinnivella, U., and Accaino, F., Compressional velocity structure and Poisson's ratio in the marine sediments with gas hydrate and free gas by inversion of reflected and refracted seismic data (South Shetland Islands Antarctica), Marine Geology, 2000, 164,13-27.
Vanneste, M., De Batist, M., Golmshtok, A., Kremlev, A., Versteeg, W., Multi-frequency seismic study of gas hydrate-bearing sediments in Lake Baikal, Siberia, Marine Geology, 2001,172,1–21.
von Huene, R., and Pecher, I.A., Vertical tectonics and the origins of BSRs along the Peru margin, Earth and Planetary Science Letters, 1999, 166, 47–55.
Westbrook, G.K., Carson, B., Musgrave, R.J., et al. Proceedings Ocean Drilling Program, Interim Reports, 146, College Station, TX, 1994, 399–419.
Wilkens, R.H., Schreiber, B.C., Caruso, L., and Simmons, G., The effects of diagnosis on the microstructure of Eocene sediments bordering the Baltimore Canyon Trough. in: Watts, A.B., et al. (eds.), Initial reports of the deep sea drilling project XCV, Washington, DC, 1987, 527–547.
Wood, W.T., and Ruppel, C., Seismic investigations of the Blake ridge gas hydrate area, in: Paull, C.K, Matsumototo, R.,Wallace, P.J., and Dillon, W.P., (eds), Proceedings of the Ocean Drilling Program, Scientific Results, 2000, 164, 253–264.
Xu, W, Ruppel, C.D., Predicting the occurrence, distribution and evolution of methane gas hydrate in porous marine sediments, Journal of Geophysical Research, 1999, 104, 5081–5095.
Yuan, T., Hyndman, R.D., Spence, G.D., and Desmons, B., Seismic velocity increase and deep-sea gas hydrate concentration above a bottom-simulating reflector on the northern Cascadia continental slope, Journal of Geophysical Research, 1996,10, 13655–13671.
Yuan, T., Spence, G.D., Hyndman, R.D., Minshull, T.A., and Singh, S.C., Seismic velocity studies of a gas hydrate bottom-simulating reflector on the northern Cascadia continental margin: Amplitude modeling and full waveform inversion, Journal of Geophysical Research, 1999, 104, 1179–1191.
Zuehlsdorff, L., Spiess, V., Huebscher, C., Villnger, H., and Rosenberger, A., BSR occurrence, near surface reflectivity anomalies and small scale tectonism imaged in a multi-frequency seismic data set from the Cascadia accretionary prism, Geology Rundschau, 2000, 88, 655–667.

Index